THE UNIVERSITY *of* EDINBURGH

Modelling the neuromechanics of exploration and taxis in larval *Drosophila*

Jane Loveless

Doctor of Philosophy

Institute of Perception, Action and Behaviour
School of Informatics
University of Edinburgh

2019

Abstract

The Drosophila larva is emerging as a useful tool in the study of complex behaviours, due to its relatively small size, its genetic tractability, and its varied behavioural repertoire. The larva executes a stereotypical exploratory routine that appears to consist of stochastic alternation between straight peristaltic crawling and reorientation events through lateral bending. The larva performs taxis by biasing this behavioural pattern, allowing it to move up or down attractive and aversive stimulus gradients. Existing explanations of exploration and taxis behaviour often neglect the larva's embodiment, focusing on central pattern generation and decision making circuits within the nervous system.

In Chapter 1 of this thesis, I review the current state of knowledge regarding larval peristalsis, exploration, and taxis behaviours, as well as existing theories of their generation. I argue that an understanding of the animal's embodiment should lead to a deeper understanding of its behaviour.

In Chapter 2, I present a model of the axial mechanics of the larva, and demonstrate how the animal's body physics can be exploited to produce peristalsis by using segmentally localised, positive feedback of strain rate. The mechanical model includes viscoelastic tissue mechanics, muscular inputs, and substrate interaction while sensory feedback is modelled as a linear feedback control law.

In Chapter 3, I extend the mechanical model to study motion in the plane, including both axial and transverse deformations of the body. The feedback law is replaced by a simple model of the larval nervous system. The model includes both a segmentally localised reflex arc as well as long-range, mutual inhibition between segments. The complete model is capable of generating both peristalsis and spontaneous reorientation, leading to emergent exploration behaviour in the form of a deterministic superdiffusion process grounded in the chaotic mechanics of the larva's body.

In Chapter 4, I consider taxis behaviour. I introduce a transverse reflex capable of modulating the effective transverse viscosity of the larval body. When the larva is experiencing an increasing attractive (aversive) stimulus, the reflex acts to increase (decrease) the effective transverse viscosity, causing bending to occur less (more) easily. As a result, the model larvae approach attractive stimuli and avoid aversive stumuli. On a population level, I show that the transverse reflex can be thought of as biasing the model animals towards sub- or super-diffusion. I compare the statistics of this behaviour to those of the real larva.

In Chapter 5, I shift focus to engineered soft systems. Having successfully deployed an energy-based modelling approach in Chapters 2–4, I argue for the adoption of an energy-focused (specifically, port-Hamiltonian) approach within the field of soft robotics.

In Chapter 6, I present some initial theoretical extensions to the models presented in chapter 2–4. I first focus on the mechanics of self-righting and rolling behaviours, before modelling the ventral nerve cord of the larva using a ring attractor architecture.

Finally, in Chapter 7, I summarise the results of the previous chapters and discuss directions for future research.

Acknowledgements

I am grateful to Balazs Szigeti for providing me with experimental eigenmaggot data, and wish to thank Matthieu Louis and Richard Ribchester for their feedback on the work presented in this thesis. I have been supported by the EU Seventh Framework Programme (FP7) grant MINIMAL (reference number FP7-618045).

Declaration

I declare that this thesis was composed by myself, that the work contained herein is my own except where explicitly stated otherwise in the text, and that this work has not been submitted for any other degree or professional qualification except as specified.

(*Jane Loveless*)

05/12/2019

Table of Contents

Chapter 1

Introduction

1.1 Overview

The larval form of *Drosophila melanogaster* has emerged as a useful model organism for investigating the generation of intelligent behaviour within a reduced system. Indeed, larval *Drosophila* produces a variety of readily quantified behaviours (Gerber and Stocker, 2006; Strecher and Sprecher, 2012; Ohyama et al., 2013; Heckscher et al., 2012) and has a small nervous system of just $10,000$ neurons which permits a great range of precisely targetted genetic perturbations (Jenett et al., 2012; Tian et al., 2009; Zhang et al., 2007).

Recent work has focused on larval taxis behaviours. When placed in a sensory gradient (e.g. temperature, light, odorant) the larva appears to direct itself towards more "favourable" conditions. Larvae may learn associations between sensory cues experienced during navigation and modify their environmental preferences accordingly. Central to almost all larval taxis behaviours is the modification of a basic exploratory routine – a sequence of relatively straight "runs" separated by lateral turning events (Lahiri et al., 2011).

Neural mechanisms involved in generating the exploratory routine have been successfully localised to the ventral nerve cord (VNC) (Berni et al., 2012; Berni, 2015), the invertebrate equivalent of the spinal cord, as well as the peripheral sensory system (Song et al., 2007). Elements within these systems have been studied individually in great detail (Kohsaka et al., 2012), including a core set of mechanoreceptors, inhibitory interneurons, motor neurons, and muscle fibres forming local circuitry within each body segment of the larva. Unfortunately, most of this research has been carried out with the aim of gaining insight into mammalian molecular and cellular neuroscience.

As a result, an understanding of how identified neural elements within the larval motor system collectively contribute to the exploratory routine and successful taxis remains elusive.

One of the largest obstacles to cultivating such an understanding has been a lack of appreciation for the role of body mechanics and environmental interaction in shaping larval behaviour. Investigation of mechanics in other organisms has given great insight into their behaviour, and has helped to interpret and direct neuroscientific research (Tytell et al., 2011). For instance, an integrated neuro-mechanical model of the nematode *C. elegans* has shown that a combination of body-environment mechanics and local sensory feedback is sufficient to explain changes in gait that occur across different substrates, without any appeal to higher order central processing (Boyle et al., 2012). Computational and experimental examination of the lamprey spinal cord revealed that mechanosensory feedback is essential for aligning ongoing waves of neural activity with mechanical resonances of the body. In many respects this work parallels earlier developments in artificial intelligence and robotics, in which the crucial role of the body and environment in producing seemingly complex behaviour using relatively simple control mechanisms was expounded (Brooks, 1991; Steels, 2007). Ultimately, to understand how identified neural elements within the *Drosophila* larva may contribute to the exploratory routine, an appreciation of body mechanics and environmental interaction will likely be extremely important.

In this document I will outline the current state of knowledge regarding *Drosophila* exploratory behaviour and its neural correlates. I will then critique the only existing model of motor control in *Drosophila*, and argue for a new approach based on modelling larval biomechanics and viewing control mechanisms within an embodied, environmentally embedded context. I will present some initial findings gained from taking such an approach before discussing planned future work.

1.2 Literature review

1.2.1 Anatomy of the *Drosophila* larva

A recurring theme in biology and embodied AI is the importance of physical structure in understanding function. Accordingly, before describing the behaviour of the *Drosophila* larva, it is useful to become familiar with its anatomy.

The *Drosophila* larva is a segmentally patterned, soft-bodied animal with a roughly

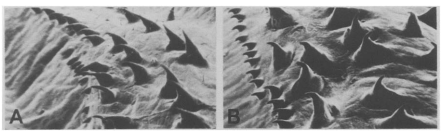

(a) Denticle bands of the *Drosophila* larva. Reproduced from (Inestrosa et al., 1996).

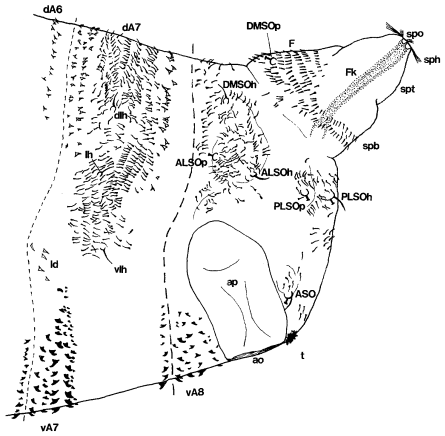

(b) Abdominal segments 7 and 8. The tail of the larva merges with A8. Reproduced from (Jürgens, 1987).

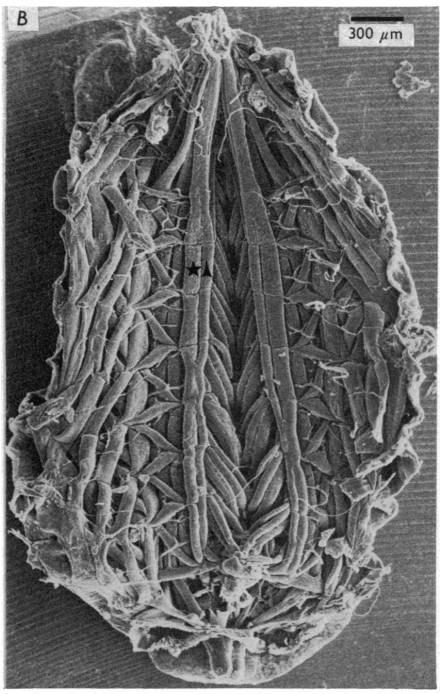

(c) Scanning electron micrograph of the larval somatic musculature. Reproduced from (Jan and Jan, 1976).

Figure 1.1: Anatomical features of the larval body.

cylindrical geometry. The integument (cuticle, epidermis, skin) of the larva is organised into three thoracic (T1–T3) and eight abdominal (A1–A8) segments (Jürgens, 1987). The segments may be identified by the location of denticle bands (rows of asymmetric tooth-like projections) present on the ventral surface of the organism, which run medio-laterally along the boundaries between cuticle segments (Inestrosa et al., 1996) (Figure 1.1a). A developmentally separable tail segment is continuous with the most posterior segment (A8), from which several thorny projections and two spiracle openings extend (Figure 1.1b) (Jürgens, 1987). The head of the larva is identifiable with thoracic segment T1, which houses the multisensory dorsal organs. T1 also contains an opening in the ventral cuticle leading to the digestive tract, flanked by two *mouth hooks* which interact with the substrate during feeding and locomotion (Schoofs et al., 2014). It is likely that the cuticle contains some form of fibre reinforcement since this is a key anatomical feature of other soft-bodied, hydrostatic animals (Kier et al., 2008), but this has not yet been shown experimentally.

Just beneath the larval epidermis lies an intricate arrangement of $\sim$600 muscle fibres (MFs), arranged in a repeating pattern of 30 MFs per *hemisegment* (half a body segment, divided by the dorso-ventral antero-posterior plane, Figure 1.1c). The majority of MFs are oriented longitudinally along the body, or at slight oblique angles (21 MFs), with a minority arranged circumferentially or at large oblique angles (9 MFs) (Bate, 1990; Enriquez et al., 2012). Each MF is attached to the integument and neighbouring MFs via tendon cells, which are mainly located at the boundaries between body segments. These cells contain dense arrays of microtubules and actin filaments, which are thought to be specialised for transmission of muscle forces (Volk, 1999; Alves-Silva et al., 2008), and likely form relatively rigid structural elements.

The somatic musculature is separated from the haemocoel (inner body cavity) by the fat body, which supplies chemical energy required for muscular contraction (Arrese and Soulages, 2010). The haemocoel itself is unsegmented – coelomic fluid (haemolymph, circulatory fluid) runs the entire length of the body, bathing the viscera and providing the larva with a hydrostatic skeleton. Several nerve bundles extend through the haemolymph from the muscle fibres, cuticle, and viscera to the central nervous system (CNS), which lies within the thoracic segments (Kohsaka et al., 2012).

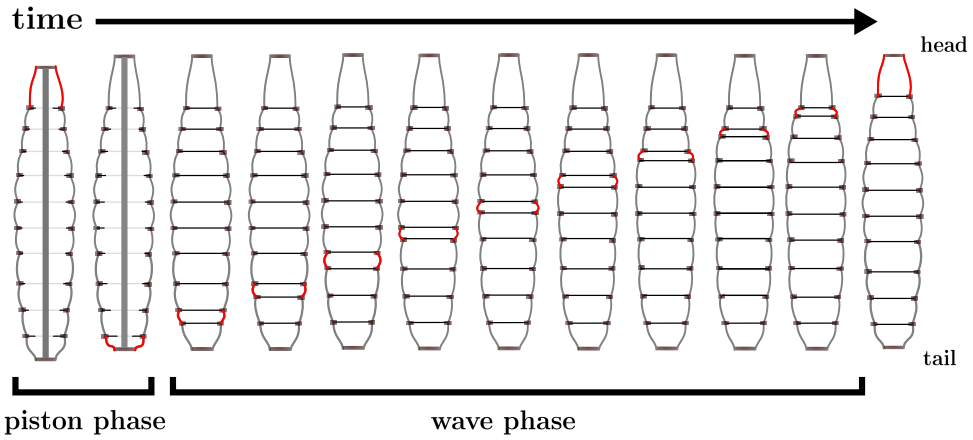

Figure 1.2: **crawling in larval *Drosophila*** :
Drosophila larvae crawl using a two-phase visceral pistoning mechanism. During piston phase the head, tail, viscera, and coelomic fluid move forward in tandem. Then, during wave phase, a longitudinal wave of segment compression travels from the posterior to anterior of the body.

1.2.2 Larval behaviour and kinematics

Having outlined the physical structure of the *Drosophila* larva, its behaviour and kinematics (i.e. what the larva *does* with this structure) may now be discussed.

The larva exhibits a variety of locomotor behaviours. When navigating on planar environments, such as the agar-coated plates used in many taxis and learning experiments (Gerber and Stocker, 2006; Yarali et al., 2009), the larva moves by alternating between relatively straight forward runs and lateral turns (Lahiri et al., 2011). Backward crawling, rearing, and rolling may be observed in this setting, but are relatively uncommon and generally occur in response to noxious or acute aversive stimuli (Oku-sawa et al., 2014; Ohyama et al., 2015; Berni, 2015). Larvae also dig and tunnel in naturalistic environments (Godoy-Herrera, 1986), and this may be observed in the laboratory when agar concentrations are low and the substrate is relatively non-rigid (Apostolopoulou et al., 2014). In what follows, the focus will lie firmly on linear crawling and turning behaviours, since they form the essential structure of the larval exploratory routine which is modified during taxis (Lahiri et al., 2011).

Of these behaviours, linear crawling has received the most attention. Kinematic evidence suggests that forward locomotion relies on a two-phase *visceral pistoning* mechanism similar to that observed in *Manduca sexta* caterpillars (Simon et al., 2010; Heckscher et al., 2012) (Figure 1.2). During *piston phase*, the head, tail, and viscera

of the organism move forward in a single step. Then, during *wave phase*, a travelling wave of compression propagates from the posterior to the anterior of the animal, moving each segment forwards in sequence. When the travelling wave reaches the head, this process repeats.

The cycle period of locomotor waves is remarkably constant within a given environment (Berrigan and Pepin, 1995; Heckscher et al., 2012), as is the phase lag between individual segment movements (personal communication, Stefan Pulver, University of St. Andrews). Larvae exposed to aversive stimuli such as an increase in temperature or illumination exhibit a decreased cycle period and a corresponding increase in overall locomotion speed (Song et al., 2007; Xiang et al., 2010; Kohsaka et al., 2014). Response to a nutrient-rich substrate is surprisingly bimodal – one population of larvae show a decrease in cycle period and increase in overall speed, while the remainder show an increase in cycle period and decrease in overall speed (Sokolowski and Hansell, 1992). Notably, there appears to be little correlation between the speed of locomotion and the magnitude of segmental movements during such responses; larvae alter speed by producing more or less locomotor waves per unit time, rather than by changing the distance stepped during each wave generated (Sokolowski and Hansell, 1992; Heckscher et al., 2012).

The other key element of exploratory behaviour, turning, is initiated by asymmetric shortening of thoracic segments following arrival of a peristaltic wave at the head. This shortening acts to "swing" the head of the larva to the left or right, and may be repeated several times in sequence (Hughes and Thomas, 2007; Lahiri et al., 2011; Berni, 2015). The head may also be lifted from the substrate during this behaviour (Okusawa et al., 2014). Once the head comes to rest, peristaltic waves resume. Each peristaltic wave appears to "drag" the animal through the bending point, while the bend appears to propagate backwards along the body. If the body is bent through a large angle, the first wave will be generated at the bending point. Otherwise, waves begin at the tail (Hughes and Thomas, 2007; Lahiri et al., 2011).

In the absence of attractive or aversive stimuli, larvae spontaneously transition between straight crawling and turning. Successful taxis hinges on modulation of this routine (Berni, 2015). The duration of straight runs is shorter if the larva is heading away from an attractive stimulus or towards an aversive stimulus, and the amount of time spent turning is correspondingly increased (Gomez-Marin et al., 2011; Tastekin et al., 2015). Turn magnitude correlates with stimulus direction, with turns of greater angle occuring if the larva is heading away from an attractive stimulus or towards an

aversive stimulus (Luo et al., 2010; Kane et al., 2013). By continually modifying its behaviour in this way, the larva is able to spend more time close to attractive stimuli, and thus accomplishes taxis.

1.2.3 Neural control of locomotion in larval *Drosophila melanogaster*

Understanding *how* the larva is capable of producing the behaviour described in the previous section is a subject of intensely active research. Most work has focused on the central nervous system (CNS), which in larval *Drosophila* consists of two brain lobes communicating with a set of fused abdominal and thoracic ganglia (collectively termed the ventral nerve cord, VNC) via the suboesophageal ganglion (SOG). Exploratory behaviour continues even after brain lobes and SOG have been inactivated through surgical or genetic means (Berni et al., 2012; Berni, 2015), suggesting that neural control of crawling and turning may be localised to the VNC and periphery.

In the following sections, I will attempt to provide an overview of the neural elements relevant to producing exploratory behaviour. This overview may appear somewhat fragmented – there has so far been little effort to integrate our understanding of each of the described elements into a cohesive model of motor control.

1.2.3.1 The ventral nerve cord

The VNC of the larva may contain up to ∼7000 neurons (∼200–300 neurons per hemisegment, based on embryonic cell counts), arranged in a ladder-like structure (Landgraf et al., 1997; Rickert et al., 2011). As with other regions of the *Drosophila* nervous system, cell bodies are arranged around the outer edges of the VNC. Neurites extend inwards and form a dense mat of connections (called neuropil), or project in bundles to the periphery.

Of the ∼310 neurons in each VNC hemisegment approximately 40 are motor neurons (Landgraf et al., 1997). These cells send axons out of the VNC towards specific muscle fibres; their dendrites form a myotopic arrangement within the dorsal VNC neuropil (Figure 1.3b) (Landgraf et al., 2003; Mauss et al., 2009; Kim et al., 2009). The remaining neural cells lying within the VNC are interneurons, many of which appear to play a modulatory role (Santos et al., 2007). Approximately 42 sensory neurons send axons into the ventral VNC neuropil per hemisegment (Kohsaka et al., 2012); their cell bodies and dendritic arborisations lie within the cuticle (Figure 1.3a). Supporting these neural cells are 30 glia per hemisegment (Ito et al., 1995; Beckervordersandforth et al.,

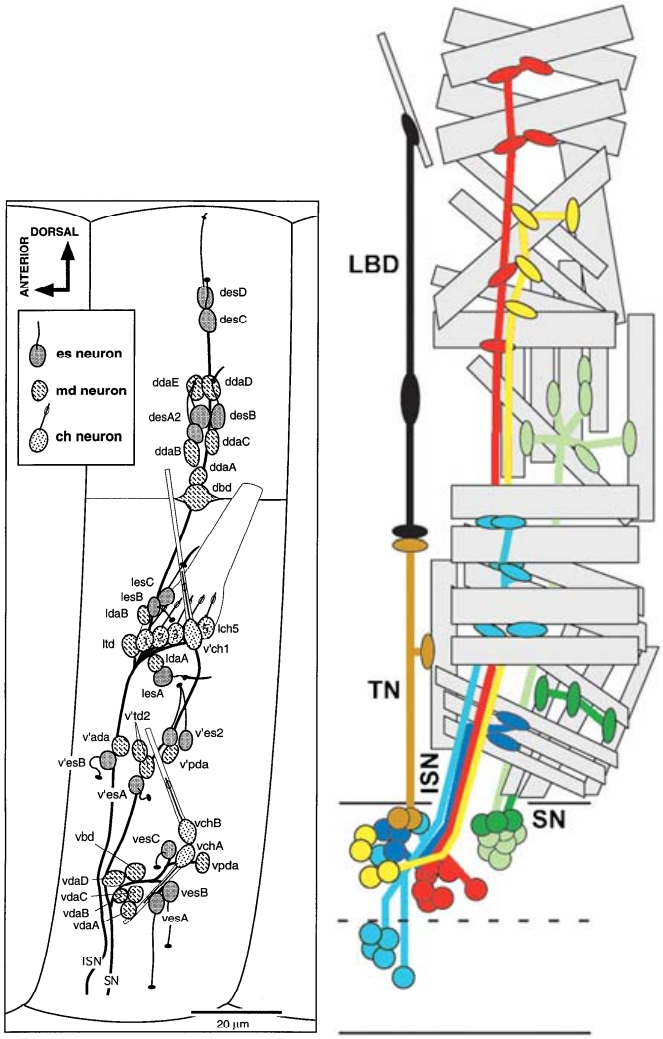

(a) Abdominal peripheral sensory neurons in the *Drosophila* larva showing cell body locations. Reproduced from (Merritt and Whitington, 1995).

(b) Abdominal motor neurons in the *Drosophila* embryo with cell body positions within the VNC (bottom) and peripheral projections to muscle fibres (top). Reproduced from (Landgraf and Thor, 2006).

Figure 1.3: Sensory and motor neuron projection patterns.

2008); the functions of these cells are presently unclear.

1.2.3.2 Motor neurons and the neuromuscular junction

Of the elements of the motor system to be discussed, motor neurons and their synapses onto muscle fibres are the most thoroughly characterised.

Electrophysiological and optogenetic recordings of motor neuron output have revealed rhythmic waves of bursting activity which propagate along the anterior-posterior axis of the VNC during fictive crawling, and correlate with peristalsis-like movement of the body wall (Fox et al., 2006). *En passant* sharp electrode recordings from motor nerves connecting the VNC to the somatic musculature show that ensemble activity slowly rises during a burst before abruptly dying down (Fox et al., 2006). Patch-clamp recordings from individual motor neuron cell bodies within the VNC illustrate the existence of distinct populations of neurons which become active at different times within a burst, despite receiving identical synaptic input (Schaefer et al., 2010). The timing with which a particular cell becomes active is correlated with the type of synaptic connection it makes with muscle fibres (Figures 1.4a and 1.4b). Cells with big synaptic boutons (type Ib) tend to start spiking immediately following depolarisation before adapting and showing a slowed firing rate. In contrast, cells with small boutons (type Is) show a delayed time-to-first-spike following depolarisation, and appear to be non-adapting or slowly adapting (Schaefer et al., 2010; Choi et al., 2004). Differences in firing properties of these two cell types have been linked to differences in potassium channel and sodium-potassium pump kinetics (Tsunoda and Salkoff, 1995; Choi et al., 2004; Pulver and Griffith, 2010; Srinivasan et al., 2012). The combination of these spiking patterns may underlie observed ensemble behaviour.

Muscle fibres become depolarised and contract in response to glutamate release from motor neuron terminals (Jan and Jan, 1976). Depolarising junction currents arising from release at type Is boutons are observed to be significantly larger than those at type Ib boutons (Kurdyak et al., 1994). As a result, the rate of muscle fibre depolarisation is often observed to increase over the course of motor neuron bursting, as more neurons with type Is boutons are recruited (Cattaert and Birman, 2001). Exactly how the activity patterns of motor neurons and muscle fibres relate to force production or motion of the larval body remains unclear.

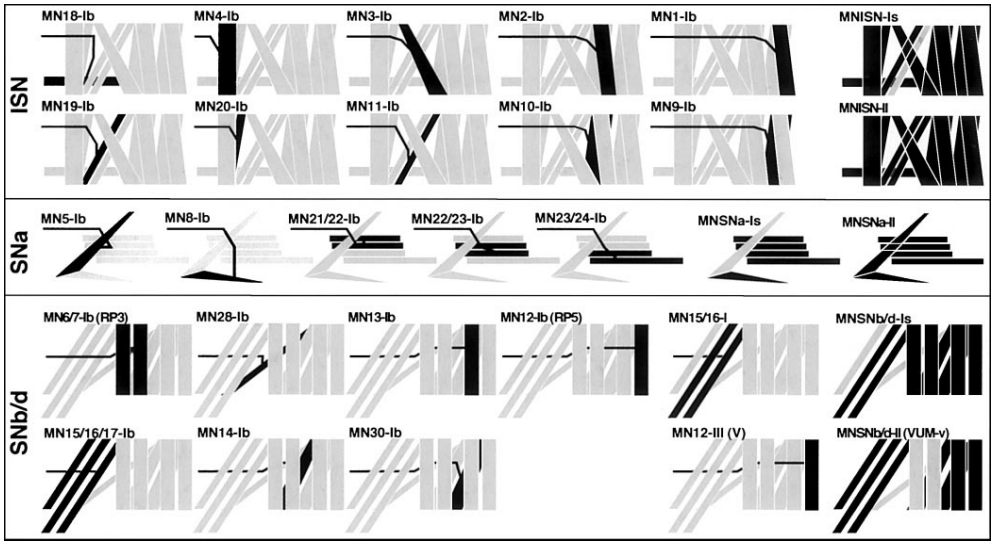

(a) Abdominal motor neurons in the *Drosophila* larva with projections to muscle fibres and synaptic bouton type. Note that neurons with Is-type boutons project to a large number of muscle fibres while those with Ib boutons project to a small number of muscle fibres. Reproduced from (Hoang and Chiba, 2001).

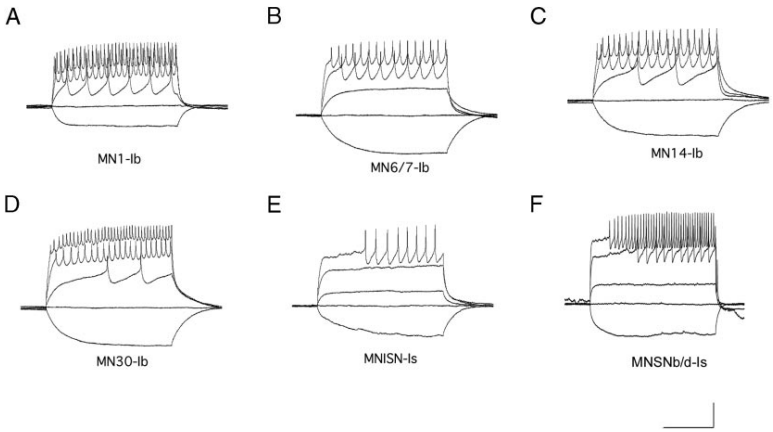

(b) Firing properties of a subset of motor neurons in the abdominal VNC. Note that neurons with Is-type boutons show higher threshold and delay-to-first-spike compared to neurons with Ib boutons. Reproduced from (Choi et al., 2004), permission pending.

Figure 1.4: Detailed motor neuron projection patterns and firing properties.

1.2.3.3 Sensory neurons and the role of feedback in motor control

As mentioned earlier, approximately 42 peripheral sensory neurons in each hemisegment send axons into the ventral neuropil of the VNC. These neurons have been split into three classes according to their morphology : external sensory organ (es) neurons, chordotonal organ (cho) neurons, and multidendritic (md) neurons. The md neurons are classified as bipolar (bp), or dendritic arborization (da) neurons; the latter are further split into classes I, II, III, and IV. cho, bp, and class I/IV da neurons have been shown to be particularly important for production of a normal exploratory routine.

bp and class I da neurons have relatively simple dendritic structures which spread linearly through the cuticle, along the anterior-posterior axis (Grueber et al., 2002; Špela Schrader and Merritt, 2007). Their axons extend to a relatively dorsal location within the VNC neuropil, close to motor neuron dendrites onto which they may directly synapse (Merritt and Whitington, 1995; Špela Schrader and Merritt, 2007; Grueber et al., 2007; Couton et al., 2015). Although direct electrophysiological or optogenetic recordings from these cells are lacking, experimental perturbations suggest they are involved in mechanosensation. Indeed, blocking synaptic transmission from these cells using the temperature-sensitive *shibire* construct results in severely decreased propagation speed and increased cycle period of locomotor waves, as well as an increase in the number of backward waves generated (Hughes and Thomas, 2007; Song et al., 2007). Larvae which have developed in the complete absence of peripheral sensory feedback also show these characteristics (Suster and Bate, 2002), as do isolated VNC preparations (Fox et al., 2006). This suggests that bp and class I da neurons may function to align centrally generated waves with the properties of the body and its environment.

Based on observations in other insect species, cho neurons are thought to relay information from vibration-sensitive organs in the cuticle to the VNC. cho mutant larvae display an increased bias toward turning rather than crawling behaviours. During linear locomotion they have a decreased average speed, reflecting an increase in peristaltic cycle period (Caldwell et al., 2003). There is some evidence that cho neurons express the same mechanosensitive ion channels as do bp and class I da neurons (Špela Schrader and Merritt, 2010), suggesting that *Drosophila* cho neurons may serve as low-frequency mechanosensors as well as high-frequency vibration sensors.

Class IV da cells have complex dendritic arborizations which spread widely through the cuticle, and respond to a wide range of nociceptive cues including increased light (Xiang et al., 2010; Strecher and Sprecher, 2012) and “sharp” objects touching the

cuticle (Ohyama et al., 2015). Mechanosensory activation of these cells is necessary and sufficient to generate rolling behaviour – an escape strategy thought to help larvae evade parasitoid wasps (Hwang et al., 2007; Robertson et al., 2013; Ohyama et al., 2013, 2015). Light activation of class IV da cells drives a negative phototaxis response involving modulation of the normal exploratory routine (Xiang et al., 2010). This is possible even when the brain lobes and SOG are inactivated (Berni et al., 2012), suggesting that the VNC is not only capable of generating exploratory behaviour alone, but can also modulate this behaviour according to sensory cues.

The epithelial sodium channel DEG/ENaC appears to be an especially important molecular component of class IV da cells (Adams et al., 1998). Mutant larvae lacking the Pickpocket1 (PPK1) subunit of DEG/ENaC show a vastly increased preference for linear crawling compared to turning behaviour, and have a large decrease in peristaltic cycle period (Ainsley et al., 2003). As a result, ppk1 mutant larvae travel in a remarkably straight line at very high speed. Exactly how this phenotype arises is unknown.

1.2.3.4 Interneurons and modulation of motor output

The previous sections have illustrated the importance of peristaltic cycle period and run/turn bias as locomotor parameters altered during taxis or by experimental manipulation, and have mainly discussed the role of primary motor and sensory neurons. The interneurons responsible for mediating and modulating sensori-motor transformations have only recently been subject to experimental investigation. In this section I will present those recent results relevant to the control of peristaltic cycle period and run/turn bias.

Within the VNC, a class of inhibitory premotor interneurons termed PMSIs have been discovered to be important for the control of crawling speed. PMSIs become active slightly after motor neurons within the same VNC segment (Kohsaka et al., 2014), and inhibit motor neurons via glutamatergic synapses (Rohrbough and Broadie, 2002; Kohsaka et al., 2014). Experimentally inhibiting PMSI activity leads to a drastic increase in peristaltic cycle period and corresponding decrease in overall speed of locomotion, with no change in the distance travelled by each segment during a wave. This appears to be due to a role of PMSIs in decreasing motor neuron burst duration (Kohsaka et al., 2014). Unpublished data suggests that PMSIs receive direct input from peripheral sensory neurons (Kohsaka et al., 2014), which may help to explain the effects of peripheral sensory deprivation on locomotor cycle period.

Cycle period has also been shown to be under descending control by a 4-cell cluster

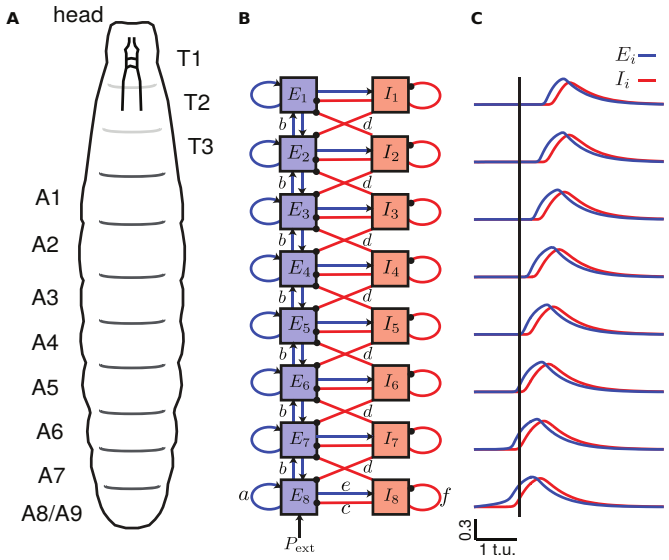

Figure 1.5: The model of peristaltic wave generation proposed by (Gjorgjieva et al., 2013). (a) the larval body. (b) each VNC hemisegment is modelled as containing an excitatory (E) and inhibitory (I) population. These populations are coupled within and between segments. (c) the model produces a propagating wave of population activity. Reproduced from Gjorgjieva et al. (2013).

of Hugin-expressing neurons in the SOG. Optogenetic activation of these cells leads to an increase in the cycle period of peristaltic waves (Schoofs et al., 2014), though the exact mechanism of their action is unclear. Interestingly, activation of a second group of 16 Hugin cells in the SOG is sufficient to terminate feeding behaviours and initiate an exploratory routine (Schoofs et al., 2014), while a (possibly overlapping) group of 12 cells (NP4820 neurons) are able to initiate turning behaviour specifically (Tastekin et al., 2015). These results suggest that while the SOG is not required for the generation of a normal exploratory routine, it does play an important role in modulating and directing motor output. This agrees with observations that the SOG is involved in processing sensory cues from across the body. Unfortunately, the VNC targets of SOG neurons are unknown at present, though they will likely be discovered in the near future.

1.2.4 The existing model of *Drosophila* motor control

At present, there are two existing computational models of *Drosophila* motor control (Figure 1.5). The first was presented in (Gjorgjieva et al., 2013). As with the experimental investigations outlined in the previous sections, this model focuses on activity

within the ventral nerve cord and makes no reference to larval mechanics. Each VNC hemisegment is modelled as containing an excitatory and an inhibitory population, and is represented by a Wilson-Cowan (WC) mean-field model.

The excitatory and inhibitory populations within a VNC hemisegment are coupled using traditional WC parameters, leading to isolated hemisegments showing oscillatory activity when given constant excitatory stimulation. Populations in different hemisegments may be coupled according to different schemes which give rise to propagating waves of activity with varying degrees of robustness and lateral synchronisation.

There are several major problems with the modelling approach taken:

1. Mean-field modelling of the hemisegmental neural population is difficult to justify given the small population sizes involved, and ignores what is known about individual neuron firing properties. The model does not take advantage of the level of detail at which the *Drosophila* nervous system can be, and has been, investigated empirically.

2. The assumption that hemisegmental populations are intrinsically oscillatory has no direct empirical basis. Non-oscillatory parameter regimes are not examined.

3. Phase relationships between head and tail population activity in the model do not match observations from the real larva. In the model, there is a refractory period following the head population becoming active causing delayed activity at the tail. In the real larva, there is a near constant phase relationship between segmental movements throughout the body.

4. The mechanics of the larval body is ignored; there is no indication that the waves produced by the model should be capable of generating motion across a substrate. In fact, plugging this neural model into the biomechanical model presented in the next chapter does not result in locomotion due to excessive overlap of activity in neighbouring segments, which causes a drastic reduction in net force production.

Ultimately, the model presented in (Gjorgjieva et al., 2013) may be useful in gaining a general understanding of the generation of activity waves in systems of large, coupled neural populations, but fares poorly as a model of peristaltic wave generation in the *Drosophila* larval VNC.

The second extant computational model of *Drosophila* motor control was presented in Pehlevan et al. (2016) (note that this model was published during preparation of this

thesis). This model combines biomechanics, sensory feedback, and central pattern generation, to reproduce many features of real larval peristalsis Pehlevan et al. (2016). However, this model only aimed to explain forward locomotion, and accordingly contained explicit symmetry-breaking elements in the form of posterior-anterior excitatory couplings between adjacent segments of the VNC, and posterior-anterior projections from proprioceptive sensory neurons in one segment into the next segment of the VNC.

No biomechanical models of turning in the larva have yet been published, but the sensory control of reorientation behaviour has been explored in more abstract models Luo et al. (2010); Gomez-Marin et al. (2011); Davies et al. (2015); Hernandez-Nunez et al. (2015); Gepner et al. (2015); Schulze et al. (2015); Wystrach et al. (2016). No current model accounts for both peristalsis and reorientation behaviours, and no current model of peristalsis can account for both forward and backward locomotion without appealing to additional neural mechanisms.

1.2.5 Taking an embodied perspective

What might be an alternative approach to modelling the production of larval exploratory behaviours?

Arguably the most important feature of any model of behavioural generation is that it should actually produce some form of behaviour. Since any behaviour exhibited by a biological organism involves physical action in a physical environment, this necessitates an amount of mechanical modelling. It must be recognised that this is not just some awkward technicality; rather, an appreciation of mechanics can be incredibly useful in understanding the role of non-mechanical elements of a behaving system. The body, in its environment, will exhibit dynamics of their own which will shape the computations that a control system must perform in order to produce a given behaviour.

The idea that an agent's embodiment is important for understanding its behaviour has received a lot of attention within the artificial intelligence and robotics communities. In the early 1990's, Rodney Brooks showed that furnishing a physical body, embedded in the real world, with extremely simple sensorimotor processing capabilities was sufficient to generate incredibly complex behaviour without requiring the use of internal representations of the world or the agent's long-term goals (Brooks, 1991). Around the same time, Tad McGeer developed his passive dynamic walkers – purely mechanical devices capable of producing naturalistic walking behaviour with-

out any sensing, actuation, or control, and powered only by moving down a slight incline (McGeer, 1990). Combining such devices with some active elements enables walking over very long distances with minimal on-board power and computational requirements (Collins et al., 2005; Bhounsule et al., 2012). Recent work has focused directly on the computational capacities of physical bodies, showing that elastic bodies may be used to implement arbitrary nonlinear input-output transformations.

Ideas developed within embodied AI and robotics have also influenced biology. An excellent review of the importance of embodiment in understanding and directing neuroscientific research is given by (Tytell et al., 2011). One particularly relevant line of investigation has focused on the locomotion of the nematode *C. elegans*. Initially, it was thought that the worm was capable of producing two distinct gaits – swimming in liquids or crawling on solids (Pierce-Shimomura et al., 2008) – hypothesized to be controlled by separate neural circuits. It was then shown that a full range of intermediate gaits could be observed by placing the worm in intermediate media, suggesting behaviour might be controlled by central modulation of a single neural circuit (Berri et al., 2009). An integrated neuromechanical model of *C. elegans* locomotion has shown that central modulation of neural activity is in fact not necessary to produce appropriate gaits in different environments. Rather, a fixed neural circuit is capable of producing the required behavioural changes by driving muscle activation within a body segment according to feedback of muscle stretch within the same segment (Boyle et al., 2012). In this way, *C. elegans* does not need to maintain an internal representation of the external world in order to appropriately modulate motor output; the worm instead relies on continuous feedback of the mechanical state of its body.

A recognition of biomechanical factors has been key to understanding the morphology and behaviour of the many animals which utilise hydrostatic skeletons for support and/or transmission of muscular force Kier (2012). For instance, the internal body cavity of earthworms is divided by septa into discrete, roughly cylindrical, compartments. The fluid within each compartment is incompressible, so that each independently conserves volume. This allows a circular muscle group (directed circumferentially around the body wall of each segment) and a longitudinal muscle group (directed axially along the body wall of each segment) to act antagonistically – active contraction of the circular muscle group causes axial extension of the segment, while active contraction of the longitudinal muscle group causes circumferential expansion of the segment, due to the conservation of fluid volume within each segment. Thus, active contraction of longitudinal muscles can be used to extend circular muscles and to provide environ-

mental support through circumferential expansion, while active contraction of circular muscles can be used to extend longitudinal muscles and to produce the axial extension which is critical for locomotion Alexander (2003); Chapman (1950). It would clearly be very difficult, if not impossible, to understand how the nervous system of this animal ought to coordinate muscle activities for locomotion without first understanding the hydrostatic coupling of circumferential and axial degrees of freedom via volume conservation.

Even in the lamprey, an animal for which great importance is placed upon "feedforward" central pattern generation of motor activity patterns rather than reflexive control (Grillner and Wallen, 1984; **?**; Grillner, 2006), an appreciation of the animals' embodiment has been crucial. Indeed, combined simulation of neural and mechanical elements in lamprey swimming were important in demonstrating that central pattern generation is sufficient to produce observed swimming and turning behaviours, and that a small set of parameters corresponding to brainstem input to the spinal cord were sufficient to produce a wide variation of swimming speeds (Ekeberg, 1993; Ekeberg and Grillner, 1999; Williams and McMillen, 2015). Furthermore, embodied modelling efforts have helped to elucidate the role sensory feedback may play in this animal. For instance, Hamlet et al. (2018) used their neuromechanical model to show that curvature feedback using different connection schemes could produce changes in the swimming beat frequency, the duration of active muscle contractions, and markedly effect the energetic cost of locomotion.

The examples given here are by no means exhaustive, but should serve to demonstrate the importance of appreciating an animal's embodiment for producing its behaviour. Again, it should be immediately obvious that biomechanics and environmental interaction are absolutely unavoidable when pursuing understanding of any animal's behaviour.

In the next chapter I will describe some of the initial steps I have taken to build an embodied model of *Drosophila* exploratory behaviour. This chapter focuses on the mechanics of linear crawling alongside a simplified, non-neural control scheme based on segmentally localised linear state feedback.

In chapter 3 I extend this model to study motion in a plane, including axial and transverse motions of the body. A neural control scheme is developed, bearing some resemblance to the linear state feedback model of chapter 2. The model of chapter 3 is capable of producing substrate exploration.

In chapter 4 the model is further extended to include taxis behaviour, by incorpo-

rating a descending sensory input that interacts with segmentally localised transverse reflexes.

Chapter 5 focuses on the use of energy-based modelling techniques in the field of soft robotics, drawing on some of the core concepts of chapters 2–4 to provide some guidance for engineering soft systems.

In chapter 6 I present some initial results on modelling two of the larva's"3-dimensional" behaviours, self-righting and rolling, which were not captured in the rectilinear model of chapter 2 or the planar models of chapters 3 and 4. I also include some results on modelling the larval ventral nerve cord by using a ring attractor, rather than rhythm generator, architecture.

The thesis closes with chapter 7, providing a summary of the presented work and a discussion of possible future research directions.

1.3 Summary

1. the *Drosophila* larva is a soft-bodied animal possessing a segmentally patterned cuticle, packed with muscle fibres and sensory neurons, surrounding a hydrostatic skeleton

2. the larva navigates planar substrates using a sequence of straight crawls punctuated by turns

3. crawling involves simultaneous motion of the head, tail, and viscera followed by a wave of bilaterally symmetric segmental movements

4. turning involves unilateral contraction localised to thoracic segments, followed by a backward wave of unilateral segmental contraction that travels down the body while "crawling" waves resume

5. central circuits in the ventral nerve cord produce waves of motor neuron activity which mirror peristaltic waves in the periphery

6. peristaltic cycle period and crawling/turning bias are key locomotor parameters; both are influenced by sensory feedback, descending control, body structure, and the environment

7. understanding an organism's mechanical properties can give deep insights into its behaviour; thus far, the relevance of body mechanics for larval *Drosophila*

peristalsis has been considered but the relevance to substrate exploration and taxis (including both peristalsis and reorientation) is yet to be investigated

Chapter 2

A neuromechanical model of peristalsis

2.1 Introduction

In this chapter, I investigate the mechanics underlying peristaltic locomotion, and develop a control scheme for producing this behaviour. This is facilitated by modelling only the axial mechanics and rectilinear motion of the larva.

The chapter is largely comprised of the published research paper, "A Model of Larval Biomechanics Reveals Exploitable Passive Properties for Efficient Locomotion", published in Lecture Notes in Computer Science 9222 – Living Machines 2015: Biomimetic and Biohybrid Systems (2015). This paper was co-authored by myself, Konstantinos Lagogiannis, and Barbara Webb. I was responsible for constructing all models in this paper, analysing them, and interpreting the results. I completed the majority of the writing for this paper and prepared all figures apart from Fig. 5 which was prepared by Konstantinos Lagogiannis. In addition, Konstantinos Lagogiannis supervised model development and analysis, conducted resonance analysis of the model (Fig. 5 and Section 3.3, *Resonance and Preferred Input Timing*) and contributed writing to the discussion section of the paper. Barbara Webb provided project supervision and contributed writing to the introduction and discussion sections of the paper.

The model in this paper is developed within the framework of Newtonian mechanics. A set of point masses represent the boundaries between body segments. The masses interact with each other via linear springs and dampers in a Kelvin-Voigt arrangement, modelling the viscoelastic properties of the larval cuticle, and interact with the substrate via an anisotropic Coulomb sliding friction model with kinetic and static

components. Incompressible coelomic fluid is modelled by holding the total length of the larva constant. This leads to the model having a ring topology, in which the head and tail are directly mechanically coupled, and their motion comprises a single degree of freedom. The equations of motion are non-dimensionalised so as to reduce the number of free parameters in the model. This process is detailed in Section 2.3 of this chapter.

To begin analying this model, I first focus on the motion of a single segment boundary under the action of viscoelastic and sliding friction forces, i.e. as a result of passive dynamics. I show that these forces can give rise to "stepping", in which an initially displaced segment boundary will move towards and possibly past its equilibrium position due to the action of elastic forces, before eventually being held in place by substrate interaction.

I also use the case of a single segment boundary to illustrate the role of the parameters in the anisotropic Coulomb sliding friction model.

Next, I determine the motion of the entire body under the action of passive forces, starting from similar initial conditions in which a single segment boundary is displaced from equilibrium (one segment is compressed). In this case the passive dynamics of the body supports the propagation of a compression wave through the body. The coupling of head and tail via the total length constraint allows a wave reaching the head to cause compression of the tail, initiating a new wave travelling in the same direction.

The presence of viscous and sliding friction causes energy to be lost from the body during motion, resulting in a gradual decay of wave amplitude. Accordingly, increasing either the viscosity of the body or the magnitude of sliding friction causes the wave to propagate a shorter distance through the body; for highly frictive cases no propagation is possible at all.

This motivates a consideration of how to orchestrate muscle tensions in order to counteract these energy losses. I proceed by calculating the power flow into the body from a sinusoidally varying force applied to the tail of the larva, finding that both the direction and timing of the force relative to the tail velocity is critical: power flow into the body is maximised when driving force is in phase with velocity.

To fulfil this condition, I construct a minimalistic, reflexive control scheme in which the muscle tension across a body segment is linearly proportional to the rate at which that segment is shortening.

I show that under this control law, the effect of the reflex is exactly opposite to the effect of viscous friction. Increasing the reflex gain leads to a lower effective damping

ratio. For sufficiently high reflex gains, the effective damping ratio becomes negative, indicating overall positive power flow into the body. In this regime, power flow into the body from active muscle tensions completely counteracts viscous energy losses and can also counteract energy loss due to sliding friction. Accordingly, compression waves propagate through the body with no attenuation, allowing continuous locomotion to be maintained.

Main conclusions:

- The passive axial mechanics of the body produces larva-like segmental "stepping" and wave motions. However, viscous and sliding friction cause waves to be attenuated as they travel through the body.
- Power transfer from the musculature into the body is maximised when muscle forces across a segment are produced while that segment is shortening.
- This condition may be achieved by a simple, segmentally decoupled, reflexive control scheme providing (linear) positive feedback of segment shortening velocity.
- The reflex is capable of counteracting friction to maintain peristaltic locomotion.

Limitations:

- In order to focus on peristaltic locomotion, only axial mechanics have been considered in this chapter. In order to understand the substrate exploration and taxis behaviours, however, the transverse mechanics and planar motion of the larval body must be considered. I present a model of planar axial-transverse motion and substrate exploration in the following chapter, and a model of taxis in the chapter after that.
- The consideration of power flow into the body focused its attention entirely on deformations of the body caused by muscle forces, without considering the relationship between deformation and overall translation of the body relative to the substrate. This relationship is investigated in the following chapter.
- Tuning the gain in the linear feedback loop is difficult – for high gains the system is unstable and amplitude grows without bound, whereas for low reflex gains energy is gradually lost from the system and locomotion eventually stops. I present a modified control scheme with a nonlinear force-velocity relationship in the following chapter, which avoids this problem.

- The particular form of the peristaltic waveform is dependent upon initial conditions. For instance, several waves may be propagated simultaneously if multiple segments are initially compressed. In the real larva, peristaltic waves are stereotyped, and are always solitary. The control scheme introduced in the following chapter avoids this limitation by incorporating interactions between distant segments.

- The control scheme introduced in this chapter was hypothetical, and was not compared to the neuroanatomy of the real larva. In the following chapter we draw extensive comparisons between a modified control scheme and known neuroanatomy.

2.2 Availability of software and supplementary videos

While the original software used to prepare the results in this chapter is no longer available, the results can be reproduced using the updated code used to prepare chapters 3 and 4. The model analysed in this chapter is itself fairly simple, and the interested reader is encouraged to build their own implementation to develop a deeper understanding of its working.

There are no supplementary videos for this chapter.

2.3 Publication: A model of Larval Biomechanics Reveals Exploitable Passive Properties for Efficient Locomotion

A Model of Larval Biomechanics Reveals Exploitable Passive Properties for Efficient Locomotion

Dylan Ross, Konstantinos Lagogiannis( ), and Barbara Webb

School of Informatics, University of Edinburgh,
10 Crichton St, Edinburgh EH8 9AB, UK
dylan.martin.ross@gmail.com, {klagogia,bwebb}@inf.ed.ac.uk

Abstract. To better understand the role of natural dynamics in motor control, we have constructed a mathematical model of crawling mechanics in larval *Drosophila*.

The model accounts for key anatomical features such as a segmentally patterned, viscoelastic outer body wall (cuticle); a non-segmented inner cavity (haemocoel) filled with incompressible fluid that enables visceral pistoning; and claw-like protrusions (denticle bands) giving rise to asymmetric friction.

Under conditions of light damping and low forward kinetic friction, and with a single cuticle segment initially compressed, the passive dynamics of this model produce wave-like motion resembling that of real larvae. The presence of a volume-conserving hydrostatic skeleton allows a wave reaching the anterior of the body to initiate a new wave at the posterior, thus recycling energy. Forcing our model with a sinusoidal input reveals conditions under which power transfer from control to body may be maximised. A minimal control scheme using segmentally localised positive feedback is able to exploit these conditions in order to maintain wave-like motion indefinitely. These principles could form the basis of a design for a novel, soft-bodied, crawling robot.

Keywords: Larval Drosophila · Biomechanical model · Positive feedback control · Peristaltic motion

1 Introduction

Felicitous use of mechanics can reduce the computational and energetic burdens faced by artificial and biological agents. As an extreme case, the passive dynamic walkers of McGeer were capable of producing naturalistic walking behaviour in the absence of any active control system and using only the energy provided by moving down a slight incline [1]. More recently, robotics has started to move beyond the confines of rigid body mechanics to exploit characteristically soft or compliant phenomena to produce complex mechanical outputs in response to simple control inputs [2,3]. Biology can provide crucial insights for designing such

S.P. Wilson et al. (Eds.): Living Machines 2015, LNAI 9222, pp. 1–12, 2015.
DOI: 10.1007/978-3-319-22979-9_1

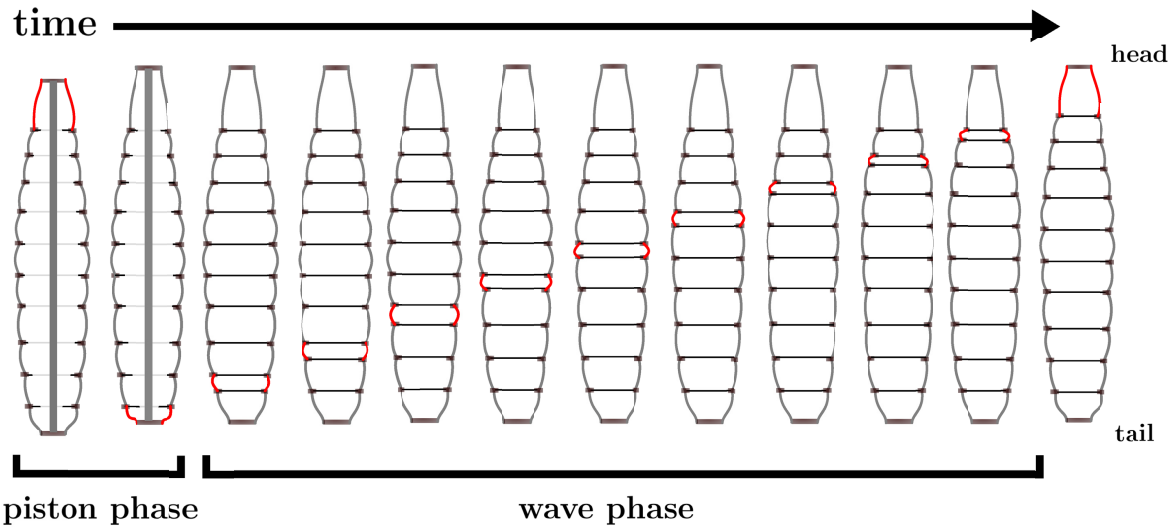

Fig. 1. Crawling in larval *Drosophila*: *Drosophila* larvae crawl using a two-phase visceral pistoning mechanism. During piston phase the head, tail, viscera, and coelomic fluid move forward in tandem. Then, during wave phase, a longitudinal wave of segment compression travels from the posterior to anterior of the body.

systems, as complex biological control problems are often simplified or solved by body mechanics rather than requiring precisely orchestrated neural control [4,5].

Larval *Drosophila melanogaster*, a tiny organism with a nervous system of less than 10,000 neurons, is an excellent example. The larva's primary goal is to acquire and store enough energy to successfully pupate and become a fruitfly; hence its locomotion should be as energy efficient as possible. The *Drosophila* larva possesses a hydrostatic skeleton that runs the entire length of its body and is surrounded by a segmentally patterned cuticle and musculature. Kinematic evidence suggests that it moves using a two-phase *visceral pistoning* mechanism similar to that observed in *Manduca sexta* caterpillars [6,7] (Figure 1). During *piston phase*, the head, tail, and viscera of the organism move forward in a single step. Then, during *wave phase*, a travelling wave of compression propagates from the posterior to the anterior of the animal, moving each segment forwards in sequence. When the travelling wave reaches the head, this process repeats.

Notably, the propagation speed and cycle period of peristaltic waves is highly stereotyped [7,8]. *Drosophila* locomotion differs from that of *Manduca* in that the larva lacks hydrostatic prolegs, and lifts very little from the substrate during crawling [8]. This is reflected by a very low number of circumferential relative to longitudinal muscle fibres in *Drosophila* [9]. Motor neuron recordings show that all muscles within a segment are activated simultaneously during fictive crawling [10], suggesting that the *Drosophila* larva may use an especially simple control scheme to direct crawling behaviour.

We have defined a one-dimensional mechanical model to explore how physical properties of the larval body may simplify its control. We examine why the larva may generate peristaltic waves with a constant period, and how peristalsis may be maintained by a minimal control scheme. Unfortunately, there is little

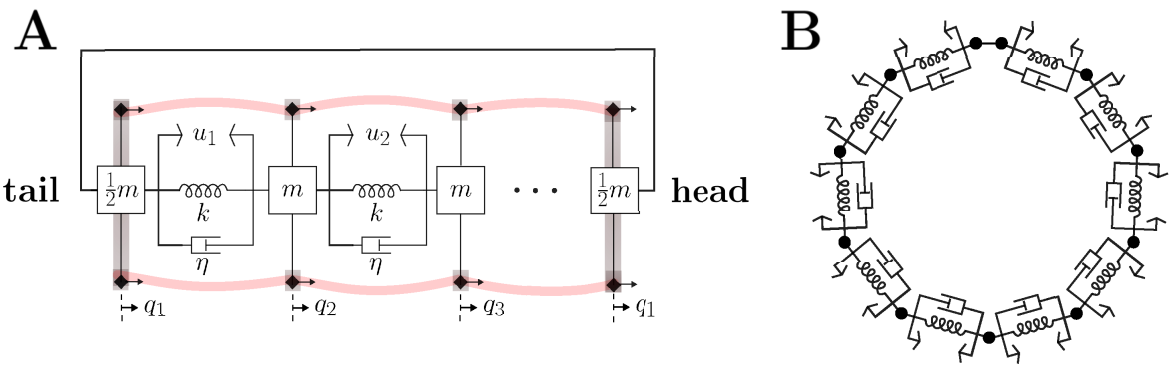

Fig. 2. Model schematic: **A** we model the segmented cuticle of the *Drosophila* larva as a set of coupled spring-mass-damper systems subject to an asymmetric Coulomb friction force. Volume-conserving coelomic fluid is incorporated as a rigid link connecting the head and tail masses. **B** The presence of this rigid link means that our model has a ring topology.

available experimental data regarding the mechanical properties of larval tissues. We therefore constructed our model in accordance with known anatomy and kinematics.

2 Model Construction

A general practice in modelling soft tissues is to use idealized mass-spring-damper systems [11–14].

Following this approach, we represent the head, tail, and segmental boundaries as 11 point masses, m_i, constrained to move along a single direction parallel to the plane of the substrate. The time varying positions q_i and velocities $\dot{q}_i$ of the masses along this direction of travel describe the state of our model. During peristalsis, the cuticle undergoes reversible viscoelastic strain, modelled here as an ideal spring and damper connected in parallel between neighbouring pairs of masses, characterised by a spring constant, k, and damping constant, η.

Very little change in axial or radial dimensions is observed during larval locomotion [7,8], suggesting that coelomic fluid may be modelled as an incompressible liquid which prevents changes in total body volume. This is enforced in our model by connecting the head and tail masses by a rigid link, which imposes the constraint $\dot{q}_1 = \dot{q}_{11} \; \forall \, t$.

Each body segment in the *Drosophila* larva contacts the substrate via a band of hard, claw-like projections called denticles. Since denticles extend primarily in the posterior direction,we model their interaction with the environment as a directionally asymmetric Coulomb friction force:

$$F_i(\mathbf{q}, \dot{\mathbf{q}}, \mathbf{u}) = \begin{cases} -\mu_{f:b}\mu_{k:s}\mu mg & \text{if } \dot{q}_i > 0 \;\vee\; F_{\text{ext},i} > \mu_{f:b}\mu mg \\ \mu_{k:s}\mu mg & \text{if } \dot{q}_i < 0 \;\vee\; F_{\text{ext},i} < -\mu mg \\ -F_{\text{ext},i} & \text{if } \dot{q}_i = 0 \;\wedge\; -\mu mg \leq F_{\text{ext},i} \leq \mu_{f:b}\mu mg \end{cases} \tag{1}$$

where g is standard gravity, μ is a coefficient of static friction specific to the denticle bands and the substrate, $\mu_{k:s}$ is the ratio of kinetic to static friction, and $\mu_{f:b}$ is the ratio of friction in the forward direction to friction in the backward direction. $F_{\text{ext},i}$ is the total non-frictive force being applied to the i-th mass.

As input to our model we allow time-varying tensions, representing muscle forces, to develop between neighbouring masses. We denote the vector of muscle tensions as $\mathbf{u}^{\mathrm{T}} = [u_1, u_2, \cdots, u_N]$ and impose the constraint $0 \leq \mathbf{u} \leq d$ to represent the fact that muscle forces saturate and are purely tensile in nature. A gain parameter $b \geq 0$ allows scaling of $\mathbf{u}$ to an appropriate range for the model's passive forces.

Assembling these elements gives the model shown in Figure 2. Isolating the forces exerted on each mass and applying Newton's second law gives a system of N second-order differential equations which must be solved for q_i and $\dot{q}_i$

$$\mathbf{M}\ddot{\mathbf{q}} = -k\mathbf{D}_2\mathbf{q} - \eta\mathbf{D}_2\dot{\mathbf{q}} + b\mathbf{D}_1\mathbf{u} + \mathbf{F} \tag{2}$$

where $\mathbf{M}$ is the $N \times N$ inertia matrix, $\mathbf{D}_2$ is an $N \times N$ circulant second difference matrix describing the coupling between the head, tail, and segment boundaries, and $\mathbf{D}_1$ is an $N \times N$ circulant backward difference matrix that describes how a particular muscle tension will pull one segment backwards and another forwards

$$\mathbf{M} = \begin{bmatrix} m & & & & \\ & m & & & \\ & & \ddots & & \\ & & & m & \\ & & & & m \end{bmatrix} \quad \mathbf{D}_2 = \begin{bmatrix} 2 & -1 & & & -1 \\ -1 & 2 & -1 & & \\ & \ddots & \ddots & \ddots & \\ & & -1 & 2 & -1 \\ -1 & & & -1 & 2 \end{bmatrix} \quad \mathbf{D}_1 = \begin{bmatrix} 1 & & & & -1 \\ -1 & 1 & & & \\ & \ddots & \ddots & & \\ & & & -1 & 1 \end{bmatrix} \tag{3}$$

By introducing spatial and temporal scaling, we can reduce the dimensionality of our parameter space and highlight useful physical relationships.

Letting $\boldsymbol{\chi}$ denote the nondimensionalised position vector, the scaled dynamics may be written

$$\ddot{\boldsymbol{\chi}} = -\mathbf{D}_2\boldsymbol{\chi} - 2\zeta\mathbf{D}_2\dot{\boldsymbol{\chi}} + \mathbf{D}_1\mathbf{u} + \mathbf{G}(\mathbf{x},\, \mathbf{u}) \tag{4}$$

where the damping ratio $\zeta = \eta/2\sqrt{km} \geq 0$ specifies the ratio of viscous to elastic and inertial forces. $\mathbf{G}$ denotes the nondimensionalised friction function

$$G_i(\boldsymbol{\chi}, \dot{\boldsymbol{\chi}}, \mathbf{u}) = \begin{cases} -\gamma_{f:b}\gamma_{k:s}\gamma & \text{if } \dot{q}_i > 0 \ \vee \ \frac{1}{b}F_{\text{ext},i} > \gamma_{f:b}\gamma \\ \gamma_{k:s}\gamma & \text{if } \dot{q}_i < 0 \ \vee \ \frac{1}{b}F_{\text{ext},i} < -\gamma \\ -\frac{1}{b}F_{\text{ext},i} & \text{if } \dot{q}_i = 0 \ \wedge \ -\gamma \leq \frac{1}{b}F_{\text{ext},i} \leq \gamma_{f:b}\gamma \end{cases} \tag{5}$$

The parameter $\gamma = \mu mg/b$ determines the magnitude of static friction in the backward direction. We have rewritten $\gamma_{f:b} = \mu_{f:b}$ and $\gamma_{k:s} = \mu_{k:s}$ for notational completeness. The details of this non-dimensionalisation process are provided in the supplementary material [21].

3 Results

We solved (4) using a fixed-step forward Euler method. Integration accuracy was assessed by calculating the summed kinetic, potential, and dissipated energy in our model system over the domain of integration. We tuned the integration timestep until error in total energy fell below 1%, finding a timestep of $10^{-3}t_c$ to be sufficient.

3.1 Passive Dynamics of a Single Segment; Role of Model Parameters

To explore the role of the parameters $\zeta, \gamma, \gamma_{f:b}$, and$\gamma_{k:s}$, we first examined the behaviour of a single segment boundary under the influence of passive mechanical forces. We simplified our analysis by assuming that all other segment boundaries were held fixed to the substrate, enforced by the constraint $\ddot{\chi}_{i\neq j} = 0$, where j specifies the freely moving segment boundary. To reflect the fact that motion of an isolated segment boundary would normally occur within the context of an ongoing peristaltic wave (Figure 1), we set initial conditions such that the free segment boundary was initially at rest away from equilibrium, in an extreme posterior or anterior position (Figure 3A, left panel, $\tau = 0$).

Passive viscoelastic and friction forces alone were able to produce trajectories that qualitatively match movements observed in the real larva (Figure 3A, left panel). Elastic forces exerted by the cuticle initially accelerate the segment boundary towards the cuticle's equilibrium position, which corresponds to the minimum of the elastic potential energy function shown in Figure 3A (right panel). Motion of the segment boundary is opposed by viscous damping and kinetic friction forces, which slow the segment boundary and eventually bring it to rest. Increasing the parameter ζ causes an increase in the magnitude of viscous forces, decreasing segment boundary velocity. When $\zeta < 1$, the moving mass may overshoot the cuticle's equilibrium position before coming to rest. Conversely, $\zeta \geq 1$ implies that the mass will move slowly towards equilibrium without overshoot (Figure 3A, left panel). Examining (5), we see that $\gamma_{k:s}\gamma$ sets the magnitude of kinetic friction when the segment boundary is moving in the posterior direction, and $\gamma_{f:b}$ scales this quantity to specify the magnitude of forward kinetic friction. Accordingly, changing $\gamma_{k:s}$ results in directionally symmetric scaling of segment boundary velocity and final displacement (Figure 3C), while changing $\gamma_{f:b}$ allows directionally asymmetric scaling (Figure 3B).

When the segment boundary comes to rest, static friction may hold it in place. By inspection of (5), γ sets the maximum magnitude of static friction in the posterior direction while $\gamma_{f:b}$ multiplies this quantity to give the maximum magnitude in the anterior direction. The expression $\gamma_{f:b}\gamma \leq \chi \leq \gamma$ thus specifies a stable range of positions in which static friction forces completely oppose elastic forces. A mass at rest within this region will remain at rest (Figure 3A, B, C).

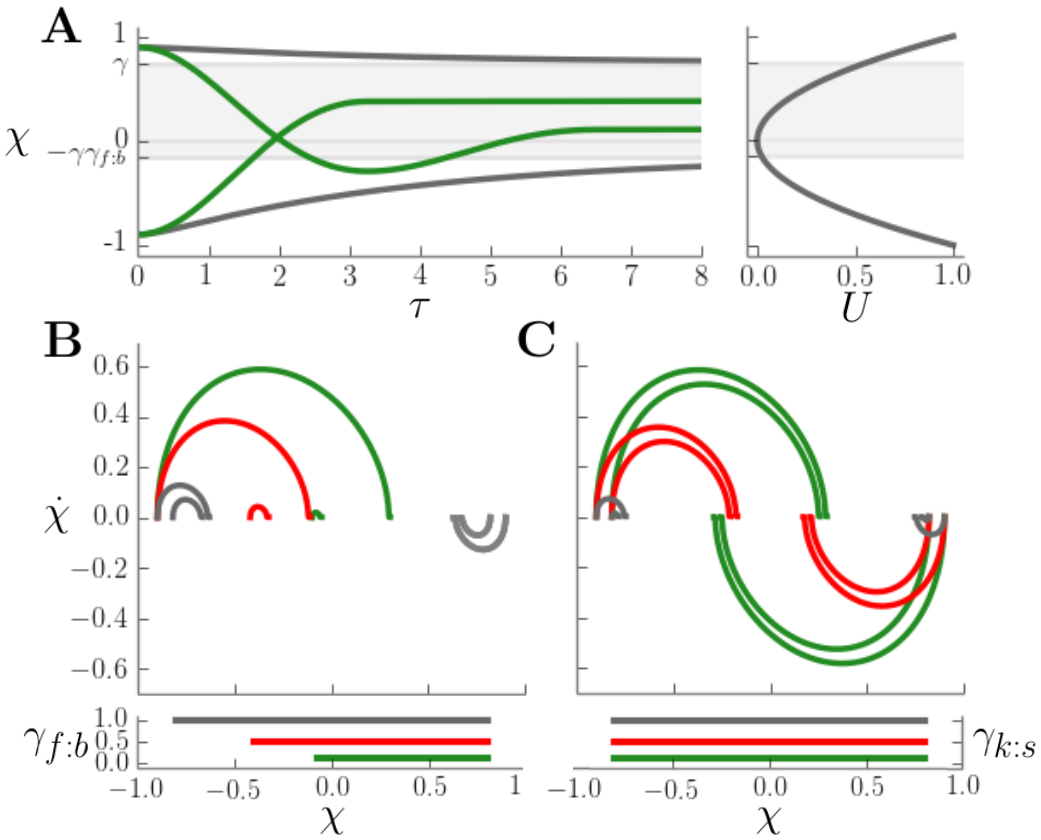

Fig. 3. Passive dynamics of a single segment: A (left) evolution of segment boundary position for $\zeta = 2$ (black) or $\zeta = 0.25$ (green), with $\gamma = 0.9$, $\gamma_{f:b} = 0.4$, $\gamma_{k:s} = 0.1$. (right) elastic energy stored in the cuticle as a function of segment boundary displacement. Shading indicates the range of positions stabilised by static friction. **B** (top) position-velocity phase trajectories for $\gamma_{f:b} = 0.1$ (green), 0.5) (red), or 1.0 (gray). Trajectories with negative velocity are unaffected by change in $\gamma_{f:b}$. (bottom) range of positions stabilised by static friction for these values of $\gamma_{f:b}$. **C** (top) phase trajectories for $\gamma_{k:s} = 0.1$ (green), 0.5 (red), or 1.0 (gray). (bottom) range of positions stabilised by static friction for these values of $\gamma_{k:s}$.

Though the range of possible values for $\zeta, \gamma, \gamma_{f:b}$, and$\gamma_{k:s}$ is very large, we focus on the following cases:

1. $\gamma = 0.9$ and $\gamma_{k:s} = 0.9$ or 0.1, i.e. kinetic friction is either equal to, or far weaker than, maximum static friction. The first case would correspond to the larva "dragging" its denticle bands across the substrate; the latter to lifting the denticles as they move.
2. $\gamma_{f:b} = 1.0$ or 0.4, i.e. either symmetrical friction, or higher backward than forward friction, which could result from denticle orientation [15].
3. $\zeta \in [0, 0.25, 0.5, 1.0, 2.0]$: a representative set of damping ratios which ranges from zero viscous damping to heavily overdamped

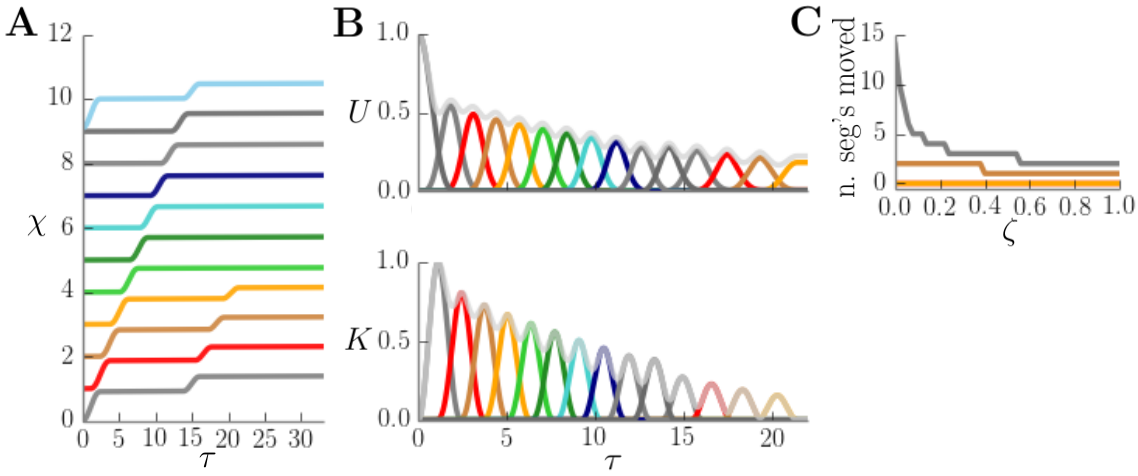

Fig. 4. Passive dynamics of the full body model: A segment boundary displacements in the absence of muscle tension, with $\zeta = 0$, $\gamma = 0.9$, $\gamma_{f:b} = 0.9$, $\gamma_{k:s} = 0.1$. **B** elastic energy stored in each cuticle segment (top, U) and kinetic energy of each segment boundary (bottom, K) during the wave shown in **A**. **C** number of discrete segment boundary movements during a passive peristaltic wave as a function of ζ, for friction conditions $\gamma_{k:s} = 0.1$, $\gamma_{f:b} = 0.4$ (gray), $\gamma_{k:s} = 0.9$, $\gamma_{f:b} = 0.4$ (brown), $\gamma_{k:s} = 0.1$, $\gamma_{f:b} = 1.0$ (orange), $\gamma_{k:s} = 0.9$, $\gamma_{f:b} = 1.0$ (orange).

3.2 Passive Dynamics of the Whole Body

Using the full model (4), we next examined the role of passive mechanics in locomotion. We set initial conditions such that the head segment was almost fully compressed, storing elastic energy. We then integrated our model equations in the absence of active muscle tensions, and observed the passive response of the system.

Under particular parameter choices, our model is capable of producing completely passive peristaltic waves (Figure 4A). In particular, with asymmetric friction forces ($\gamma_{f:b} = 0.4$), low kinetic friction ($\gamma_{k:s} = 0.1$), and low viscous damping ($\zeta < 0.6$), a wave may propagate from posterior to anterior while moving the body across the substrate (Figure 4C). The elastic energy stored in the compressed head segment is converted to kinetic energy as the segment expands. The asymmetry in our friction function means that expansion occurs through forward movement of the head, and due to the rigid link constraint (representing volume conservation of the internal coloemic fluid) this causes compression of the tail segment. The tail segment in turn expands forward, transferring energy to the neighbouring segment boundary, and the process continues. Since friction and viscous damping dissipate an amount of energy each time a segment boundary moves, the travelling wave is gradually attenuated. Nevertheless, if dissipative forces are sufficiently low, the energy supplied by compressing the head segment may propagate through the entire body and even "loop" again from head to tail (Figure 4A). This phenomenon is possible due to hydrostatic coupling between the head and tail, and is prevented by removing the rigid link

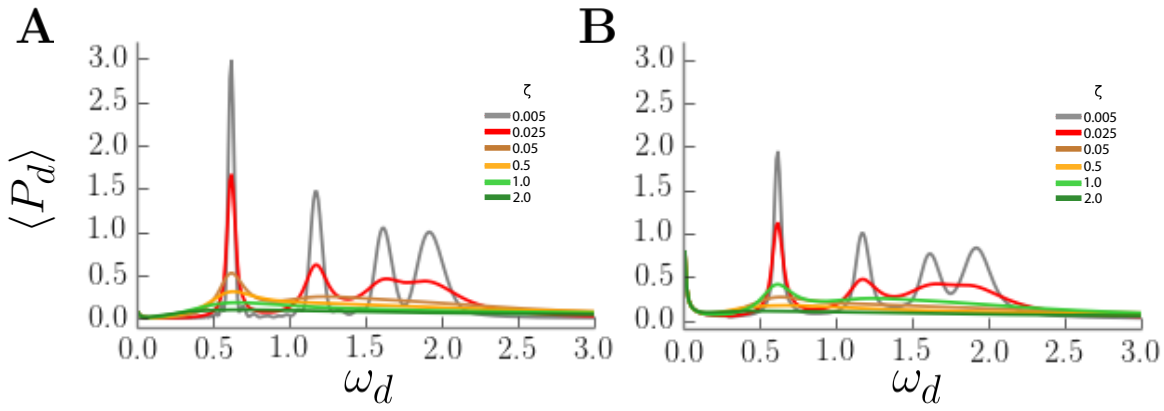

Fig. 5. Resonant frequencies: A Frictionless system with $\zeta \in \{0.005, 0.025, 0.05, 0.5, 1, 2\}$; shows peak resonant frequencies with power going lower as damping ζ increases. Increasing damping ζ drops the peak power and makes the tuning wider. (In the non-dimensionalized system units are $\frac{F_d t_c}{m}$) **B** adding friction does not affect the location of the resonant frequencies but does reduce the amount of power absorbed, without broadening the spectrum of peak responses. Friction also adds an efficient mode close to zero frequency.

constraint in our model. Our analysis suggests a view of the larval body as a ring of energy storage devices with rectified, dissipative connections (Figure 2B).

3.3 Resonance and Preferred Input Timing

We next examined the response of our system to energy input by applying sinusoidal forcing to the tail mass. The work done by a force F_d acting upon a mass to move it a distance dq is given by $dW = F_d dq$. The rate of this process gives the power supplied $P_d = F_d \dot{q}$. Thus, the power provided by applying sinusoidal forcing to the tail mass in the non-dimensionlized system is

$$P_d = \frac{F_d t_c}{m} \cos(\omega_d \tau) \frac{d\chi}{d\tau}. \tag{6}$$

Note that direction and timing of input force are important as power is maximised when force is in phase with velocity $\dot{\chi}$. In general the driving force may add or remove energy during different parts of the cycle and the two may balance, giving on average $\langle P_d(\omega_d) \rangle = 0$ for driving frequency ω_d.

We predicted that in order to maximise energy input, our stimulation frequency would have to relate to the body's passive properties, that define $\dot{\chi}$. Indeed, it is a well known property of n spring-coupled masses to exhibit N (possibly redundant) resonant frequencies at which energy absorption is maximized. Figure 5A shows the average $\langle P_d(\omega_d) \rangle$ power supplied by the driving force, numerically evaluated over 10^2 cycles at frequency ω_d in the absence of friction forces. With low damping coefficient ζ, four peaks are evident. The location of these peaks has been verified by an analysis of the normal modes of our system (not shown).

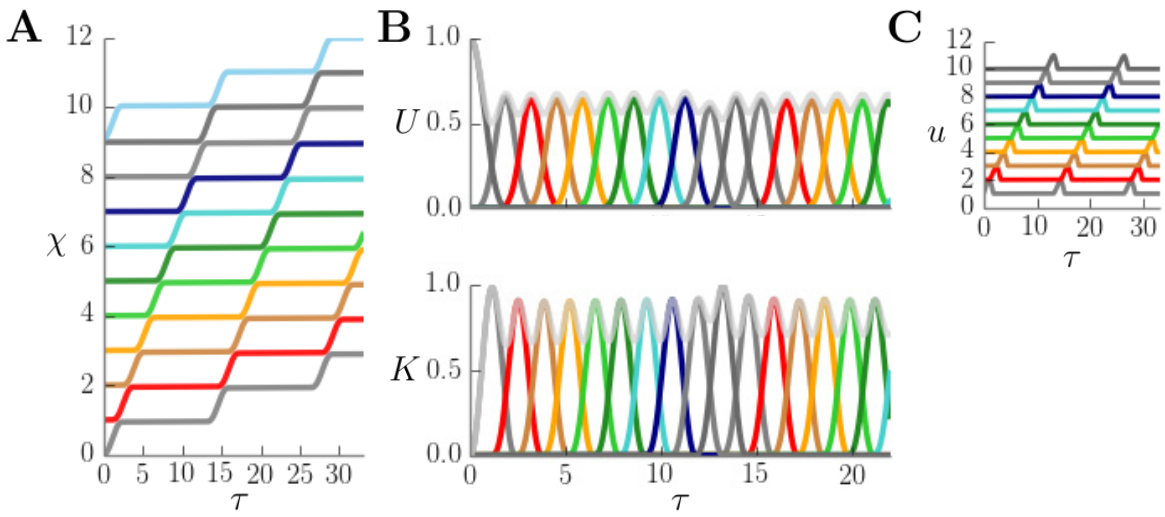

Fig. 6. Local positive feedback control: A segment boundary displacements under positive feedback control (gain $\beta = 0.105$, parameter choices as in Figure 4A). **B** elastic energy stored in each segment (top) and kinetic energy of each segment boundary (bottom) during **A**. **C** muscle tensions produced by the positive feedback control law (7) during **A**. Tensions have been normalized and offset for presentation.

In the frictionless case, viscous damping is the only dissipative force. Increasing damping reduces and broadens the peaks of power absorption. Introducing asymmetric friction decreases the amplitude of the peaks without simultaneous broadening, and also adds a peak towards low frequencies (Figure 5B). The increase in efficiency at low driving frequencies comes due to the reduction of the higher derivatives making the velocity of the driven mass effectively in phase with the driving force as it is dragged against the friction. If the driving force is provided by muscle activation then we can conclude the timing of muscle activation is important in order to achieve efficient locomotion, and this becomes even more evident as damping is decreased.

3.4 Generating Locomotion Through Local Positive Feedback

We constructed a control scheme that would exploit our model's passive dynamics in order to generate forward locomotion. This controller uses segmentally localised positive feedback of cuticle strain rate to produce muscle tensions according to the control law:

$$\mathbf{u} = \beta \mathbf{D}_1^{\mathrm{T}} \dot{\boldsymbol{\chi}} \qquad 0 \leq \mathbf{u} \leq d \tag{7}$$

which can be interpreted as producing muscle tension across a segment in proportion to the rate at which the segment is shortening, parametrised by the strain rate-tension gain β. Substituting this definition for $\mathbf{u}$ into (4) gives the closed-loop system

$$\ddot{\boldsymbol{\chi}} = -\mathbf{D}_2 \boldsymbol{\chi} - 2\zeta \mathbf{D}_2 \dot{\boldsymbol{\chi}} + \beta \mathbf{D}_1 \mathbf{D}_1^{\mathrm{T}} \dot{\boldsymbol{\chi}} + \mathbf{G} \tag{8}$$

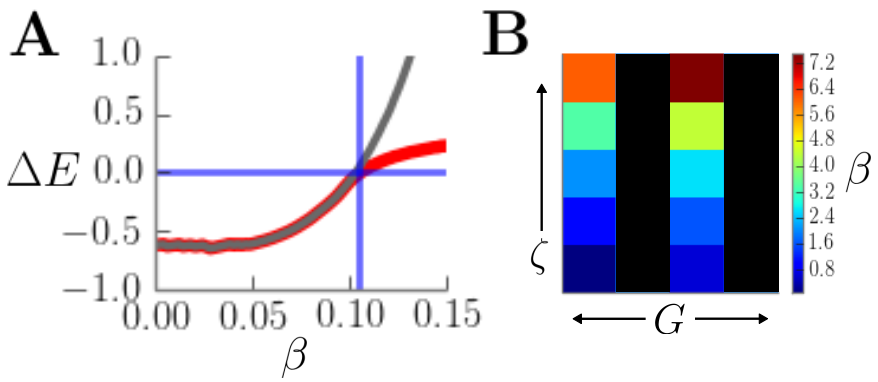

Fig. 7. Tuning feedback gain: A change in total elastic and kinetic energy (ΔE) as feedback gain β is varied (parameters as in Figure 4A). β may be tuned to achieve zero change in total energy (blue lines). With non-saturating muscle tensions, ΔE increases exponentially with β (gray line, $d = \infty$). Decreasing maximum muscle tension d causes ΔE to saturate as β increases (red line, $d = 0.1$). **B** β required to achieve continuous locomotion under various damping conditions. Friction varies left to right as ($\gamma_{k:s} = 0.1$, $\gamma_{f:b} = 0.4$), ($\gamma_{k:s} = 0.1$, $\gamma_{f:b} = 1.0$), ($\gamma_{k:s} = 0.9$, $\gamma_{f:b} = 0.4$), ($\gamma_{k:s} = 0.9$, $\gamma_{f:b} = 1.0$). ζ increases from bottom to top as $[0.0, 0.25, 0.5, 1.0, 2.0]$. Conditions are coloured black if no value of β was able to produce continuous locomotion.

Noting that $\mathbf{D}_1\mathbf{D}_1^{\mathrm{T}} = \mathbf{D}_2$ lets us rewrite this as

$$\ddot{\boldsymbol{\chi}} = -\mathbf{D}_2\boldsymbol{\chi} + (\beta - 2\zeta)\mathbf{D}_2\dot{\boldsymbol{\chi}} + \mathbf{G} \tag{9}$$

This control can be thought of as actively amplifying any passively occurring segment strain, mitigating the effects of dissipative forces and counteracting the attenuation of passive waves described above. Inspection of the closed-loop system (9) shows that as β increases, local positive feedback first acts to cancel viscous damping forces. Increasing β further effectively introduces a positive damping term, which can offset frictional losses. Tuning β allowed us to produce continuous, naturalistic, wave-like locomotion with near-constant total body energy across a range of damping and friction conditions (Figures 6, 7).

Note, however, that this controller cannot produce waves in the absence of passive body motion. If the environment is too frictive, or the head and tail are decoupled, positive feedback fails to produce continuous locomotion.

4 Discussion

We have constructed the first model of crawling mechanics in larval *Drosophila*. The model contains key anatomical features such as a segmentally patterned, viscoelastic cuticle; a non-segmented hemocoel filled with an incompressible fluid that enables visceral pistoning; and asymmetrically frictive denticle bands. Under conditions of light damping and low forward kinetic friction, the passive dynamics of this model naturally produce wave-like motion resembling that of real larvae. Using localised positive feedback of strain rate to produce muscle tensions

results in a control that is matched to the passive dynamics of the body and permits an elegant, distributed implementation.

Our model provides insight into the generation of behaviour in larval *Drosophila*. For instance, the propagation speed of peristaltic waves and thus the overall speed of locomotion are highly stereotyped within a given experimental setup [7,8]. Our model suggests that this is due to the existence of resonant modes within the larval body that may be exploited to minimize the energetic costs of locomotion. Locomotion speed has been observed to vary with substrate composition as well as denticle structure [16,17]. Increase in speed over hard substrates has been suggested to represent an escape behaviour in response to undesirable conditions [16], but our model suggests that it may simply represent a change in the frictive forces experienced by the cuticle and denticle bands.

We stress that it is unlikely that crawling behaviour in the real larva is entirely controlled by decoupled, local positive feedback, since propagating waves of motor neuron activity persist in completely isolated nervous system preparations [10]. Positive feedback may still be used to align ongoing neural motor control signals with the mechanics of the body and environment. This is consistent with the observation that waves of muscle activation travel slower in larvae which have been experimentally deprived of mechanosensory input [18,19].

Future work may investigate locomotion in two or three dimensions. This could be accomplished by adding revolute joints and torsional springs at each of the masses in the current model. This would enable investigation of turning in addition to linear crawling, the two key behaviours involved in larval navigation [20]. Of particular interest is whether positive feedback of strain rate can produce both behaviours.

The model and control schemes presented in this paper may serve as the basis for an efficient crawling robot able to exploit its passive dynamics in order to reduce the energetic and computational burden of control.

References

1. McGeer, T.: Passive Dynamic Walking. The International Journal of Robotics Research **62**(82), 62–82 (1990)
2. Hauser, H., Ijspeert, A.J., Füchslin, R.M., Pfeifer, R., Maass, W.: Towards a theoretical foundation for morphological computation with compliant bodies. Biological Cybernetics **105**, 355–370 (2011)
3. Shepherd, R.: Multigait soft robot. Proceedings of the National Academy of Sciences of the United States of America **108**(51), 20400–20403 (2011)
4. Tytell, E.D., Holmes, P., Cohen, A.H.: Spikes alone do not behaviour make: Why neuroscience needs biomechanics. Current Opinion in Neurobiology **21**(5), 816–822 (2011)
5. Kier, W.M.: The diversity of hydrostatic skeletons. The Journal of Experimental Biology **215**(8), 1247–1257 (2012)
6. Simon, M.A., Woods, W.A., Serebrenik, Y.V., Simon, S.M., van Griethuijsen, L.I., Socha, J.J., Lee, W.K., Trimmer, B.A.: Visceral-locomotory pistoning in crawling caterpillars. Current Biology **20**(16), 1458–1463 (2010)

7. Heckscher, E.S., Lockery, S.R., Doe, C.Q.: Characterization of *Drosophila* larval crawling at the level of organism, segment, and somatic body wall musculature. The Journal of Neuroscience **32**(36), 12460–12471 (2012)
8. Berrigan, D., Pepin, D.J.: How Maggots Move: Allometry and Kinematics of Crawling in Larval Diptera. J. Insect Physiol. **41**(4), 329–337 (1995)
9. Landgraf, M., Bossing, T., Technau, G.M., Bate, M.: The origin, location, and projections of the embryonic abdominal motorneurons of *Drosophila*. The Journal of Neuroscience **17**(24), 9642–9655 (1997)
10. Fox, L.E., Soll, D.R., Wu, C.: Coordination and modulation of locomotion pattern generators in *Drosophila* larvae: effects of altered biogenic amine levels by the tyramine β hydroxlyase mutation. The Journal of Neuroscience **26**(5), 1486–1498 (2006)
11. Boyle, J.H., Berri, S., Cohen, N.: Gait Modulation in *C. elegans*: An Integrated Neuromechanical Model. Frontiers in Computational Neuroscience **6**, 1–10 (2012)
12. Fung, Y.C.: Biomechanics: Mechanical Properties of Living Tissues. Springer-Verlag, New York (1993)
13. Skierczynski, B.A., Wilson, R.J., Kristan, W.B., Skalak, R.: A model of the hydrostatic skeleton of the leech. Journal of Theoretical Biology **181**(4), 329–342 (1996)
14. Alscher, C.: Simulating the motion of the leech : A biomechanical application of DAEs. Numerical Algorithms **19**, 1–12 (1998)
15. Alexandre, C.: Cuticle preparation of *Drosophila* embryos and larvae. In: Dahmann, C (ed) Methods in Molecular Biology : *Drosophila*: Methods and Protocols, Ch. 11, pp. 197–205. Humana Press Inc. (2008)
16. Apostolopoulou, A.A., Hersperger, F., Mazija, L., Widmann, A., Wüst, A., Thum, A.S.: Composition of agarose substrate affects behavioral output of *Drosophila* larvae. Frontiers in Behavioral Neuroscience **8**, 1–11 (2014)
17. Inestrosa, N.C., Sunkel, C.E., Arriagada, J., Garrido, J., Herrera, R.G.: Abnormal development of the locomotor activity in *yellow* larvae of *Drosophila*: a cuticular defect? Genetica **97**, 205–210 (1996)
18. Hughes, C.L., Thomas, J.B.: A Sensory Feedback Circuit Coordinates Muscle Activity in *Drosophila*. Mol. Cell. Neurosci. **35**(2), 383–396 (2007)
19. Inada, K., Kohsaka, H., Takasu, E., Nose, A.: Optical dissection of neural circuits responsible for *Drosophila* larval locomotion with halorhodopsin. PLOS ONE **6**(12), 1–10 (2011)
20. Lahiri, S., Shen, K., Klein, M., Tang, A., Kane, E., Gershow, M., Garrity, P., Samuel, A.: Two alternating motor programs drive navigation in *Drosophila* larva. PLOS ONE **6**(8), 1–12 (2011)
21. Ross, D., Lagogiannis, K., Webb, B.: Online supplementary material. http://maggot.eu/documents/2015/04/SuppMechBodymodel.pdf

SUPPLEMENTARY MATERIAL : derivation of nondimensionalised equations of motion

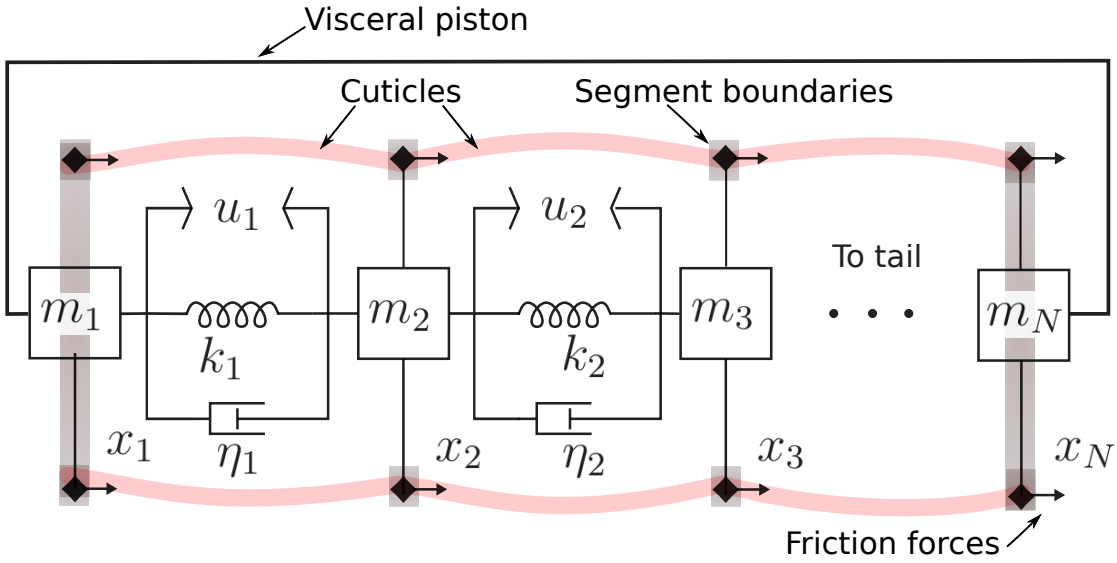

Figure 1: **model schematic and physical parameters**

1 Model construction

A schematic of our model's mechanics is shown in Figure 1. Note that there are N degrees of freedom (DOF), since the "head" and "tail" masses are connected by a rigid link and thus move identically (see main text). To simplify our model, we assign equal mass to each DOF. Isolating the forces exerted on each mass and applying Newton's second law thus gives a system of N second-order differential equations which must be solved to find positions q_i and velocities $\dot{q}_i$ for each DOF :

$$\begin{aligned} m\ddot{q}_1 = &-k(2q_1 - q_2 - q_N) \\ &-\eta(2\dot{q}_1 - \dot{q}_2 - \dot{q}_N \\ &-b(u_N - u_1) \\ &+F_1(\mathbf{q}, \dot{\mathbf{q}}, \mathbf{u}) \end{aligned} \qquad \begin{aligned} m\ddot{q}_i = &-k(-q_{i-1} + 2q_i - q_{i+1}) \\ &-\eta(-\dot{q}_{i-1} + 2\dot{q}_i - \dot{q}_{i+1}) \\ &-b(u_{i-1} - u_i) \\ &+F_i(\mathbf{q}, \dot{\mathbf{q}}, \mathbf{u}) \end{aligned} \qquad \begin{aligned} m\ddot{q}_N = &-k(-q_1 - q_{N-1} + 2q_N) \\ &-\eta(-\dot{q}_1 - \dot{q}_{N-1} + 2\dot{q}_N) \\ &-b(u_{N-1} - u_N) \\ &+F_N(\mathbf{q}, \dot{\mathbf{q}}, \mathbf{u}) \end{aligned} \tag{1}$$

$$i \in [2, \cdots, N-1]$$

where k and η are the spring constant and coefficient of viscosity of the cuticle, m is the mass associated with a single segment boundary, $\mathbf{u} = [u_1, u_2, \cdots, u_N]^{\mathrm{T}}$ is a vector of applied tensions, b is input gain, $\mathbf{q}$ is the vector of

segment boundary positions, and $\dot{\mathbf{q}}$ is the vector of segment boundary velocities. The vector-valued function F gives the friction force experienced by each segment boundary, and is defined as

$$F_i(\mathbf{q}, \dot{\mathbf{q}}, \mathbf{u}) = \begin{cases} -\mu_{f:b}\mu_{k:s}\mu mg & \text{if } \dot{q}_i > 0 \ \vee \ F_{\text{ext},i} > \mu_{f:b}\mu mg \\ \mu_{k:s}\mu mg & \text{if } \dot{q}_i < 0 \ \vee \ F_{\text{ext},i} < -\mu mg \\ -F_{\text{ext},i} & \text{if } \dot{q}_i = 0 \ \wedge \ -\mu mg \leq F_{\text{ext},i} \leq \mu_{f:b}\mu mg \end{cases} \qquad i \in [1, 2, \cdots, N] \tag{2}$$

where g is Standard gravity, μ is the coefficient of static friction in the backward direction, $\mu_{k:s}$ is the ratio of kinetic to static friction, and $\mu_{f:b}$ is the ratio of friction in the forward direction to friction in the backward direction. $F_{\text{ext},i}$ is the total non-frictive force being applied to the i-th mass, and depends upon the position vector $\mathbf{q}$, velocity vector $\dot{\mathbf{q}}$, and input vector $\mathbf{u}$.

Our model equations may be written in matrix form as

$$\ddot{\mathbf{q}} = -\eta\mathbf{M}^{-1}\mathbf{D}_2\dot{\mathbf{q}} - k\mathbf{M}^{-1}\mathbf{D}_2\mathbf{q} + b\mathbf{M}^{-1}\mathbf{D}_1\mathbf{u} + \mathbf{M}^{-1}\mathbf{F} \tag{3}$$

where $\mathbf{M}$ is the $N \times N$ inertia matrix, $\mathbf{D}_2$ is an $N \times N$ circulant second difference matrix, and $\mathbf{D}_1$ is an $N \times N$ circulant backward difference matrix

$$\mathbf{M} = \begin{bmatrix} m & & & & & \\ & m & & & & \\ & & \ddots & & & \\ & & & m & & \\ & & & & m & \end{bmatrix} \tag{4}$$

$$\mathbf{D}_2 = \begin{bmatrix} 2 & -1 & & & & -1 \\ -1 & 2 & -1 & & & \\ & -1 & 2 & -1 & & \\ & & \ddots & \ddots & \ddots & \\ & & & -1 & 2 & -1 \\ -1 & & & & -1 & 2 \end{bmatrix} \tag{5}$$

$$\mathbf{D}_1 = \begin{bmatrix} 1 & & & & & -1 \\ -1 & 1 & & & & \\ & -1 & 1 & & & \\ & & \ddots & \ddots & & \\ & & & -1 & 1 & \\ 1 & & & & -1 & \end{bmatrix} \tag{6}$$

2 Nondimensionalisation

We introduce the spatial and temporal scaling

$$\begin{aligned} q_i &= \chi_i q_c \\ t &= \tau t_c \end{aligned} \tag{7}$$

where q_c and t_c are characteristic length and time units, respectively, and are to be determined. Substituting these definitions into (1) gives

$$
\begin{aligned}
\frac{mq_c}{t_c^2}\ddot{\chi}_1 =& -kq_c(2\chi_1 - \chi_2 - \chi_N) \\
&- \frac{\eta q_c}{t_c}(2\dot{\chi}_1 - \dot{\chi}_2 - \dot{\chi}_N) \\
&- b(u_N - u_1) \\
&+ F_1(\boldsymbol{\chi} q_c, \dot{\boldsymbol{\chi}}\frac{q_c}{t_c}, \mathbf{u})
\end{aligned}
\qquad
\begin{aligned}
\frac{mq_c}{t_c^2}\ddot{\chi}_i =& -kq_c(-\chi_{i-1} + 2\chi_i - \chi_{i+1}) \\
&- \frac{\eta q_c}{t_c}(-\dot{\chi}_{i-1} + 2\dot{\chi}_i - \dot{\chi}_{i+1}) \\
&- b(u_{i-1} - u_i) \\
&+ F_i(\boldsymbol{\chi} q_c, \dot{\boldsymbol{\chi}}\frac{q_c}{t_c}, \mathbf{u})
\end{aligned}
\qquad
\begin{aligned}
\frac{mq_c}{t_c^2}\ddot{\chi}_N =& -kq_c(-\chi_1 - \chi_{N-1} + 2\chi_N) \\
&- \frac{\eta q_c}{t_c}(-\dot{\chi}_1 - \dot{\chi}_{N-1} + 2\dot{\chi}_N) \\
&- b(u_{N-1} - u_N) \\
&+ F_N(\boldsymbol{\chi} q_c, \dot{\boldsymbol{\chi}}\frac{q_c}{t_c}, \mathbf{u})
\end{aligned}
$$

$$
i \in [2, \cdots, N-1] \tag{8}
$$

Multiplying each term by $\frac{mq_c}{t_c^2}$ gives

$$
\begin{aligned}
\ddot{\chi}_1 =& -\frac{kt_c^2}{m}(2\chi_1 - \chi_2 - \chi_N) \\
&- \frac{\eta t_c}{m}(2\dot{\chi}_1 - \dot{\chi}_2 - \dot{\chi}_N) \\
&- \frac{bt_c^2}{mq_c}(u_N - u_1) \\
&+ \frac{t_c^2}{mq_c}F_1(\boldsymbol{\chi} q_c, \dot{\boldsymbol{\chi}}\frac{q_c}{t_c}, \mathbf{u})
\end{aligned}
\qquad
\begin{aligned}
\ddot{\chi}_i =& -\frac{kt_c^2}{m}(-\chi_{i-1} + 2\chi_i - \chi_{i+1}) \\
&- \frac{\eta t_c}{m}(-\dot{\chi}_{i-1} + 2\dot{\chi}_i - \dot{\chi}_{i+1}) \\
&- \frac{bt_c^2}{mq_c}(u_{i-1} - u_i) \\
&+ \frac{t_c^2}{mq_c}F_i(\boldsymbol{\chi} q_c, \dot{\boldsymbol{\chi}}\frac{q_c}{t_c}, \mathbf{u})
\end{aligned}
\qquad
\begin{aligned}
\ddot{\chi}_N =& -\frac{kt_c^2}{m}(-\chi_1 - \chi_{N-1} + 2\chi_N) \\
&- \frac{\eta t_c}{m}(-\dot{\chi}_1 - \dot{\chi}_{N-1} + 2\dot{\chi}_N) \\
&- \frac{bt_c^2}{mq_c}(u_{N-1} - u_N) \\
&+ \frac{t_c^2}{mq_c}F_N(\boldsymbol{\chi} q_c, \dot{\boldsymbol{\chi}}\frac{q_c}{t_c}, \mathbf{u})
\end{aligned}
$$

$$
i \in [2, \cdots, N-1] \tag{9}
$$

We next choose to set $\frac{kt_c^2}{m} = 1$, which implies $t_c = \sqrt{\frac{m}{k}}$. Setting $\frac{bt_c^2}{mq_c} = 1$ and using our new definition for t_c implies $q_c = \frac{b}{k}$. Further defining the damping ratio $\zeta = \frac{\eta}{2\sqrt{km}}$ allows us to rewrite (9) as

$$
\begin{aligned}
\ddot{\chi}_1 =& -(2\chi_1 - \chi_2 - \chi_N) \\
&- 2\zeta(2\dot{\chi}_1 - \dot{\chi}_2 - \dot{\chi}_N) \\
&- (u_N - u_1) \\
&+ G_1(\boldsymbol{\chi}, \dot{\boldsymbol{\chi}}, \mathbf{u})
\end{aligned}
\qquad
\begin{aligned}
\ddot{\chi}_i =& -(-\chi_{i-1} + 2\chi_i - \chi_{i+1}) \\
&- 2\zeta(-\dot{\chi}_{i-1} + 2\dot{\chi}_i - \dot{\chi}_{i+1}) \\
&- (u_{i-1} - u_i) \\
&+ G_i(\boldsymbol{\chi}, \dot{\boldsymbol{\chi}}, \mathbf{u})
\end{aligned}
\qquad
\begin{aligned}
\ddot{\chi}_N =& -(-\chi_1 - \chi_{N-1} + 2\chi_N) \\
&- 2\zeta(-\dot{\chi}_1 - \dot{\chi}_{N-1} + 2\dot{\chi}_N) \\
&- (u_{N-1} - u_N) \\
&+ G_N(\boldsymbol{\chi}, \dot{\boldsymbol{\chi}}, \mathbf{u})
\end{aligned}
\tag{10}
$$

$$
i \in [2, \cdots, N-1]
$$

where we have also introduced the nondimensionalised friction function G, defined as

$$
G_i(\boldsymbol{\chi}, \dot{\boldsymbol{\chi}}, \mathbf{u}) = \frac{t_c^2}{mq_c}F_i(\boldsymbol{\chi} q_c, \dot{\boldsymbol{\chi}}\frac{q_c}{t_c}, \mathbf{u}) = \begin{cases} -\gamma_{f:b}\gamma_{k:s}\gamma & \text{if } \dot{q}_i > 0 \ \vee \ \frac{1}{b}F_{\text{ext},i} > \gamma_{f:b}\gamma \\ \gamma_{k:s}\gamma & \text{if } \dot{q}_i < 0 \ \vee \ \frac{1}{b}F_{\text{ext},i} < -\gamma \\ -\frac{1}{b}F_{\text{ext},i} & \text{if } \dot{q}_i = 0 \ \wedge \ -\gamma \leq \frac{1}{b}F_{\text{ext},i} \leq \gamma_{f:b}\gamma \end{cases}
$$

$$
i \in [1, 2, \cdots, N] \tag{11}
$$

$\gamma = \frac{\mu mg}{b}$ is a dimensionless parameter specifying the magnitude of static friction in the backward direction, and we have rewritten $\gamma_{f:b} = \mu_{f:b}$ and $\gamma_{k:s} = \mu_{k:s}$. By introducing the state vector $x = [\chi_1, \chi_2, \cdots, \chi_N, \dot{\chi}_1, \dot{\chi}_2, \cdots, \dot{\chi}_N]^{\mathrm{T}}$, we may write our nondimensionalised system (10), (11) in state-space form

$$
\dot{\mathbf{x}} = \begin{bmatrix} \mathbf{0} & \mathbf{I} \\ -\mathbf{D}_2 & -2\zeta\mathbf{D}_2 \end{bmatrix}\mathbf{x} + \begin{bmatrix} \mathbf{0} \\ \mathbf{D}_1 \end{bmatrix}\mathbf{u} + \begin{bmatrix} \mathbf{0} \\ \mathbf{I} \end{bmatrix}\mathbf{G} \tag{12}
$$

Chapter 3

A neuromechanical model of peristalsis, turning, and exploration

3.1 Introduction

In this chapter, I investigate the mechanics and control of substrate exploration in the larva.

The chapter is largely comprised of the published research paper, "Modelling the mechanics of exploration in *Drosophila*", published in PLoS Computational Biology (2019). This paper was co-authored by myself, Konstantinos Lagogiannis, and Barbara Webb. I was responsible for constructing all models in this paper, analysing them, and interpreting the results. I completed the majority of the writing for this paper and prepared all figures. Konstantinos Lagogiannis supervised model development and analysis, and contributed writing to the discussion section of the paper. Barbara Webb provided project supervision and contributed writing to the introduction and discussion sections of the paper.

In this paper I extend the mechanical model detailed in the previous chapter to include transverse bending and planar motion of the body relative to the substrate. This is accomplished by introducing damped torsional springs between adjacent body segments, representing storage of elastic energy in larval tissues during bending.

In contrast to the previous chapter, I formulate the mechanical model within a Hamiltonian, rather than Newtonian, framework. While these frameworks are equivalent (Hamiltonian and Newtonian mechanics give different yet equivalent mathematical descriptions of the same physics), the Hamiltonian approach has been more prevalent in the study of dynamical systems, and it provides more powerful tools for

analysing the dynamics of a mechanical system (see Introduction chapter).

I also extend the neuromuscular model presented in the previous chapter. Firstly, the local feedback of stretch rate is now passed through a hard nonlinearity, such that the muscle tension is a binary-valued function of the local stretch rate. This nonlinearity is intended to limit the power flow into the body from the musculature, so that the closed-loop system is less sensitive to the feedback gain, and the amplitude of motion cannot grow without bound (power loss due to viscous friction is quadratic in velocity, while power gained due to muscle tension is now linear in velocity). While different forms of nonlinearity could accomplish this, I chose to use a piecewise constant function in order to minimise the conceptual complexity of the model and limit the number of model parameters. The second modification to the neuromuscular system is the addition of inhibitory connections between reflex arcs in distant segments. When a reflex arc activates within a particular segment, amplifying that segment's motion, it simultaneously turns off the reflex arcs in distant This ensures that only a single peristaltic wave can propagate through the body at a time, and also ensures that this wave can cause motion of the body's centre of mass relative to the substrate by limiting the number of simultaneously moving segments (this observation will be explained later in this chapter). In the discussion section, I compare this neuromuscular model to known larval anatomy.

I also comment on the model's requirement/assumption of stretch-rate sensitive mechanoreceptors. As explored within the discussion section, general models of mechanotransduction suggest that larval mechanosensory cells may be sensitive to both rate of stretch as well as absolute stretch (Suslak et al., 2011). Indeed, it has long been observed that mammalian mechanosensory endings as well as insect and other arthropod proprioceptors may be sensitive to both the rate of stretch, encoded by a phasic sensory response, and the absolute stretch, encoded by a tonic sensory response, of mechanical stimuli (Wiersma and Boettiger, 1959; Bush, 1965; Hoyle, 1977; Zill, 1985; Suslak et al., 2011; Proske and Gandevia, 2012). There are several possible arrangements that could satisfy the model's assumption of a signal encoding only the segmental stretch-rate. Firstly, individual proprioceptors may respond only to stretch-rate, as seen, for example, in the encoding of joint velocity by the purely phasic responses of some units within the metathoracic femoral chordotonal organ of the locust hindleg (Zill, 1985). Secondly, there may be central neural processing of a "mixed" tonic-phasic mechanosensory input (as discussed in the main paper discussion section). Alternatively, the larva may simply utilise a "mixed" phasic-tonic input without any additional

processing. The effects of such a reflex, producing muscle forces in response to both absolute stretch as well as stretch-rate, are considered within an appendix to the main paper.

As before, I proceed by first studying the dynamics of the body in the absence of driving forces. I also restrict my analysis to the case of conservative motion only (i.e. no viscous or sliding friction), motivated by the observation in the previous chapter that a simple control scheme can be used to recover these dynamics in the presence of friction.

I begin by focusing only on the small-amplitude motions of the body. This is accomplished by taking a quadratic approximation to the Hamiltonian. In this case the axial and transverse motions of the body are energetically isolated and dynamically uncoupled. The Liouville-Arnold integrability theorem holds, so that the motion of the body must be (quasi)periodic. Indeed, by transforming to the eigenbasis of the Hamiltonian I show that the motion can be decomposed into a set of axial travelling compression waves and transverse standing waves, each of which independently conserves energy.

I then re-introduce friction and driving forces. Since the axial and transverse motions are decoupled in the small-amplitude regime, and the neuromuscular system transfers power only into axial degrees of freedom, the transverse motion eventually terminates due to friction under all cases. Considering the axial motion, for low values of reflex gain frictive power losses dominate and the system gradually loses energy and comes to a stop at a stable equilibrium configuration (all masses aligned at equal distances from each other). Beyond a critical value of reflex gain, the axial dynamics undergoes a pitchfork-like symmetry breaking bifurcation, leading to two stable and two unstable long-term behaviours. The stable behaviours correspond to the generation of forward- or backward-propagating compression waves, driving forward or backward motion relative to the substrate, respectively. The unstable behaviours correspond to the passive equilibrium state (i.e. all masses stationary and aligned, at equal distances from each other), or generation of standing waves of compression and expansion with no overall translation relative to the substrate.

To study the large-amplitude motion of the larva, I restrict analysis to a limited number of degrees of freedom, namely the bending and stretching of the head segment, in the absence of friction and driving forces. This facilitates visualisation of the dynamics by the method of Poincare section, and simplifies the mathematical analysis. I show that for finite amplitudes, the axial and transverse degrees of freedom become

coupled, so that each motion no longer independently conserves energy. In this case the Liouville-Arnold theorem no longer holds, so that the motion is in principle chaotic for some initial conditions and choices of the model parameters. Through numerical investigation I show that the motion becomes increasingly chaotic as the amplitude of motion increases, in line with the KAM theorem (which is technically not directly applicable to our model). I then confirm that these results translate to the model of the entire body, not just the restricted model of the head, showing that the overall conservative motion of the body at large amplitudes is indeed chaotic.

I then reintroduce friction and driving forces once more, and analyse the resulting deformations of the body. Travelling axial compression waves persist in the large-amplitude regime, but in this case the coupling of axial and transverse motions leads to ongoing transfer of power from the directly driven axial degrees of freedom into the passive transverse degrees of freedom. This means that transverse frictive losses can be counteracted, and transverse motion can be maintained, without direct power transfer into these degrees of freedom from the musculature. By deploying the same numerical measures as used in the previous conservative case, I show that the motion of the body remains chaotic in the presence of friction and driving forces.

Shifting focus to the path of the model larvae (i.e. the motion of the centre of mass of the larva), I show that the deterministic chaotic deformations of the body are capable of producing apparently "random" exploration. I characterise this behaviour using several measures, concluding that the exploration behaviour of the larva may arise from a deterministic chaotic superdiffusion process grounded in the mechanics of the body.

In the appendices, I provide a detailed mathematical specification of the mechanical model, a detailed derivation of the results on small-amplitude motion, and a detailed derivation of the reduced model of the head's degrees of freedom (all of which were too lengthy to be included in the main body of the paper). I provide a mathematical argument regarding the trade-off between power transfer into the body and force on the centre of mass, showing that power is most efficiently transferred into low-frequency axial modes (which have a lower damping ratio), but the production of large forces on the centre of mass requires the recruitment of high-frequency modes. I also show that for small amplitude motion, segmentally localised reflex arcs can be decomposed into a stretch-dependent component and a stretch rate-dependent component, and that these give rise to an effective mechanical stiffness (stretch-dependent) and viscosity (stretch rate-dependent).

Finally, in a section following the published work, I examine the mechanism by which power is transferred from axial to transverse degrees of freedom. Using a first-order perturbation analysis of the mechanical dynamics of the head, I show that this can be understood in terms of parametric excitation and that power transfer should occur through a 2:1 resonance relationship between axial and transverse degrees of freedom, matching results on the large-amplitude behaviour of the model and observations of real larval behaviour.

Main conclusions:

- The mechanical model from the previous chapter has been extended to include both axial and transverse deformations, and planar translation and rotation of the larva as a whole. The mechanics has been reformulated in a Hamiltonian framework in order to facilitate its analysis.

- The neuromuscular model from the previous chapter has been extended to include a hard nonlinearity within the reflex arc and mutual inhibition between distant reflex arcs. The nonlinearity serves to model the saturating neuromuscular activation and to limit the amplitude of motion (so that solutions can not grow without bound as in the previous chapter). The long-range inhibitory connections ensure that a single peristaltic wave is propagated at a time, and to ensure that these waves cause centre of mass motion.

- The modified neuromuscular model shows striking similarities to known larval anatomy.

- For conservative, small-amplitude motion, the axial and transverse degrees of freedom are energetically decoupled. The motion of the body can be decomposed into a set of axial travelling waves of compression and transverse standing waves of bending.

- In the presence of friction and driving forces, the closed-loop system produces stable forward and backward peristalsis.

- For conservative, large-amplitude motion, the axial and transverse degrees of freedom become energetically coupled. The motion of the body becomes chaotic, and cannot be decomposed into separate axial and transverse motions.

- Reintroducing friction and driving forces, the closed-loop system now produces forward and backward axial compression waves in addition to apparently “ran-

dom" transverse bending. The motion of the system shows signatures of deterministic chaos.

- The chaotic deformations of the body drive an exploratory routine, in which a population of larvae in similar initial states will spread out over the substrate. This can be considered as a deterministic superdiffusion process.

Limitations:

- The model does not explicitly include active driving of transverse degrees of freedom, i.e. the model musculature cannot directly bend the body. While this helps us illustrate the role of axial-transverse energetic coupling and reduce the number of parameters in our model, the larva is known to actively bend. I introduce active bending forces in the following chapter.

- The model produces only unbiased exploratory behaviour, and cannot account for taxis behaviour. I extend the model presented in this chapter to produce taxis in the following chapter.

- Although the neuromuscular model displays striking similarities to larval anatomy, it does not reproduce the experimentally observed endogenous waves of activity in the absence of mechanical input. I will return to this problem in the discussion chapter.

3.2 Availability of software and supplementary videos

The original code used to produce all figures in this chapter has been made publicly available (doi 10.5281/zenodo.1432637, github link https://github.com/janeloveless/mechanics-of-exploration/). The software outputs individual subplots, which were assembled and labelled prior to publication using Inkscape.

The supplementary videos for this chapter will be available upon publication of the paper "Modelling the mechanics of exploration in *Drosophila*" in PLoS Computational Biology.

3.3 Publication: Modelling the mechanics of exploration in larval *Drosophila*

PLOS | SUBMISSION

Modelling the mechanics of exploration in larval *Drosophila*

Jane Loveless[1], Konstantinos Lagogiannis[1, 2], Barbara Webb[1*],

1 Institute for Perception, Action, and Behaviour, School of Informatics, University of Edinburgh, 10 Crichton Street, Edinburgh EH8 9AB, Scotland, UK
2 MRC Centre for Developmental Neurobiology, New Hunt's House, King's College London, Guy's Hospital Campus, London SE1 1UL, UK

* bwebb@inf.ed.ac.uk

Abstract

The *Drosophila* larva executes a stereotypical exploratory routine that appears to consist of stochastic alternation between straight peristaltic crawling and reorientation events through lateral bending. We present a model of larval mechanics for axial and transverse motion over a planar substrate, and use it to develop a simple, reflexive neuromuscular model from physical principles. The mechanical model represents the midline of the larva as a set of point masses which interact with each other via damped translational and torsional springs, and with the environment via sliding friction forces. The neuromuscular model consists of : 1. segmentally localised reflexes that amplify axial compression in order to counteract frictive energy losses, and 2. long-range mutual inhibition between reflexes in distant segments, enabling overall motion of the model larva relative to its substrate. In the absence of damping and driving, the mechanical model produces axial travelling waves, lateral oscillations, and unpredictable, chaotic deformations. The neuromuscular model counteracts friction to recover these motion patterns, giving rise to forward and backward peristalsis in addition to turning. Our model produces spontaneous exploration, even though the nervous system has no intrinsic pattern generating or decision making ability, and neither senses nor drives bending motions. Ultimately, our model suggests a novel view of larval exploration as a deterministic superdiffusion process which is mechanistically grounded in the chaotic mechanics of the body. We discuss how this may provide new interpretations for existing observations at the level of tissue-scale activity patterns and neural circuitry, and provide some experimental predictions that would test the extent to which the mechanisms we present translate to the real larva.

Author summary

We investigate the relationship between brain, body and environment in the exploratory behaviour of fruitfly larva. A larva crawls forward by propagating a wave of compression through its segmented body, and changes its crawling direction by bending to one side or the other. We show first that a purely mechanical model of the larva's body can produce travelling compression waves, sideways bending, and unpredictable, chaotic motions. For this body to locomote through its environment, it is necessary to add a neuromuscular system to counteract the loss of energy due to friction, and to limit the simultaneous compression of segments. These simple additions allow our model larva to generate life-like forward and backward crawling as well as spontaneous turns, which occur without any direct sensing or control of reorientation. The unpredictability

inherent in the larva's physics causes the model to explore its environment, despite the lack of any neural mechanism for rhythm generation or for deciding when to switch from crawling to turning. Our model thus demonstrates how understanding body mechanics can generate and simplify neurobiological hypotheses as to how behaviour arises.

Introduction

Exploratory search is a fundamental biological behaviour, observed in most phyla. It has consequently become a focus of investigation in a number of model species, such as larval *Drosophila*, in which neurogenetic methods can provide novel insights into the underlying mechanisms. However, appropriate consideration of biomechanics is needed to understand the control problem that the animal's nervous system needs to solve.

When placed on a planar substrate (typically, an agar-coated petri dish), the *Drosophila* larva executes a stereotypical exploratory routine [1] which appears to consist of a series of straight runs punctuated by reorientation events [2]. Straight runs are produced by laterally symmetric peristaltic compression waves, which propagate along the larval body in the same direction as overall motion (i.e. posterior-anterior waves carry the larva forwards relative to the substrate, anterior-posterior waves carry the larva backwards) [3]. Reorientation is brought about by laterally asymmetric compression and expansion of the most anterior body segments of the larva, which causes the body axis of the larva to bend [2].

Peristaltic crawling and reorientation are commonly thought to constitute discrete behavioural states, driven by distinct motor programs [2]. In exploration, it is assumed, alternation between these states occurs stochastically, allowing the larva to search its environment through an unbiased random walk [1, 4–6]. The state transitions or direction and magnitude of turns can be biased by sensory input to produce taxis behaviours [4, 5, 7–13]. The neural circuits involved in producing the larval exploratory routine potentially lie within the ventral nerve cord (VNC), since silencing the synaptic communication within the brain and subesophageal ganglia (SOG) does not prevent substrate exploration [1]. Electrophysiological and optogenetic observations of fictive locomotion patterns within the isolated VNC [14, 15] support the prevailing hypothesis that the exploratory routine is primarily a result of a centrally generated motor pattern. As such, much recent work has focused on identifying and characterising the cells and circuits within the larval VNC [16–32]. However, behaviour rarely arises entirely from central mechanisms; sensory feedback and biomechanics often play a key role [33–35] including the potential introduction of stochasticity. Indeed, thermogenetic silencing of somatosensory feedback in the larva leads to severely retarded peristalsis [36] or complete paralysis [37, 38].

In line with the ethological distinctions drawn between runs and turns, computational modelling of the mechanisms underlying larval behaviour has so far focused on either peristaltic crawling or turning. An initial model based on neural populations described a possible circuit architecture and dynamics underlying the fictive peristaltic waves observed in the isolated ventral nerve cord [39]. A subsequent model described the production of peristaltic waves through interaction of sensory feedback with biomechanics, in the absence of any centrally generated motor output [40], in a manner similar to earlier models of wave propagation via purely sensory mechanisms in *C. elegans* [41, 42]. This model produced only forward locomotion as it incorporated strongly asymmetric substrate interaction. Recently, a model combining biomechanics, sensory feedback, and central pattern generation reproduced many features of real larval peristalsis [43]. However, this model only aimed to explain forward locomotion, and accordingly contained explicit symmetry-breaking elements in the form of posterior-anterior excitatory couplings between adjacent segments of the VNC, and

posterior-anterior projections from proprioceptive sensory neurons in one segment into the next segment of the VNC. No biomechanical models of turning in the larva have yet been published, but the sensory control of reorientation behaviour has been explored in more abstract models [4, 5, 8, 11–13, 44]. No current model accounts for both peristalsis and reorientation behaviours, and no current model of peristalsis can account for both forward and backward locomotion without appealing to additional neural mechanisms.

Here we present a model of unbiased substrate exploration in the *Drosophila* larva that captures forward and backward peristalsis as well as reorientation behaviours. We provide a deterministic mathematical description of body mechanics coupled to a simple, reflexive nervous system. In contrast to previous models, our nervous system has no intrinsic pattern-generating ability [39, 43, 44], and does not explicitly encode discrete behavioural states or include any stochasticity [4, 5, 8, 11–13]. Nevertheless, the model is capable of producing apparently random "sequences" of crawling and reorientation behaviours, and is able to effectively explore in a two-dimensional space. We argue that the core of this behaviour lies in the chaotic mechanical dynamics of the body, which result from an energetic coupling of axial ("peristaltic") and transverse ("turning") motions.

Our choice not to explicitly model navigational decision-making and central pattern generation circuits is motivated by our desire to illustrate the powerful insights offered by focusing upon the mechanics of the body with which the nervous system interacts. The model neuromuscular system we have constructed is based upon simple physical arguments, yet ultimately bears a striking resemblance to known features of the larval nervous system. By starting from the mechanics of the body, and not assuming the existence of particular neural circuits, we are able to provide a new explanatory framework within which to re-interpret existing neurophysiological observations, including observations of central pattern generation within the larval VNC, and also provide unique predictions for future neurophysiological experiments.

In what follows, we first outline the key components and assumptions of our model of body mechanics. We then follow simple arguments to guide the construction of a neuromuscular model capable of producing power flow into the body, and motion of the body's centre of mass relative to the substrate. Crucially, the neuromuscular model neither senses nor drives transverse motions. In analysing the behaviour of our model, we begin by focusing on the small-amplitude, energy-conservative behaviour of the body in the absence of frictive and driving forces. In this case, the motion of the body is quasiperiodic and decomposes into a set of energetically isolated axial travelling waves and transverse standing waves. Reintroducing friction and driving forces, we demonstrate the emergence of a pair of limit cycles corresponding to forward and backward peristaltic locomotion, with no differentiation of the neural activity for the two states. We then shift focus to the behaviour of the model at large amplitudes. In this case the axial and transverse motions of the body are energetically coupled, and the conservative motion becomes chaotic. The energetic coupling allows our neuromuscular model to indirectly drive transverse motion, producing chaotic body deformations capable of driving substrate exploration. Analysis of our model supports a view of larval exploration as an (anomalous) diffusion process grounded in the deterministic chaotic mechanics of the body.

Models

Mechanics

To explore larval crawling and turning behaviours, we choose to describe the motion of the larval body axis (midline) in a plane parallel to the substrate (Fig 1, S1 Fig). The

larval body is capable of more diverse motions including lifting/rearing [21], rolling [45], digging [46], self-righting / balancing, and denticle folding which we have recently observed to occur during peristalsis (S1 Video). However, while exploring flat surfaces, the larva displays fairly little out-of-plane motion (neither translation perpendicular to the substrate nor torsion around the body axis) and only small radial deformations [47]. Furthermore, the majority of ethological characterisations of larval exploration treat the animal as if it were executing purely planar motion [4, 6, 8–13, 48]. A planar model is thus a reasonable abstraction for the issues addressed in this paper, i.e., the generation of peristalsis, bending, and substrate exploration.

Fig 1. Our model of axial and transverse motion over a planar substrate. The midline of the larva is modelled as a set of discrete point masses interacting with each other via linear, damped translational and torsional springs, and with the environment via Coulomb sliding friction. We model the larva's incompressible coelomic fluid by constraining the total length of the midline to remain constant (see main text). Quantities used to describe deformations of the body, and interaction with the substrate, are shown in S1 Fig.

The segmented anatomy of the *Drosophila* larva allows us to focus our description of the midline to a set of $N = 12$ points in the cuticle, located at the boundaries between body segments and at the head and tail extremities. We assign each point an identical mass, and measure its position and velocity relative to a two dimensional cartesian coordinate frame fixed in the substrate (the laboratory or lab frame). We therefore have $N_{DOF} = 2N = 24$ mechanical degrees of freedom. We note that our assumption of a uniform mass distribution along the midline is somewhat inaccurate, since thoracic segments are smaller than abdominal segments. However, simulations with non-uniform mass distribution give results which are qualitatively close to those presented here.

We assume that the larval body stores elastic energy in both axial compression/expansion and transverse bending, due to the presence of elastic proteins in the soft cuticle. We assume that energy is lost during motion due to viscous friction within the larva's tissues and sliding friction between the body and the substrate. Sliding friction also allows shape changes (deformations) of the body to cause motion of the larva as a whole relative to the substrate (centre of mass motion).

Since the mechanical response of the larva's tissues is yet to be experimentally determined, we assume a linear viscoelastic model. This is equivalent to placing linear (Hookean) translational and torsional springs in parallel with linear (Newtonian) dampers between the masses in the model, as shown in Fig 1, or to taking quadratic approximations to the elastic potential energy and viscous power loss (as in S1 Appendix). We note that the accuracy of the approximation may decrease for large deformations, in which nonlinear viscoelastic effects may become important.

As with larval tissue mechanics, there has been little experimental investigation of the forces acting between the larva and its environment. We therefore assume a simple anisotropic Coulomb sliding friction model, in which the magnitude of friction is independent of the speed of motion, but may in principle depend upon the direction of travel. This anisotropy could be thought of as representing the biased alignment of the larva's denticle bands, or directional differences in vertical lifting or denticle folding motions which are not captured by our planar model. A mathematical formulation of our sliding friction model is given in S1 Appendix.

In addition to power losses due to friction, we also allow power flow due to muscle activation. For the sake of simplicity, we choose to allow only laterally symmetric muscle tensions. In this case, the musculature cannot directly cause bending of the midline, and can only explicitly drive axial motions. We will see later that even indirect

driving of bending motion can lead to surprisingly complex behaviour, due to energetic coupling of axial and transverse degrees of freedom.

The choice to neglect asymmetric muscle tensions is made in order to simplify our model and provide a clearer illustration of the potential role of body mechanics in generating complex larval behaviour. We note that there is only one way for muscle activations to be symmetric – if we were to allow asymmetry we would have to specify exactly what form that asymmetry should take, and we have little empirical or theoretical grounds on which to do so. Nevertheless, there are some interesting cases which may be considered in passing – the presence of a constant torque about the model's segment boundaries should cause a shift in the equilibrium posture towards a resting curved shape. The presence of torques which are a linear function of the local body bending angle or local angular velocity should shift the effective transverse stiffness or viscosity of the body S5 Appendix. In this sense the model presented here could be considered to already include the effect of asymmetric muscle tensions, they have simply been incorporated into the passive stiffness and viscosity of the body. We have recently developed an extension of the model presented here which uses a similar local reflex to modulate the body's effective transverse viscosity in proportion to a stimulus input, allowing the model to exhibit taxis behaviour [49].

Finally, we model the internal coelomic fluid of the larva. Given the extremely small speed of the fluid motion compared to any reasonable approximation to the speed of sound in larval coelomic fluid, we can safely approximate the fluid flow as incompressible [50]. This would ordinarily require that the volume contained within the larval cuticle remain constant. However, since we are modelling only the motion of the midline and neglecting radial deformations, we constrain the total length of the larva to remain constant. We note that this constraint is not entirely accurate to the larva, as the total length of the animal has been observed to vary during locomotion [47]. Nevertheless, for the sake of simplicity we will continue with this constraint in place, noting that this approximation has been used with success in previous work focused on peristalsis [40, 43], and that there is experimental support for kinematic coupling via the internal fluid of the larva [3]. We note that we satisfy the incompressibility condition only approximately in some sections (*Model behaviour – Conservative chaos, Dissipative chaotic deformations*, and *Deterministic exploration*), by introducing an additional potential energy associated with the constraint, which produces an energetic barrier preventing large changes in the total length of the body (see S1 Appendix for details of this approximation along with specifics of the mathematical formulation of our mechanical model).

Note that in the absence of transverse bending, the total length constraint causes the head and tail extremities of the larva to become mechanically coupled and move in unison [40, 43]. The axial mechanics thus has periodic boundary conditions, and the most anterior (T1) and posterior (A8) segments of the larva may be considered adjacent. This means, for instance, that a compression wave travelling from tail to head will cause motion of the tail on termination at the head, thus initiating a new compression wave. This view also allows us to reason about what should happen if we relax the total length constraint. In particular, if we were to replace the direct coupling of head and tail by a viscoelastic coupling, representing the capacity for storage and dissipation of energy within the internal fluid or in radial expansion of the cuticle, the axial mechanics would still have periodic boundary conditions but would now have a step change in mechanical impedance. Waves hitting such "sudden" impedance boundaries in their transmission media will generally be partially transmitted (i.e. passing directly from head to tail in the larva) and partially reflected (i.e. changing direction and moving backwards from the head extremity), providing one possible cause of transitions between forward and backward locomotion in the animal. As will be seen, however,

these transitions may occur even in the absence of an impedance discontinuity, and we will continue with the total length constraint in place in order to simplify our model.

Neuromuscular System

Let us now consider how we should use muscle activity to produce locomotion. There are two basic requirements. First, we must have power flow into the body from the musculature, so that the effects of friction may be overcome and the larva will not tend towards its equilibrium configuration. Second, we must be able to produce a net force on the centre of mass of the larva, so that it can accelerate as a whole relative to the lab frame. Note that in this section, we motivate the neural circuits in the model from this purely functional point of view, but will present relevant biological evidence in the discussion.

To satisfy the first criterion, let us examine the flow of power into the body due to the action of the musculature

$$P = -\sum_{i=1}^{N-1} b_i \mathrm{MF}_i \dot{q}_i \tag{1}$$

Here, q_i describes the change in length of the i'th body segment away from its equilibrium length, $\dot{q}_i$ is the rate of expansion of the i'th body segment, b_i is a (positive) gain parameter, MF_i is a (positive) dimensionless control variable representing muscle activation, and the product $b_i\mathrm{MF}_i$ is the total axial tension across the i'th body segment. From this expression, it is clear that if we produce muscle tensions ($\mathrm{MF}_i > 0$) only while segments are shortening ($\dot{q}_i < 0$), we will always have positive power flow into the body ($P > 0$). This is a mathematical statement of the requirement for the larva's muscles to function as *motors* during locomotion, rather than as springs, brakes, or struts [33].

A simple way to fulfil this condition is to introduce a segmentally localised reflex circuit (Fig 2, [40]). We place a single sensory neuron in each segment which activates when that segment is compressing ($\dot{q}_i < 0$). Each sensory neuron then projects an excitatory connection onto a local motor neuron, which in turn projects to a muscle fibre within the same segment. Assuming for now that there are no other influences on the motor neurons, so that sensory activation implies local motor neuron activation, segmental shortening will produce an immediate muscle tension serving to amplify compression of the segment and thus counteract frictive energy losses.

Fig 2. The neuromuscular model. A local reflex amplifies motion via positive feedback : sensory neurons SN activate during segmental shortening, exciting motor neurons MN, and causing muscle fibre activation MF which accelerates shortening. Reflexes in distant segments i and $i + j$ ($|j| > 1$) mutually inhibit one another via interneurons IN. This limits the number of moving segments to allow centre of mass motion (see text).

Let us now consider the second criterion for peristaltic locomotion. Assuming all segment boundaries are of equal mass, the force on the centre of mass of the larva is proportional to the sum of the forces acting on each segment boundary, i.e.

$$F_{COM} \propto \sum_{i=1}^{N-1} F_{segment} \tag{2}$$

Newton's third law tells us that any forces of interaction between segment boundaries (i.e. viscoelastic and muscle forces) must be of equal magnitude and opposite direction, so that they cancel in this summation and we are left only with

contributions arising from substrate interaction. If the motion of the body is such that some number n_f of segments move forward at a given time, against a frictional force $-\mu_f$, while n_b segments remain anchored or move backward, experiencing a frictional force μ_b, then the summation becomes

$$F_{COM} \propto n_b\mu_b - n_f\mu_f \tag{3}$$

In the limiting case of isotropic (direction-independent) substrate interaction we have $\mu_b = \mu_f$, and this expression tells us that the centre of mass will accelerate in the forward direction only when there are less segments moving forward than are moving backward or anchored to the substrate. Similarly, moving a small number of segments backward while the others remain anchored will result in backward acceleration of the centre of mass. Therefore, if the animal is to move relative to its substrate, it must ensure that only a limited number of its segments move in the overall direction of travel at a given time (indeed, this matches observations of the real larva [3,22]). A more lengthy exposition of this requirement on limbless crawling behaviours can be found in [51].

We fulfil the requirement for a small number of moving segments by introducing mutually inhibitory interactions between the segmentally localised reflex circuits (Fig 2). We add a single inhibitory interneuron within each segment. When the sensory neuron within the local reflex activates, it excites this interneuron, which then strongly inhibits the motor neurons and inhibitory interneurons in non-adjacent segments, effectively turning off the local reflexes in distant neighbours. Adjacent segments do not inhibit each other in our model, allowing reflex activity to track mechanical disturbances as they propagate from one segment to the next. We comment on the plausibility of this feature of our model, given the experimental observation of nearest-neighbour inhibitory connections in the larval ventral nerve cord [28], in the discussion. Similarly, the head and tail segments do not inhibit each other, which permits peristaltic waves to be (mechanically) reinitiated at one extremity as they terminate at the other (see discussion at the end of the previous subsection). This effectively introduces a ring-like topology into the neural model, matching our model of axial mechanics which couples head and tail motion through the total length constraint [40].

We now have a neuromuscular model consisting of four cell types repeated in each segment – sensory neurons, inhibitory interneurons, motor neurons, and muscle fibres. For the sake of simplicity we model all neurons as having a binary activation state governed by the algebraic relation

$$V_i = \begin{cases} 1 & \sum_j w_j V_j > \theta_i \\ 0 & \text{otherwise} \end{cases} \tag{4}$$

where V_i is the activation of the i'th cell, θ_i is its activation threshold, V_j is the activation of the j'th presynaptic cell, and w_j is the associated synaptic weight. Numerical values for the weights and thresholds used in our model are given in S1 Table, supplemental. Note that the muscle tension over a segment either vanishes (when the muscle fibre is in the inactive state) or has fixed magnitude b_i (when the muscle fibre is activated by local sensory feedback). For this reason we refer to b_i as the *reflex gain*.

Our choice to neglect neural dynamics is based on the large difference in timescales between the neural and mechanical dynamics. Typical motor neuron spiking occurs with a timescale on the order of 10^{-3} seconds. Spiking is observed to be significantly "averaged out" by the graded (non-spiking) muscle fibre responses, and respond on the order of $\sim 10^{-1}$ seconds to prolonged motor neuron spiking [52,53]. During locomotion, segmental compressions are driven by several longitudinal muscle fibres activating simultaneously [3,14,29] in response to largely independent motor neuron

populations [54, 55] which are unlikely to spike with identical timing. This spatial integration should further "mask" the effects of neural dynamics. Note that the lack of neural dynamics in our model immediately rules out central pattern generation. However, this does not prevent our model from producing complex, larva-like behaviour, and we consider how our model could account for observations of central pattern generation in the discussion.

To summarise, the neural model we have constructed can be seen as consisting of two parts, a segmentally repeating local reflex and a mutual inhibition circuit acting between non-adjacent reflexes. The local reflex is constructed so that muscles will act as motors, amplifying segmental compressions and counteracting friction. The mutual inhibition circuit couples distant reflexes to allow only localised amplification. By limiting the number of moving segments, this should ensure that the model larva can produce a net force on its centre of mass.

Results

Larva-like axial compression waves and lateral oscillations result from conservative mechanics

One of the advantages of grounding our model of larval exploration in the body's physics is that we are now able to apply powerful analytical results from classical mechanics in order to understand the model's behaviour. In this section we attempt to elucidate the naturally preferred motions of the larva by focusing our attention on the conservative mechanics of the body while neglecting friction forces, which would cause all motion to stop, and driving forces, which might impose a particular pattern of motion.

In this case, the general character of motion is specified by the Liouville-Arnold integrability theorem. This theorem asks us to look for a set of conserved quantities associated with a mechanical system, which remain unchanged as the system moves (energy, momentum, and angular momentum are examples of some commonly conserved quantities). If we can find a number of these quantities equal to the number of mechanical degrees of freedom in our model, then the theorem tells us that the motion of the body is *integrable* – it can be expressed analytically, and must be either periodic or quasiperiodic. If there are not enough conserved quantities, then the system is said to be *nonintegrable*. In this case the motion is much more complicated and will be chaotic for some initial conditions. These chaotic motions do not permit analytical expression and must be approximated through simulation.

In this section, we explicitly seek a case for which there is a "full set" of conserved quantities (we provide only major results here, for detailed derivations see S2 Appendix). We begin by restricting ourselves to considering only small deformations of the larval midline, in the case where all segments are of identical axial stiffness k_a, transverse stiffness k_t, mass m, and length l. Under these assumptions, the total mechanical energy of the body may be written

$$H(\mathbf{x}, \mathbf{y}, \mathbf{p}_x, \mathbf{p}_y) = \frac{1}{2}\left[\mathbf{p}_x^T \mathbf{p}_x + \omega_a^2 \mathbf{x}^T \mathbf{D}_2 \mathbf{x}\right] + \frac{1}{2}\left[\mathbf{p}_y^T \mathbf{p}_y + \omega_t^2 \mathbf{y}^T \mathbf{D}_4 \mathbf{y}\right] \tag{5}$$

where $\mathbf{x}$ and $\mathbf{y}$ are vectors giving the displacement of each segment boundary along the body axis and perpendicular to the body axis, respectively, $\mathbf{p}_x$ and $\mathbf{p}_y$ give the translational momentum associated with each direction, $\mathbf{D}_2$ and $\mathbf{D}_4$ are difference matrices arising from a Taylor series expansion of our model's potential energy (see S2 Appendix), and $\omega_a = \sqrt{k_a/m}$ and $\omega_t = \sqrt{k_t/ml^2}$ are characteristic axial and transverse frequency scales. By making a linear change of coordinates

$\{\mathbf{x}, \mathbf{y}, \mathbf{p}_x, \mathbf{p}_y\} \rightarrow \{\mathbf{X}, \mathbf{Y}, \mathbf{p}_X, \mathbf{p}_Y\}$ to the eigenbasis of $\mathbf{D}_2$ and $\mathbf{D}_4$ (see S2 Appendix) this simplifies to

$$H(\mathbf{X}, \mathbf{Y}, \mathbf{p}_X, \mathbf{p}_Y) = \sum_{i=1}^{N-1} \frac{1}{2}\left[p_{X,i}^2 + \omega_a^2 \lambda_{a,i} X_i^2\right] + \sum_{i=1}^{N} \frac{1}{2}\left[p_{Y,i}^2 + \omega_t^2 \lambda_{t,i} Y_i^2\right] \tag{6}$$

where $\lambda_{a,i}$ and $\lambda_{t,i}$ are eigenvalues associated with the coordinate transformation. This expression is a sum of component energies, each of which is independently conserved. The Liouville-Arnold theorem immediately tells us that the motion of the body must be (quasi)periodic in the case of conservative small deformations. Indeed, the energy associated with each of the new coordinates X_i, Y_i is in the form of a harmonic oscillator, and each coordinate executes pure sinusoidal oscillations. By transforming back to the original coordinates $\mathbf{x}, \mathbf{y}$ we obtain a set of collective motions (modes) of the body which are energetically isolated and have a sinusoidal time dependence, corresponding to axial and transverse standing waves. We will refer to the X_i, Y_i as modal coordinates since they describe the time dependence of each of the collective motions.

Each transverse standing wave corresponds to a periodic lateral oscillation of the body, with a unique frequency given by $\omega_{t,i} = \omega_t\sqrt{\lambda_{t,i}}$. We determined these frequencies numerically, along with the spatial components of the lowest frequency standing waves (Fig 3A). These can be seen to match the eigenmaggot shapes extracted from observations of unbiased larval behaviour [56].

Fig 3. Conservative, small-amplitude motions of the body decompose into a set of axial and transverse standing waves. A: spatial component of first four transverse standing waves (top, black) compared to first four experimentally determined eigenmaggots [56] (top, blue), with natural frequencies of oscillation (bottom). B: spatial component of first four axial standing waves (top), with natural frequencies of oscillation (bottom). Note that axial standing waves come in pairs with identical frequency. C: Pairs of axial standing waves can be combined to produce forward-propagating (top, solid black line) and backward-propagating (bottom, solid black line) travelling waves. Head and tail extremities move in phase (dashed black line) due to our total length constraint (see text), reminiscent of the "visceral pistoning" observed in the real animal [3].

The axial standing waves correspond to oscillating patterns of segmental compression and expansion. While each transverse standing wave had its own unique frequency of oscillation, the axial standing waves come in pairs with identical frequency but different spatial components – each member of the pair corresponds to a different spatial pattern of segmental compression/expansion spread across the body, but these patterns oscillate in time with the same frequency. We were able to analytically determine the frequency of oscillation of the i'th pair of axial standing waves to be

$$\omega_{a,i} = \omega_a\sqrt{\lambda_{a,i}} = 2\omega_a\left|\sin\left(\frac{\pi i}{N-1}\right)\right|, \quad i \in [0, N/2-1] \tag{7}$$

The spatial components of the axial standing waves could also be determined analytically

$$x_{k,i} = \frac{1}{\sqrt{N-1}}\cos\left(2\pi i\frac{k}{N-1}\right), \text{ or } x_{k,i} = \frac{1}{\sqrt{N-1}}\sin\left(2\pi i\frac{k}{N-1}\right), \quad i \in [0, N/2-1] \tag{8}$$

Where $x_{k,i}$ is the displacement of the k'th segment boundary for the i'th pair of standing waves. We plot the axial frequencies $\omega_{a,i}$ and spatial components $x_{k,i}$ in Fig 3B.

The fact that the axial oscillation frequencies come in identical pairs allows us to combine the axial standing waves with a $\pm 90°$ relative phase shift to form pairs of forward and backward travelling wave solutions (see S2 Appendix for the full derivation)

$$x_{k,i}(t) = \cos\left(\omega_{a,i}t \pm 2\pi i \frac{k}{N-1}\right), \quad i \in [0, N/2-1] \tag{9}$$

where $x_{k,i}(t)$ gives the displacement of the k'th segment boundary as a function of time for the i'th pair of travelling waves. The choice of a plus or minus sign corresponds to the choice between forward or backward wave propagation. These solutions correspond to propagating waves of segmental compression and expansion similar to those seen during larval peristalsis. We plot the lowest frequency pair of axial travelling wave solutions in Fig 3C, and directly visualise the synthesis of travelling wave solutions from standing wave solutions in S2 Video.

To summarise, in this section we have shown that for the case of conservative, small oscillations, the motion of the body may be decomposed into a combination of transverse standing waves and axial travelling waves. This is of clear relevance to understanding the behaviour of the larva, which moves across its substrate by means of axial peristaltic waves while reorienting using lateral oscillations. Indeed, the transverse modes of oscillation that we have derived here match principal components of bending computed from actual larval behaviour [56]. Our results can be interpreted as providing a physical basis for these observations – the principal components extracted from real larval data correspond to a "natural" coordinate basis that is grounded in the animal's mechanics. Furthermore, the proportion of postural variance explained by each principal component of the experimental data decreases with increasing modal frequency in our model (and thus increasing energy). We can therefore help to explain the observed ordering of principal components, as this corresponds to the larva "preferring" to occupy low-frequency, low-energy modes during most of its behaviour. We comment further on this observation in S3 Appendix in the context of axial modes. We will now focus on the small-amplitude motion of the body in the presence of energy dissipation due to friction and driving forces.

Forward and backward peristaltic locomotion can be obtained from simple reflexes

Reintroducing friction will clearly lead the motions described above to eventually terminate due to energy dissipation, unless opposed by transfer of power. In a previous section (*Models – Neuromuscular system*, see also S1 Appendix), we introduced a neuromuscular system to produce power flow into the body, but as described, it can only directly transfer power into the axial degrees of freedom. In the small deformation model we have just analysed, the axial and transverse degrees of freedom are energetically decoupled. It follows that transverse friction is unopposed and any transverse motion must eventually terminate in the case of small deformations. In this section we will therefore focus only on the axial degrees of freedom, which correspond to the peristaltic locomotion of the larva.

In Fig 4, we show the effect of coupling our neuromuscular model to the axial mechanics. For small reflex gains, the power flow into the body from the musculature is too low to effectively counteract frictive losses and the larva tends towards its passive equilibrium state, in which there is complete absence of motion. However, increasing reflex gain past a certain critical value leads to the emergence of long-term behaviours

in which the larva remains in motion, away from its passive equilibrium. These motions correspond to forward and backward locomotion, driven by forward and backward propagating compression waves (see below), as predicted from our earlier description of the conservative motions of the body, and as observed in the real larva [3]. The qualitative changes in behaviour that occur as reflex gain is varied are depicted in Fig 4A, where we have measured the long-term centre of mass momentum of the larva, along with the long-term relative phase of the lowest frequency modal coordinates.

The exact value of reflex gain required for onset of locomotion depends on the particular mechanical parameters used in our model (see table S2 Table for parameters used in Fig 4). In principle, this bifurcation point of the dynamics should be amenable to analytical investigation by studying the stability of the linearised model dynamics around the passive equilibrium state [57, 58]. In practise, however, the presence of hard nonlinearities in the sliding friction model makes such an approximation inaccurate.

Fig 4. Emergence of limit cycles for forward and backward locomotion in the dissipative, small-amplitude model. A: as reflex gain is increased past a critical point, the model larva attains a positive or negative long-term average centre of mass momentum (top, red and blue lines), signifying continuous forward or backward motion relative to the substrate, and a $\pm\pi/2$ relative phase difference between the two lowest frequency axial standing wave modes (bottom, red and blue lines), signifying the presence of forward- or backward-propagating axial travelling waves. B: trajectories of individual point masses in the model for forward (top) or backward (bottom) locomotion (see S2 Fig for corresponding neural state). C: projection of model trajectories onto the lowest frequency axial modes and the centre of mass momentum reveals a pair of (putative) stable limit cycles for forward (blue) and backward (red) locomotion. Parameters used to generate this figure are given in S2 Table.

For low reflex gains the centre of mass momentum tends to 0 as the body comes to a stop and enters a passive equilibrium state. The relative phase of the low frequency modal coordinates tends to either 0 or 180 degrees, which also corresponds to a loss of momentum. For larger values of reflex gain, the total momentum is either positive, zero, or negative. Positive and negative total momentum represent forward and backward locomotion, respectively, while zero momentum corresponds to two unstable cases which we discuss below. The relative phase of the lowest frequency modal coordinates tends to $\pm 90°$ at high reflex gains, corresponding to the presence of forward- or backward-propagating compression waves (see previous section). As in the larva [1, 3], forward-propagating waves drive forward locomotion while backward-propagating waves drive backward locomotion (Fig 4B).

We believe that these behaviours arise from the production of a pair of limit cycle attractors in the system's phase space, which we visualise in figure Fig 4C by projecting the system state onto the lowest frequency pair of axial modes, and plotting the associated modal coordinates along with the centre of mass momentum. Since wave motion implies that pairs of modal coordinates should perform pure sinusoidal oscillations with equal amplitude and frequency, and a $\pm 90°$ relative phase shift (see previous section and S2 Appendix), the travelling wave trajectories of the system become circles in this coordinate system (see discussion of Lissajous figures, [59]). Forward and backward locomotion can then be distinguished by the momentum of the centre of mass.

In this model, the speed of forward and backward locomotion are equal for a fixed value of reflex gain, while in the real larva the speeds are known to differ [15]. We comment on some possible explanations for this difference in the discussion.

In S2 Fig we show the neural state of the model larva during forwards and backwards locomotion. As expected given our previous exposition, we observe waves of

activity in the nervous system which track the mechanical waves propagating through the body. Our sensory neurons also show a second, brief period of activation following propagation of the mechanical wave caused by a slight compression that occurs as segments return to equilibrium. This activity is "cancelled out" by the mutual inhibition circuit, so that motor neurons do not exhibit a secondary burst of activity.

The larva has zero long-term total momentum in the presence of large reflex gain in only two cases, both of which are highly unstable. First, if we start the larva so that it is already in its passive equilibrium state, so that no relative motion of segment boundaries occurs, it is obvious that there will be no activation of local reflexes and the larva will not spontaneously move out of equilibrium. The second case corresponds to a pure axial standing wave. In this case the larva is divided into two regions by nodal points where the axial displacement is zero. During the first half-cycle of the standing wave, one region will experience compression while the other experiences expansion, and in the second half-cycle these roles will reverse. The neural circuit we have constructed can amplify compression during both half-cycles since they are separated by a configuration in which no compression or expansion occurs, and this allows the entire nervous system to become inactive and "reset". Since these behaviours are extremely unstable and require very specific initial conditions to be observed, we have not visualised them here.

While the mutually inhibitory connections in our model are not required for the propagation of locomotor waves, which can be maintained entirely by local reflexes [40], these connections do greatly enhance stability. In the absence of the mutual inhibition circuit, small mechanical disturbances in any stationary body segments can be amplified, giving rise to multiple compression waves which travel through the body simultaneously . If this instability produces an equal number of forward and backward moving segments then overall motion of the larva relative to the substrate will stop, in line with the argument presented earlier. We have also observed that roughly symmetrical substrate interaction is required to produce both forward and backward locomotion in our model. If friction is too strongly anisotropic, then locomotion can only occur in one direction regardless of the direction of wave propagation .

It is worth noting that the axial model presented in this section does display discrete behavioural states. However, there are no explicit decisions regarding which behavioural states to enter, since the particular neural states occupied during forwards and backwards locomotion are indistinguishable. Rather, both the apparent decision and the eventual direction of travel can only be understood by examining the dynamics and mechanical state of the body.

Conservative chaos from mechanical coupling

Having successfully produced peristaltic locomotion using our model, we will now turn our attention to the larva's turning behaviours. As before, we will start from physical principles. In a previous section (*Results – Conservative axial compression waves and transverse oscillations*) we showed that, for the case of conservative small oscillations, transverse motions of the body were energetically decoupled from axial motions, and could be decomposed into a set of periodic standing waves. We will first extend our previous analysis to the case of energy-conservative, large amplitude motions in the absence of damping and driving; and then in the following section consider the impact of energy dissipation and the neuromuscular system on transverse motion,

To keep our presentation simple and allow visualisation of model trajectories, we will focus on a reduced number of the mechanical degrees of freedom. Namely, we will examine the bending angle ϕ and axial stretch q of the head segment (Fig 5A). We introduce an amplitude parameter ϵ by making the substitutions $q \to \epsilon q$ and $\phi \to \epsilon\phi$, so that the total mechanical energy of the head may be written in nondimensional form as (see S4 Appendix)

$$H = \frac{1}{2}\left[p_q^2 + \frac{1}{(1+\epsilon q)^2}p_\phi^2 + q^2 + \lambda^2\phi^2\right] \tag{10}$$

where p_q, p_ϕ are the radial and angular momentum of the head mass, and we have scaled the time axis of the model so that the natural frequency of axial oscillation is unity. The parameter $\lambda = \omega_t/\omega_a = k_t/k_a l^2$ is the ratio of transverse and axial frequencies.

Fig 5. A reduced model of large amplitude motion. A: we focus on the conservative dynamics of the head's strain q and bend ϕ coordinates as amplitude ϵ is varied. B: head trajectories are visualised by Poincare section, in which the head's configuration q, ϕ is plotted at successive turning points of the transverse bending motion (at which angular velocity vanishes, $\mathrm{d}\phi/\mathrm{dt} = 0$).

In the case of small oscillations, i.e. $\epsilon \to 0$, the mechanical energy reduces to the simpler expression

$$H = \frac{1}{2}\left[p_q^2 + q^2\right] + \frac{1}{2}\left[p_\phi^2 + \lambda^2\phi^2\right] \tag{11}$$

which is clearly a sum of independent axial and transverse energies. These energies are individually conserved, so that the Liouville-Arnold theorem applies, and the motion of the head is integrable and (quasi)periodic. This is in clear agreement with our earlier results. For the more general case of large amplitude motion ($\epsilon > 0$), we may have in principle only a single conserved quantity – the total energy of the system. Indeed, it should be clear from the presence of a "mixed" term in the mechanical energy (Eq 10) that the axial and transverse motions are energetically coupled at large amplitudes, so that the individual energies associated with each motion are no longer independently conserved. Given that we have only one conserved quantity for a two degree of freedom system, we can no longer rely on the Liouville-Arnold theorem to prove (quasi)periodicity of the motion, and must accept that the system's behaviour may be chaotic.

To investigate this possibility further, we first note that conservation of energy implies that flow within the four dimensional phase space must be constrained to lie on the energy surface given implicitly by the relation $H(q, \phi, p_q, p_\phi) = E$. Therefore, given a particular value E for the total energy, the system dynamics becomes three dimensional. This allows us to visualise the behaviour of the system by plotting the points at which trajectories intersect a two-dimensional Poincare section [57, 58]. We define our Poincare section by the condition that the angular momentum vanishes $p_\phi = 0$ (equivalently, angular velocity vanishes $\mathrm{d}\phi/\mathrm{dt} = 0$), and plot successive crossings of the section as points in the q, ϕ plane. This allows us to intuitively interpret points in the Poincare section as configurations of the head at successive turning points (extrema) in the transverse motion (Fig 5B).

In what follows, we set the total energy to be $E = \frac{1}{2}$ so that when $\epsilon = 1$ we can in principle obtain complete compression of the head ($q = -1$). We choose to set $\lambda = \frac{e}{6} \approx 0.45$, giving an irrational frequency ratio. This loosely matches observations of the real larva in which the frequency of transverse oscillations is approximately half that of axial oscillations but does not satisfy an exact (rational) resonance relationship [44]. The results we obtain with these parameters do not differ much from results for other energies or other frequency ratios, including resonant relationships .

Poincare plots for the cases $\epsilon \to 0$ and $\epsilon \in \left\{\frac{1}{3}, \frac{2}{3}, 1\right\}$ are shown in Fig 6. When $\epsilon \to 0$ (Fig 6A), conservation of transverse energy implies that the turning points of the transverse motion must remain constant. The fact that the frequency ratio λ is

irrational implies that the overall motion is quasiperiodic, and the values of q obtained at successive transverse turning points should not repeat. In accordance with these observations, the Poincare section for $\epsilon \to 0$ consists of a series of verticle lines (Fig 6Ai). For $\epsilon = \frac{1}{3}$ the Poincare plot becomes distorted, but the majority of trajectories still trace out one-dimensional curves in the section (Fig 6Bi), which is indicative of persistent quasiperiodic behaviour. At $\epsilon = \frac{2}{3}$ the Poincare plot appears qualitatively different. There is now a large region of what appears to be "noise", indicating that the configuration of the head at successive transverse turning points has become unpredictable. This is a clear signature of deterministic chaos. There are, however, several regions of the section indicative of (quasi)periodic behaviour. These appear as one-dimensional curves or discrete points in the Poincare section (Fig 7Ai). At $\epsilon = 1$, the region of the Poincare plot occupied by chaos has expanded, although there still appear to be some regions corresponding to (quasi)periodic behaviour (Fig 7Bi). These results qualitatively agree with the Kolmogorov-Arnold-Moser theorem [59], which tells us that quasiperiodic behaviour should persist under small nonintegrable (chaotic) perturbations of an integrable Hamiltonian, and that the region of phase space corresponding to chaotic behaviour should grow with the perturbation size (in our case, the perturbation size corresponds to the amplitude of motion ϵ). However, our model as presented here does not formally meet the requirements of this theorem (see S4 Appendix).

Fig 6. Emergence of deterministic chaos in the conservative head dynamics as amplitude of motion is increased. A, B: for small amplitudes ($\epsilon \to 0, \epsilon = 1/3$), Poincare section shows quasiperiodic head oscillations (i), while the maximum Lyapunov characteristic exponent (MLCE), which quantifies the dominant rate of separation of nearby phase trajectories, converges to ~ 0bits s^{-1} (ii), the power spectra of head stretch q and bend ϕ coordinates show clear peaks with little "noise" component (iii), and autocorrelations of these variables decay linearly (iv). These results betray non-chaotic, quasiperiodic oscillations for small amplitudes. MLCE, power spectra, and autocorrelations were computed for initial conditions shown by black dot in panel i. Parameters used to generate this figure are detailed in the main text, and reported in S3 Table.

Fig 7. (continued from Figure 6) Emergence of deterministic chaos in the conservative head dynamics as amplitude of motion is increased. A, B: for large amplitudes ($\epsilon = 2/3, \epsilon = 1$), the Poincare section contains a large chaotic sea (i), while the MLCE converges to a positive value (ii), power spectra become "noisy" (iii), and autocorrelations decay rapidly (iv). These results strongly suggest the existence of deterministic chaotic head dynamics for large amplitudes. MLCE, power spectra, and autocorrelations were computed for initial conditions shown by black dot in panel i. Parameters used to generate this figure are detailed in the main text, and reported in S3 Table.

Analysis by Poincare section provides an invaluable method to determine the character of overall system behaviour by direct visualisation of trajectories, but cannot be applied to higher dimensional systems. This is problematic, since we would like to assess the existence of chaos beyond our reduced model of the larva's head. We therefore deployed a series of other methods which are possibly less reliable than the method of Poincare section but can be applied equally well to higher dimensional systems. These included estimation of the maximal Lyapunov characteristic exponent (MLCE) for the dynamics along with calculation of the power spectrum and autocorrelation of internal variables [57, 58, 60]. The MLCE can be thought of as

quantifying the rate of separation of nearby trajectories, or, equivalently, the rate at which information is generated by the system being analysed [61]. A positive MLCE is generally considered a good indicator of chaotic behaviour. The power spectrum of a periodic or quasiperiodic process should consist of a "clean" set of discriminable peaks, whereas that of a chaotic process should appear "noisy" and contain power across a wide range of frequencies. Meanwhile, the autocorrelation of a periodic or quasiperiodic process should show a strong oscillatory component with an envelope that decays linearly with time, while that of a chaotic process should show a much quicker decay, similar to a coloured noise process. In Fig 6 we plot these measures at each value of ϵ, for a trajectory starting with initial conditions indicated on the corresponding Poincare plot by a filled black circle. These measures confirm increasingly chaotic behaviour as the amplitude ϵ increases, in agreement with our Poincare analysis. In Fig 8 we show a solution including all degrees of freedom in our conservative mechanical model (i.e. not just those of the head). The trajectory of individual segments relative to the substrate appears qualitatively irregular, while the indirect measures we introduced above (MLCE, power spectrum, autocorrelation) are all indicative of deterministic chaotic behaviour.

Fig 8. Conservative planar motion of the body is chaotic at large amplitudes. A: trajectories of individual segment boundaries appear qualitatively irregular, B: our estimate of the maximum Lyapunov characteristic exponent converges to a positive value, C: power spectra of head stretch q and bend ϕ show a strong "noise" component, and D: their autocorrelations decay rapidly. All are indicators of deterministic chaos. Parameters used to generate this figure are given in S4 Table.

Spontaneous turning and reversals require no additional control

We will now reintroduce dissipative effects into our model of larval motion in the plane. We previously saw that conservative mechanics predicted axial travelling waves and transverse oscillations. These were lost in the presence of friction, but the axial travelling waves could be recovered with the addition of a neuromuscular system designed to selectively counteract frictive effects. We have now seen that conservative mechanics predicts chaotic planar motion. Although our neuromuscular model transfers power only into the axial degrees of freedom, we recall from the previous section that axial and transverse motions are energetically coupled at large amplitudes. We therefore tentatively expect that we may be able to recover the complete chaotic planar motion without requiring any additional mechanism for direct neuromuscular power transfer into tranverse motion.

To investigate whether our dissipative planar model shows chaotic behaviour, we ran $n = 1000$ simulations starting from almost identical initial conditions (euclidean distance between initial mechanical state vectors $< 10^{-7}$, with no initial neural activity) and identical parameters (see S5 Table). We can indeed observe that the simulated larva perform peristalsis with interspersed bending of the body (turns), and that the fully deterministic system produces apparently random turning such that the simulations rapidly diverge (S3 Video). Since most working definitions of chaos require strictly bounded dynamics, we here restrict our analysis to the coordinates describing deformation of the body (segmental stretches and bending angles), ignoring motions of, or overall rotations about, the centre of mass (i.e., the trajectory through space of the body, which we will analyse in the following section).

Qualitatively, the deformations of the large amplitude dissipative model appear irregular (Fig 9A). However, there are persistent features reminiscent of the ordered small-amplitude behaviour described in previous sections. In particular, there are clear axial travelling waves and lateral oscillations. However, whereas forward- and

backward-propagating axial waves previously corresponded to stable limit behaviours, the large amplitude system appears to go through occasional "transitions" between these behaviours . In addition, apparently spontaneous large bends appear occasionally, suggesting that the neuromuscular system is effectively driving transverse motion.

Fig 9. Dissipative planar motion is chaotic. A: representative segmental stretch (left) and bend (right) time series (see S3 Fig for corresponding neural state). Note the occurence of a large bend starting at $\sim$ 1–2 seconds at the larva's head, which appears to propagate backwards along the body while triggering a "transition" from forward to backward wave propagation at $\sim$ 3.5 seconds. Forward wave propagation resumes at $\sim$ 6 seconds. B: power spectra of the head stretch q (top) and bend ϕ (bottom) showing significant "noise" component. C: Autocorrelations of q and ϕ rapidly decay. D: probability density of correlation dimension estimates for 1000 mechanical trajectories. The dimension of the system's limit set is estimated as $\sim$ 3.5 (median, vertical blue line). E: maximum Lyapunov characteristic exponent estimates converge to a positive value. All measures suggest the presence of deterministic chaotic dynamics. Parameters used to generate this figure are given in S5 Table.

The irregularity of the axial motion is reflected in the pattern of sensory neuron activation (S3 Fig). However, the mutual inhibitory interactions in our model act to filter this input, allowing only a small window of excitability within the central nervous system. As a result, interneuron and motor neuron activity appears fairly ordered, tracking and reinforcing axial compression waves.

We used four measures to assess whether our qualitative observation of irregular motion betrays the existence of deterministic chaos. First, we analysed the power spectrum of individual cooordinates (Fig 9B). The power spectra of all degrees of freedom showed consistent harmonic peaks along with a strong "noisy" non-harmonic component, a pattern consistent with chaos and incommensurate with (quasi)periodicity (Fig 9B shows data for head bending angle and stretch Next, we computed the autocorrelation of the same degrees of freedom. The autocorrelations of all degrees of freedom showed a periodic pattern with a peak at 0 seconds time lag followed by a rapid decay (Fig 9C). This is characteristic of oscillatory chaotic behaviour, and the exponential loss of information regarding initial conditions that chaotic systems display. We then estimated the correlation dimension (D_c) of the limit set of our model's dynamics. Note that we did not apply this measure to the conservative models in the previous section since the Liouville theorem rules out attracting limit sets for these systems. The distribution of correlation dimension estimates for our dissipative system across all 1000 trials is shown in Fig 9D. Estimates were clustered around $\sim$ 3.5 (median dimension 3.46), with 93% of estimates lying in the range [3–4]. These results are suggestive of a limit set with fractal dimension, which is a signature of "strange" chaotic attractors. Finally, we computed an estimate of the maximal Lyapunov characteristic exponent (MLCE). As in the previous section, we estimated the MLCE for our system to be positive ($\sim 13 textrm bits s^{-1}$, Fig 9D), a very strong indicator of chaotic behaviour. All of these results point to the presence of a chaotic dynamical regime in our dissipative large amplitude model.

Exploration emerges without decisions or stochasticity

As the coupled biomechanical and neuromuscular system produces both forward and backward peristalsis and lateral oscillations, each simulated larva will trace out a 2D trajectory over time. As shown in Fig 10A, the chaotic deformations characterised in the previous section caused the larvae to disperse across their two-dimensional substrate, following paths reminiscent of the real animal's exploratory behaviour.

Fig 10. Deterministic exploration. A: dispersion of the centres of mass of 1000 simulated larvae, starting from almost identical mechanical initial conditions (overlayed in inset). B: tortuosity and fractal (box-counting) dimension for all 1000 paths indicate plane-filling behaviour (blue line = mean tortuosity, red line = mean dimension, see text; see S4 Fig for power law analysis of trajectory curvature and angular speed). C: mean-squared displacement (black line) shows transient quadratic growth (blue line) followed by asymptotic linear growth (red line, asymptotic diffusion constant $\approx 144 \text{segs}^2\text{s}^{-1}$; see also log-log plot, S5 Fig). D: distribution of body bends (black) with maximum likelihood von Mises (red) and wrapped Cauchy (blue) fits. E: distribution of run lengths with maximum likelihood exponential fit (red). Run lengths were calculated as duration between successive crossings of a threshold body bend (20°), indicated by blue lines in panel D. See S6 Fig for analysis of tail speed and head angular velocity. Parameters used to generate this figure are given in S5 Table.

To characterise the trajectories of our model, we first investigated them at a global level, based on the centre of mass (COM) trajectory of each simulated larva, computing the tortuosity and fractal dimension of the paths (Fig 10B) [62]. We defined our tortuosity measure as

$$T = 1 - \frac{D}{L} \tag{12}$$

where D is the net displacement of the COM between initial and final times, and L is the total distance travelled by the COM along its path. Note that if the COM travels in a straight line between initial and final times we will have $D = L$ so that $T = 0$. In the limit $L \to \infty$, corresponding to the COM taking an extremely long path between its initial and final states, we have $\frac{D}{L} \to 0$ so that $T \to 1$. We calculated the mean tortuosity of our COM trajectories to be $\langle T \rangle = 0.43$, with a variance of $\langle (T - \langle T \rangle)^2 \rangle = 0.05$. The lowest (highest) tortuosity observed was $T = 0.05$ ($T = 0.95$).

We estimated the fractal dimension D_b of the COM trajectories using a box-counting algorithm. The minimum expected dimension $D_b = 1$ would correspond to curvilinear paths (e.g. straight line or circular paths), while the maximum expected dimension of $D_b = 2$ corresponds to plane-filling paths (e.g. brownian motion). We calculated the mean dimension of the COM trajectories to be $\langle D_b \rangle = 1.37$, with variance $\langle (D_b - \langle D_b \rangle)^2 \rangle = 0.01$. The lowest (highest) path dimension observed was $D_b = 1.17$ ($D_b = 1.95$). We have plotted the tortuosity and fractal dimension of every path in Fig 10B. These results show that the trajectories of the model differed markedly from straight lines (tortuosity $T > 0$ and box-counting dimension $D_b > 1$), and displayed a good ability to cover the planar substrate (box-counting dimension $1 < D_b < 2$). We also note that our COM trajectories display the power-law relationship between angular speed and curvature reported by [63], with a scaling exponent ($\beta \approx 0.8$) falling within the range reported for freely exploring larvae (S4 Fig).

We next investigated the rate at which the simulated larvae explored their environment. To do this, we calculated the mean-squared displacement (MSD) of the COM over time (Fig 10C). This is a standard measure used to characterise diffusion processes, and is defined as

$$\langle d^2 \rangle(t) = \frac{1}{n} \sum_{i=1}^{n} (R_i(t) - R_i(0))^2 \tag{13}$$

where $R_i(t)$ is the position of the i'th larva's COM at time t and $n = 1000$ is the number of trials being averaged over. We observed an initial transient, lasting on the order of 10 seconds, during which the MSD grew as $\sim t^2$ (blue line, S5 Fig), after which

growth slowed and tended to $\sim t$ (linear fit for $t > 80$ seconds shown by red line, Fig 10C and S5 Fig, $r^2 = 0.99$, diffusion constant $D = 144\text{segs}^2\text{s}^{-1}$). The initial transient was not due to our particular initial conditions, since it remained even after discarding > 60s of initial data . These results therefore tell us that, although on long timescales our model appears to execute standard Fick diffusion or a Brownian random walk (linear growth of MSD), on short timescales the model's behaviour is superdiffusive (approximately quadratic growth of MSD) [64, 65]. This is in good agreement with observations of the real larva [6, 48]. The superdiffusive behaviour of the larva was previously explained in terms of a persistent random walk [6], in which the larva's current and previous headings are highly correlated during straight runs so that the animal follows an approximately ballistic trajectory on short timescales. We believe that persistence effects arise in our model due to the finite time required for the deterministic chaotic dynamics to destroy information regarding initial conditions.

We next calculated some other standard measures found in the larva literature. To do so, we built a two-segment representation of each simulated larva by drawing vectors from the tail extremity to the A2-A3 segment boundary (the tail vector, $\mathbf{T}$), and from the A2-A3 boundary to the head extremity (the head vector, $\mathbf{H}$). We then defined the body bend, θ, to be the angle between tail and head vectors, $\theta = \text{atan}(H_y/H_x) - \text{atan}(T_y/T_x)$. The head angular velocity ν was computed as the cross-product of the head vector and the head extremity's translational velocity $\dot{\mathbf{r}}_{\text{head}}$ measured relative to the lab frame, $\nu = \mathbf{H} \times \dot{\mathbf{r}}_{\text{head}}$, while the tail speed v was taken to be the magnitude of the tail extremity's translational velocity $\dot{\mathbf{r}}_{\text{tail}}$ measured relative to the lab frame, $v = \sqrt{\dot{\mathbf{r}}_{\text{tail}} \cdot \dot{\mathbf{r}}_{\text{tail}}}$. The tail speed and head angular velocity both show a strong oscillatory component, which can be seen in the time and frequency domains (S6 Fig). The power spectra of these variables contains considerable "noise" over a wide spread of frequencies, in accordance with the results of the previous section. The distribution of tail speeds for our model is bimodal, similar to that of the real larva [44]. The body bend angle was observed to be symmetrically distributed (Fig 10D), with roughly zero mean ($\langle\theta\rangle = 0.005$), small variance ($\langle\langle(\theta - \langle\theta\rangle)^2\rangle = 0.13$), slight positive skew ($SK(\theta) = 0.23$), and high excess kurtosis $KU(\theta) = 7.9$. The kurtosis of our data precludes a good fit by the von Mises distribution (maximum likelihood estimate shown by red line in Fig 10D). Our data appears to be better fitted by a wrapped Cauchy distribution, though this overestimates the central tendency of our data (maximum likelihood estimate shown by blue line in Fig 10D). The high excess kurtosis of the body bend distribution gives a quantitative measure of the rare large bending events mentioned at the beginning of the previous section, and qualitatively matches experimentally observed distributions of real larval bends [44, 66]. Our model also reproduces the observed overall speed of larval locomotion (median model speed= 0.26 body lengths s^{-1}, real larval range $\sim 0.1 - -0.35$ body lengths s^{-1}), the turn rate (median model turn rate = 2.08 turns min^{-1}, real larval range $\sim 0 - -4.5$ turn min^{-1}, threshold body bend for turn classification = 30^{deg} to match relevant literature), and the relative distance gained during free locomotion (median model distance gained = 0.14 body lengths s^{-1}, real larval range $\sim 0 - -0.2$), with our results being more consistent with observations of third instar than first instar larvae [66].

Finally, we computed a run-length distribution by setting a threshold body bend angle $\theta_{turn} = 20^\circ$ (as in [13]) and calculating the length of time between successive crossings of this threshold. The distribution we obtained appears approximately linear on a log-linear plot (Fig 10E, linear fit $r^2 = 0.99$ with slope $\lambda = -0.075$), and is better fit by an exponential than a power law distribution (maximum likelihood estimates, log likelihood ratio = 5281, $p < 0.01$). Together with our observation of asymptotic linear growth of MSD, the exponential distribution of run lengths suggests that the model can be considered to be effectively memoryless on long timescales [65]. This again agrees

with the observed rapid loss of information from the system due to its chaotic dynamics, as quantified by the Lyapunov exponent and autocorrelation analysis of the previous section.

Ultimately, the analysis of our model supports a view of the larval exploratory routine as an (anomalous) diffusion process arising from the deterministic chaotic dynamics of the body. The model nervous system functions purely to recover these dynamics from the effects of frictive energy dissipation, and to ensure centre of mass motion, rather than explicitly directing exploration.

Discussion

The intrinsic capabilities of an organism's body determine the field of possibilities that neural circuits for behaviour can exploit. Here, by focusing first on the biomechanics of *Drosophila* larva, we find that its body already contains an inherent exploratory routine. This is demonstrated through a combined biomechanical and neuromuscular model that is the first to be able to generate both forward and backward peristalsis and turning, allowing 2D motion in the plane to be simulated. We show that, in the absence of friction, the body's conservative mechanics alone supports both axial travelling waves and transverse standing waves. These are energetically coupled at larger amplitudes, such that no driving, sensing, or control of body bend is required for the system to start producing spontaneous coordinated bending motions. Frictional losses can be recovered, to maintain axial waves, by a neuromuscular system consisting of only simple local sensorimotor reflexes and long-range inhibitory interactions. This is sufficient to produce emergent crawling, reversal and turning that resembles larval exploratory behaviour, and which is chaotic in nature. At a population level, we observe a deterministic anomalous diffusion process in which an initial superdiffusive transient evolves towards asymptotic Fickian/Brownian diffusion, matching observations of real larvae [6, 48]. We therefore propose that the role of biomechanical feedback in *Drosophila* larvae goes beyond the periphery of basic neuromuscular rhythms [40, 43], to provide the essential "higher order" dynamics on which exploratory behaviour is grounded.

Most existing models of larval exploration abstract away from the mechanics underlying the production of runs and reorientations [4–6, 8, 11–13]. The larva is often described as executing a stochastic decision-making process which determines which state (running or turning) should be occupied, and when to initiate a change of behavioural state. In contrast, our model produces the entire exploratory routine without making any decisions (the transverse motion is neither sensed nor driven by the nervous system) nor introducing any stochastic process (neural or otherwise). Similarly, transient "switching" is seen to occur between forward and backward peristalsis even though there is no neural encoding or control of the direction of wave propagation. In other words, the body dynamics generate the basis of a chaotic exploratory routine which only needs to be amplified by the neural circuitry, making the search for underlying stochastic or state switching circuitry superfluous for this behaviour.

The work presented here also stands in contrast to previous models of larval peristalsis [39, 43] and the prevailing hypotheses regarding this phenomenon [15, 67] by eschewing any role for intrinsic neural dynamics. Such stereotyped and rhythmic locomotion is widely assumed to be the signature of a central pattern generator (CPG), that is, a neural circuit that intrinsically generates a rhythmic output, and thus determines a particular mechanical trajectory to be followed by the body [68–70]. However it is recognised that systems vary in the degree to which coordinated behaviour is independent of biomechanical and sensory feedback [70]. Indeed, evidence from studies employing genetic manipulations to disrupt sensory neuron input suggest that proprioceptive feedback is necessary for correct larval locomotive patterns [16, 36–38, 71];

although in some cases coordinated waves of forward and backward peristalsis can be produced, in both intact [16, 36, 71] and isolated VNC preparations [14, 15], these are reported as abnormal with the most evident defects being time-dilation [15, 36, 71] and abnormal frequency in polarity changes [71].

In fact, our intent is not to adjudicate between the roles of intrinsically generated activation sequences vs. biomechanical feedback in this system, but rather to note that we should expect neural circuits of locomotion to adhere to the dynamical modes of the associated body, instead of working against them. Thus it should be unsurprising if these dynamics also exist (potentially in a latent form) in the neural circuitry. For example, a simple modification of the neural circuit presented here could produce instrinsic 'peristaltic' waves. Recall that the long-range global inhibition pattern in our model treats head and tail segments as 'neighbouring' nodes (see *Models – Neuromuscular system*). If local constant input or recurrent feedback were added to each segment, the circuit would then resemble a ring attractor [72–74] and a stable activity bump would be formed. Breaking the forward/backward symmetry of the circuit, e.g., by introducing asymmetric nearest-neighbour excitatory connections [75], would cause the activity bump to move along the network, giving rise to intrinsic travelling waves. This would complement any mechanical compression waves travelling through the body, i.e., remain consistent with the principles set out in this paper. Would such a network be a CPG? The answer is unclear. On the one hand, it would show spontaneous rhythmic activity in the absence of sensory input. On the other, sensory feedback would do much more than simply correct deviations from the CPG output or provide a "mission accomplished" signal [36]. Rather, feedback would play a crucial role in orchestrating motor output to ensure power flow into the body, consistently with its dynamical modes.

It is important to note that the emergence of rhythmic peristalsis and spontaneous turns in our model is not strongly dependent on the specific assumptions made in our mechanical abstraction. For example, the observation for small amplitude motions of sinusoidal axial travelling waves, along with transverse standing waves whose shapes match the experimentally observed "eigenmaggots" [56], is a direct result of the second-order Taylor series approximation of the model Hamiltonian (S2 Appendix). The small-amplitude model is thus non-unique, since many different mechanical models could have identical second-order approximations. Similarly, we expect that the deterministic chaotic behaviour derived from our conservative model for large amplitude motions will hold for other models of the larval body, given that it is conjectured that the majority of Hamiltonian systems are nonintegrable. This may also mean that our results can be applied to other animals with body morphologies and mechanics similar to the *Drosophila* larva.

In our model we constrain the total length of the larva to be constant. This constraint is intended to represent the fact that there is minimal observable radial deformation of the larva's body during behaviour, yet its body is filled with fluid which should conserve volume. We were further motivated by the experimental observation of "visceral pistoning" [3] in which the head and tail extremities of the larva appear to be mechanically coupled via the coelomic fluid during peristalsis. However, the total length of the real larva is known to change during behaviour [47], and it is therefore important to consider the effect of weakening the length constraint in our model. When restricted to small-amplitude motion, the total length constraint appears as periodic boundary conditions in the axial mechanics, allowing waves of compression to propagate from head to tail and vice versa. In the complete absence of the length constraint, these waves will instead be reflected back from the head and tail extremities, leading to alternating forward and backward waves. Alternatively, replacing the constraint with a simple linear viscoelastic model to represent energy storage and dissipation within the

internal fluid and in radial cuticle deformation leads to the presence of a new mechanical impedance between the head and tail. It is well known that sudden impedance changes in wave transmission media lead to simultaneous reflection and transmission of waves – in our model, this means that some amount of the axial compression wave will be transmitted between head and tail while some will be reflected. Since our neural model cannot sustain two peristaltic waves concurrently due to the presence of mutual inhibition between distant segments, this causes occasional "switching" between forward and backward peristalsis. If the extent of radial deformations is under neural control in the larva, this could provide a potential route for control or biasing of transitions between forward and backward peristalsis.

As a consequence of exploiting body mechanics, our model explains a wider range of behaviour than previous models, using a simpler nervous system. The properties included in the neuromuscular circuitry were derived from basic physical considerations, i.e., what was necessary and sufficient to produce exploration, rather than from known neuroanatomy or neurophysiology. However, it is useful to now examine what insights and predictions regarding this circuitry can be derived from our model.

Firstly, we consider the connections between segments. Unlike the model from [43], we did not require assymmetric connections to obtain forward (or backward) waves as these (and spontaneous switching between them) arise inherently in the mechanics. Rather, obtaining centre of mass motion of the entire body required the "ring attractor" layout of mutual inhibition between distant segments described above. The model thus predicts that motor output should be strongly inhibited (by signalling from other segments) the majority of the time, so that motor neurons only activate as the (mechanical) peristaltic wave passes through the corresponding body segment. This is in contrast to previous models which appealed only to local, nearest-neighbour inhibitory connections [39, 43].

What might be the neural substrate for the proposed inhibition? There are two currently known intersegmental inhibitory pathways in the larva. GVLI premotor inhibitory neurons synapse onto motor neurons within the same segment but extend their dendritic fields several segments further anterior along the VNC. Accordingly, the GVLIs inhibit motor neurons at a late phase during the local motor cycle [22]. Our model predicts that there should be a larger set of GVLI-like neurons within each segment, with dendritic fields tiling distant segments. Although in our model the mutual inhibition is (for simplicity) arranged to act on all non-adjacent segments, we would in practice expect that active compression is actually spread across more segments [3, 22] to transfer power to the body more efficiently (S3 Appendix), and this should be reflected in the inhibitory connection pattern. The second inhibitory pathway involves GDL inhibitory interneurons, which receive input from the excitatory premotor neuron A27h in the nearest posterior segment, and synapse onto A27h within the same segment while simultaneously disinhibiting premotor inhibitory neurons in distant segments [28]. Thus, GDL effectively produces both local and long-range inhibition of motor output. However, GDL receives axo-axonic connections from vdaA and vdaC mechanosensory cells within the same segment, so local inhibition is likely gated by sensory input. This would match our model, in which sensory activation within a segment should be sufficient to produce motor output when one of the neighbouring segments is active. We thus predict that simultaneous experimental suppression of GDL, GVLI, and all other long-range inhibition in the VNC should allow the propagation of several, concurrent locomotor waves in response to mechanical input.

Secondly, within a segment, our model highlights the importance of the timing of neuromuscular forces relative to body motion. Specifically, during locomotion, the larva's muscles should act primarily as motors rather than as springs, brakes, or struts (see [33] for a discussion of these differences), and thus should activate in phase with the

segmental stretch rate. This hypothesis could be tested by performing work-loop experiments, for which we predict the existence of a counterclockwise cycle in a plot of muscle force (potentially measurable by calcium imaging) over segment length during locomotion.

Can our model's requirement that neurons sensing stretch-rate provide a direct excitatory connection to motor neurons, within the same segment, be mapped to identified pathways in the larva? One possible monosynaptic implementation of such a link are the dda mechanosensory cells which have been observed to make synapses onto aCC and RP2 motor neurons [23]. However, synapse counts show high variability both within and across individuals, so it seems unlikely to be a core component of the locomotor circuitry. A more promising candidate is the excitatory premotor interneuron A27h, which receives input from vpda and vdaC and sends bilaterally symmetric outputs to aCC and RP5 [28]. It is known that A27h activation is sufficient to activate downstream motor neurons, but it remains unknown whether proprioceptive sensory input is sufficient to activate A27h. Additionally, we hypothesise that A02 (PMSI) interneurons [20], which have been recently shown to form an inhibitory sensory-motor feedback pathway between dbd mechanosensory cells and motor neurons [27], could play a role in filtering this signal to obtain the necessary stretch-rate activation independently of stretch. General models of mechanotransduction suggest that larval mechanosensory cells may be sensitive to both rate of stretch as well as absolute stretch, depending upon the mechanical properties of the sensory dendrites and the biophysics of the relevant mechanosensitive ion channels [76]. If PMSIs have a slow-activating, integrator dynamics that encodes stretch, while A27h activate quickly in response to proprioceptive sensory input to encode stretch and stretch-rate, the combined input to motor neurons would be only stretch-rate dependent excitation, as our model requires. This could explain the observation that optogenetic disturbance of PMSIs [20] slows the timescale of peristaltic waves, as the inclusion of absolute stretch in this feedback loop would produce muscle forces that not only counteract friction but also decrease the effective stiffness of the cuticle, slowing peristalsis (see S5 Appendix).

It is clear the real larval nervous system exhibits many complexities not reflected in our model, and likewise that the real larva performs many more behaviours than exploration. These include appropriate (directed) reactions to sensory stimuli such as stopping, withdrawal and reverse in response to touch stimuli [38]; differences in the speed of forward and backward locomotion [15]; and modulation of the frequency and direction of (large) turns in response to sensory gradients such as odour, heat or light [4, 8–10, 12, 13, 77–82] to produce positive or negative taxis. In a previous model of taxis [44] we have shown that by a continuous coupling of the amplitude of a regular lateral oscillation to the experienced change in stimulus strength in a gradient, a larva-like response to gradients can emerge, again without requiring active switching between states. In the current model, this could be effected by incorporating direct neuromuscular driving of bending degrees of freedom, since the real larva can likely use asymmetric activation of its lateralised muscles to produce active bending torques to influence the transverse motion. Alternatively, the degree of bend could be influenced indirectly by altering the stiffness and viscosity of segments (as explored in our upcoming paper [49]), or their frictional interaction with the substrate. We note that the effective viscoelasticity of body segments can be neurally controlled by local reflex arcs (see S4 Appendix and [40]). Indeed, this could partially explain the experimental observation of increased bending on perturbation of a contralateral segmental reflex mediated by Eve^{+} interneurons [24]. The muscle activation caused by this reflex should produce bending torques which are proportional to current bend or bending rate, thus effectively modulating transverse stiffness or viscosity, respectively. Notably, in the taxis model of [44], it is not required that the descending signal that alters turn amplitude is

lateralised, but rather that it has the right temporal coordination, which itself is naturally created by the interaction of body and environment.

Backward locomotion is observed to be slower than forward locomotion in the real larva [15], yet in our model both behaviours are of equal speed for a fixed value of reflex gain. We believe that this is due to the preservation of mechanical symmetry between forward and backward motion in our model. The real larva likely experiences asymmetric substrate interaction forces. For instance, this could be due to the exact coordination of denticle folding/lifting during forward and backward locomotion (S1 Video) or due to the geometry of the larva's denticle bands, which display a degree of anisotropy [83]. Alternatively, there may be asymmetries within the larva's neural circuitry responsible for this difference. Indeed, there do appear to be neurons in the larval VNC which are only active specifically during forwards or backwards locomotion, and these may be functionally asymmetric [28].

The model presented in this paper does occasionally produce stops (cessation of peristalsis) during exploration, but this only occurs in concert with a large body bend (this stored transverse energy can subsequently and spontaneously restart the peristalsis); whereas in larva slowing, stopping and resumption of peristalsis (or transition from a stop to a large bend) can occur while the body is relatively straight [2, 10]. As for 'directed' turning, this suggests that additional neural control might be needed to terminate or initiate movement in response to sensory stimuli. It is worth noting that our model predicts that peristalsis can be restarted by almost any small disturbance of the physical equilibrium provided the local feedback gain is high enough; similarly, lowering the gain means that energy losses due to friction are not compensated and the animal will stop. In general, we have found that altering assumptions about the sliding friction forces by which the model interacts with the substrate can often have unexpected and subtle effects on the motion produced, thus it would be interesting to further explore the functions provided by segmental lifting [3, 84], folding of the denticle bands (S1 Video), and extrusion of the mouth-hooks [3, 85] during locomotion. Indeed, detailed experimental characterisation of the substrate interaction forces experienced by the larva would be a major advance in understanding how the animal behaves. Inspiration for approaches to this problem could perhaps be taken from the literature on *C. elegans* substrate interaction (see for instance [42, 86–90], though this list is not exhaustive). In the more extreme case, larva are capable of burrowing through a soft substrate, and it is clear that a complex interaction of forces, mechanics, sensing and neural control must be involved that go well beyond the scope considered here.

Supporting information

S1 Fig. Coordinate system and substrate interaction schematics. Internal coordinate system used to describe deformations of the larval body (left), and quantities used to describe substrate interaction (right). The friction force $F_{friction}$ acting on the i'th segment boundary is directed opposite to that boundary's velocity vector $\mathbf{v}_i$, and has a magnitude which depends only upon the direction θ_i of the velocity vector relative to a unit vector $\hat{\mathbf{n}}_i$ aligned with the local body axis (see text). Note that $\hat{\mathbf{v}}_i = \mathbf{v}_i / \|\mathbf{v}_i\|$ denotes a unit vector aligned with the boundary's velocity vector.

S2 Fig. Neural activation during peristalsis. (from top to bottom) stretch rate, sensory neuron, interneuron, and motor neuron activation during forwards (left) and backwards (right) peristalsis.

S3 Fig. Neural activation during planar locomotion. (from top to bottom) stretch, stretch rate, sensory neuron, interneuron, and motor neuron activation during planar motion.

S4 Fig. Relationship between path curvature and angular velocity. A: representative time-series of angular velocity and curvature. B: model data from all trials (grey points) compared to fit by a power law with scaling exponent $\beta \approx 0.8$ (blue line, $r^2 \approx 0.94$).

S5 Fig. log-log plot of mean-squared displacement. Initial quadratic growth (blue line, slope=2) leads to asymptotic linear growth (red line, slope=1).

S6 Fig. tail speed v and head angular velocity ν during planar motion. A: representative time series for v and ν. B: probability density of v and ν across all 1000 trials. C: individual (faint) and mean (bold) power spectra of v and ν

S1 Video. Denticle bands fold into the larval cuticle during peristalsis. The larva was placed on its side, on a Sylgard 184 PDMS plate, beneath a dissection microscope. The video was taken at 45x magnification with an Allied Vision Technologies Marlin F131B digital camera. Denticle bands are visible as repeated "rough" patches on the ventral surface of the larval cuticle, towards the top-left of the video frame. As the peristaltic wave passes a denticle band, the denticles visibly "fold" or are "squeezed" into the cuticle.

S2 Video. Synthesis of travelling wave solutions from standing wave solutions.

S3 Video. Simulated larval exploratory behaviour.

S1 Appendix. Detailed model specification.

S2 Appendix. Detailed small-amplitude analysis.

S3 Appendix. A trade-off between power flow into the body and force on the centre of mass.

S4 Appendix. Modelling and analysis of head motion.

S5 Appendix. Effective body physics arising due to relationship of neuromuscular action to body motion.

S6 Appendix. Computer algebra and numerical methods.

S1 Table. Neural parameter values. All segments are identical. Values given in larval units (seg = resting segment length, segmass = mass of a single segment boundary, nondim = dimensionless/nondimensional).

S2 Table. Mechanical parameters for Fig 4 – *emergence of limit cycles for forward and backward locomotion in the dissipative, small-amplitude model*. All segments are identical. Values given in larval units (seg = resting segment length, segmass = mass of a single segment boundary, nondim = dimensionless/nondimensional).

S3 Table. Mechanical parameters for Fig 6 and Fig 7– *emergence of deterministic chaos in the conservative head dynamics as amplitude of motion is increased.*. Values given in larval units (seg = resting segment length, segmass = mass of a single segment boundary, nondim = dimensionless/nondimensional).

S4 Table. Mechanical parameters for Fig 8 – *conservative planar motion of the body is chaotic at large amplitudes*. All segments are identical. Values given in larval units (seg = resting segment length, segmass = mass of a single segment boundary, nondim = dimensionless/nondimensional).

S5 Table. Mechanical parameters for Fig 9 – *dissipative planar motion is chaotic* and Fig 10 – *deterministic exploration*. Values given in larval units (seg = resting segment length, segmass = mass of a single segment boundary, nondim = dimensionless/nondimensional).

Acknowledgments

We are grateful to Balazs Szigeti for providing us with experimental eigenmaggot data, and wish to thank Matthieu Louis and Richard Ribchester for their feedback on our manuscript.

References

1. Berni J, Pulver SR, Griffith LC, Bate M. Autonomous circuitry for substrate exploration in freely moving *Drosophila* larvae. Current Biology. 2012;22(20):1861–70. doi:10.1016/j.cub.2012.07.048.

2. Lahiri S, Shen K, Klein M, Tang A, Kane E, Gershow M, et al. Two alternating motor programs drive navigation in *Drosophila* larva. PLOS ONE. 2011;6(8):e23180. doi:10.1371/journal.pone.0023180.

3. Heckscher ES, Lockery SR, Doe CQ. Characterization of Drosophila larval crawling at the level of organism, segment, and somatic body wall musculature. The Journal of Neuroscience. 2012;32(36):12460–71. doi:10.1523/JNEUROSCI.0222-12.2012.

4. Luo L, Gershow M, Rosenzweig M, Kang K, Fang-Yen C, Garrity PA. Navigational Decision Making in *Drosophila* Thermotaxis. The Journal of Neuroscience. 2010;30(12):4261–4272. doi:10.1523/JNEUROSCI.4090-09.2010.

5. Davies A, Louis M, Webb B. A Model of *Drosophila* Larva Chemotaxis. PLOS Computational Biology. 2015;11(11):1–24. doi:10.1371/journal.pcbi.1004606.

6. Gunther MN, Guilherme N, Shubeita GT. Quantifying and predicting *Drosophila* larvae crawling phenotypes. Scientific Reports. 2016;6:1–10. doi:10.1038/srep27972.

7. Green CH, Burnet B, Connolly KJ. Organization and patterns of inter- and intraspecific variation in the behaviour of *Drosophila* larvae. Animal Behaviour. 1983;31:282–291.

8. Gomez-Marin A, Stephens GJ, Louis M. Active sampling and decision making in *Drosophila* chemotaxis. Nature Communications. 2011;2(441):1–10. doi:10.1038/ncomms1455.

9. Kane EA, Gershow M, Afonso B, Larderet I, Klein M, Carter AR, et al. Sensorimotor structure of *Drosophila* larva phototaxis. Proceedings of the National Academy of Sciences. 2013;110(40):E3868–E3877. doi:10.1073/pnas.1215295110.

10. Gomez-Marin A, Louis M. Multilevel control of run orientation in *Drosophila* larval chemotaxis. Frontiers in Behavioral Neuroscience. 2014;8(38):1–14. doi:10.3389/fnbeh.2014.00038.

11. Hernandez-Nunez L, Belina J, Klein M, Si G, Claus L, Carlson JR, et al. Reverse-correlation analysis of navigation dynamics in *Drosophila* larva using optogenetics. eLife. 2015;4:e06225. doi:10.7554/eLife.06225.

12. Gepner R, Mihovilovic Skanata M, Bernat NM, Kaplow M, Gershow M. Computations underlying *Drosophila* photo-taxis, odor-taxis, and multi-sensory integration. eLife. 2015;4:e06229. doi:10.7554/eLife.06229.

13. Schulze A, Gomez-Marin A, Rajendran VG, Lott G, Musy M, Ahammad P, et al. Dynamical feature extraction at the sensory periphery guides chemotaxis. eLife. 2015;4:e06694. doi:10.7554/eLife.06694.

14. Fox LE, Soll DR, Wu CF. Coordination and modulation of locomotion pattern generators in *Drosophila* larvae: effects of altered biogenic amine levels by the tyramine beta hydroxlyase mutation. The Journal of Neuroscience. 2006;26(5):1486–98. doi:10.1523/JNEUROSCI.4749-05.2006.

15. Pulver SR, Bayley TG, Taylor AL, Berni J, Bate M, Hedwig B. Imaging fictive locomotor patterns in larval *Drosophila*. Journal of Neurophysiology. 2015;114(5):2564–2577. doi:10.1152/jn.00731.2015.

16. Inada K, Kohsaka H, Takasu E, Matsunaga T, Nose A. Optical Dissection of Neural Circuits Responsible for *Drosophila* Larval Locomotion with Halorhodopsin. PLOS ONE. 2011;6(12):1–10. doi:10.1371/journal.pone.0029019.

17. Crisp SJ, Evers JF, Bate M. Endogenous Patterns of Activity Are Required for the Maturation of a Motor Network. The Journal of Neuroscience. 2011;31(29):10445–10450. doi:10.1523/JNEUROSCI.0346-11.2011.

18. Iyengar BG, Chou CJ, Vandamme KM, Klose MK, Zhao X, Akhtar-Danesh N, et al. Silencing synaptic communication between random interneurons during *Drosophila* larval locomotion. Genes, Brain and Behaviour. 2011;10:883–900. doi:10.1111/j.1601-183X.2011.00729.x.

19. Rickert C, Kunz T, Harris KL, Whitington PM, Technau GM. Morphological Characterization of the Entire Interneuron Population Reveals Principles of Neuromere Organization in the Ventral Nerve Cord of *Drosophila*. The Journal of Neuroscience. 2011;31(44):15870–15883. doi:10.1523/JNEUROSCI.4009-11.2011.

20. Kohsaka H, Takasu E, Morimoto T, Nose A. A Group of Segmental Premotor Interneurons Regulates the Speed of Axial Locomotion in *Drosophila* Larvae. Current Biology. 2014;24:2632–2642. doi:10.1016/j.cub.2014.09.026.

21. Okusawa S, Kohsaka H, Nose A. Serotonin and Downstream Leucokinin Neurons Modulate Larval Turning Behavior in *Drosophila*. The Journal of Neuroscience. 2014;34(7):2544–2558. doi:10.1523/JNEUROSCI.3500-13.2014.

22. Itakura Y, Kohsaka H, Ohyama T, Zlatic M, Pulver SR, Nose A. Identification of Inhibitory Premotor Interneurons Activated at a Late Phase in a Motor Cycle during *Drosophila* Larval Locomotion. PLOS ONE. 2015;10(9). doi:10.1371/journal.pone.0136660.

23. Couton L, Mauss AS, Yunusov Y, Diegelmann S, F EJ, Landgraf M. Development of Connectivity in a Motorneuronal Network in *Drosophila* Larvae. Current Biology. 2015;25(5):568–576. doi:10.1016/j.cub.2014.12.056.

24. Heckscher ES, Zarin AA, Faumont S, Clark MQ, Manning L, Fushiki A, et al. Even-Skipped^{+} Interneurons Are Core Components of a Sensorimotor Circuit that Maintains Left-Right Symmetric Muscle Contraction Amplitude. Neuron. 2015;88:314–329. doi:10.1016/j.neuron.2015.09.009.

25. Berni J. Genetic Dissection of a Regionally Differentiated Network for Exploratory Behaviour in *Drosophila* Larvae. Current Biology. 2015;25:1319–1326. doi:10.1016/j.cub.2015.03.023.

26. Ohyama T, Schneider-Mizell CM, Fetter RD, Aleman JV, Franconville R, Rivera-Alba M, et al. A multilevel multimodal circuit enhances action selection in *Drosophila*. Nature. 2015;520:644–639. doi:10.1038/nature14297.

27. Schneider-Mizell CM, Gerhard S, Longair M, Kaimiers T, Li F, Zwart MF, et al. Quantitative neuroanatomy for connectomics in *Drosophila*. eLife. 2016;5.

28. Fushiki A, Zwart MF, Kohsaka H, Fetter RD, Cardona A, Nose A. A circuit mechanism for the propagation of waves of muscle contraction in *Drosophila*. eLife. 2016;5:e13253. doi:10.7554/eLife.13253.

29. Zwart MF, Pulver SR, Truman JW, Fushiki A, Fetter RD, Cardona A, et al. Selective Inhibition Mediates the Sequential Recruitment of Motor Pools. Neuron. 2016;91:615–628. doi:10.1016/j.neuron.2016.06.031.

30. Hasegawa E, Truman JW, Nose A. Identification of excitatory premotor interneurons which regulate local muscle contraction during *Drosophila* larval locomotion. Scientific Reports. 2016;6:1–13. doi:10.1038/srep30806.

31. Yoshikawa S, Long H, Thomas JB. A subset of interneurons required for *Drosophila* larval locomotion. Molecular and Cellular Neuroscience. 2016;70:22–29. doi:10.1016/j.mcn.2015.11.008.

32. Matsunaga T, Kohsaka H, Nose A. Gap Junction-Mediated Signaling from Motor Neurons Regulates Motor Generation in the Central Circuits of Larval *Drosophila*. The Journal of Neuroscience. 2017;37(8):2045–2060. doi:10.1523/JNEUROSCI.1453-16.2017.

33. Dickinson MH, Farley CT, Full RJ, Koehl MAR, Kram R, Lehman S. How Animals Move: An Integrative View. Science. 2000;288(5463):100–106. doi:10.1126/science.288.5463.100.

34. Tytell ED, Holmes P, A H Cohen. Spikes alone do not behaviour make: Why neuroscience needs biomechanics. Current Opinion in Neurobiology. 2011;21(5):816–822. doi:10.1016/j.conb.2011.05.017.Spikes.

35. Chiel HJ, Beer RD. The brain has a body: adaptive behavior emerges from interactions of nervous system, body and environment. Trends in Neurosciences. 1997;20(12):553–557. doi:10.1016/S0166-2236(97)01149-1.

36. Hughes CL, Thomas JB. A sensory feedback circuit coordinates muscle activity in *Drosophila*. Molecular and Cellular Neuroscience. 2007;35(2):383 – 396. doi:10.1016/j.mcn.2007.04.001.

37. Song W, Onishi M, Jan LY, Jan YN. Peripheral multidendritic sensory neurons are necessary for rhythmic locomotion behavior in *Drosophila* larvae. Proceedings of the National Academy of Sciences. 2007;104(12):5199–5204. doi:10.1073/pnas.0700895104.

38. Zhou Y, Cameron S, Chang WT, Rao Y. Control of directional change after mechanical stimulation in Drosophila. Molecular Brain. 2012;5(39):1–13. doi:10.1186/1756-6606-5-39.

39. Gjorgjieva J, Berni J, Evers JF, Eglen SJ. Neural circuits for peristaltic wave propagation in crawling *Drosophila* larvae: analysis and modeling. Frontiers in computational neuroscience. 2013;7:1–24. doi:10.3389/fncom.2013.00024.

40. Ross D, Lagogiannis K, Webb B. In: A Model of Larval Biomechanics Reveals Exploitable Passive Properties for Efficient Locomotion. Springer International Publishing; 2015. p. 1–12.

41. Boyle J, Berri S, Cohen N. Gait Modulation in C. elegans: An Integrated Neuromechanical Model. Frontiers in Computational Neuroscience. 2012;6:10. doi:10.3389/fncom.2012.00010.

42. Cohen N, Sanders T. Nematode locomotion: dissecting the neuronal–environmental loop. Current Opinion in Neurobiology. 2014;25:99 – 106. doi:https://doi.org/10.1016/j.conb.2013.12.003.

43. Pehlevan C, Paoletti P, Mahadevan L. Integrative neuromechanics of crawling in *D. melanogaster* larvae. eLife. 2016;5:e11031. doi:10.7554/eLife.11031.

44. Wystrach A, Lagogiannis K, Webb B. Continuous lateral oscillations as a core mechanism for taxis in *Drosophila* larvae. eLife. 2016;5:e15504. doi:10.7554/eLife.15504.

45. Ohyama T, Jovanic T, Denisov G, Dang TC, Hoffmann D, Kerr RA, et al. High-Throughput Analysis of Stimulus-Evoked Behaviors in *Drosophila* Larva Reveals Multiple Modality-Specific Escape Strategies. PLOS ONE. 2013;8(8):1–21. doi:10.1371/journal.pone.0071706.

46. Godoy-Herrera R. The development and genetics of digging behaviour in *Drosophila* larvae. Heredity. 1986;56:33–41. doi:10.1038/hdy.1986.6.

47. Berrigan D, Pepin DJ. How maggots move: Allometry and kinematics of crawling in larval Diptera. Journal of Insect Physiology. 1995;41(4):329 – 337.

48. Jakubowski BR, Longoria RA, Shubeita GT. A high throughput and sensitive method correlates neuronal disorder genotypes to Drosophila larvae crawling phenotypes. Fly. 2012;6(4):303–308. doi:10.4161/fly.21582.

49. Loveless J, Webb B. A Neuromechanical Model of Larval Chemotaxis. Integrative and Comparative Biology. in review;.

50. Landau LD, Lifshitz EM. Fluid Mechanics. vol. 6 of Course of Theoretical Physics. 2nd ed. Butterworth-Heinemann; 1987.

51. Alexander RM. Principles of Animal Locomotion. 1st ed. Princeton University Press; 2003.

52. Paterson BA, Anikin IM, Krans JL. Hysteresis in the production of force by larval Dipteran muscle. Journal of Experimental Biology. 2010;213(14):2483–2493. doi:10.1242/jeb.043026.

53. Ormerod KG, Hadden JK, Deady LD, Mercier AJ, Krans JL. Action of octopamine and tyramine on muscles of Drosophila melanogaster larvae. Journal of Neurophysiology. 2013;110(8):1984–1996. doi:10.1152/jn.00431.2013.

54. Landgraf M, Bossing T, Technau GM, Bate M. The Origin, Location, and Projections of the Embryonic Abdominal Motorneurons of Drosophila. Journal of Neuroscience. 1997;17(24):9642–9655. doi:10.1523/JNEUROSCI.17-24-09642.1997.

55. Hoang B, Chiba A. Single-Cell Analysis of Drosophila Larval Neuromuscular Synapses. Developmental Biology. 2001;229(1):55 – 70. doi:https://doi.org/10.1006/dbio.2000.9983.

56. Szigeti B, Deogade A, Webb B. Searching for motifs in the behaviour of larval *Drosophila melanogaster* and *Caenorhabditis elegans* reveals continuity between behavioural states. Journal of The Royal Society Interface. 2015;12(113).

57. Strogatz H S. Nonlinear Dynamics and Chaos: With Applications to Physics, Biology, Chemistry, and Engineering. 1st ed. Perseus Books; 1994.

58. Guckenheimer J, Holmes P. Nonlinear Oscillations, Dynamical Systems, and Bifurcations of Vector Fields. vol. 42 of Applied Mathematical Sciences. 1st ed. Springer; 1983.

59. Arnol'd VI. Mathematical Methods of Classical Mechanics. vol. 60 of Graduate Texts in Mathematics. 2nd ed. Springer; 1989.

60. Cuerno R, Rañada AF, Ruiz-Lorenzo JJ. Deterministic chaos in the elastic pendulum: A simple laboratory for nonlinear dynamics. American Journal of Physics. 1992;60(1):73–79. doi:10.1119/1.17047.

61. Shaw R. Strange Attractors, Chaotic Behaviour, and Information Flow. Zeitschrift Naturforschung Teil A. 1981;36:80–112. doi:10.1515/zna-1981-0115.

62. Benhamou S. How to reliably estimate the tortuosity of an animal's path: straightness, sinuousity, or fractal dimension? Journal of Theoretical Biology. 2004;229:209–220. doi:10.1016/j.jtbi.2004.03.016.

63. Zago M, Lacquaniti F, Gomez-Marin A. The speed-curvature power law in *Drosophila* larval locomotion. Biology Letters. 2016;12. doi:10.1098/rsbl.2016.0597.

64. Vlahos L, Isliker H, Kominis Y, Hizanidis K. Normal and Anomalous Diffusion: A Tutorial. pre-print: arXiv:08050419 [nlinCD]. 2008;.

65. Méndez V, Campos D, Bartumeus F. Stochastic Foundations in Movement Ecology: Anomalous Diffusion, Front Propagation, and Random Searches. 1st ed. Springer Series in Synergetics. Springer-Verlag Berlin Heidelberg; 2014.

66. Almeida-Carvalho MJ, Berh D, Braun A, Chen Yc, Eichler K, Eschbach C, et al. The Ol1mpiad: concordance of behavioural faculties of stage 1 and stage 3 Drosophila larvae. Journal of Experimental Biology. 2017;220(13):2452–2475. doi:10.1242/jeb.156646.

67. Kohsaka H, Okusawa S, Itakura Y, Fushiki A, Nose A. Development of larval motor circuits in *Drosophila*. Development, Growth, and Differentiation. 2012;54(3):408–419. doi:10.1111/j.1440-169X.2012.01347.x.

68. Grillner S. Locomotion in Vertebrates: Central Mechanisms and Reflex Interaction. Physiological Reviews. 1975;55(2):247–304.

69. Marder E, Bucher D. Central pattern generators and the control of rhythmic movements. Current Biology. 2001;11(23):986–996.

70. Marder E, Bucher D, Schulz DJ, Taylor AL. Invertebrate Central Pattern Generation Moves Along. Current Biology. 2005;15(17):685–699. doi:10.1016/j.cub.2005.08.022.

71. Suster ML, Bate M. Embryonic assembly of a central pattern generator without sensory input. Nature. 2002;416(6877):174–178. doi:10.1038/416174a.

72. Skaggs WE, Knierim JJ, Kudrimoti HS, McNaughton BL. A Model of the Neural Basis of the Rat's Sense of Direction. Advances in Neural Information Processing Systems. 1995;7:173–180.

73. Zhang K. Representation of Spatial Orientation by the Intrinsic Dynamics of the Head-Direction Cell Ensemble: A Theory. The Journal of Neuroscience. 1996;16(6):2112–2126.

74. Song P, Wang X. Angular Path Integration by Moving "Hill of Activity": A Spiking Neuron Model without Recurrent Excitation of the Head-Direction System. The Journal of Neuroscience. 2005;25(4):1002–1014.

75. Merritt D, Whitington P. Central projections of sensory neurons in the *Drosophila* embryo correlate with sensory modality, soma position, and proneural gene function. The Journal of Neuroscience. 1995;15(3):1755–1767.

76. Suslak TJ, Armstrong JD, Jarman AP. A general mathematical model of transduction events in mechano-sensory stretch receptors. Network: Computation in Neural Systems. 2011;22(1-4):133–142. doi:10.3109/0954898X.2011.638967.

77. Sawin EP, Harris LR, Campos AR, Sokolowski MB. Sensorimotor transformation from light reception to phototactic behavior in *Drosophila* larvae (Diptera: Drosophilidae). Journal of Insect Behavior. 1994;7(4):553. doi:10.1007/BF02025449.

78. Busto M, Iyengar B, Campos AR. Genetic Dissection of Behavior: Modulation of Locomotion by Light in the *Drosophila melanogaster* Larva Requires Genetically Distinct Visual System Functions. The Journal of Neuroscience. 1999;19(9):3337–3344.

79. Scantlebury N, Sajic R, Campos AR. Kinematic Analysis of *Drosophila* Larval Locomotion in Response to Intermittent Light Pulses. Behavior Genetics. 2007;37(3):513–524. doi:10.1007/s10519-007-9146-3.

80. Louis M, Huber T, Benton R, Sakmar TP, Vosshall LB. Bilateral olfactory sensory input enhances chemotaxis behaviour. Nature Neuroscience. 2008;11(2):187–199. doi:10.1038/nn2031.

81. Gershow M, Berck M, Mathew D, Luo L, Kane EA, Carlson JR, et al. Controlling airborne cues to study small animal navigation. Nature Methods. 2012;9(3):290–296. doi:10.1038/nmeth.1853.

82. Klein M, Afonso B, Vonner AJ, Hernandez-Nunez L, Berck M, Tabone CJ, et al. Sensory determinants of behavioral dynamics in *Drosophila* thermotaxis. Proceedings of the National Academy of Sciences. 2015;112(2):E220–E229. doi:10.1073/pnas.1416212112.

83. Alexandre C, Lecourtois M, Vincent J. Wingless and Hedgehog pattern Drosophila denticle belts by regulating the production of short-range signals. Development. 1999;126(24):5689–5698.

84. Dixit R, VijayRaghavan K, Bate M. Hox genes and the regulation of movement in *Drosophila*. Developmental Neurobiology. 2008;68(3):309–316. doi:10.1002/dneu.20589.

85. Bhatt PK, Neckameyer WS. Functional Analysis of the Larval Feeding Circuit in *Drosophila*. Journal of Visualised Experiments. 2013;81. doi:10.3791/51062.

86. Berri S, Boyle JH, Tassieri M, Hope IA, Cohen N. Forward locomotion of the nematode C. elegans is achieved through modulation of a single gait. HFSP journal. 2009;3 3:186–93.

87. Gjorgjieva J, Biron D, Haspel G. Neurobiology of Caenorhabditis elegans Locomotion: Where Do We Stand? BioScience. 2014;64(6):476–486. doi:10.1093/biosci/biu058.

88. Rabets Y, Backholm M, Dalnoki-Veress K, Ryu WS. Direct Measurements of Drag Forces in C. elegans Crawling Locomotion. Biophysical Journal. 2014;107(8):1980 – 1987. doi:https://doi.org/10.1016/j.bpj.2014.09.006.

89. Backholm M, Kasper AKS, Schulman RD, Ryu WS, Dalnoki-Veress K. The effects of viscosity on the undulatory swimming dynamics of C. elegans. Physics of Fluids. 2015;27(9):091901. doi:10.1063/1.4931795.

90. Keaveny EE, Brown AEX. Predicting path from undulations for C. elegans using linear and nonlinear resistive force theory. Physical Biology. 2017;14(2):025001.

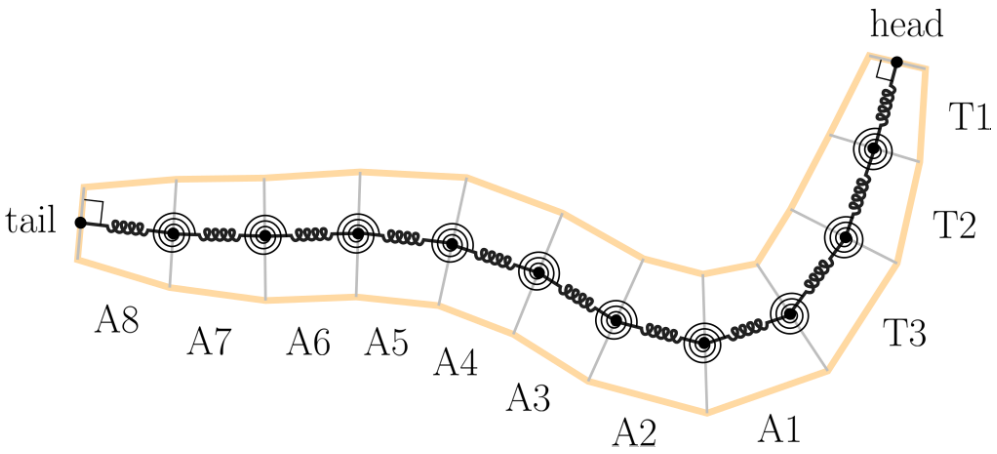

Figure 3.1: **Our model of axial and transverse motion over a planar substrate** (Figure 1 main text). The midline of the larva is modelled as a set of discrete point masses interacting with each other via linear, damped translational and torsional springs, and with the environment via Coulomb sliding friction. We model the larva's incompressible coelomic fluid by constraining the total length of the midline to remain constant (see main text). Quantities used to describe deformations of the body, and interaction with the substrate, are shown in S1 Fig.

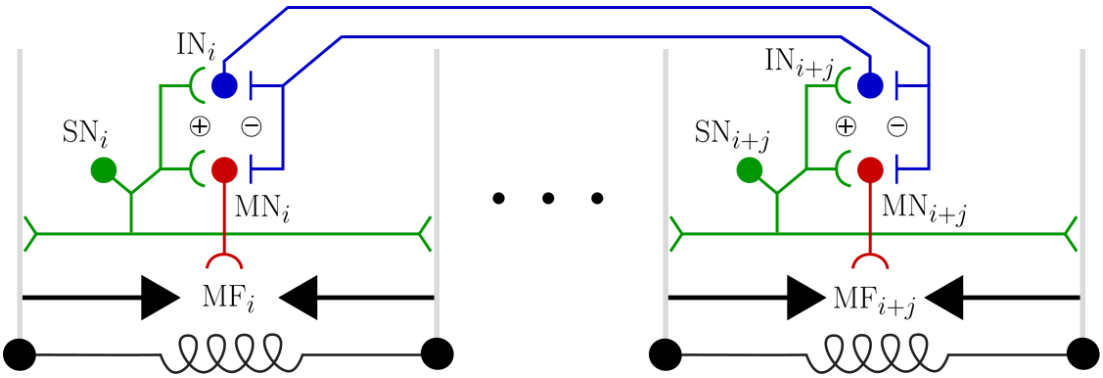

Figure 3.2: **The neuromuscular model** (Figure 2 main text) A local reflex amplifies motion via positive feedback : sensory neurons SN activate during segmental shortening, exciting motor neurons MN, and causing muscle fibre activation MF which accelerates shortening. Reflexes in distant segments i and $i+j$ ($|j|>1$) mutually inhibit one another via interneurons IN. This limits the number of moving segments to allow centre of mass motion (see text).

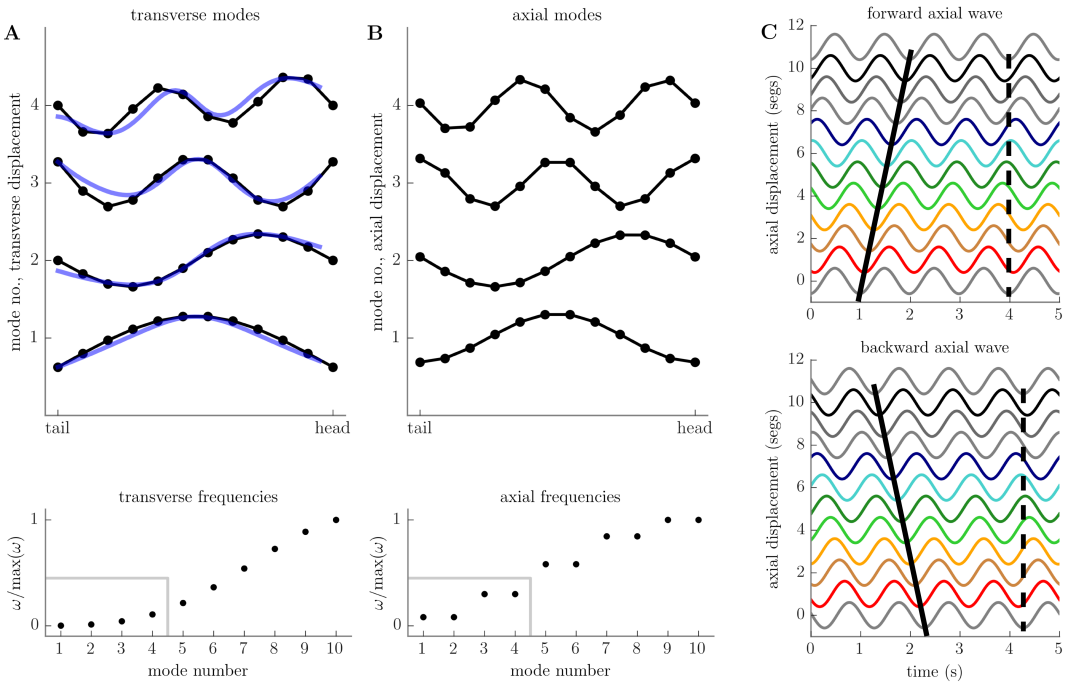

Figure 3.3: **Conservative, small-amplitude motions of the body decompose into a set of axial and transverse standing waves** (Figure 3 main text) A: spatial component of first four transverse standing waves (top, black) compared to first four experimentally determined eigenmaggots (Szigeti et al., 2015) (top, blue), with natural frequencies of oscillation (bottom). B: spatial component of first four axial standing waves (top), with natural frequencies of oscillation (bottom). Note that axial standing waves come in pairs with identical frequency. C: Pairs of axial standing waves can be combined to produce forward-propagating (top, solid black line) and backward-propagating (bottom, solid black line) travelling waves. Head and tail extremities move in phase (dashed black line) due to our total length constraint (see text), reminiscent of the “visceral pistoning” observed in the real animal (Heckscher et al., 2012).

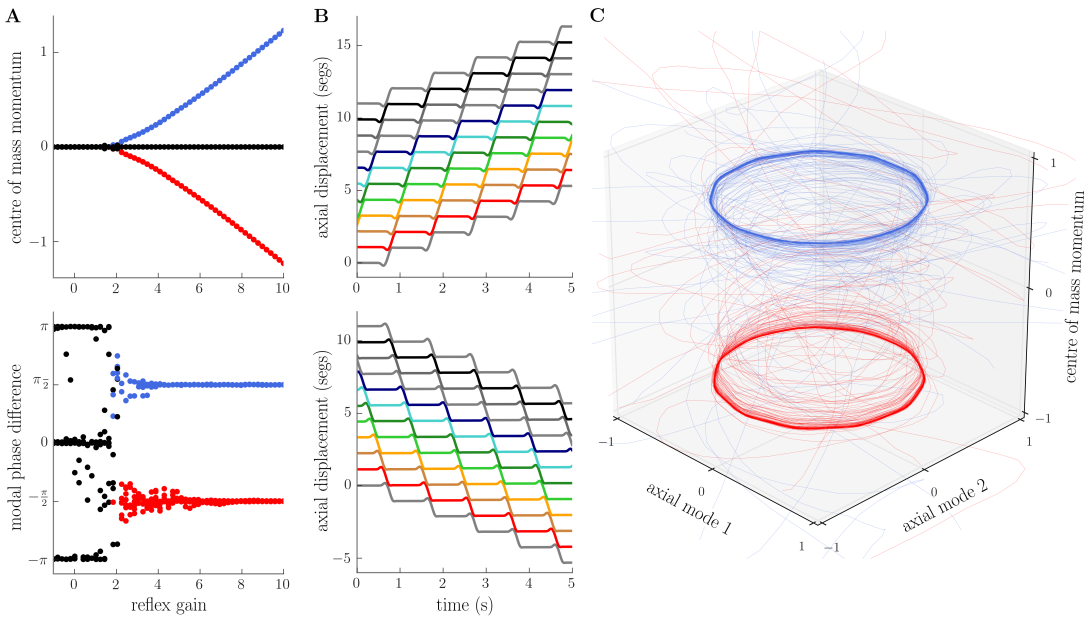

Figure 3.4: **Emergence of limit cycles for forward and backward locomotion in the dissipative, small-amplitude model** (Figure 4 main text). A: as reflex gain is increased past a critical point, the model larva attains a positive or negative long-term average centre of mass momentum (top, red and blue lines), signifying continuous forward or backward motion relative to the substrate, and a $\pm\pi/2$ relative phase difference between the two lowest frequency axial standing wave modes (bottom, red and blue lines), signifying the presence of forward- or backward-propagating axial travelling waves. B: trajectories of individual point masses in the model for forward (top) or backward (bottom) locomotion (see S2 Fig for corresponding neural state). C: projection of model trajectories onto the lowest frequency axial modes and the centre of mass momentum reveals a pair of (putative) stable limit cycles for forward (blue) and backward (red) locomotion. Parameters used to generate this figure are given in S2 Table.

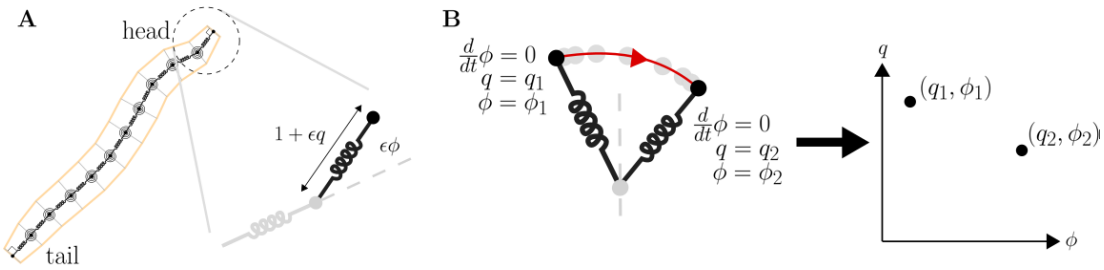

Figure 3.5: **A reduced model of large amplitude motion** (Figure 5 main text). A: we focus on the conservative dynamics of the head's strain q and bend ϕ coordinates as amplitude ε is varied. B: head trajectories are visualised by Poincare section, in which the head's configuration q, ϕ is plotted at successive turning points of the transverse bending motion (at which angular velocity vanishes, $d\phi/dt = 0$).

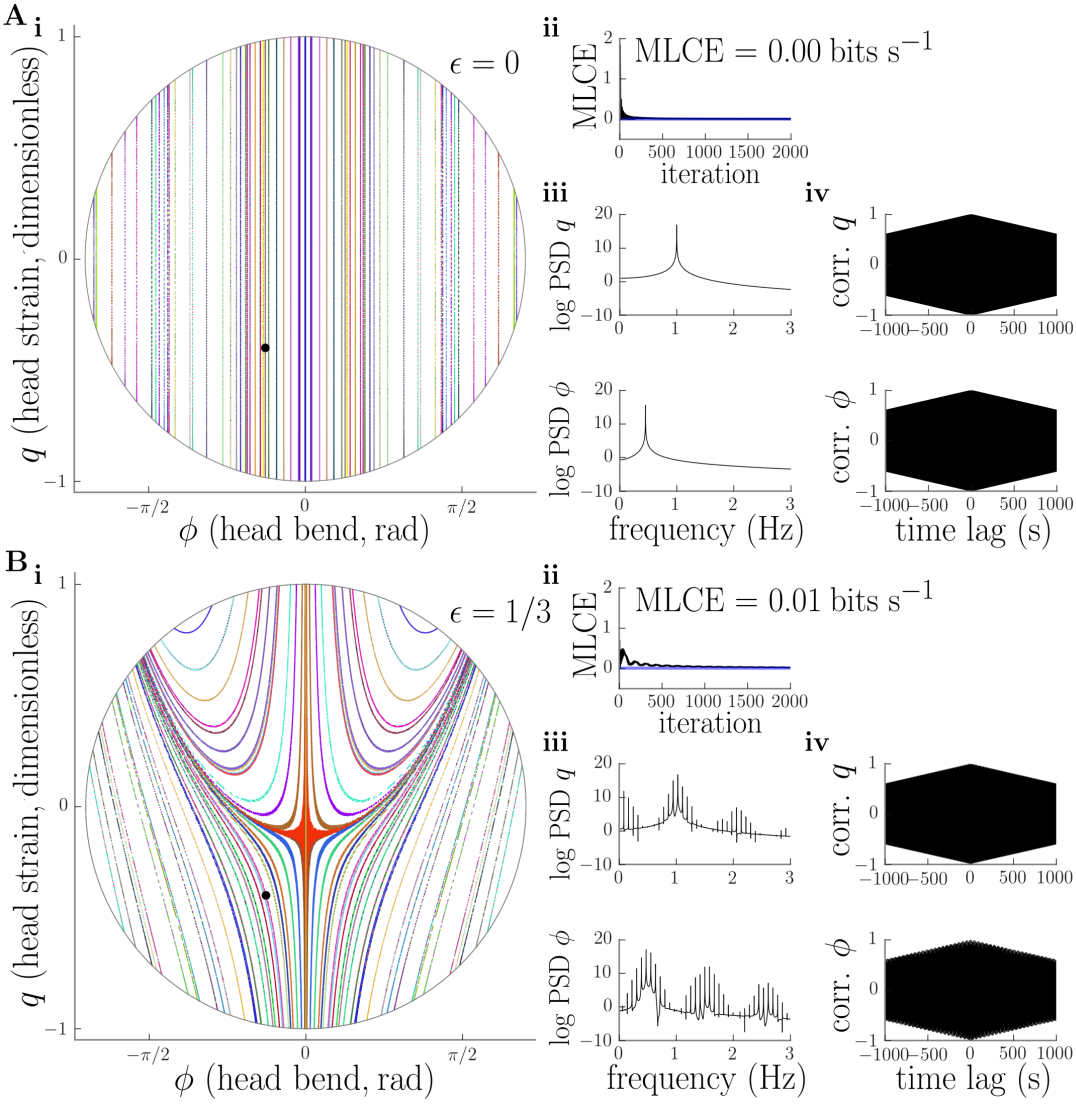

Figure 3.6: **Emergence of deterministic chaos in the conservative head dynamics as amplitude of motion is increased.** (Figure 6 main text) A, B: for small amplitudes ($\varepsilon \to 0, \varepsilon = 1/3$), Poincare section shows quasiperiodic head oscillations (i), while the maximum Lyapunov characteristic exponent (MLCE), which quantifies the dominant rate of separation of nearby phase trajectories, converges to ~ 0bits s^{-1} (ii), the power spectra of head stretch q and bend ϕ coordinates show clear peaks with little "noise" component (iii), and autocorrelations of these variables decay linearly (iv). These results betray non-chaotic, quasiperiodic oscillations for small amplitudes. MLCE, power spectra, and autocorrelations were computed for initial conditions shown by black dot in panel i. Parameters used to generate this figure are detailed in the main text, and reported in S3 Table.

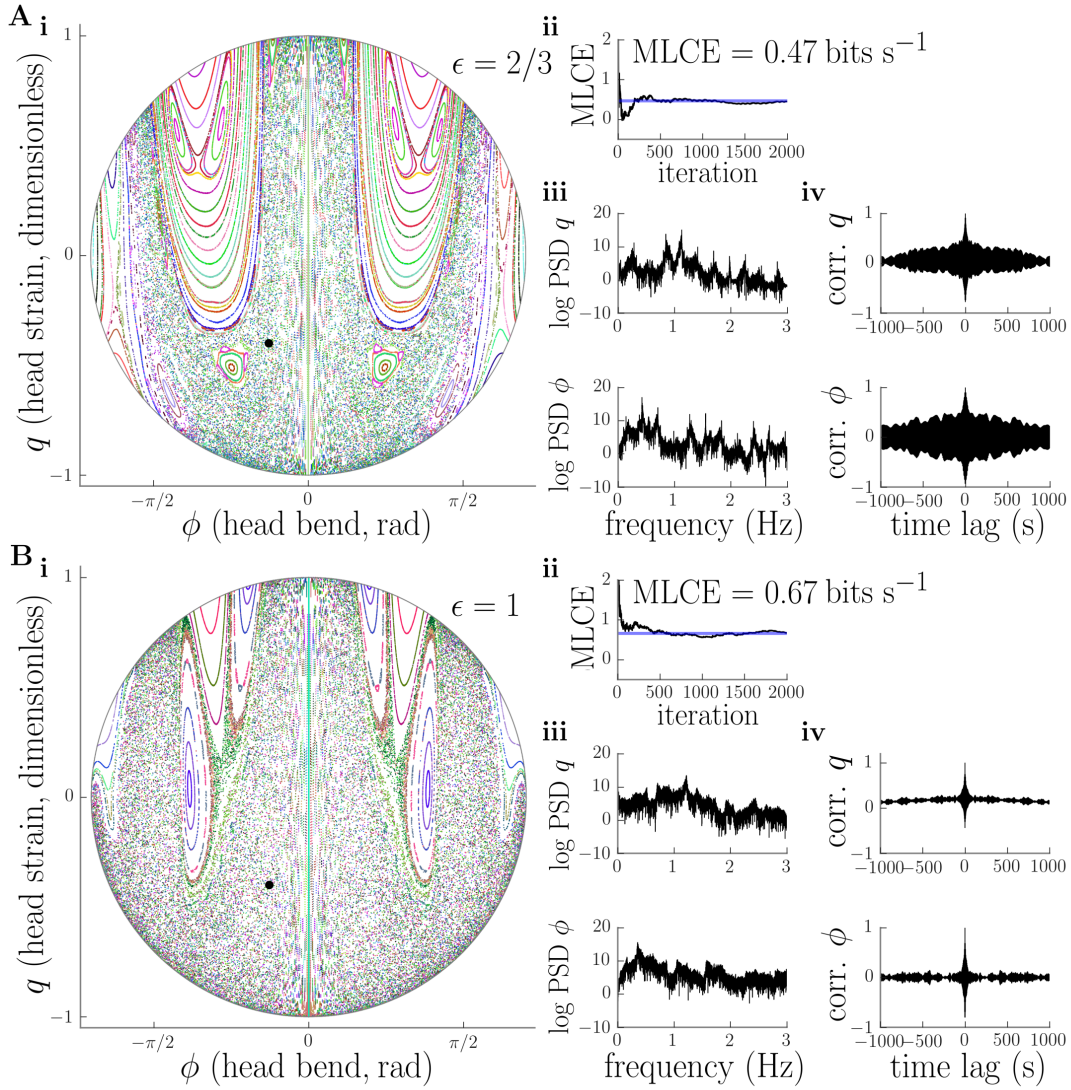

Figure 3.7: **(continued from Figure 6) Emergence of deterministic chaos in the conservative head dynamics as amplitude of motion is increased.** (Figure 7 main text) C, D: for large amplitudes ($\varepsilon = 2/3, \varepsilon = 1$), the Poincare section contains a large chaotic sea (i), while the MLCE converges to a positive value (ii), power spectra become "noisy" (iii), and autocorrelations decay rapidly (iv). These results strongly suggest the existence of deterministic chaotic head dynamics for large amplitudes. MLCE, power spectra, and autocorrelations were computed for initial conditions shown by black dot in panel i. Parameters used to generate this figure are detailed in the main text, and reported in S3 Table.

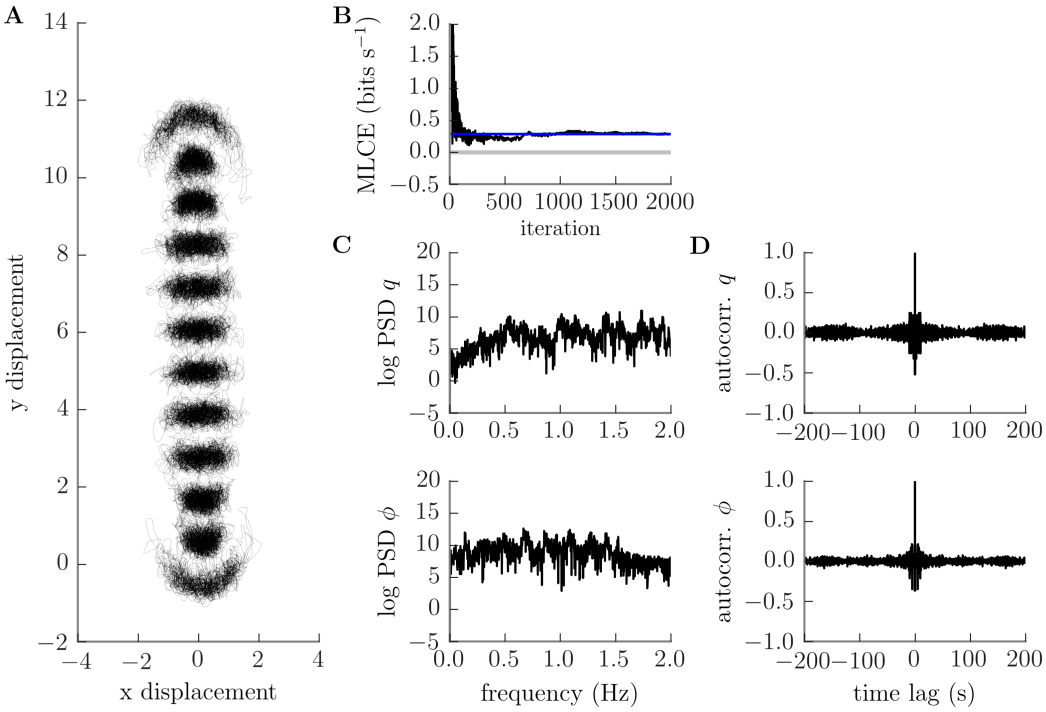

Figure 3.8: **Conservative planar motion of the body is chaotic at large amplitudes** (Figure 8 main text). A: trajectories of individual segment boundaries appear qualitatively irregular, B: our estimate of the maximum Lyapunov characteristic exponent converges to a positive value, C: power spectra of head stretch q and bend ϕ show a strong "noise" component, and D: their autocorrelations decay rapidly. All are indicators of deterministic chaos. Parameters used to generate this figure are given in S4 Table.

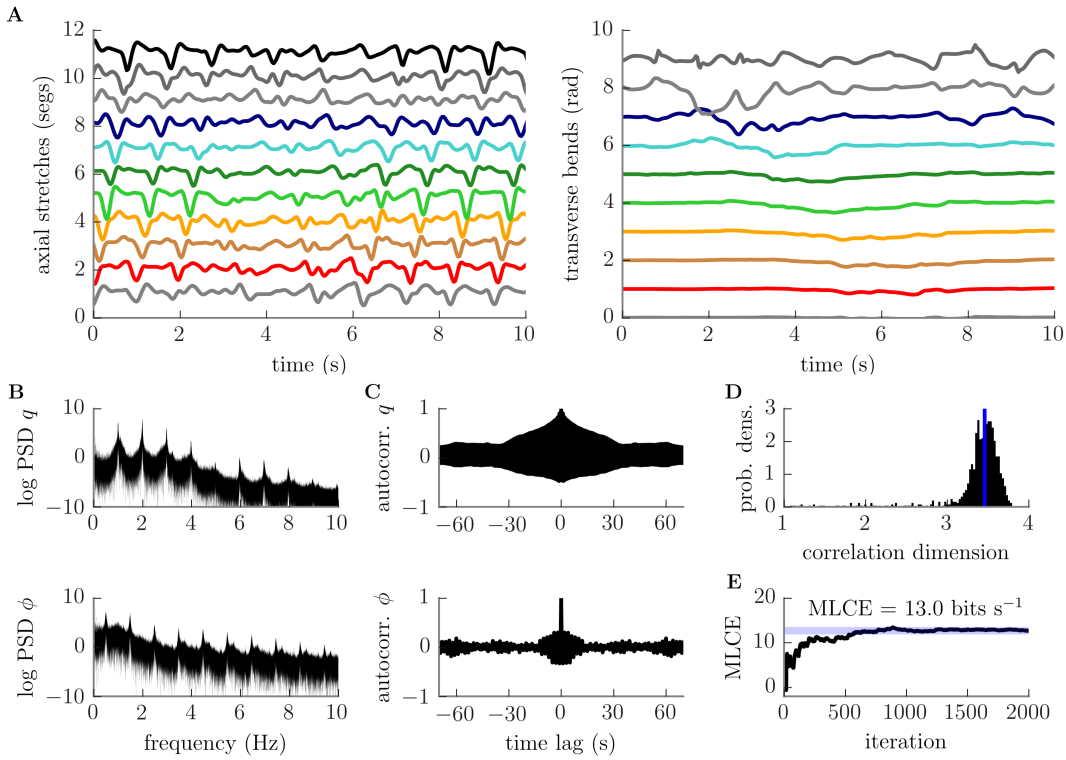

Figure 3.9: **Dissipative planar motion is chaotic** (Figure 9 main text). A: representative segmental stretch (left) and bend (right) time series (see S3 Fig for corresponding neural state). Note the occurence of a large bend starting at $\sim$ 1–2 seconds at the larva's head, which appears to propagate backwards along the body while triggering a "transition" from forward to backward wave propagation at ~ 3.5 seconds. Forward wave propagation resumes at ~ 6 seconds. B: power spectra of the head stretch q (top) and bend ϕ (bottom) showing significant "noise" component. C: Autocorrelations of q and ϕ rapidly decay. D: probability density of correlation dimension estimates for 1000 mechanical trajectories. The dimension of the system's limit set is estimated as ~ 3.5 (median, vertical blue line). E: maximum Lyapunov characteristic exponent estimates converge to a positive value. All measures suggest the presence of deterministic chaotic dynamics. Parameters used to generate this figure are given in S5 Table.

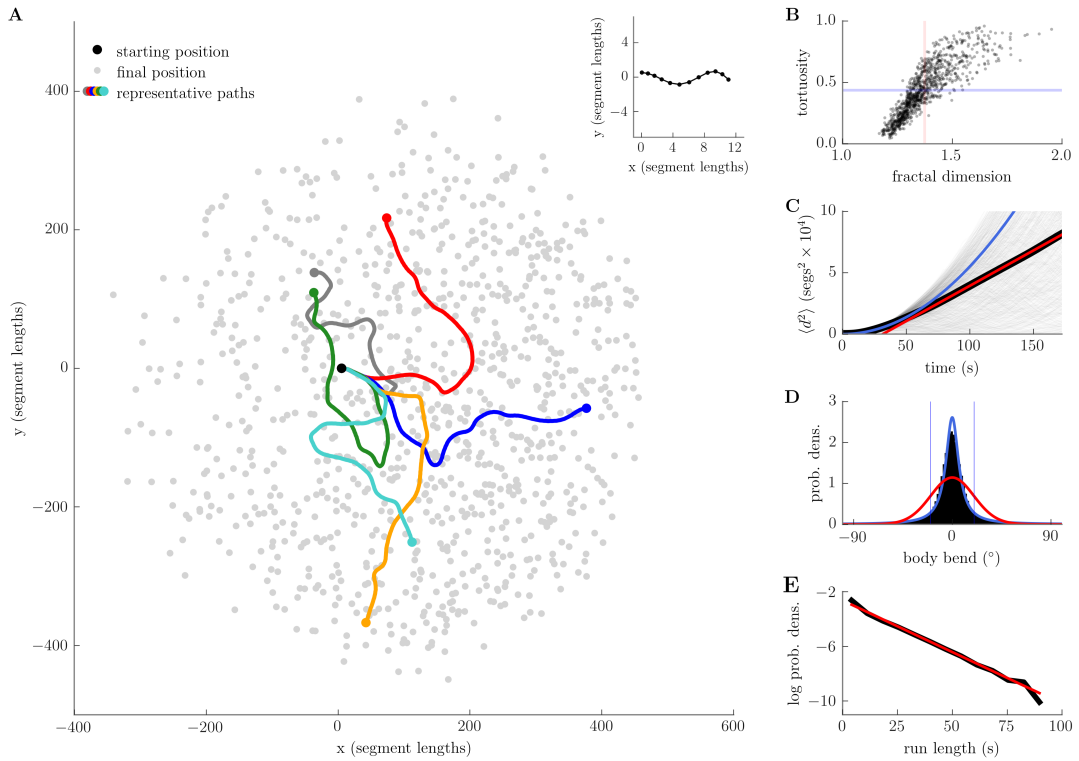

Figure 3.10: **Deterministic exploration** (Figure 10 main text). A: dispersion of the centres of mass of 1000 simulated larvae, starting from almost identical mechanical initial conditions (overlayed in inset). B: tortuosity and fractal (box-counting) dimension for all 1000 paths indicate plane-filling behaviour (blue line = mean tortuosity, red line = mean dimension, see text; see S4 Fig for power law analysis of trajectory curvature and angular speed). C: mean-squared displacement (black line) shows transient quadratic growth (blue line) followed by asymptotic linear growth (red line, asymptotic diffusion constant $\approx 144 \text{segs}^2 \text{s}^{-1}$; see also log-log plot, S5 Fig). D: distribution of body bends (black) with maximum likelihood von Mises (red) and wrapped Cauchy (blue) fits. E: distribution of run lengths with maximum likelihood exponential fit (red). Run lengths were calculated as duration between successive crossings of a threshold body bend (20°), indicated by blue lines in panel D. See S6 Fig for analysis of tail speed and head angular velocity. Parameters used to generate this figure are given in S5 Table.

Table S1: neural parameter values. All segments are identical. Values given in larval units (seg = resting segment length, segmass = mass of a single segment boundary, nondim = dimensionless/nondimensional).

symbol	description	value
θ_{SN}	sensory neuron threshold	1/100 seg s^{-1}
θ_{IN}	interneuron threshold	1/2 (nondim.)
θ_{MN}	motor neuron threshold	1/2 (nondim.)
$w_{\mathrm{SN}\to\mathrm{MN}}$	sensory neuron → motor neuron synaptic weight	1 (nondim.)
$w_{\mathrm{MN}\to\mathrm{MF}}$	motor neuron → muscle fibre synaptic weight	1 (nondim.)
$w_{\mathrm{SN}\to\mathrm{IN}}$	sensory neuron → interneuron synaptic weight	1 (nondim.)
$w_{\mathrm{IN}\to\mathrm{MN}}$	interneuron → motor neuron synaptic weight	-2 (nondim.)
$w_{\mathrm{IN}\to\mathrm{IN}}$	interneuron → interneuron synaptic weight	-2 (nondim.)

Table S2: mechanical parameters for **Fig 4. Emergence of limit cycles for forward and backward locomotion in the dissipative, small-amplitude model**. All segments are identical. Values given in larval units (seg = resting segment length, segmass = mass of a single segment boundary, nondim = dimensionless/nondimensional).

symbol	description	value
b	reflex gain	varies (see figure) segmass seg s^{-2}
l	equilibrium segment length	1 seg
m	segment mass	1 segmass
k_a	axial stiffness	$(2\pi)^2$ segmass s^{-2}
η_a	axial coefficient of viscosity	2π segmass s^{-1}
μ	coefficient of friction	1 segmass seg s^{-2}

Table S3: mechanical parameters for **Fig 6** and **Fig 7. Emergence of deterministic chaos in the conservative head dynamics as amplitude of motion is increased**. Values given in larval units (seg = resting segment length, segmass = mass of a single segment boundary, nondim = dimensionless/nondimensional).

symbol	description	value
ϵ	amplitude	varies (see figure) (nondim.)
λ	ratio of transverse and axial frequencies	$e/6$ (nondim.)
E	total mechanical energy	1/2 (nondim.)

Table S4: mechanical parameters for **Fig 8. Conservative planar motion of the body is chaotic at large amplitudes**. All segments are identical. Values given in larval units (seg = resting segment length, segmass = mass of a single segment boundary, nondim = dimensionless/nondimensional).

symbol	description	value
l	equilibrium segment length	1 seg
m	segment mass	1 segmass
k_a	axial stiffness	3.15 segmass s^{-2}
k_t	transverse stiffness	8.45 segmass seg^2 s^{-2} rad^{-1}
k_c	incompressibility constraint stiffness	1000 segmass s^{-2}

Table S5: mechanical parameters for **Fig 9. Dissipative planar motion is chaotic** and **Fig 10. Deterministic exploration**. Values given in larval units (seg = resting segment length, segmass = mass of a single segment boundary, nondim = dimensionless/nondimensional)

symbol	description	value
l	equilibrium segment length	1 seg
m	segment mass	1 segmass
k_a	axial stiffness	2 segmass s^{-2}
η_a	axial coefficient of viscosity	0.25 segmass s^{-1}
$k_{t,11}$	transverse stiffness about T1-T2 boundary	0.05 segmass seg^2 s^{-2} rad^{-1}
$k_{t,10}$	transverse stiffness about T2-T3 boundary	0.07 segmass seg^2 s^{-2} rad^{-1}
$k_{t,9}$	transverse stiffness about T3-A1 boundary	0.1 segmass seg^2 s^{-2} rad^{-1}
$k_{t,8}$	transverse stiffness about A1-A2 boundary	0.15 segmass seg^2 s^{-2} rad^{-1}
$k_{t,2}, k_{t,3}, \ldots, k_{t,7}$	transverse stiffness about A7-A8, A6-A7, ..., A2-A3 boundaries	0.2 segmass seg^2 s^{-2} rad^{-1}
$\eta_{t,11}$	transverse viscosity about T1-T2 boundary	0.033 segmass seg^2 s^{-1} rad^{-1}
$\eta_{t,10}$	transverse viscosity about T2-T3 boundary	0.067 segmass seg^2 s^{-1} rad^{-1}
$\eta_{t,9}$	transverse viscosity about T3-A1 boundary	0.33 segmass seg^2 s^{-1} rad^{-1}
$\eta_{t,8}$	transverse viscosity about A1-A2 boundary	0.67 segmass seg^2 s^{-1} rad^{-1}
$\eta_{t,2}, \eta_{t,3}, ldots, \eta_{t,7}$	transverse viscosity about A7-A8, A6-A7, ..., A2-A3 boundaries	1.67 segmass seg^2 s^{-1} rad^{-1}
$\mu_{f,1}, \mu_{f,2}, \ldots, \mu_{f,12}$	(forward) coefficient of friction, all segments	0 segmass seg s^{-2}
$\mu_{b,12}$	(backward) coefficient of friction at head extremity	100 segmass seg s^{-2}
$\mu_{b,11}$	(backward) coefficient of friction at T1-T2 boundary	100 segmass seg s^{-2}
$\mu_{b,10}$	(backward) coefficient of friction at T2-T3 boundary	0.2 segmass seg s^{-2}
$\mu_{b,9}$	(backward) coefficient of friction at T3-A1 boundary	0.2 segmass seg s^{-2}
$\mu_{b,1}, \mu_{b,2}, \ldots, \mu_{b,8}$	(backward) coefficient of friction at tail extremity and A7-A8, ..., A1-A2 boundaries	5 segmass seg s^{-2}
$\mu_{p,12}$	directional "focus" of friction at head extremity	4.5 (nondim.)
$\mu_{p,11}$	directional "focus" of friction at T1-T2 boundary	4.5 (nondim.)
$\mu_{p,1}, \mu_{p,2}, \ldots, \mu_{p,10}$	directional "focus" of friction at tail extremity and A7-A8, ..., T2-T3 boundaries	1.5 (nondim.)
b_9, b_{10}, b_{11}	reflex gain in segments T3, T2, T1	0.09 segmass seg s^{-2}
$b_1, b_2, \ldots, b_8$	reflex gain in segments A8, A7, ..., A1	0.48 N
k_c	incompressibility constraint stiffness	1000 segmass s^{-2}

S1 Appendix – Detailed model specification

In this appendix we provide a mathematical specification of our neuromechanical model. We will describe our mechanical model using the framework of Hamiltonian mechanics, since this is the natural setting for discussions of deterministic chaos within classical mechanics. To specify our model, we provide descriptions of the mechanical energy stored in the body and the power flow through the body. First, the total kinetic energy of the body is given by

$$T = \frac{1}{2}\sum_{i=1}^{N} m_i \dot{\mathbf{r}}_i^2 \tag{1}$$

where m_i is the mass of the i'th segment boundary and $\dot{\mathbf{r}}_i$ is its velocity measured relative to the substrate.

We assume that the cuticle stores elastic potential energy in both axial compression/expansion and in transverse bending. We further assume that there exists some equilibrium state where the potential energy is at a minimum, and at which point the length of the i'th body segment (bounded by masses m_i and m_{i+1}) is l_i. Axial deformation can then be conveniently described by a set of *axial stretches*, which measure the difference between each segment's current length and its equilibrium length

$$q_i = \|\mathbf{r}_{i+1} - \mathbf{r}_i\| - l_i, \quad i \in [1, N-1] \tag{2}$$

where the double bars indicate the standard Euclidean norm. We assume that the transverse potential energy is at a minimum when the masses are arranged in a straight line (i.e. when the midline is not curved). In this case it is convenient to measure transverse deformation by the *bending angle* made between successive body segments

$$\phi_i = \cos^{-1}\frac{\left[\mathbf{r}_i - \mathbf{r}_{i-1}\right]^T\left[\mathbf{r}_{i+1} - \mathbf{r}_i\right]}{\|\mathbf{r}_i - \mathbf{r}_{i-1}\|\|\mathbf{r}_{i+1} - \mathbf{r}_i\|}, \quad i \in [2, N-1] \tag{3}$$

The internal coordinate system q_i, ϕ_i which we have constructed is shown in S1 Fig. We use these coordinates to define quadratic approximations to the axial and transverse potential energies around the equilibrium state. The axial potential is given by

$$U_a = \frac{1}{2}\sum_{i=1}^{N-1} k_{a,i} q_i^2 \tag{4}$$

where $k_{a,i}$ is the axial stiffness of the i'th body segment. The transverse potential may be written similarly as

$$U_t = \frac{1}{2}\sum_{i=2}^{N-1} k_{t,i} \phi_i^2 \tag{5}$$

where $k_{t,i}$ is the transverse (bending) stiffness about the i'th segment boundary. We account for dissipation of mechanical energy due to viscous friction within the tissues of the larva by approximating axial and transverse power losses by negative definite, quadratic forms in the generalised velocities associated with our internal coordinate system. The axial power loss is then given by

$$P_a = -\sum_{i=1}^{N-1} \eta_{a,i} \dot{q}_i^2 \tag{6}$$

where $\eta_{a,i}$ is the coefficient of viscosity of the i'th body segment. The transverse power loss is

$$P_t = -\sum_{i=2}^{N-1} \eta_{t,i}\dot{\phi}_i^2 \tag{7}$$

where $\eta_{t,i}$ is the coefficient of viscosity associated with bending about the i'th segment boundary. We allow the larva to interact with its substrate via Coulomb kinetic friction, which causes negative definite power losses from the body. During our investigation of small-amplitude dissipative motion, we assume isotropic (direction independent) substrate interaction, with power loss given by

$$P_f = -\sum_{i=1}^{N} \mu_i \|\dot{\mathbf{r}}_i\| \tag{8}$$

where μ_i is a parameter characterising the magnitude of sliding friction forces, and is related to the terrestrial gravitational acceleration g and the coefficient of kinetic friction $\mu_{kinetic}$ of the i'th mass by $\mu_i = \mu_{kinetic} m_i g$. During our investigation of large-amplitude dissipative motion, we allow anisotropic substrate interaction. In this case, the i'th mass is acted upon by a force $F_{friction,i}$ which is directed opposite to its velocity vector v_i and has a magnitude which depends upon the angle θ_i between the velocity vector and the local body axis (see S1 Fig),

$$\mathbf{F}_{friction,i} = -F(\theta_i)\frac{\mathbf{v}_i}{\|\mathbf{v}_i\|} \tag{9}$$

with

$$F(\theta_i) = \mu_{f,i} + (\mu_{b,i} - \mu_{f,i})\left[\frac{1-\cos\theta_i}{2}\right]^{\mu_{p,i}} \tag{10}$$

where $\mu_{f,i}$ sets the magnitude of friction opposing motion forward along the body axis ($\theta_i = 0$), $\mu_{b,i}$ sets the magnitude of friction opposing motion backward along the body axis ($\theta_i = \pi$), and $\mu_{p,i} > 0$ sets the directional "focus" of the friction force.

We also allow for flow of power due to muscle activation

$$P_u = -\sum_{i=1}^{N-1} b_i u_i \dot{q}_i \tag{11}$$

where b_i is a (positive) gain parameter, u_i is a dimensionless control variable (identified with muscle activation MF_i in the main text), and the product $b_i u_i$ is the total axial tension across the i'th body segment. As described in the main text, the internal coelomic fluid of the larva gives rise to a constraint on the total length of the larval midline,

$$\sum_{i=1}^{N-1}(l_i + q_i) = L \tag{12}$$

where the summands on the left are the time-dependent lengths of the individual segments of the midline, and L is a constant. Noting that in equilibrium ($q_i = 0$) we must have $\sum_i l_i = L$, we can rewrite the constraint as

$$\sum_{i=1}^{N-1} q_i = 0 \tag{13}$$

It is easy to enforce the total length constraint directly in the case of small amplitude motion or purely axial motion, but in the general case of large amplitude axial and transverse motion this constraint can be difficult to enforce. We therefore attempt to satisfy the constraint only approximately, by introducing an additional potential energy

$$U_c = k_c \left[\sum_{i=1}^{N-1} q_i \right]^2 \tag{14}$$

where the constraint stiffness k_c is chosen to be very large relative to the other stiffness parameters k_a and k_t. Numerically, we satisfy this condition by setting $k_c = \max(k_a, k_t) \times 10^3$.

To derive the dynamics for our system in a form suitable for simulation, we start by using the coordinate transformations 2 and 3 and the definition of the linear momenta $\mathbf{p}_i = m_i \dot{\mathbf{r}}_i$ to write the Hamiltonian function

$$H(\mathbf{r}, \mathbf{p}) = T(\mathbf{p}) + U_a(\mathbf{r}) + U_t(\mathbf{r}) + U_c(\mathbf{r}) \tag{15}$$

which corresponds to the total mechanical energy of the body. We then construct the Rayleigh dissipation function R, which is the sum of the expressions for power transfer into the body, weighted by the inverse homogeneity of each expression [1]. This must also be expressed in terms of the lab frame coordinates and momenta by means of the transformations (2) and (3) and their time derivatives, so that we have

$$R(\mathbf{r}, \mathbf{p}; \mathbf{u}) = \frac{1}{2} P_a(\mathbf{r}, \mathbf{p}) + \frac{1}{2} P_t(\mathbf{r}, \mathbf{p}) + P_f(\mathbf{r}, \mathbf{p}) + P_u(\mathbf{r}, \mathbf{p}; \mathbf{u}) \tag{16}$$

From these two functions, the entire body dynamics can be derived as a system of $2N_{DOF}$ first order differential equations using the dissipative Hamilton's equations

$$\dot{\mathbf{r}}_i = \frac{\partial H}{\partial \mathbf{p}_i} \tag{17}$$

$$\dot{\mathbf{p}}_i = -\frac{\partial H}{\partial \mathbf{r}_i} + \frac{\partial R}{\partial \mathbf{p}_i} \frac{d\mathbf{p}_i}{d\dot{\mathbf{r}}_i} \tag{18}$$

Where our expression for anistropic friction (9) must be added to the right hand side of (18) where appropriate. These differential equations can be solved to find the positions $\mathbf{r}_i$ and momenta $\mathbf{p}_i$ of the masses in the lab frame.

For the sake of brevity we will not write out $H(\mathbf{r}, \mathbf{p})$, $R(\mathbf{r}, \mathbf{p})$, or the dissipative Hamilton's equations in full here. We stress, however, that our model is entirely specified by the expressions for the kinetic and potential energy and the power transfer into the body, along with the transformations between the lab frame and internal coordinates, and the anistropic friction function. We manipulate these expressions in practise using a computer algebra system (`SymPy`). For simulation, we numerically integrate the dissipative Hamilton's equations with pre-specified initial conditions and parameters.

References

1. Landau LD, Lifshitz EM. Mechanics. vol. 1 of Course of Theoretical Physics. 3rd ed. Butterworth-Heinemann; 1976.

S2 Appendix – Detailed small-amplitude analysis

In this appendix we present an analysis of the conservative, small oscillations of the larval body. We will attempt to apply the Liouville-Arnold integrability theorem, which tells us that the motion of a mechanical system must be (quasi)periodic if there exist a number of conserved quantities equal to the number of degrees of freedom, and which are in involution (a condition we will define later) [1]. We will find conserved quantities by *separating* the Hamiltonian describing our small-amplitude model. To illustrate this method, suppose we have a Hamiltonian $H(q,p)$ which depends upon a set of generalised coordinates q (not necessarily the axial stretches defined earlier) and their canonically conjugate momenta p, and that this Hamiltonian can be separated into a sum of independent Hamiltonians

$$H(q,p) = H_1(q^1,p^1) + H_2(q^2,p^2) \tag{1}$$

where q^1, q^2 are non-intersecting subsets of q, and p^1, p^2 are the momenta conjugate to these coordinates. Taking the derivative of H_1 and H_2 with respect to time, we find

$$\dot{H}_1 = \frac{\partial H_1}{\partial q^1}\dot{q}^1 + \frac{\partial H_1}{\partial p^1}\dot{p}^1 \tag{2}$$

and

$$\dot{H}_2 = \frac{\partial H_2}{\partial q^2}\dot{q}^2 + \frac{\partial H_2}{\partial p^2}\dot{p}^2 \tag{3}$$

meanwhile, the (conservative) Hamilton's equations tell us that

$$\dot{q}^1 = \frac{\partial H}{\partial p^1} = \frac{\partial H^1}{\partial p^1} \tag{4}$$

$$\dot{q}^2 = \frac{\partial H}{\partial p^2} = \frac{\partial H^2}{\partial p^2} \tag{5}$$

$$\dot{p}^1 = -\frac{\partial H}{\partial q^1} = -\frac{\partial H^1}{\partial q^1} \tag{6}$$

$$\dot{p}^2 = -\frac{\partial H}{\partial q^2} = -\frac{\partial H^2}{\partial q^2} \tag{7}$$

substitution into the expressions above then gives

$$\dot{H}_1 = -\dot{p}^1\dot{q}^1 + \dot{p}^1\dot{q}^1 = 0 \tag{8}$$

$$\dot{H}_2 = -\dot{p}^2\dot{q}^2 + \dot{p}^2\dot{q}^2 = 0 \tag{9}$$

which shows that both H_1 and H_2 are conserved quantities. To test whether these quantities are in involution, we must check that their Poisson bracket vanishes [1, 2], i.e. we must check that

$$\{H_1, H_2\} = \sum_k \left(\frac{\partial H_1}{\partial p_k}\frac{\partial H_2}{\partial q_k} - \frac{\partial H_1}{\partial q_k}\frac{\partial H_2}{\partial p_k} \right) = 0 \tag{10}$$

Noting that $q_k \in q^1$ implies $p_k \in p^1$, we see that the partial derivates $\frac{\partial H_2}{\partial q_k}$ and $\frac{\partial H_2}{\partial p_k}$ vanish. Similarly, if $q_k \in q^2$ then $p_k \in p^2$ so that the partial derivatives $\frac{\partial H_1}{\partial q_k}$ and $\frac{\partial H_1}{\partial p_k}$ also vanish. Therefore, every term of the

summation must be equal to zero, so that the Poisson bracket of H_1 and H_2 vanishes, and the quantities are in involution. The above argument can be applied recursively to show that if a Hamiltonian is separable into more than two parts, then those parts are conserved quantities which are in mutual involution.

Let us now begin our investigation of the small-amplitude motions of the larval body. We will do this by taking a Taylor series approximation to the Hamiltonian about the body's equilibrium state, and keeping only terms up to second order. Since the Hamilton's equations give us the dynamics of the larval body by differentiating the Hamiltonian, this second-order approximation is equivalent to linearising the dynamics about the equilibrium.

We first align the midline along the x-axis of the lab frame, with all segment boundaries in their equilibrium positions (i.e. separated by distances l_i along the x-axis). We then construct a new coordinate system such that the variables x_i and y_i denote the displacement of the i'th mass along the x and y axes of the lab frame, respectively, relative to the equilibrium configuration. The canonical momenta $p_{x,i}$, $p_{y,i}$ conjugate to these coordinates are then simply the x and y components of the lab frame momenta $\mathbf{p}_i$. Expanding the Hamiltonian as a Taylor series about the equilibrium $\mathbf{x} = \mathbf{y} = \mathbf{p}_x = \mathbf{p}_y = \mathbf{0}$, and keeping terms up to second order, we obtain the small oscillation Hamiltonian

$$H_{SO}(\mathbf{x}, \mathbf{y}, \mathbf{p}_x, \mathbf{p}_y) = \underbrace{\frac{1}{2}\left[\mathbf{p}_x^T\mathbf{p}_x + \omega_a^2\mathbf{x}^T\mathbf{D}_2\mathbf{x}\right]}_{H_a(\mathbf{x},\mathbf{p}_x)} + \underbrace{\frac{1}{2}\left[\mathbf{p}_y^T\mathbf{p}_y + \omega_t^2\mathbf{y}^T\mathbf{D}_4\mathbf{y}\right]}_{H_t(\mathbf{y},\mathbf{p}_y)} \tag{11}$$

where we have further assumed that all segments of the body are identical, i.e. $m_i = m$, $l_i = l$, $k_{a,i} = k_a$, $k_{t,i} = k_t$, and we have scaled the coordinates $\mathbf{x} \to \mathbf{x}/\sqrt{m}$, $\mathbf{y} \to \mathbf{y}/\sqrt{m}$ to simplify the kinetic energy and absorb all of the mechanical parameters into the potential energy, so that $\omega_a^2 = k_a/m$ and $\omega_t^2 = k_t/ml^2$. $\mathbf{D}_2$ is the $(N-1)\times(N-1)$ circulant second difference matrix

$$\mathbf{D}_2 = \begin{bmatrix} 2 & -1 & & & -1 \\ -1 & 2 & -1 & & \\ & \ddots & \ddots & \ddots & \\ & & -1 & 2 & -1 \\ -1 & & & -1 & 2 \end{bmatrix} \tag{12}$$

and $\mathbf{D}_4$ is the $N \times N$ fourth difference matrix with free boundary conditions

$$\mathbf{D}_4 = \begin{bmatrix} 1 & -2 & 1 & & & & \\ -2 & 5 & -4 & 1 & & & \\ 1 & -4 & 6 & -4 & 1 & & \\ & \ddots & \ddots & \ddots & \ddots & \ddots & \\ & & 1 & -4 & 6 & -4 & 1 \\ & & & 1 & -4 & 5 & -2 \\ & & & & 1 & -2 & 1 \end{bmatrix} \tag{13}$$

For the case of small oscillations the full Hamiltonian is clearly separable into an axial and a transverse Hamiltonian, which we labelled H_a and H_t above. These terms correspond to the total axial and transverse mechanical energy in the larval body, respectively. Our earlier investigation of separable Hamiltonians tells us that each term is an independently conserved quantity, so that no energy transfer may occur between small amplitude axial and transverse motions. Let us now attempt to further separate these Hamiltonians. We will do this by introducing a new set of coordinates $\mathbf{X}, \mathbf{Y}$, called *modal* coordinates, which are linearly related to the axial and transverse coordinates $\mathbf{x}, \mathbf{y}$ by

$$\mathbf{x} = \mathbf{\Phi}_a\mathbf{X}, \quad \mathbf{y} = \mathbf{\Phi}_t\mathbf{Y} \tag{14}$$

The canonical momenta conjugate to $\mathbf{X}, \mathbf{Y}$ are denoted $\mathbf{p}_X, \mathbf{p}_Y$ and are given by the relations $\mathbf{p}_x = \mathbf{\Phi}_a\mathbf{p}_X$ and $\mathbf{p}_y = \mathbf{\Phi}_t\mathbf{p}_Y$. Using these transformations, we may write the axial and transverse Hamiltonians in terms of the modal coordinates and their canonically conjugate momenta as

$$H_a(\mathbf{X}, \mathbf{p}_X) = \frac{1}{2}\left[\mathbf{p}_X^T\mathbf{\Phi}_a^T\mathbf{\Phi}_a\mathbf{p}_X + \omega_a^2\mathbf{X}^T\mathbf{\Phi}_a^T\mathbf{D}_2\mathbf{\Phi}_a\mathbf{X}\right] \tag{15}$$

$$H_t(\mathbf{Y}, \mathbf{p}_Y) = \frac{1}{2}\left[\mathbf{p}_Y^T \mathbf{\Phi}_t^T \mathbf{\Phi}_t \mathbf{p}_Y + \omega_t^2 \mathbf{Y}^T \mathbf{\Phi}_t^T \mathbf{D}_2 \mathbf{\Phi}_t \mathbf{Y}\right] \tag{16}$$

If the coordinate transformations described by $\mathbf{\Phi}_a$ and $\mathbf{\Phi}_t$ are to separate the axial and transverse Hamiltonians into sums of independent terms, we see that the results of the matrix products $\mathbf{\Phi}_a^T \mathbf{\Phi}_a$, $\mathbf{\Phi}_a^T \mathbf{D}_2 \mathbf{\Phi}_a$ and $\mathbf{\Phi}_t^T \mathbf{\Phi}_t$, $\mathbf{\Phi}_t^T \mathbf{D}_4 \mathbf{\Phi}_t$ must be diagonal. We may use this condition to find the form of the transformation matrices $\mathbf{\Phi}_a$ and $\mathbf{\Phi}_t$. To do this, we first note that $\mathbf{D}_2$ and $\mathbf{D}_4$ are real and symmetric, and that each can therefore be factored by eigendecomposition into a product of an orthogonal matrix of eigenvectors and a diagonal matrix of eigenvalues. Therefore, we can write

$$\mathbf{D}_2 = \mathbf{A} \mathbf{\Lambda}_a \mathbf{A}^T, \quad \mathbf{D}_4 = \mathbf{B} \mathbf{\Lambda}_t \mathbf{B}^T \tag{17}$$

where $\mathbf{A}$ is the orthogonal eigenvector matrix and $\mathbf{\Lambda}_a$ the diagonal eigenvalue matrix of $\mathbf{D}_2$. Similarly, $\mathbf{B}$ is the orthogonal eigenvector matrix and $\mathbf{\Lambda}_t$ the diagonal eigenvalue matrix of $\mathbf{D}_4$. We choose to identify the axial coordinate transformation with the axial eigenvector matrix, so that $\mathbf{\Phi}_a = \mathbf{A}$, and identify the transverse coordinate transformation with the transverse eigenvector matrix, so that $\mathbf{\Phi}_t = \mathbf{B}$. By the orthogonality of these matrices, we then have $\mathbf{\Phi}_a^T = \mathbf{\Phi}_a^{-1}$ and $\mathbf{\Phi}_t^T = \mathbf{\Phi}_t^{-1}$. Effecting the eigendecomposition of $\mathbf{D}_2$, the axial Hamiltonian becomes

$$H_a(\mathbf{X}, \mathbf{p}_X) = \frac{1}{2}\left[\mathbf{p}_X^T \mathbf{\Phi}_a^{-1} \mathbf{\Phi}_a \mathbf{p}_X + \omega_a^2 \mathbf{X}^T \mathbf{\Phi}_a^{-1} \mathbf{\Phi}_a \mathbf{\Lambda}_a \mathbf{\Phi}_a^{-1} \mathbf{\Phi}_a \mathbf{X}\right] = \frac{1}{2}\left[\mathbf{p}_X^T \mathbf{p}_X + \omega_a^2 \mathbf{X}^T \mathbf{\Lambda}_a \mathbf{X}\right] \tag{18}$$

or, denoting the i'th eigenvalue of $\mathbf{D}_2$ as $\lambda_{a,i}$,

$$H_a(\mathbf{X}, \mathbf{p}_X) = \sum_{i=1}^{N-1} \frac{1}{2}\left[p_{X,i}^2 + \omega_a^2 \lambda_{a,i} X_i^2\right] \tag{19}$$

Effecting the eigendecomposition of $\mathbf{D}_4$, the transverse Hamiltonian similarly decouples to give

$$H_t(\mathbf{Y}, \mathbf{p}_Y) = \sum_{i=1}^{N} \frac{1}{2}\left[p_{Y,i}^2 + \omega_t^2 \lambda_{t,i} Y_i^2\right] \tag{20}$$

where $\lambda_{t,i}$ denotes the i'th eigenvalue of $\mathbf{D}_4$. These final expressions show that the axial and transverse Hamiltonians are reduced to sums of independent terms, each of which contains just one modal coordinate and its conjugate momentum. Each term corresponds to the total mechanical energy associated with that mode, and is independently conserved according to our earlier results on separable Hamiltonians. This means that no energy transfer can occur between modal coordinates in the case of small oscillations. Given that we now have a number of conserved quantities equal to the number of degrees of freedom of our system, and these quantities are involution with one another, we can invoke the Liouville-Arnold integrability theorem to tell us that our mechanical system must execute periodic or quasiperiodic motion in the case of small oscillations. Indeed, the Hamilton's equations for the i'th modes are

$$\dot{X}_i = \frac{\partial H}{\partial p_{X,i}} = p_{X,i}, \quad \dot{Y}_i = \frac{\partial H}{\partial p_{Y,i}} = p_{Y,i} \tag{21}$$

and

$$\dot{p}_{X,i} = -\frac{\partial H}{\partial X_i} = -\omega_{a,i}^2 X_i, \quad \dot{p}_{Y,i} = -\frac{\partial H}{\partial Y_i} = -\omega_{t,i}^2 Y_i \tag{22}$$

where we have introduced the parameters $\omega_{a,i} = \omega_a \sqrt{\lambda_{a,i}} = (k_a/m)\sqrt{\lambda_{a,i}}$ and $\omega_{t,i} = \omega_t \sqrt{\lambda_{t,i}} = (k_t/ml^2)\sqrt{\lambda_{t,i}}$. These are harmonic oscillator equations in first order form. We can recover the familiar second-order harmonic oscillator equation by differentiating the first equation with respect to time, finding $\dot{p}_{X,i} = \ddot{X}_i$, $\dot{p}_{Y,i} = \ddot{Y}_i$, before substituting into the second equation to give

$$\ddot{X}_i + \omega_{a,i}^2 X_i = 0, \quad \ddot{Y}_i + \omega_{t,i}^2 Y_i = 0, \tag{23}$$

The solution to the harmonic oscillator problem is well known [3], and in this case tells us

$$X_i = A_{a,i}\sin\left(\omega_{a,i}t + \theta_{a,i}\right), \qquad Y_i = A_{t,i}\sin\left(\omega_{t,i}t + \theta_{t,i}\right) \tag{24}$$

These solutions tell us that the modal coordinates execute sinusoidal oscillations with constant amplitude $A_{a,i}$, $A_{t,i}$, phase shift $\theta_{a,i}$, $\theta_{t,i}$, and frequency $\omega_{a,i}$ and $\omega_{t,i}$. To relate this back to our original small oscillation coordinates $\mathbf{x}$ and $\mathbf{y}$ we need to find the eigenvectors $\mathbf{\Phi}_a$, $\mathbf{\Phi}_t$, and the corresponding eigenvalues $\lambda_{a,i}$, $\lambda_{t,i}$, of $\mathbf{D}_2$ and $\mathbf{D}_4$. We can find both $\mathbf{\Phi}_a$ and $\mathbf{\Lambda}_a$ analytically by noting that $\mathbf{D}_2$ is a circulant matrix. Indeed, the i'th eigenvector of an arbitrary circulant matrix is given by [4]

$$\mathbf{\Phi}_{a,i} = \frac{1}{\sqrt{N-1}}\left[1, z_i, z_i^2, \cdots, z_i^{N-2}\right]^T \tag{25}$$

where we have used $\mathbf{\Phi}_{a,i}$ to denote the i'th column of the eigenvector matrix $\mathbf{\Phi}_a$, and $z_i = e^{\frac{2\pi ij}{N-1}}$ is the i'th element of the $(N-1)$'th roots of unity, with $j = \sqrt{-1}$ the imaginary unit. Using Euler's complex exponential formula the k'th element of the i'th axial mode shape may be written

$$\mathbf{\Phi}_{a,k,i} = \frac{1}{\sqrt{N-1}}\left[\cos\left(2\pi i\frac{k}{N-1}\right) + j\sin\left(2\pi i\frac{k}{N-1}\right)\right] \tag{26}$$

The real and complex parts of each vector can be considered as independent mode shapes, so that the modes thus come in pairs with identical spatial frequency,

$$\mathbf{\Phi}_{a,k,i} = \frac{1}{\sqrt{N-1}}\cos\left(2\pi i\frac{k}{N-1}\right), \text{ or } \mathbf{\Phi}_{a,k,i} = \frac{1}{\sqrt{N-1}}\sin\left(2\pi i\frac{k}{N-1}\right), \quad i \in [0, N/2-1] \tag{27}$$

For an arbitrary $(N-1)\times(N-1)$ circulant matrix with entries

$$\mathbf{A} = \begin{bmatrix} c_0 & c_{N-2} & \cdots & c_2 & c_1 \\ c_1 & c_0 & c_{N-2} & & c_2 \\ \vdots & c_1 & c_0 & \ddots & \vdots \\ c_{N-3} & & \ddots & \ddots & c_{N-2} \\ c_{N-2} & c_{N-3} & \cdots & c_1 & c_0 \end{bmatrix} \tag{28}$$

the eigenvalue corresponding to the i'th eigenvector is given by [4]

$$\lambda_i = c_0 + c_{N-2}z_i + c_{N-3}z_i^2 + \cdots + c_1 z_i^{N-2} \tag{29}$$

In the case of $\mathbf{D}_2$ we have $c_0 = 2$ and $c_1 = c_{N-2} = -1$, so that this reduces to

$$\lambda_i = 2 - z_i - z_i^{N-2} \tag{30}$$

However, the $N-1$'th roots of unity satisfy $z_i^{N-2} = \bar{z}_i$, where the bar indicates the complex conjugate. Therefore,

$$\lambda_i = 2 - 2\mathrm{Re}[z_i] \tag{31}$$

the real part of z_i can be found by using Euler's complex exponential formula, yielding

$$\lambda_i = 2 - 2\cos\left(\frac{2\pi i}{N-1}\right) \tag{32}$$

By using the trigonometric identity $\sqrt{2-2\cos(x)} = 2\sin\left(\frac{x}{2}\right)$ we may now calculate the frequency of oscillation of the i'th axial mode to be

$$\omega_{a,i} = 2\omega_a\left|\sin\left(\frac{\pi i}{N-1}\right)\right| \tag{33}$$

It is marked that the axial modes come in pairs with identical temporal and spatial frequencies. This property allows us to construct travelling wave solutions for the axial motion by combining sinusoidal

oscillations within a pair of modes with equal magnitude and a 90° temporal phase shift relative to each other. To see this mathematically, we re-examine our expression for the axial mode shapes (27). We multiply these vectors by modal coordinates oscillating with unity amplitude, identical temporal frequency $\omega_{a,i}$ and a $\pm 90°$ phase shift, and sum the result, so that the k'th segment boundary displacement for the i'th axial mode can be written

$$x_k = \cos\left(\omega_{a,i} t\right) \cos\left(2\pi i \frac{k}{N-1}\right) + \cos\left(\omega_{a,i} t \pm \frac{\pi}{2}\right) \sin\left(2\pi i \frac{k}{N-1}\right) \tag{34}$$

where we have dropped the normalising factor $\frac{1}{\sqrt{N-1}}$ in (27). This is equivalent to

$$x_k = \cos\left(\omega_{a,i} t\right) \cos\left(2\pi i \frac{k}{N-1}\right) \pm \sin\left(\omega_{a,i} t\right) \sin\left(2\pi i \frac{k}{N-1}\right) \tag{35}$$

Using the identity $\cos(a)\cos(b) \pm \sin(a)\sin(b) = \cos(a \pm b)$, this further simplifies to

$$x_k = \cos\left(\omega_{a,i} t \pm 2\pi i \frac{k}{N-1}\right) \tag{36}$$

Interpreting $0 \leq \frac{k}{N-1} \leq 1$ as a spatial coordinate ranging over the undeformed configuration of the body, this is in the form of a sinusoidal travelling wave, and the choice of a minus or plus sign in the argument corresponds to the choice of a forward- or backward-propagating wave, respectively.

References

1. Arnol'd VI. Mathematical Methods of Classical Mechanics. vol. 60 of Graduate Texts in Mathematics. 2nd ed. Springer; 1989.

2. Landau LD, Lifshitz EM. Mechanics. vol. 1 of Course of Theoretical Physics. 3rd ed. Butterworth-Heinemann; 1976.

3. Tenenbaum M, Pollard H. Ordinary Differential Equations. 1st ed. Dover Books on Mathematics. Dover Publications, Inc.; 1985.

4. Gray RM. Toeplitz and Circulant Matrices: A review. 1st ed. Now Publishers Inc.; 2006.

S3 Appendix – A trade-off between power flow into the body and force on the centre of mass

The neural model we have constructed in this paper was motivated by the requirement for power flow from the musculature to the body, and by the requirement that a small number of segments should move in the direction of centre of mass motion at any given time. There is in fact an inherent trade-off between the need to transfer power into the body and the need to move only a small number of segments, as we will now show by extending the modal analysis of the previous appendix to the dissipative axial mechanics. The Hamiltonian and Rayleigh dissipation function in this case reduce to

$$H_a(\mathbf{x}, \mathbf{p}_x) = \frac{1}{2}\left[\mathbf{p}_x^T\mathbf{p}_x + \omega_a^2\mathbf{x}^T\mathbf{D}_2\mathbf{x}\right] \tag{1}$$

$$R_a(\mathbf{x}, \mathbf{p}_x) = -\zeta_a\omega_a\mathbf{p}_x^T\mathbf{D}_2\mathbf{p}_x + b\mathbf{p}_x^T\mathbf{D}_1\mathbf{u} \tag{2}$$

where we have again assumed that all segments have identical parameters and we have neglected sliding friction for simplicity, and we have defined the axial damping ratio $\zeta_a = \eta_a/2\sqrt{k_a m}$. $\mathbf{D}_1$ is the circulant first difference matrix

$$D_1 = \begin{bmatrix} 1 & & & -1 \\ -1 & 1 & & \\ & \ddots & \ddots & \\ & & -1 & 1 \end{bmatrix} \tag{3}$$

We now move to the axial modal basis $\mathbf{X}$, $\mathbf{p}_X$ defined in the previous appendix by $\mathbf{x} = \mathbf{\Phi}_a\mathbf{X}$, $\mathbf{p}_x = \mathbf{\Phi}_a\mathbf{p}_X$, and introduce modal control variables $\mathbf{U}$ defined by $\mathbf{u} = \mathbf{\Phi}_a\mathbf{U}$, finding

$$H_a(\mathbf{X}, \mathbf{p}_X) = \frac{1}{2}\left[\mathbf{p}_X^T\mathbf{p}_X + \omega_a^2\mathbf{X}^T\mathbf{\Lambda}_a\mathbf{X}\right] \tag{4}$$

$$R_a(\mathbf{X}, \mathbf{p}_X) = -\zeta_a\omega_a\mathbf{p}_X^T\mathbf{\Lambda}_a\mathbf{p}_X + b\mathbf{p}_X^T\mathbf{\Sigma}\mathbf{U} \tag{5}$$

where we have used the fact that the matrix $\mathbf{D}_1$ is circulant and is therefore diagonalised by the eigenvector matrix $\mathbf{\Phi}_a$ of $\mathbf{D}_2$, since all circulant matrices have the same eigenvectors. We write the diagonal eigenvalue matrix of $\mathbf{D}_1$ as $\mathbf{\Sigma}$, with the i'th eigenvalue being $\mathbf{\Sigma}_{i,i} = \sigma_i$. The dissipative Hamilton's equations for the i'th axial mode are then

$$\dot{X}_i = \frac{\partial H_a}{\partial p_{X,i}} = p_{X,i} \tag{6}$$

$$\dot{p}_{X,i} = -\frac{\partial H_a}{\partial X_i} + \frac{\partial R_a}{\partial p_{X,i}}\frac{dp_{X,i}}{d\dot{X}_i} = -\omega_a^2\lambda_{a,i}X_i - 2\zeta_a\omega_a\lambda_{a,i}p_{X,i} + b\sigma_i U_i \tag{7}$$

Where we have used the first equation to tell us that $\frac{d\mathbf{p}_X}{d\dot{\mathbf{X}}} = 1$ in the second equation. We now convert this system of first-order equations to a single second order equation by using the first equation to write $\dot{X}_i = p_{X,i}$ and $\ddot{X}_i = \dot{p}_{X,i}$ in the second, finding

$$\ddot{X}_i + 2\zeta_a\omega_a\lambda_{a,i}\dot{X}_i + \omega_a^2\lambda_{a,i}X_i = b\sigma_i U_i \tag{8}$$

Finally, if we introduce the modal frequencies as $\omega_{a,i} = \omega_a\sqrt{\lambda_{a,i}}$, the modal damping ratios as $\zeta_{a,i} = \zeta_a\sqrt{\lambda_{a,i}}$, and the modal gain factors as $b_i = b\sigma_i$, we obtain the equation of motion for a damped, driven, harmonic oscillator in standard form

$$\ddot{X}_i + 2\zeta_{a,i}\omega_{a,i}\dot{X}_i + \omega_{a,i}^2 X_i = b_i U_i \tag{9}$$

The ratio of energy stored to energy dissipated per cycle of oscillation for a damped harmonic oscillator is given by the Q-factor, defined as $Q = 1/2\zeta$. The lower frequency modes, corresponding to small eigenvalues $\lambda_{a,i}$, will have lower damping ratios $\zeta_{a,i}$ and therefore higher Q-factors. In other words, energy is more efficiently transferred into the low-frequency modes. However, solely driving the lowest frequency modes would fail to produce any force on the centre of mass, because the resulting peristaltic wave would involve equal numbers of segments moving forward and backward, and the resulting frictive forces would cancel out. This necessitates some involvement of higher-frequency modes in order to localise segmental motion and allow overall acceleration of the body. Thus, there is a trade-off between efficiently transferring power into low-frequency modes and producing large forces on the centre of mass.

S4 Appendix – Modelling and analysis of head motion

In this appendix we will consider bending and compression/expansion of the head segment, as viewed from a coordinate frame fixed at the posterior end of the head segment and aligned with the local body axis (the head frame). To simplify our notation we will drop indices, denoting the head's bending angle as $\phi = \phi_{N-1}$ and the head's stretch as $q = q_{N-1}$. The potential energy of the head segment in this frame of reference is then simply

$$U_h = \frac{1}{2}k_a q^2 + \frac{1}{2}k_t \phi^2 \tag{1}$$

Meanwhile, the kinetic energy takes the form

$$T_h = \frac{1}{2m}p_q^2 + \frac{1}{2m(l+q)^2}p_\phi^2 + m(l+q)\left[W_x cos(\phi) + W_y sin(\phi)\right] - \Omega p_\phi \tag{2}$$

where W_x, W_y give the translational acceleration, and Ω the angular velocity, of the head frame relative to the lab frame. The first two terms in this expression can be seen as the kinetic energy obtained by treating the head frame as an inertial reference frame, while the second two terms involving W_x, W_y, and Ω are a correction accounting for non-inertial effects (i.e. fictitious forces) arising in the head frame. Aiming to simplify our analysis as far as possible, we choose to neglect the non-inertial effects, so that the Hamiltonian of the system becomes

$$H_h = \frac{1}{2m}p_q^2 + \frac{1}{2m(l+q)^2}p_\phi^2 + \frac{1}{2}k_a q^2 + \frac{1}{2}k_t \phi^2 \tag{3}$$

We can simplify this expression further by choosing to measure length, mass, and time in convenient units, such that $m = 1$, $l = 1$, and $\omega_a = \sqrt{k_a/m} = 1$. In this case, the Hamiltonian becomes

$$H_h = \frac{1}{2}\left[p_q^2 + \frac{1}{(1+q)^2}p_\phi^2 + q^2 + \lambda^2\phi^2\right] \tag{4}$$

where $\lambda = \omega_t/\omega_a$ is the ratio of transverse to axial frequencies. We can also introduce an explicit amplitude scale by multiplying all dynamical variables by a parameter ϵ. The head Hamiltonian then becomes

$$H_h = \frac{1}{2}\left[\epsilon^2 p_q^2 + \frac{1}{(1+\epsilon q)^2}\epsilon^2 p_\phi^2 + \epsilon^2 q^2 + \epsilon^2\lambda^2\phi^2\right] \tag{5}$$

or, dividing through by ϵ^2,

$$H_h^* = \frac{H_h}{\epsilon^2} = \frac{1}{2}\left[p_q^2 + \frac{1}{(1+\epsilon q)^2}p_\phi^2 + q^2 + \lambda^2\phi^2\right] \tag{6}$$

We can see immediately that for the case of small oscillations, i.e. $\epsilon \to 0$, the head Hamiltonian reduces to the simpler expression

$$H_{h,SO}^* = \frac{1}{2}\left[p_q^2 + q^2\right] + \frac{1}{2}\left[p_\phi^2 + \lambda^2\phi^2\right] \tag{7}$$

which is clearly separable into an axial and a transverse Hamiltonian. By our investigation of separable Hamiltonians (S2 Appendix) theorems we know that these are both conserved quantities, and that they are in involution with one another. Furthermore, this tells us that the motion of the head has a closed-form solution and must be (quasi)periodic. Indeed, the Hamilton's equations in this case tell us

$$\dot{q} = \frac{\partial H^*_{h,SO}}{\partial p_q} = p_q, \quad \dot{\phi} = \frac{\partial H^*_{h,SO}}{\partial p_\phi} = p_\phi \tag{8}$$

and

$$\dot{p}_q = -\frac{\partial H^*_{h,SO}}{\partial q} = -q, \quad \dot{p}_\phi = -\frac{\partial H^*_{h,SO}}{\partial \phi} = -\lambda^2\phi \tag{9}$$

which are harmonic oscillator equations in first order form. As before (S2 Appendix), we can recover the familiar second-order harmonic oscillator equation by differentiating the first equations with respect to time, finding $\dot{p}_q = \ddot{q}$, $\dot{p}_\phi = \ddot{\phi}$, before substituting this result into the second equations to find

$$\ddot{q} + q = 0, \quad \ddot{\phi} + \lambda^2\phi = 0 \tag{10}$$

The solution to the harmonic oscillator problem is well known [1], and in this case tells us

$$q(t) = A_q\cos(t + \theta_q), \quad \phi(t) = A_\phi\cos(\lambda t + \theta_\phi) \tag{11}$$

where the A's are constant amplitudes and the θ's are constant phase shifts. It should be clear from this solution that if λ is rational, the head motion will be periodic while for irrational λ the motion will be quasiperiodic.

To gain insight into the more general case of large amplitude head motion, we attempt to apply the Kolmogorov-Arnold-Moser (KAM) theorem, a key result in classical mechanics [2]. The KAM theorem tells us that for sufficiently small conservative perturbations of an integrable Hamiltonian the motion remains quasiperiodic for a majority of initial conditions, while the region of phase space occupied by chaotic behaviour increases in size with the magnitude of perturbation. The KAM theorem first requires that we write the head Hamiltonian as a sum of an integrable unperturbed Hamiltonian H_0 and a small conservative perturbation ϵH_1, i.e.

$$H^*_h = H_0 + \epsilon H_1 \tag{12}$$

There are in principle several ways of accomplishing this. We proceed by taking a Taylor series expansion in ϵ,

$$H^*_h = H_0 + \epsilon\frac{\partial H^*_h}{\partial \epsilon} + \frac{\epsilon^2}{2}\frac{\partial^2 H^*_h}{\partial \epsilon^2} + \cdots = H_0 + \epsilon\underbrace{\left[\frac{\partial H^*_h}{\partial \epsilon} + \frac{\epsilon}{2}\frac{\partial^2 H^*_h}{\partial \epsilon^2} + \cdots\right]}_{H_1} \tag{13}$$

where we have identified H_0 with the zero'th order term in the expansion, which is simply the small oscillation head Hamiltonian $H_0 = H^*_h(\epsilon = 0) = H^*_{h,SO}$, which we know to be integrable. Unfortunately, this means that the unperturbed system is governed by a harmonic oscillator Hamiltonian (see above), which fails to meet the isoenergetic nondegeneracy condition of the KAM theorem [2]. We therefore cannot formally apply the KAM theorem to the problem of head motion. Nevertheless, numerical experiments do suggest that quasiperiodic behaviour persists for small perturbations, while larger perturbations imply that a greater region of phase space will be occupied by chaos (see main text).

References

1. Tenenbaum M, Pollard H. Ordinary Differential Equations. 1st ed. Dover Books on Mathematics. Dover Publications, Inc.; 1985.

2. Arnol'd VI. Mathematical Methods of Classical Mechanics. vol. 60 of Graduate Texts in Mathematics. 2nd ed. Springer; 1989.

S5 Appendix – Effective body physics arising due to relationship of neuromuscular action to body motion

In this appendix we describe how the action of the neuromuscular system can effectively alter physical properties of the body. Consider an arbitrary segment of the larval body, whose kinematics are described by an axial stretch q and a transverse bending angle ϕ. This segment's contributions to the elastic potential energy and Rayleigh dissipation function are

$$U = \frac{1}{2}k_a q^2 + \frac{1}{2}k_t \phi^2 \tag{1}$$

$$R = -\frac{1}{2}\eta_a \dot{q}^2 - \frac{1}{2}\eta_t \dot{\phi}^2 \tag{2}$$

Suppose the nervous system activates the local musculature so as to exert upon the segment an axial tension u_a and a bending torque u_t, both having a fixed relationship to the local mechanical state, so that we may write $u_a = u_a(q, \dot{q})$, $u_t = u_t(\phi, \dot{\phi})$. This could correspond to the action of local reflex arcs or to the action of a central pattern generator which has been entrained to the body's motion. The total generalised axial and transverse forces Q_a, Q_t due to viscoelastic body mechanics and muscular activation are then given by

$$Q_a = -\frac{\partial U}{\partial q} + \frac{\partial R}{\partial \dot{q}} + u_a(q, \dot{q}) = -k_a q - \eta_a \dot{q} + u_a(q, \dot{q}) \tag{3}$$

$$Q_t = -\frac{\partial U}{\partial \phi} + \frac{\partial R}{\partial \dot{\phi}} + u_t(\phi, \dot{\phi}) = -k_t \phi - \eta_t \dot{\phi} + u_t(\phi, \dot{\phi}) \tag{4}$$

Expanding the muscular terms as Taylor series up to first order gives

$$u_a(q, \dot{q}) \approx u_a(0,0) + \frac{\partial u_a}{\partial q}(0,0)q + \frac{\partial u_a}{\partial \dot{q}}(0,0)\dot{q} \tag{5}$$

$$u_t(\phi, \dot{\phi}) \approx u_t(0,0) + \frac{\partial u_t}{\partial \phi}(0,0)q + \frac{\partial u_t}{\partial \dot{\phi}}(0,0)\dot{\phi} \tag{6}$$

We neglect the leading constant terms, since these correspond only to shifts of the equilibrium stretch and bending angle. Keeping only the linear terms, and labelling the coefficients by α and β as shown, the generalised forces become

$$Q_a = -(k_a - \alpha_a)q - (\eta_a - \beta_a)\dot{q} \tag{7}$$

$$Q_t = -(k_t - \alpha_t)\phi - (\eta_t - \beta_t)\dot{\phi} \tag{8}$$

From which it should be clear that stretch- or bend-dependent muscle activation gives an effective shift in the axial or transverse stiffness (and therefore also the natural frequencies of axial and transverse motion, see earlier appendices), while stretch rate- or bend rate-dependendent muscle activation gives an effective shift in the axial or transverse coefficient of viscosity.

S6 Appendix – Computer algebra and numerical methods

In preparing this paper we have made use of the `SymPy` computer algebra package for Python. In particular, we used `SymPy` to convert our mathematical expressions for kinetic and potential energies, power losses, and friction forces into a consistent cartesian coordinate system (the lab frame), before combining them to form expressions for the Hamiltonian and Rayleigh dissipation function (see S1 Appendix for definitions of these quantitites). We then used `SymPy` to derive our mechanical equations of motion using the dissipative Hamiltons equations (see S1 Appendix for definitions of these equations).

We carried out our modal analysis using a combination of manual methods and `SymPy`, and used the `NumPy` function `numpy.linalg.eig` to numerically estimate the eigenvalues and eigenvectors of $\mathbf{D}_4$.

We also formulated our neuromuscular model in `SymPy`. In order to avoid algebraic inconsistencies associated with the mutual inhibitory connections in our model, we used a fast switching dynamics. We replaced the algrebaic binary activation function (Eq 4, main text) with the first-order dynamics

$$\dot{V}_i = \begin{cases} r - rV_i & \sum_j w_j V_j > \theta_i \\ -rV_i & \text{otherwise} \end{cases} \tag{1}$$

where r is a switching rate constant. We set $r = 1$ ms^{-1}, so that neural state changes occured on a far faster timescale than the evolution of the mechanics.

Having assembled the dynamical equations for our model in `SymPy`, we then used the `sympy.fcode` function to generate equivalent `FORTRAN` source code, and called the `odespy` package to compile this source code and numerically integrate our model equations via the `LSODES` solver. We chose timesteps and absolute/relative tolerances for `LSODES` by requiring that integration of our conservative equations lead to a change in total energy of less than 0.1%. Following simulation, we scaled the time axis so that the fundamental frequency of tail segment length oscillations was 1 Hz, to roughly match observations of the real larva. Note that this is equivalent to scaling the axial and transverse natural frequencies of our model, via stiffness or mass parameters (see S2 Appendix). After scaling, we downsampled to a 30 Hz sampling rate to match typical video recording apparatus.

Given the time series of a quantity x obtained from a simulation run of duration T with timestep Δt, we computed the power spectral density of x as

$$\mathcal{S}\left[x\right](\omega) = \frac{\Delta t^2}{T} \left|\mathcal{F}\left[x\right](\omega)\right|^2 \tag{2}$$

where ω is frequency and F is the fast Fourier transform of x, obtained via the `scipy.fftpack.fft` function in `SciPy`. We computed the autocorrelation of x as

$$\mathcal{A}\left[x\right](t) = x(t) * x(-t) \tag{3}$$

where the star denotes convolution, which we achieved via the `scipy.fftpack.fftconvolve` function. At several points in the paper we were required to fit data by known distributions or curves. We performed linear least-squares fitting of mean-squared displacement (Fig 10, S5 Fig) and log angular speed (S4 Fig) using the `sympy.stats.linregress` function. We computed maximum-likelihood von Mises and wrapped Cauchy fits to the body bend distribution (Fig 10) using `sp.stats.vonmises.fit` and `sp.stats.wrapcauchy.fit`, respectively. We compared exponential and power law fits to the run length distribution (Fig 10) using the `powerlaw` Python package.

To examine the putative chaotic behaviour of our model we calculated the maximal Lyapunov characteristic exponent (MLCE). The MLCE is defined as

$$\lambda = \lim_{t\to\infty} \frac{1}{t} ln \frac{\|\delta x(t)\|}{\|\delta x(0)\|} \tag{4}$$

where $\delta x(0)$ is some initial separation distance between two mechanical trajectories of the system and $\delta x(t)$ is the separation distance at a time t in the future. Technically, limit sets of an N-dimensional system will have a spectrum of N Lyapunov exponents, but the dynamics on the set will be dominated by the largest (maximal) exponent.

We estimated the MLCE using a standard "pullback" algorithm in which two trajectories of the system are numerically integrated in parallel while periodically resetting one to be a distance d_0 away from the other. This procedure can be described as follows :

1. choose some initial conditions for the model and numerically integrate until transient behaviour has diminished; call the final state x_0
2. pick a random vector y_0 which is a distance $\delta x(0)$ from x_0
3. numerically integrate the model dynamics starting from x_0 and y_0 over some time t until reaching states x_1 and y_1
4. calculate the distance between x_1 and y_1 using any vector norm (we use the standard Euclidean norm); denote this distance $\delta x(t)$
5. compute and store a finite time estimate of the MLCE by substituting into the definition above
6. reset $x_0 \to x_1$ and $y_0 \to x_1 + \delta x(0)\frac{(y_1-x_1)}{\|y_1-x_1\|}$; i.e. "pull back" y_1 along the vector from x_1 to y_1 until a distance $\delta x(0)$ from x_1
7. repeat steps 3–6 for some fixed number of iterations
8. average over the stored finite time estimates of the MLCE to obtain a single MLCE estimate; some of the initial stored estimates may be discarded first to ensure the y trajectory has aligned along the direction with the largest Lyapunov exponent

3.4 Axial-transverse power transfer via parametric resonance

Next we will investigate the transfer of energy between axial and transverse degrees of freedom. To do so we will focus on an intermediate amplitude scale. In particular, we note that the head Hamiltonian can be expanded in a perturbation series in the amplitude parameter ε,

$$H_h^* = [H_h^*]_{\varepsilon\to 0} + \varepsilon \left[\frac{\partial H_h^*}{\partial \varepsilon}\right]_{\varepsilon\to 0} + \varepsilon^2 \left[\frac{\partial^2 H_h^*}{\partial \varepsilon^2}\right]_{\varepsilon\to 0} + \cdots \tag{3.1}$$

To keep our focus on the simplest model demonstrating axial-transverse coupling, we will keep only the terms $H_0 = H_{h,SO}^*$ and εH_1, finding

$$H_1 = \left[\frac{\partial H_h^*}{\partial \varepsilon}\right]_{\varepsilon\to 0} = -q p_\phi^2 \tag{3.2}$$

so that the intermediate amplitude Hamiltonian becomes

$$H_{h,IA}* = \frac{1}{2}\left[p_q^2 + (1-2\varepsilon q)p_\phi^2 + q^2 + \lambda^2\phi^2\right] \tag{3.3}$$

Since this coupled system is still fairly difficult to analyse, we choose to focus only on the transfer of energy from axial to transverse degrees of freedom. To do so, we will set the axial motion q to a prescribed function of time. We choose for this purpose $q = \cos(\omega t)$, which represents both the axial solution to the small amplitude model (see previous section), as well as a first-order approximation of the Fourier series expansion of a more complicated periodic function. Since the terms in p_q^2 and q^2 in the Hamiltonian do not effect the transverse dynamics, they can be discarded, leaving us with

$$H_{h,IA}* = \frac{1}{2}\left[1 - 2\varepsilon\cos(\omega t)\right] p_\phi^2 + \frac{1}{2}\lambda^2\phi^2 \tag{3.4}$$

In order to simplify this Hamiltonian, we next take a canonical transformation to new phase space coordinates given by $\Phi = p_{\phi/\lambda}$, $P = -\lambda\phi$, which allows us to group all parameters in one term and interpret the axial-transverse interaction as a sinusoidal modulation of frequency

$$H_{h,IA}* = \frac{1}{2}P^2 + \frac{1}{2}\lambda^2\left[1 - 2\varepsilon\cos(\omega t)\right]\Phi^2 \tag{3.5}$$

Finally we derive the intermediate amplitude transverse dynamics via the Hamilton's equations, finding

$$\dot{\Phi} = \frac{\partial H^*_{h,IA}}{\partial P} = P, \tag{3.6}$$

and

$$\dot{P} = -\frac{\partial H^*_{h,IA}}{\partial \Phi} = -\lambda^2 \left[1 - 2\varepsilon\cos(\omega t)\right]\Phi \tag{3.7}$$

or, converting to second-order form by differentiating the first equation with respect to time and substituting into the second, we can write the dynamics in momentum space as

$$\ddot{\Phi} + \lambda^2 \left[1 - 2\varepsilon\cos(\omega t)\right]\Phi = 0 \tag{3.8}$$

which is in the form of the Matthieu equation (McLachlan, 1947). It is well known that this equation exhibits the phonemenon of *parametric resonance*, in which the passively stable equilibrium at $\Phi = 0$ becomes unstable for certain values of ε and ω, giving rise to solutions which grow with time.

For infinitesimal parametric perturbations (i.e. $\varepsilon \to 0$), resonance occurs when the axial forcing frequency ω is exactly an even multiple of the natural frequency λ (i.e. $\omega = 2\lambda$, $\omega = 4\lambda$, etc.). For larger perturbations ($\varepsilon > 0$), resonance occurs for a larger spread of frequencies centred on the even multiples of the natural frequency (Landau and Lifshitz, 1976; McLachlan, 1947).

In the presence of friction, larger perturbations are required to produce resonance, and the magnitude of the required perturbation grows with the forcing frequency, so that only the lower-order frequencies are practically accessible (Landau and Lifshitz, 1976; McLachlan, 1947). The most readily excited resonance is therefore the $2:1$ axial-transverse resonance. This matches experimental observations showing a roughly $2:1$ frequency ratio between peristaltic (axial) and lateral (transverse) motions in the larva (Wystrach et al., 2016).

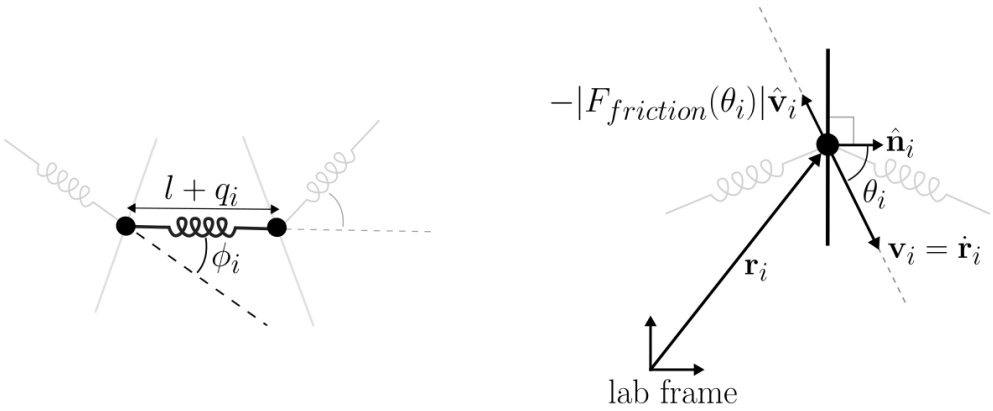

Figure 3.11: **Coordinate system and substrate interaction schematics.** Internal coordinate system used to describe deformations of the larval body (left), and quantities used to describe substrate interaction (right). The friction force $F_{friction}$ acting on the i'th segment boundary is directed opposite to that boundary's velocity vector $\mathbf{v}_i$, and has a magnitude which depends only upon the direction θ_i of the velocity vector relative to a unit vector $\hat{\mathbf{n}}_i$ aligned with the local body axis (see text). Note that $\hat{\mathbf{v}}_i = \mathbf{v}_i / \|\mathbf{v}_i\|$ denotes a unit vector aligned with the boundary's velocity vector.

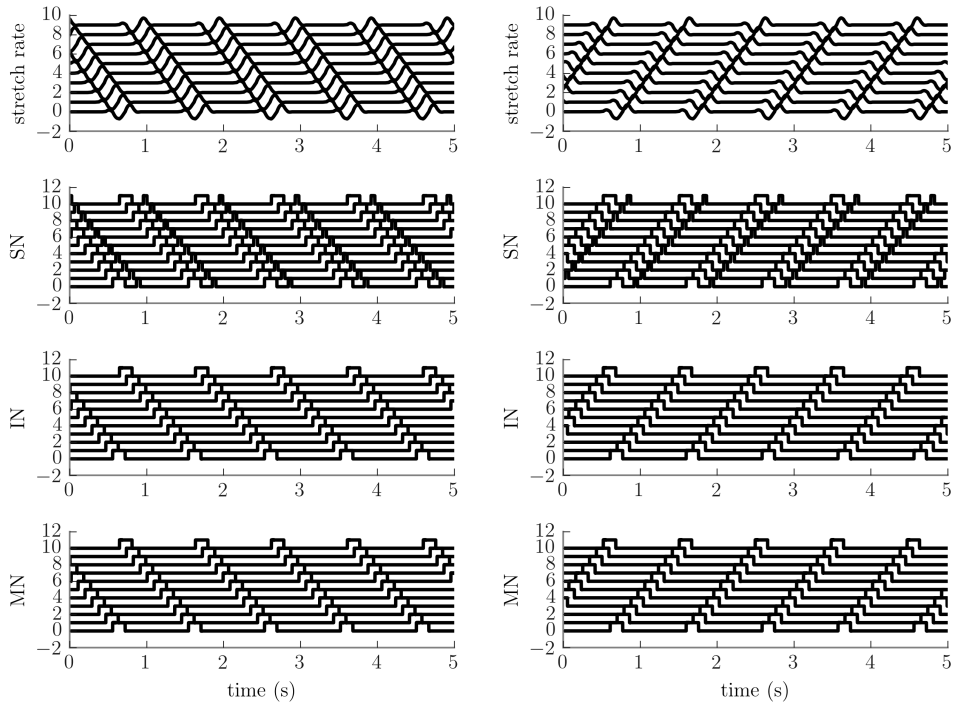

Figure 3.12: **Neural activation during peristalsis.** (from top to bottom) stretch rate, sensory neuron, interneuron, and motor neuron activation during forwards (left) and backwards (right) peristalsis.

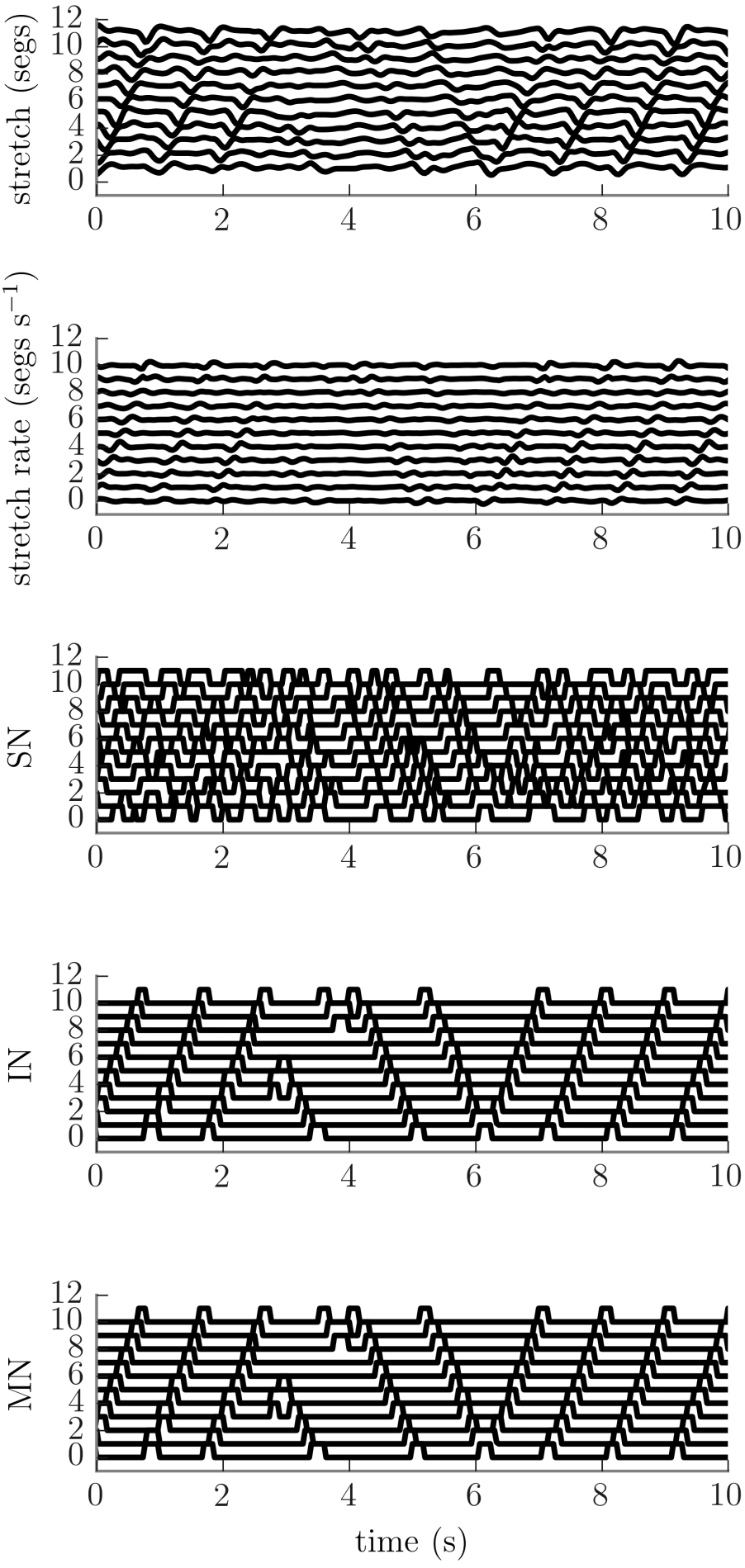

Figure 3.13: **Neural activation during planar locomotion.** (from top to bottom) stretch, stretch rate, sensory neuron, interneuron, and motor neuron activation during

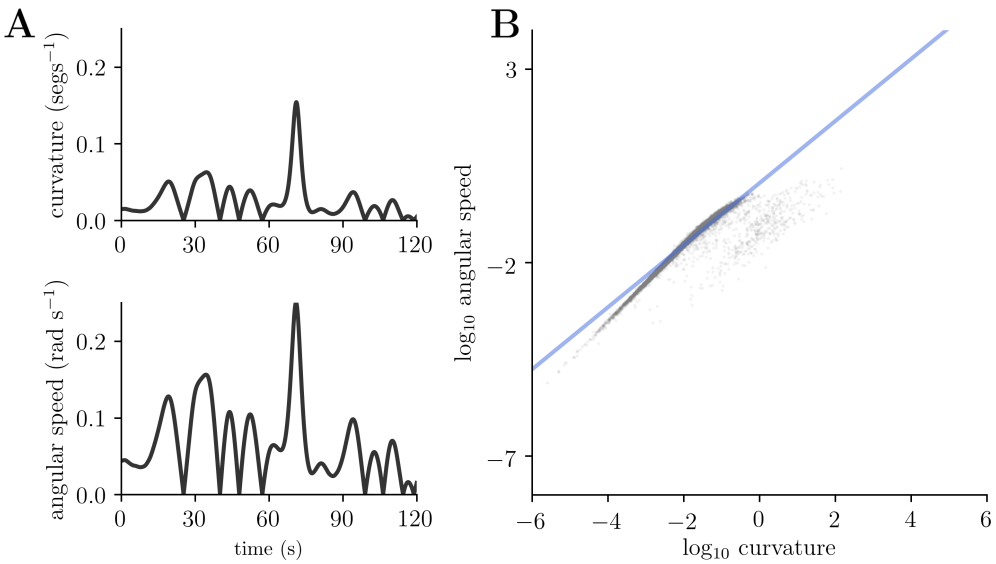

Figure 3.14: **Relationship between path curvature and angular velocity.** Model data (grey points) compared to fit by a power law with scaling exponent $\beta \approx 0.8$ (blue line, $r^2 \approx 0.94$).

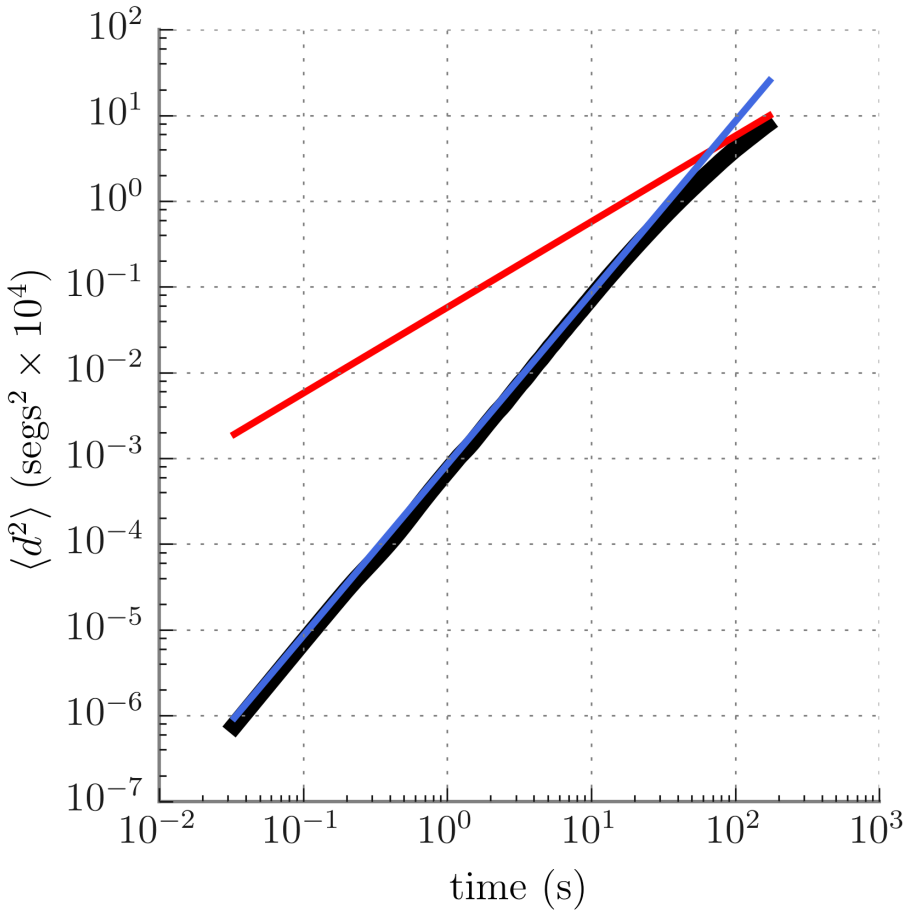

Figure 3.15: **log-log plot of mean-squared displacement.** Initial quadratic growth (blue line, slope=2) leads to asymptotic linear growth (red line, slope=1).

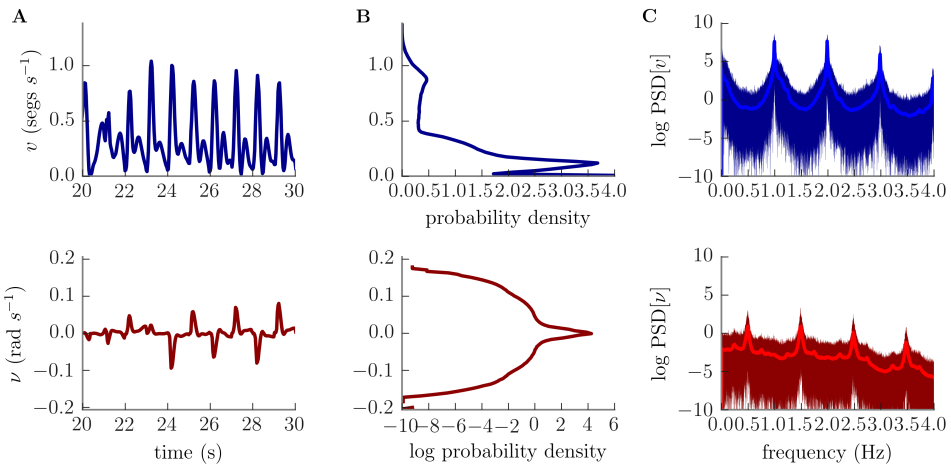

Figure 3.16: **tail speed v and head angular velocity ν during planar motion.** A: representative time series for v and ν. B: probability density of v and ν across all 1000 trials. C: individual (faint) and mean (bold) power spectra of v and ν

Chapter 4

A neuromechanical model of chemotaxis

4.1 Introduction

In this chapter, I investigate larval chemotaxis. The chapter is largely comprised of the published research paper, "A Neuromechanical Model of Larval Chemotaxis", published in Integrative and Comparative Biology (2018). This paper was co-authored by myself and Barbara Webb. I was responsible for constructing all models in this paper, analysing them, and interpreting the results. I completed the majority of the writing for this paper and prepared all figures. Barbara Webb provided project supervision and contributed writing to the introduction and discussion sections of the paper.

In this paper, I use the same neuromechanical model as was used in the previous chapter to investigate substrate exploration, but incorporate an additional transverse reflex circuit that operates to either reinforce or counteract the effects of transverse viscosity. Taxis is achieved by modifying the action of this reflex according to an instantaneous perception input, modelled as the logarithmic time derivative of the stimulus intensity experienced at the head, which is positive when the head is travelling up a sensory gradient, and negative when the head is travelling down gradient. For positive taxis, a positive perception input causes the transverse reflex to increase the effective transverse viscosity of the body, so that lateral bending motions and thus reorientation are suppressed, and the larva will tend to travel in a roughly straight line up the sensory gradient. A negative perception input causes the transverse reflex to decrease the effective transverse viscosity, facilitating lateral bending motions and reorientation, so that the larva will turn and eventually travel back up the sensory gradient. For negative

taxis, this situation is reversed – positive perception input causes the transverse reflex to decrease the effective transverse viscosity of the body, while negative perception input causes an increase in the transverse viscosity, leading to promotion of rectilinear motion when travelling down the sensory gradient and turning when travelling up gradient.

The key parameter influencing taxis behaviour in our model is referred to as *perception gain*, denoted symbolically as γ. To get a feel for the behaviour of the model, I first produce several representative trajectories for different values of the perception gain. For $\gamma > 0$ the model larvae reliably demonstrate negative taxis, while for $\gamma < 0$ the model produces positive taxis.

I then produce $N = 1000$ trajectories for each of the cases $\gamma = \pm 200$, since these parameter choices correspond to strong attraction ($\gamma = -200$) or aversion ($\gamma = 200$) behaviour, allowing the differences in these behaviours to be clearly observed. I subject the trajectories for each parameter choice to the same measures developed in the previous chapter – tortuosity, fractal dimension, and mean-squared displacement. Combined with the results from the previous chapter, our analysis ultimately suggests that our modelled taxis reflex can be interpreted as biasing an ongoing deterministic anomalous diffusion process into either superdiffusive (aversion) or subdiffusive (attraction) regimes.

I next analyse the behaviour using common measures in the literature on larval taxis, namely the body bend distribution, run length distribution, bearing-to-stimulus distribution, turn probability as a function of absolute bearing, and left-turn probability over bearing. All measures give results matching the real larva, with the exception of left-turn probability over bearing, which demonstrates a very slight preference for turning towards the stimulus during avoidance behaviour in our model, while in real larvae there is no preference.

In the discussion, I compare the model behaviour to that of the real larva and comment on the similarities between our modelled reflex circuit and the experimentally observed Eve+ interneuron circuit.

The approach taken in this chapter bears some similarity to an earlier model of *Drosophila* chemotaxis in which a descending sensory input innervated a half-center oscillator CPG driving lateral oscillatory reorientation movements (Wystrach et al., 2016), with the descending input essentially adjusting the amplitude of ongoing oscillations to produce taxis. Both the model presented in this chapter, as well as this earlier model, stand in contrast to other existing models of larval chemotaxis in which

the behaviour is produced by a decision-making architecture which biases the stochastic transition between discrete behavioural states (a review of this literature is provided in the main paper of this chapter).

More broadly, the model presented here bears similarities to a large family of earlier taxis models in which simple reflexive coupling of sensory input to motor output drives motion towards or away from a stimulus. This idea was beautifully embodied in the "Tortoise" robots, Elmer and Elsie, developed by neurobiologist William Grey Walter in the 1940's (Walter, 1953; Holland, 2003). These robots were capable of phototaxis thanks to a simple analogue coupling of a single light sensor to two drive motors. Valentino Braitenberg later discussed his hypothetical Vehicles 2a and 2b (Braitenberg, 1986), which would be capable of driving towards or away from a stimulus according to the simple connection scheme between lateralised pairs of sensors and drive motors. If the sensor on a given side of the body was wired to speed up the motor on the same side of the Vehicle and/or slow down the motor on the opposite side (configuration 2a), an increase in stimulus intensity on the side of the sensor should cause the Vehicle to turn to the opposite side, away from the stimulus. Meanwhile, if the sensor was wired to slow down the motor on the same side of the body and/or speed up the motor on the opposite side (configuration 2b), an increase in stimulus intensity on the side of the sensor should cause the Vehicle to turn towards that side, bringing it towards the stimulus.

Taxis arising from sensorimotor coupling has also been observed in biological systems, with particularly large bodies of work describing taxis behaviour in the bacteria *E. Coli* and the nematode worm *C. elegans*. In *E. Coli*, alternation between "tumble" events, which reorient the bacterium in a random new direction, and relatively straight "runs" is controlled by setting the flagellar motor in either a clockwise (tumble) or counterclockwise (run) motion according to changes in sensory input (chemical, pH, temperature, etc.). A decrease in favourable sensory input, or an increase in unfavourable sensory input, promotes clockwise rotation of the flagellum and thus biases the bacterium towards reorientation, while an increase in favourable input or decrease in unfavourable input promotes counterclockwise flagellar rotation and therefore biases the bacterium towards straight-line running. In this way the bacterium makes longer runs in the preferred direction, thus accomplishing taxis. A large body of work has detailed not only the trajectories taken by *E. coli* bacteria during taxis but also the intracellular pathways involved in the behaviour (Adler, 1966; Berg and Brown, 1972; Macnab and Koshland, 1972; Sherman et al., 1982; Qi and Adler, 1989; Greer-Phillips

et al., 2003; Hu and Tu, 2014; **?**). In *C. elegans*, a similar pattern is commonly thought to drive taxis. The nematode undergoes relatively straight movement which is interrupted by "pirouettes", in which the worm reverses and/or produces a series of sharp turns, according to sensory input (Ward, 1973; Rutherford and Croll, 1979; Pierce-Shimomura1999, 1999), producing taxis through a mechanism which is functionally very similar to that used by *E. coli*. However, on average, the nematode is observed to be pointing in the preferred direction following a pirouette manuevre, in contrast to *E. coli* in which the reorientation direction is essentially uniformly random (Berg and Brown, 1972; Pierce-Shimomura1999, 1999). Furthermore, recent work has demonstrated that the behavioural repertoire of the nematode may be better understood as a *continuum* rather than a discrete set of behavioural states (Szigeti et al., 2015).

In some sense the model of larval chemotaxis presented in this chapter resembles the models of *E. coli* and *C. elegans* taxis, in that a detected increase (decrease) in favourable (unfavourable) sensory input promotes rectilinear motion (reorientation). In contrast to *E. coli*, and similar to *C. elegans*, the larva and the model of taxis that I present is biased towards reorienting towards the stimulus source rather than producing unbiased reorientations. Furthermore, the model larva has a continuous behavioural state space, unlike those existing models of taxis in *E. coli*, *C. elegans*, and the *Drosophila* larva which rely on switching between discrete "run" and "reorientation" states. In this sense the model presented here is closer to William Grey Walter's Tortoises, Braitenberg's Vehicles, and the oscillator model of larval chemotaxis.

My choice of modelling early sensory processing by taking the logarithmic derivative of stimulus intensity is common within the literature on *Drosophila* olfaction and chemotaxis (Gomez-Marin et al., 2011; Davies et al., 2015; Kadakia and Emonet, 2019) as well as the broader sensation and taxis literature (Adler et al., 2014). Indeed, this approach is grounded in some of the earliest models developed in the field of psychophysics – the Weber-Fechner law, and in particular the Weber constrast (Fechner, 1860). The Weber constrast specifies the relationship between the perceived change in stimulus dp and the actual change in stimulus dS as

$$dp = \frac{dS}{S} \tag{4.1}$$

More recent models of *Drosophila* chemotaxis have used more realistic models of olfactory receptor neuron dynamics (which nevertheless provides a normalised derivative output which is functionally similar to that of the Weber-Fechner model) (Schulze et al., 2015). I chose to use the simpler Weber-Fechner model in order to more clearly

demonstrate the effectiveness of simple sensorimotor reflexes, and their interaction with body mechanics, for driving taxis.

In conclusion, the main contribution of this chapter is to show that a simple sensorimotor reflex is capable of driving taxis behaviours in the larva through the interaction with body mechanics and the sensory environment. The model in this chapter stands in constrast to those existing models of chemotaxis in the larva and other animals which rely on decision-making architectures and (biased) stochastic transitions between discrete behavioural states. The model in this chapter is closest to the previous work of Wystrach et al. (2016), the Vehicles of Braitenberg (1986), and the Tortoises of William Grey Walter, since these models rely on sensory input continuously driving, and being driven by, ongoing dynamical behaviour to produce a continuum of behavioural states. However, in contrast to the model presented by Wystrach et al. (2016), the model presented here produces taxis without requiring central pattern generation to drive lateral oscillations, and is instead thoroughly grounded in the chaotic mechanics of the larval body.

Main conclusions:

- The neuromuscular model from the previous chapter has been extended to include direct transverse driving forces.

- A simple reflex which modifies the local transverse viscosity of the body in response to a perception input is capable of producing negative and positive taxis.

- The transverse reflex model shows striking similarity to the experimentally observed Eve+ interneuron circuit.

Limitations:

- As in the previous chapter, the neuromuscular model does not reproduce the experimentally observed endogenous waves of activity in the absence of mechanical input, or endogenous asymmetrical activity in the thorax. I will return to these problems in the discussion chapter.

- In the real larva, sensory preferences may be learned. Our model does not include the neural circuitry required to produce learning.

4.2 Availability of software and supplementary videos

The original code used to produce all figures in this chapter has been made publicly available in a github repository (https://github.com/janeloveless/neuromech). This repository contains a multitude of projects and experiments at various degrees of completion – the scripts most relevant to this chapter are `E23_SPC_taxis.py`, `D4_taxis_analysis.py`, and `D5_taxis_animations_SICB.py`. I am happy to answer questions regarding this codebase, its dependencies, and how to install and run it on a target machine.

Supplementary videos for this chapter are available on vimeo (unbiased behaviour: https://vimeo.com/344054728, negative and positive taxis behaviour: https://vimeo.com/344067082).

4.3 Publication: A Neuromechanical Model of Larval Chemotaxis

From the symposium "Sensory feedback and animal locomotion: perspectives from biology and biorobotics" presented at the annual meeting of the Society for Integrative and Comparative Biology, January 2018, at San Francisco, CA

Research article

A Neuromechanical Model of Larval Chemotaxis

Jane Loveless* and Barbara Webb*[1]

*School of Informatics, University of Edinburgh, 10 Crichton St, Edinburgh, EH8 9AB, UK

[1]Email:B.Webb@ed.ac.uk

April 3, 2018

Synopsis

Larval Drosophila move up attractive chemical gradients, and down aversive ones. Although their movement is often characterised as a series of runs and directed turns, it can also be modelled as a continuous modulation of turning extent by the detected change in stimulus intensity as the animal moves through the gradient. We show that a neuromechanical model of peristaltic crawling and spontaneous bending in the larva can be adapted to produce taxis behaviour by the simple addition of a local segmental reflex to modulate transverse viscosity (or 'bendiness') proportionally to the intensity change detected in the head. Altering the gain produces weaker or stronger, negative or positive taxis, with behavioural statistics that qualitatively match the larva.

1 Introduction

For many animals, oriented movement along sensory gradients (taxis) is an important behaviour to locate key resources such as food or mates. Research into the underlying mechanisms often focusses on how taxis can be generated by the animal's nervous system, e.g., through a combination of inherent locomotion patterns for propulsion, and decisions to alter direction based on sensory information. An alternative view is to consider the whole animal, embedded in its environment, as a closed loop dynamical system that can maintain a consistent output but also be biased by inputs. Importantly, in this view, the biophysical system is not just the mechanical 'plant' used by the animal to execute its actions but can be a crucial part of establishing the right dynamics, by exploiting physical interactions. Similarly, this view stresses the role of the output in shaping the sensory input, potentially in just such a way as to provide the requisite input when it is needed for control.

Larval Drosophila exhibit a typical, and widely studied, taxis behaviour: moving up attractive chemical gradients, and down aversive ones (Gomez-Marin et al., 2011; Gershow et al., 2012; Khurana and Siddiqi, 2013; Gomez-Marin and Louis, 2014). They also orient with respect to light gradients, gravity and even electrical fields (Gepner et al., 2015); and in the absence of any clear stimulus directionality, perform exploratory behaviour, with apparently spontaneous changes of direction interrupting approximately straight runs (Lahiri et al., 2011; Berni, 2015). We have previously suggested that taxis could be controlled through a simple mechanism that couples the change in experienced stimulus strength directly to the amplitude of oscillation in heading direction (Wystrach et al., 2016). In the larva, this oscillation is the result of bending in the head and body segments, which alters the direction of propulsion caused by the peristaltic crawling. The larva senses odour primarily through its dorsal organ on the head (Cobb, 1999), which is thus actively propelled through the gradient. In our abstracted model, we assumed the animal maintains a constant forward speed, and has a regular left/right oscillation in heading direction. The sensed change in odour concentration due to forward or lateral movement alters the subsequent oscillation amplitude. For example, an increase in concentration, indicating motion up the gradient, decreases the oscillation so the larva maintains this heading direction; whereas a concentration decrease causes it to make larger bends and hence turn back towards the source. Notably, in this control mechanism, neither the sensing or its effect on the output is lateralised, so the 'perception' of the gradient only emerges from the animal's underlying motor pattern, and subsequently shapes this pattern, in a tightly coupled feedback loop.

Although this model suggests there may be no neural correlate of 'decisions to turn' in the larva, it nevertheless assumed the underlying locomotor pattern is produced by inherent control, e.g., a central pattern generator (CPG) circuit for the lateral oscillation.

More recently, we have used a biomechanical model of the larva's segmented body to explore how peristaltic crawling and lateral bending might emerge without explicit neural generation of the underlying patterns (Loveless et al., in review). We treat the segments as discrete point masses interacting via damped translational and torsional springs, and show that using simple local reflexes to enhance the passive mechanics of the system leads to the emergence of coordinated peristaltic crawling (forward or backward) and spontaneous (chaotic) body bending. The resulting system, given frictional interaction with a substrate, produces behaviour that closely resembles exploratory crawling in the larva.

In this paper, we augment this biomechanical model with a taxis reflex, following the same simple control concept as the previous abstracted model. That is, we use the change of sensory input at the head segment to influence, with a particular gain, the amplitude of the ongoing bend in each segment. The production of bends remains a purely emergent property of the mechanics without any neural control. We show that this is sufficient to produce positive or negative taxis in the simulated agent, depending on the sign of the gain, and stronger or weaker taxis depending on the size of the gain. We discuss similarities and differences from taxis behaviour in real larva.

2 Methods

2.1 Neuromechanical model

The work presented here builds on an existing model of larval crawling, described in detail in (Loveless et al., in review). We here provide an overview of the model, but refer readers to that paper for detailed specification (see appendix S1), justification and analysis. The model describes the motion of the midline of the larval body in the plane using 12 points that represent the boundaries between body segments and the head and tail extremities. Each point is treated as an identical mass, and each is linked to adjacent points with linear translational and torsional springs in parallel with linear dampers in a Kelvin-Voigt arrangement (Fung, 1993), to represent elasticity in the soft cuticle of the larva (Figure 1. The current body configuration can thus be expressed as a set of axial stretches q_i (the difference in length of the ith segment from its length at equilibrium) and transverse bending angles between segments ϕ_i. The head and tail are additionally linked, representing the effect of the incompressible internal coelemic fluid of the larva, by maintaining a constant overall length. Without friction, the passive mechanics of this system produce axial and transverse standing waves, i.e., coordinated motions of the segments that resemble peristalsis and body bends.

We assume there is sliding friction between the larval body and the substrate, and energy is also lost to viscous friction within the body during both axial compression/extension

and transverse bending. We allow power flow due to muscle activation, controlled by two reflexes (figure 1). The first is local to each segment and acts to overcome the effects of friction, by activating whenever a segment is compressing, producing a muscle tension that amplifies the compression. The axial tension Q_i in the i'th segment produced by this reflex is given in terms of the local stretch rate $\dot{q}_i$ and local axial reflex gain b_i as

$$Q_i = \begin{cases} -b_i, & \text{if } \dot{q}_i < 0 \\ 0, & \text{if } \dot{q}_i \geq 0 \end{cases} \tag{1}$$

The second neural circuit is a mutual inhibition between non-adjacent segments (the head and tail are treated as adjacent) that restricts the active compression to a small number of segments at any time. This enables acceleration of the center of mass relative to the substrate, i.e., peristaltic crawling (Ross et al., 2015; Alexander, 2003; Loveless et al., in review). Due to energetic coupling of axial and transverse motion, through the body mechanics, the model also produces spontaneous body bending, which reorients the crawling direction, i.e., turning occurs without any explicit neural control.

This emergent turning produces a 'random' (actually a deterministically chaotic) exploration of the 2D plane. To convert the resulting exploration into taxis, we note that the larva should travel in a roughly straight line while going up an attractive gradient, or while going down an aversive gradient, and that the larva should tend to reorient when it is going down an attractive gradient, or going up an aversive gradient. In other words, the extent of the body bending should be linked to the changing perceptual experience. We can affect bending by altering the effective physics of the body: specifically, we reason that an effective increase in transverse viscosity should lead to a damping of transverse motion and a corresponding tendency towards straight line motion, while an effective decrease in transverse viscosity should reduce the damping of transverse motion and therefore tend to encourage bending and reorientation. We thus posit the following local segmental reflex for transverse motion:

$$\tau_i = c_i \tanh(\beta \dot{\phi}_i) \tanh(\gamma P(t)) \tag{2}$$

where τ_i is the torque applied about the i'th segment boundary, $P(t)$ is the time-varying perception input (defined below), β is an angular velocity gain, γ is a perception gain, and c_i is an overall reflex gain for the i'th segment boundary. We limit the choice of parameters by setting $\beta > 0$ and $c_i > 0$, so that the sign of the torque is determined by γ.

The rationale of our reflex model can be understood by splitting it into two factors. The first factor $c_i \tanh(\beta \dot{\phi}_i)$ represents (saturating) feedback of the local angular velocity. The torque resulting from this first factor only should act in the same direction as the angular velocity, opposing the torque produced by transverse friction, and thereby reducing

the effective transverse viscosity of the body. Following this line of reasoning, we choose to set the local reflex gain c_i to be dependent upon the local transverse viscosity $\eta_{t,i}$

$$c_i = c\frac{\eta_{t,i}}{\max_i \eta_{t,i}} \tag{3}$$

where normalisation by $\max_i \eta_{t,i}$ is intended to nondimensionalise the transverse viscosity, allowing the new *global* reflex gain parameter c to have dimensions of torque. In practise we set $c = 1$ for simplicity, leaving

$$c_i = \frac{\eta_{t,i}}{\max_i \eta_{t,i}} \tag{4}$$

so that the reflex torque becomes

$$\tau_i = \frac{\eta_{t,i}}{\max_i \eta_{t,i}}\tanh(\beta\dot{\phi}_i)\tanh(\gamma P(t)) \tag{5}$$

The second factor $\tanh(\gamma P(t))$ acts to modulate the change in effective transverse friction based on perception. If this factor is positive, the overall effect of the reflex is to reduce effective transverse viscosity, while if it is negative the effect is reversed and effective transverse viscosity increases. If the overall feedback torque is small (e.g. if β, γ, or c are relatively close to zero) then the perception input will have a small effect on the transverse viscosity, while if the overall feedback torque is large there is the possibility for the perception input to have a large effect on the transverse viscosity. This provides an interpretation of the perception gain γ as a preference parameter – if the absolute value of γ is large, the model larva should show a strong behavioural response to the stimulus, while for small γ the behavioural response may be weak. Furthermore, following our arguments above, if $\gamma > 0$ we expect an aversive response, while for $\gamma < 0$ we expect an attractive response. We note a further expectation that the strength of the behavioural response when $\gamma \gg 1$ may be diminished due to saturation of the second factor in Eq. 2 and a corresponding inability to distinguish small changes in perception – in this case, the second factor can only detect whether the head is travelling up or down gradient, but not how strong the local gradient is.

2.2 Perceptual model

We model the larva as moving within an exponential stimulus field centred on the origin of our cartesian coordinate frame

$$S = A_s e^{-\lambda_s \|\mathbf{r}\|} \tag{6}$$

where A_s is a parameter which sets the absolute intensity of the stimulus field, and λ_s sets the rate at which the stimulus decays away from the origin, while $\mathbf{r}$ is the radius

vector from the origin to the site of measurement of the stimulus. In practice, we take $\mathbf{r}$ to be the radius vector from the stimulus source to the model larva's head, since this is the location of most of the sensory organs involved in taxis.

The early stages of sensory processing in the larva tend to respond strongly to changes in stimulus intensity more than to the absolute stimulus intensity, and show a normalised response across a range of absolute stimulus intensities. Following (Davies et al., 2015), we model the output of the early stages of sensory processing as a "perception" signal given by

$$P = \frac{1}{S}\frac{\mathrm{d}S}{\mathrm{dt}} \tag{7}$$

Denoting the coordinates of the larva's head as $\mathbf{r} = [x, y]^T$ and the linear velocity of the larva's head as $\dot{\mathbf{r}} = [\dot{x}, \dot{y}]$, this becomes

$$P = \frac{1}{S}\left(\frac{\partial S}{\partial x}\dot{x} + \frac{\partial S}{\partial y}\dot{y}\right) = \frac{1}{S}\nabla S \cdot \dot{\mathbf{r}} \tag{8}$$

substituting the expression for the exponential stimulus field given above, we find

$$\nabla S = -\frac{A_s \lambda_s}{\sqrt{x^2 + y^2}}[x, y]^T \tag{9}$$

so that

$$P = -\lambda_s \frac{x\dot{x} + y\dot{y}}{\sqrt{x^2 + y^2}} = -\lambda_s \frac{\mathbf{r} \cdot \dot{\mathbf{r}}}{\|\mathbf{r}\|} = \lambda_s \|\dot{\mathbf{r}}\| \cos\theta \tag{10}$$

where θ is the angle between the head's velocity vector $\dot{\mathbf{r}}$ and the vector pointing from the head position to the origin $-\mathbf{r}$. As expected, P is positive when the larva is travelling up the sensory gradient ($\|\theta\| < \pi/2$), negative when the larva is travelling down the sensory gradient ($\|\theta\| > \pi/2$), and has a magnitude which depends on both the speed at which the head is travelling and on the bearing of the head to the odor source. Note that due to normalisation of the sensory input, the absolute intensity parameter A_s has no effect on the perception signal.

Substituting this definition of P into to the transverse reflex equation 2, we have

$$\tau_i = \frac{\eta_{t,i}}{\max_i \eta_{t,i}} \tanh(\beta\dot{\phi}_i) \tanh(\gamma\lambda_s \|\dot{\mathbf{r}}\| \cos\theta) \tag{11}$$

which makes it clear that there is some redundancy in the parameters γ and λ_s, so that we may set $\lambda_s = 1$ without loss of generality. This leaves two free parameters in the transverse reflex model, β and γ. We choose to set $\beta = 1000 \gg 1$ so that the factor $\tanh(\beta\dot{\phi}_i)$ saturates to ± 1, matching our binary-valued axial reflex (Equation 1). This leaves us to explore possible values of the perception gain / preference parameter γ.

We set all mechanical parameters and the parameters for the axial reflex circuits to

the values chosen in our previous paper (Loveless et al., in review), with the exception of the transverse viscosity $\eta_{t,i}$ which has been set to twice its previous value. This choice was made in order to more clearly demonstrate the action of the transverse reflex on the model behaviour.

3 Results

In figure 3 we show some representative trajectories generated by our taxis model (see also supplementary videos). In each case the larva starts at the peak of the gradient. For positive gains it crawls away, eventually exiting the space. For negative gains, it consistently loops back towards the peak, with the extent of excursions decreasing as the strength of the gain is increased.

To analyse the behaviour of our taxis model, we generated $N = 1000$ trajectories for each of the cases $\gamma = \pm 200$. As expected the larvae with $\gamma = -200$ showed a strong approach behaviour, remaining localised near the peak of the stimulus field (Fig 4A), while larvae with $\gamma = 200$ showed strong avoidance behaviour, following fairly direct paths away from the peak (Fig 4B).

We first quantified the paths of the simulated larvae using the same methods we applied to the unbiased exploratory paths presented in our previous paper Loveless et al. (in review). Paths in the approach group ($\gamma = -200$) had a high tortuosity and fractal dimension (mean tortuosity = 0.72, mean fractal dimension = 1.51) relative to the avoidance group ($\gamma = 200$, mean tortuosity = 0.11, mean fractal dimension = 1.22; Fig 4C), indicating that approach paths tended to be plane-filling and less linear than avoidance paths (Benhamou, 2004). In accordance with these results, the mean-squared displacement measured within the avoidance group followed an approximately quadratic growth across the duration of the entire experimental trial, typical of rectilinear motion, whereas the approach group showed an initial quadratic growth followed by linear and then sub-linear growth (Fig 4D). We previously found that our model of unbiased exploration produced initially quadratic growth of the mean-squared displacement, followed by asymptotic linear growth (Loveless et al., in review), as has also been observed during unbiased exploration in the real larva (Jakubowski et al., 2012; Gunther et al., 2016). This suggests that our modelled taxis reflex can be interpreted, at the population level, as biasing an ongoing deterministic anomalous diffusion process into either superdiffusive ($\gamma > 0$, quadratic growth) or subdiffusive ($\gamma < 0$, sub-linear growth) regimes.

The distribution of body bending angles (Fig 4E) shows that the modelled larvae take on "straighter" configurations during avoidance behaviour (mean = 4.6×10^{-3} deg, variance = 75.5 deg^2, kurtosis = 13.17) , and tend to take on larger curvatures during approach behaviour (mean = 0.11 deg, variance = 853.52 deg^2, kurtosis = 1.94) , in accordance with the rationale for our taxis reflex model and in agreement with the shape

of paths taken by the two groups. During both avoidance and approach, the body bend distribution is symmetric (avoidance skewness = 0.02, approach skewness = 0.07) and centred around 0 (avoidance mean = 4.6×10^{-3} deg, approach mean = 0.11 deg), demonstrating that larvae are not, on aggregate, biased towards bending either to the left or the right.

The run length distribution of both avoidance and approach groups is well fit by an exponential, but avoidance behaviour is biased towards longer runs when compared to approach behaviour (avoidance time constant = 44.49 seconds, approach time constant = 10.67 seconds; Fig 4F), as is also seen in the real larva during thermotaxis (Luo et al., 2010).

We also analysed the behaviour of our model using three measures which are common in the extant literature on taxis behaviour. These measures depend upon the *bearing* angle between our larva's centre of mass velocity and the local gradient of the stimulus field.

First, we examined the overall distribution of bearing angles for our simulated larvae (Fig 4G). Similar to results for the real larva (Wystrach et al., 2016), the bearing distribution for avoidance behaviour was unimodal, symmetric, and centred on 180°, and fell to zero outside of the range $[90°, 270°]$, corresponding to travel directly away from the stimulus peak. In contrast, the bearing distribution for approach behaviour was trimodal, with a pair of large, symmetric peaks centred close to 90° and 270° and a single shallow peak at 180°. This corresponds to a large amount of time spent "spiralling" towards the stimulus peak, with the peak located directly to the left or right of the animal.

Next, we computed the probability density of turns (defined to occur at the onset of a body bend $> 20°$) across absolute bearing angle (Fig 4H). Both approach and avoidance behaviours showed a monotonic increase in turn probability as absolute bearing increased from 0° (bearing towards stimulus peak) to 180° (bearing away from stimulus peak). Similar to the real larva (Davies et al., 2015), the turn probability for approach behaviour in our model showed a roughly sigmoid shape, with greater probability assigned to intermediate bearings ($\sim 90°$) and less to large bearings ($\sim 180°$) than during avoidance behaviour, which followed a roughly exponential distribution.

Finally, we measured the probability of the larva turning to the left rather than right side, across bearing angles (Fig 4I). The model larvae exhibiting approach behaviour showed a strong bias for turning towards the stimulus peak (probability of left turn < 0.5 for bearing $\in (0°, 180°)$, probability of left turn > 0.5 for bearing $\in (180°, 360°)$), which is similar to results for the real larva (Davies et al., 2015). Model larvae exhibiting avoidance behaviour showed a much weaker bias, though perhaps surprisingly, in the same direction. For real larvae this curve appears flat for aversive behaviour.

4 Discussion

Behaviour emerges from the coupling of brains and bodies. We have combined a model of segmented larval biomechanics with a simple, non-lateralised reflex and shown this can produce directed taxis up or down a sensory gradient. The key mechanism is to modulate spontaneous mechanically-driven bending by adjusting transverse viscosity in each segment proportionally to the immediately perceived change in stimulus intensity. By altering the gain factor, the behaviour produced can be stronger or weaker attraction (with negative gain) or stronger or weaker aversion (with positive gain). That is, if an increase in the sensory signal is coupled to a damping of transverse motion, the larva will tend to go straight when going up a gradient and reorient more when going down it, ultimately leading it towards the sensory source, and vice versa for the opposite signal-damping coupling.

We note that, for the values of negative gain examined here, this mechanism tends to produce 'orbiting' behaviour with the sensory source predominantly at around 90 degrees to the larva, while for positive gain larvae display dispersive behaviour with the source remaining behind the larva. Similar distributions of bearing angles are observed for real larva (Wystrach et al., 2016). Indeed, our model also qualitatively reproduces the distribution of run durations observed during approach and avoidance (Luo et al., 2010), as well as the experimentally observed distributions of turn probability and left-turn probability over bearing angle (Davies et al., 2015)

Several of these characteristics have been captured in previous models of larval chemotaxis. In (Davies et al., 2015), the probability of transition from a 'run' to a 'turn' was altered by the change in odour intensity, and a similar approach coupled to a more realistic model of olfactory sensory neuron responses in (Schulze et al., 2015). In (Wystrach et al., 2016) it was proposed that the distinction between runs and turns be replaced by a continuum of smaller or larger oscillations in heading direction, and shown that this could replicate many aspects of the behaviour without requiring 'decisions' to turn. The current model is in the spirit of this latter approach, but dispenses with any need to posit an underlying CPG to generate body bends, as these emerge spontaneously from the inherent dynamics of forward crawling in coupled segments (Loveless et al., in review). As such, if 'turns' are identified with larger bends, then their chaotic generation can replace the probabilistic approach of the earlier models and the distinction between these explanations becomes less marked.

Although the presented model uses direct control of torque to counter or reinforce the effects of transverse viscosity, a biologically plausible means to achieve this effect would be a neural reflex circuit that couples the muscles on one side of a body segment to proprioceptive sensory neurons on the opposite side (see figure 2). The effective transverse viscosity will be increased if muscles on one side of the body contract while the opposite

side is shortening, while the effective viscosity will be decreased if muscles contract while the opposite side is lengthening. The EL neurons reported in (Heckscher et al., 2015) appear to be a possible substrate for this function. We then need only add a general signal (to all segments) that modulates the action of this local reflex. Neurons that run throughout the ventral nerve cord and connect the brain to all segments have been identified (Fushiki et al., 2016). It is also of interest that a small set of neurons in the brain's premotor subesophgeal zone appear to directly affect the production of large reorientations (high head angular speeds) in larva, with the same effects observed for taxis in odour, light and temperature gradients (Tastekin et al., 2015). Finally, we note that the action of the local reflex could be enhanced by the presence of reciprocal inhibition, acting to relax the muscles on one side of the body while those on the other side contract – such inhibitory pathways are a common feature in the spinal reflexes of jointed animals, including humans (Purves et al., 2004).

Acknowledgements

References

R. M. Alexander. *Principles of Animal Locomotion*. Princeton University Press, 1 edition, 2003. ISBN 9781400849512.

Simon Benhamou. How to reliably estimate the tortuosity of an animal's path: straightness, sinuousity, or fractal dimension? *Journal of Theoretical Biology*, 229:209–220, 2004. doi: 10.1016/j.jtbi.2004.03.016.

Jimena Berni. Genetic Dissection of a Regionally Differentiated Network for Exploratory Behaviour in *Drosophila* Larvae. *Current Biology*, 25:1319–1326, 2015. doi: 10.1016/j.cub.2015.03.023.

M. Cobb. What and how do maggots smell? *Biological Reviews*, 74(4):425–459, 1999.

Alex Davies, Matthieu Louis, and Barbara Webb. A Model of *Drosophila* Larva Chemotaxis. *PLOS Computational Biology*, 11(11):1–24, 2015. doi: 10.1371/journal.pcbi.1004606.

Y. Fung. *Biomechanics: Mechanical Properties of Living Tissues*. Springer-Verlag New York, 2 edition, 1993. ISBN 978-0-387-97947-2.

Akira Fushiki, Maarten F. Zwart, Hiroshi Kohsaka, Richard D. Fetter, Albert Cardona, and Akinao Nose. A circuit mechanism for the propagation of waves of muscle contraction in *Drosophila*. *eLife*, 5:e13253, 2016. doi: 10.7554/eLife.13253.

Ruben Gepner, Mirna Mihovilovic Skanata, Natalie M Bernat, Margarita Kaplow, and Marc Gershow. Computations underlying *Drosophila* photo-taxis, odor-taxis, and multi-sensory integration. *eLife*, 4:e06229, 2015. ISSN 2050-084X. doi: 10.7554/eLife.06229.

Marc Gershow, Matthew Berck, Dennis Mathew, Linjiao Luo, Elizabeth A. Kane, John R. Carlson, and Aravinthan D. T. Samuel. Controlling airborne cues to study small animal navigation. *Nature Methods*, 9(3):290–296, 2012. doi: 10.1038/nmeth.1853.

Alex Gomez-Marin and Matthieu Louis. Multilevel control of run orientation in *Drosophila* larval chemotaxis. *Frontiers in Behavioral Neuroscience*, 8(38):1–14, 2014. doi: 10.3389/fnbeh.2014.00038.

Alex Gomez-Marin, Greg J. Stephens, and Matthieu Louis. Active sampling and decision making in *Drosophila* chemotaxis. *Nature Communications*, 2(441):1–10, 2011. doi: 10.1038/ncomms1455.

Maximilian N. Gunther, Nettesheim Guilherme, and George T. Shubeita. Quantifying and predicting *Drosophila* larvae crawling phenotypes. *Scientific Reports*, 6:1–10, 2016. doi: 10.1038/srep27972.

Ellie S. Heckscher, Aref Arzan Zarin, Serge Faumont, Matthew Q. Clark, Laurina Manning, Akira Fushiki, Casey M. Schneider-Mizell, Richard D. Fetter, James W. Truman, Maarten F. Zwart, Matthias Landgraf, Albert Cardona, Shawn R. Lockert, and Chris Q. Doe. Even-Skipped^{+} Interneurons Are Core Components of a Sensorimotor Circuit that Maintains Left-Right Symmetric Muscle Contraction Amplitude. *Neuron*, 88:314–329, 2015. doi: 10.1016/j.neuron.2015.09.009.

Brandon R. Jakubowski, Rafael A. Longoria, and George T. Shubeita. A high throughput and sensitive method correlates neuronal disorder genotypes to Drosophila larvae crawling phenotypes. *Fly*, 6(4):303–308, 2012. doi: 10.4161/fly.21582.

S. Khurana and O. Siddiqi. Olfactory responses of drosophila larvae. *Chemical Senses*, 38(4):315–323, 2013.

Subhaneil Lahiri, Konlin Shen, Mason Klein, Anji Tang, Elizabeth Kane, Marc Gershow, Paul Garrity, and Aravinthan D. T. Samuel. Two alternating motor programs drive navigation in *Drosophila* larva. *PLOS ONE*, 6(8):e23180, 2011. ISSN 1932-6203. doi: 10.1371/journal.pone.0023180.

J. Loveless, K. Lagogiannis, and B. Webb. Modelling the mechanics of exploration in larval *Drosophila*. *PLOS Computational Biology*, in review.

Linjiao Luo, Marc Gershow, Mark Rosenzweig, KyeongJin Kang, Christopher Fang-Yen, and Paul A. Garrity. Navigational Decision Making in *Drosophila* Thermotaxis. *The Journal of Neuroscience*, 30(12):4261–4272, 2010. doi: 10.1523/JNEUROSCI.4090-09.2010.

D. Purves, G. J. Augustine, D. Fitzpatrick, W. C. Hall, A. LaMantia, J. O. McNamara, and S. M. Williams, editors. *Neuroscience*. Sinauer Associates, Inc., 3 edition, 2004.

Dylan Ross, Konstantinos Lagogiannis, and Barbara Webb. *A Model of Larval Biomechanics Reveals Exploitable Passive Properties for Efficient Locomotion*, pages 1–12. Springer International Publishing, 2015. doi: 10.1007/978-3-319-22979-9_1.

Aljoscha Schulze, Alex Gomez-Marin, Vani G Rajendran, Gus Lott, Marco Musy, Parvez Ahammad, Ajinkya Deogade, James Sharpe, Julia Riedl, David Jarriault, Eric T Trautman, Christopher Werner, Madhusudhan Venkadesan, Shaul Druckmann, Vivek Jayaraman, and Matthieu Louis. Dynamical feature extraction at the sensory periphery guides chemotaxis. *eLife*, 4:e06694, 2015. ISSN 2050-084X. doi: 10.7554/eLife.06694.

Ibrahim Tastekin, Julia Riedl, Verena Schilling-Kurz, Alex Gomez-Marin, James W Truman, and Matthieu Louis. Role of the subesophageal zone in sensorimotor control of orientation in drosophila larva. *Current Biology*, 25(11):1448–1460, 2015.

A. Wystrach, K. Lagogiannis, and B. Webb. Continuous lateral oscillations as a core mechanism for taxis in *Drosophila* larvae. *eLife*, 5:e15504, 2016. doi: 10.7554/eLife.15504.

5 Figure Captions

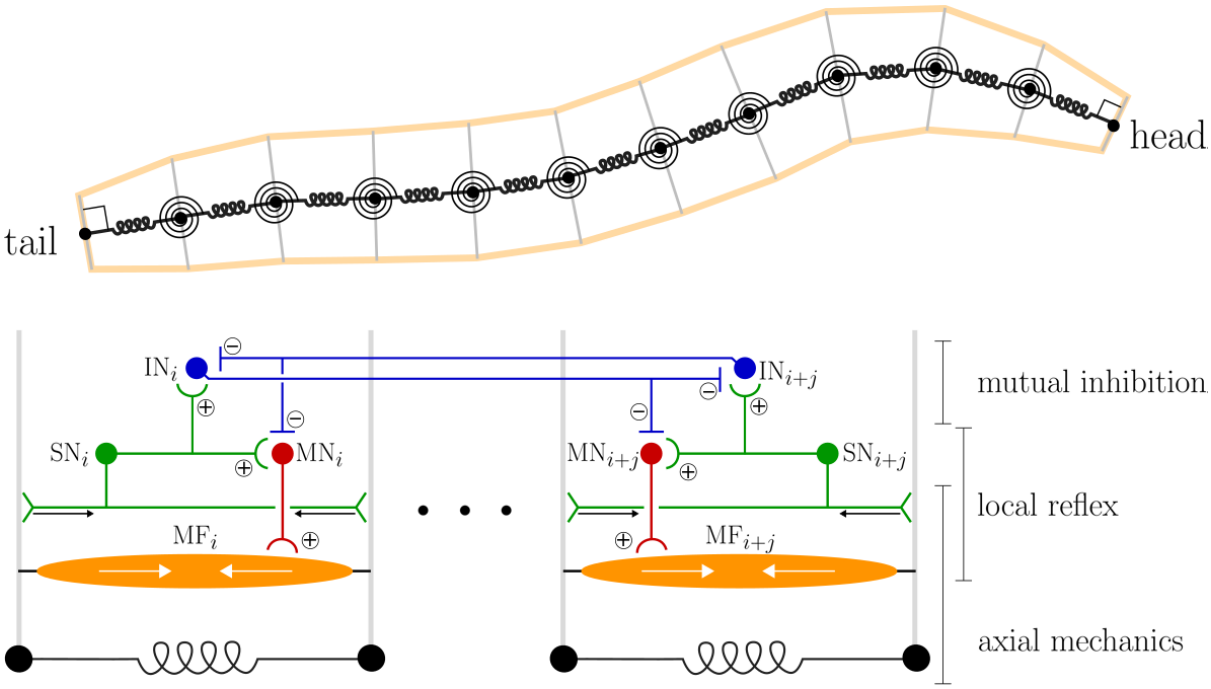

Figure 1: **(reprinted from) The larva is represented by a mechanical model (top) of its midline with 11 segments. The boundaries between segments are treated as point masses linked by linear translational and torsional springs in parallel with linear dampers in a Kelvin-Voigt arrangement Fung (1993). The controller (bottom) uses positive feedback within each segment (green) to counteract friction and distant inhibition (blue) between non-adjacent segments to create a coherent peristaltic wave of contraction capable of driving locomotion. The mechanics produce spontaneous body bending without any explicit neural control.**

$$\uparrow \text{attractive stim.} \quad \textit{or} \quad \downarrow \text{aversive stim.} \Rightarrow \uparrow \text{bending viscosity} \Rightarrow \downarrow \text{bending / turning}$$

$$\downarrow \text{attractive stim.} \quad \textit{or} \quad \uparrow \text{aversive stim.} \Rightarrow \downarrow \text{bending viscosity} \Rightarrow \uparrow \text{bending / turning}$$

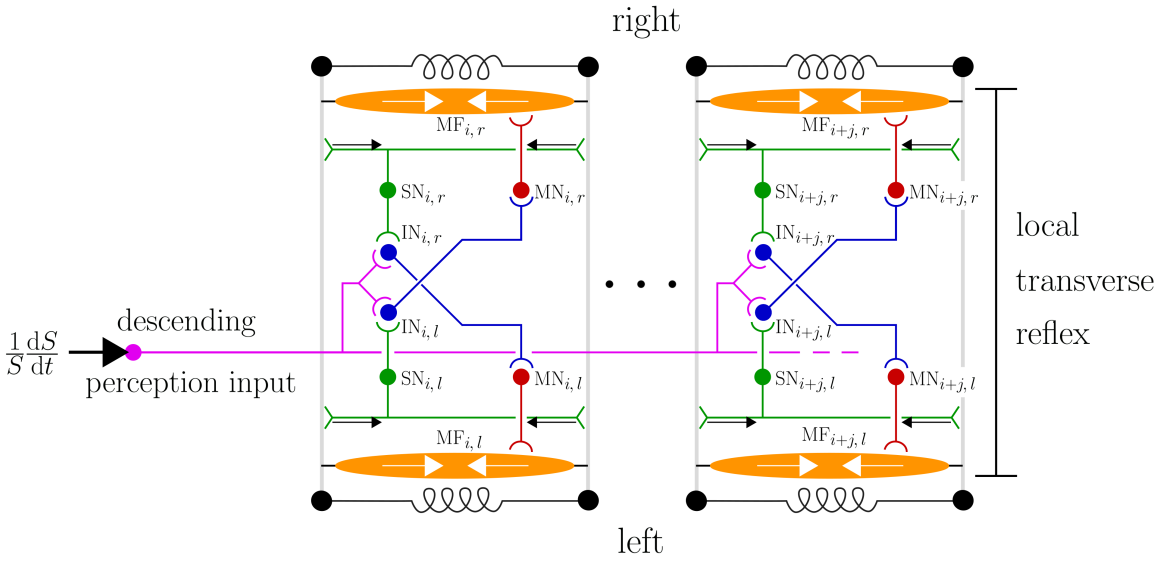

Figure 2: **taxis is achieved by increasing (decreasing) transverse viscosity during favourable (unfavourable) stimulus conditions, thus leading to decreased (increased) bend/turn amplitude (top panel). This could be achieved through descending chemosensory innervation of a segmentally localised contralateral reflex acting to modulate the effective local transverse viscosity (bottom panel, see text).**

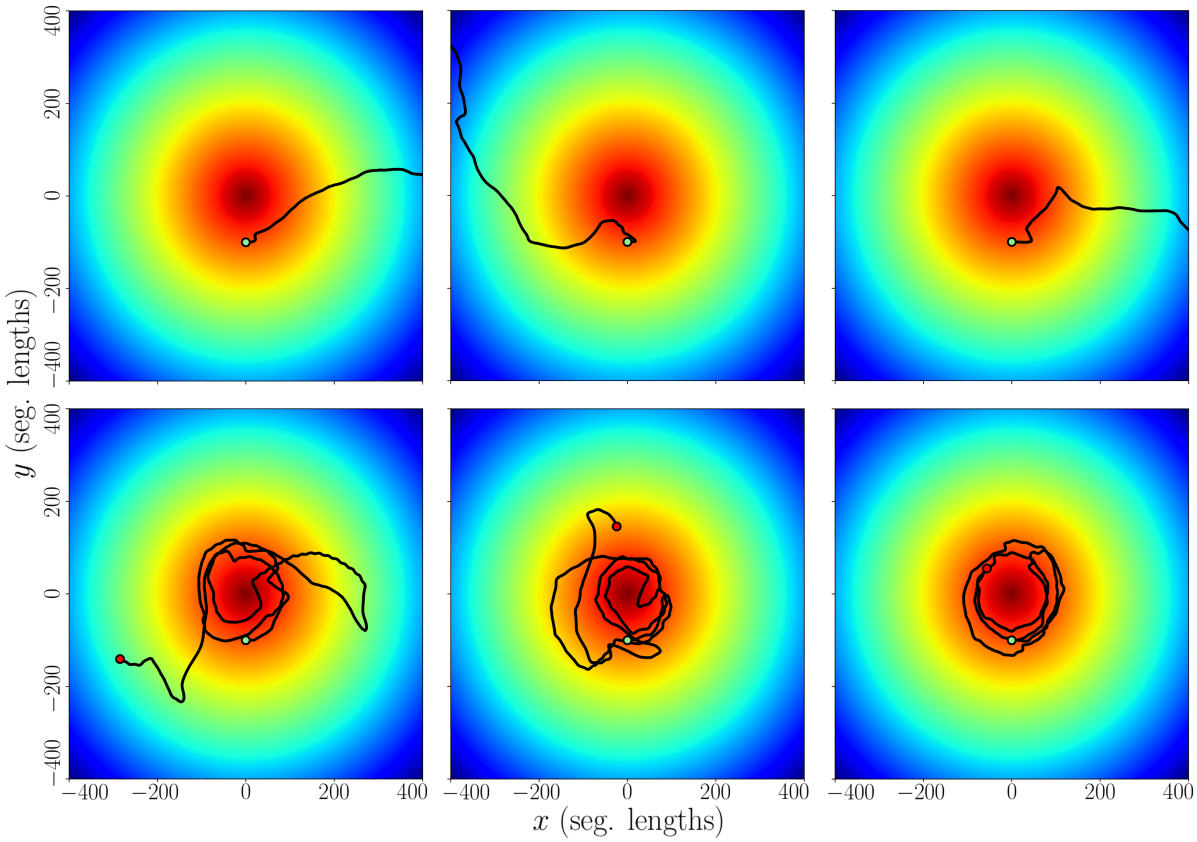

Figure 3: **decreasing the perception gain / preference parameter γ causes the model larvae to exhibit increasingly attractive behaviour. Representative trajectories are shown for $\gamma = 1000, 200, 100$ (aversive behaviour, top row, left-to-right) and $\gamma = -100, -200, -1000$ (attractive behaviour, bottom row, left-to-right). Trajectories start at the green circle, end at the red circle (larvae doing negative taxis escaped the area shown), and are superimposed on a colormap of the log stimulus intensity.**

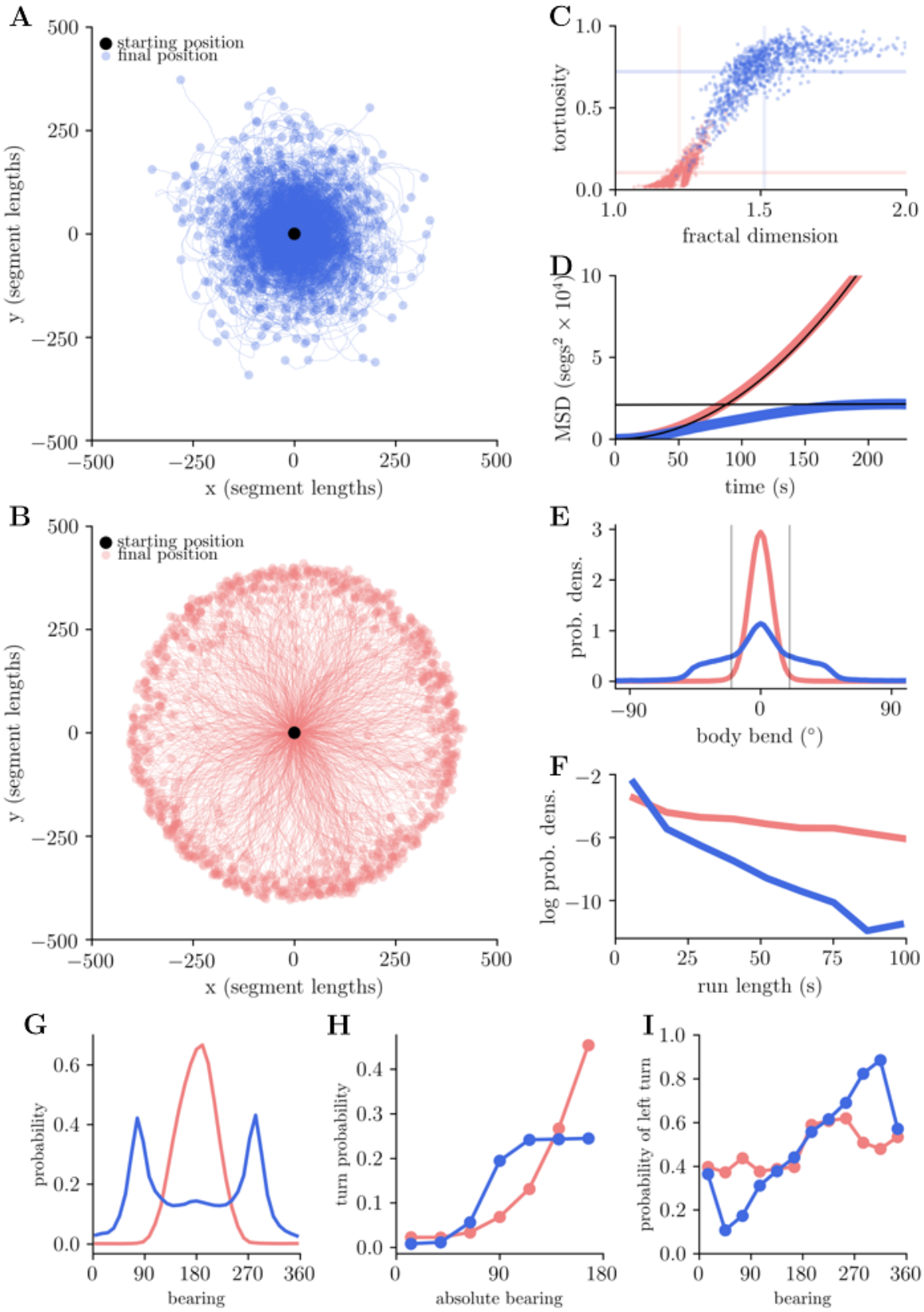

Figure 4: **Analysis of positive ($\gamma = -200$) and negative ($\gamma = 200$) taxis behaviour in N = 1000 simulated larvae. A: centre of mass trajectories for the simulated larvae during positive taxis. B: trajectories during negative taxis. Larvae started from almost identical configurations but with random orientation. C: larval paths show higher tortuosity and fractal dimension during positive taxis (blue) compared to negative taxis (red; horizontal lines = mean tortuosity, vertical lines = mean dimension), indicating rectilinear motion during negative taxis and plane-filling motion during positive taxis. D: mean-squared displacement shows asymptotic quadratic growth (red) during negative taxis**

Chapter 5

Energetic considerations in soft robotics

5.1 Introduction

In this chapter, I discuss the utility of an energy-based approach to modelling and controlling soft robotic systems.

The chapter is largely comprised of the published opinions paper, "Controlling and Simulating Soft Robotic Systems: Insights from a Thermodynamic Perspective", published in Soft Robotics (2016). This paper was co-authored by myself (under my previous name, Dylan Ross), Markus Nemitz, and Adam Stokes. I was responsible for describing the bond graph/port-Hamiltonian modelling framework contained within the paper, as it pertains to soft robotics, for developing the appendices providing examples of this modelling framework in action, and for both supervising and taking part in the writing process. Adam Stokes provided project supervision, expert knowledge on existing soft robotic systems and design processes, and took part in the writing process for the main paper. Markus Nemitz prepared most of the figures in the main paper.

Design of soft robotic systems is most often conducted through a process of experimental trial-and-error, while traditional "hard" robotics benefits from the power of computer simulation within the design process.

One of the main barriers to designing soft robots is the fact that the systems themselves include components or mechanisms ranging across a very wide range of physical domains, e.g. mechanical, electromagnetic, and chemical domains. It is very difficult to build a single dynamical model describing the behaviour of a soft robotic system

that includes all of these domains.

Within the paper I argue for the adoption of a modelling approach based upon bond graph schematics and the port-Hamiltonian framework. These tools are energy-based – they treat the energy storage within components and the power flow between components as the primary quantities of interest during the modelling process, from which the dynamics of a system are then mathematically derived. Because energy is a "common currency" between different physical domains, this allows simultaneous modelling of all components of a soft robotic system.

By focusing on energy and power during the modelling and design process, the suggested approach also allows the roboticist to immediately gain intuition on the efficiency of a system. Furthermore, the approach can guide the development of sensors for a robotic system, by elucidating which quantities are of particular interest from an energetic perspective.

In many ways the approach suggested in this chapter is inspired by the work in chapters 2, 3, and 4. In the previous chapters I took an energy-focused approach to studying the behaviour of the *Drosophila* larva. The mechanical energy stored in the larva's body was explicitly treated as a primary quantity of interest during model construction in chapter 3, and in designing neural/control systems to interface with the larva's body I have been principally concerned with the energy losses due to friction and the power flow into the body from the musculature. By focusing on energy and power flow, it became clear that the larva should be concerned with sensing the rate at which its body segments were shortening, in order to produce peristalsis and exploration, and should be concerned with the rate at which body segments were bending, in order to direct taxis behaviour. This chapter presents a methodology by which I hope similar insights can be gained for soft robotic systems.

Main conclusions:

- An energy-based modelling and design methodology is well suited to soft robotics, as energy is a "common currency" amongst the many physical domains involved in this field.

- Use of bond graph schematics during the modelling and design process is well-suited to the multidomain requirements of soft robotics. An entire soft robotic system can be captured in a single schematic illustrating power flow between components of the system.

- Bond graph schematics can be readily transformed into dynamical models suit-

able for simulation via the port-Hamiltonian framework.

Limitations:

- At present there are few examples of complex soft robotic systems modelled using a port-Hamiltonian approach. Such examples would ease adoption of this modelling framework in soft robotics.
- The bond graph/port-Hamiltonian modelling approach I have championed requires the experimental elucidation of accurate constitutive models for the materials used within soft robotics. Without such models, accurately predicting the (often very large) deformations of these materials will be very difficult.
- While using the port-Hamiltonian approach allows derivation of multidomain physical dynamics from a single schematic, it is still difficult to choose appropriate discretisations for simulation of these dynamics. In particular, fluid-phase systems are most conveniently discretised by finite differences or finite volumes while solid-phase systems are often most conveniently discretised by finite elements. Therefore the transformation from bond graph schematic/model to working simulation is still conceptually difficult and may be difficult to streamline.

5.2 Publication: Controlling and Simulating Soft Robotic Systems: Insights from a Thermodynamic Perspective

SOFT ROBOTICS
Volume 3, Number 4, 2016
Mary Ann Liebert, Inc.
DOI: 10.1089/soro.2016.0010

SoRo
Soft Robotics

ORIGINAL ARTICLE

Controlling and Simulating Soft Robotic Systems: Insights from a Thermodynamic Perspective

Dylan Ross, Markus P. Nemitz, and Adam A. Stokes

Abstract

Soft robots are machines, and like all machines their function is to convert energy from one form into another to perform tasks. One key figure of merit for machines is their efficiency, which is defined as the ratio of task-oriented work out to total energy in. All soft robots convert stored energy (from e.g., batteries, pressurized gas, chemicals) into task-oriented work (picking up objects, locomoting, jumping). These systems are complex hybrids of chemical, mechanical, pneumatic, hydraulic, and electrical components. This complexity makes it difficult to analyze and measure their total efficiency and to identify the sources of energy loss between chemical, electrical, and mechanical domains. As the field of soft robotics matures, the design-flow process will shift from one in which building is central to one in which simulation takes precedence. That is, there is a shift from an empirical experimental methodology toward a well-characterized engineering workflow. At this point, questions such as ''For how long will this robot run on a 2000 mAh battery?'' will need to be answered, and predictive capabilities will become paramount as designers need to understand: (1) the large-scale deformations inherent to soft robotic systems; and (2) the transduction of energy in these complex, dissipative, systems to enable them to design an efficient and a well-controlled system. In this perspective piece, we discuss one possible predictive approach: a framework that uses port-based modeling. This approach uses bond-graphs and the recently developed port-Hamiltonian theory to provide a step-by-step system for analyzing hybrid, multi-domain, soft robotic systems. We discuss how this framework could be applied to controlling and optimizing soft robotic systems for energy efficiency, thereby increasing their utility. An energy-based approach is useful as a domain-free linker in analyzing complex systems; the use of ports promotes a clear distinction between energy conservation and dissipation and facilitates the analysis of efficiency. In addition, the parallels with hardware description languages and object-oriented programming will make it easier for engineers to design, for soft robots, control systems that optimize for efficiency.

Keywords: soft robotics, thermodynamics, simulation

Introduction

Soft robotic systems are complex hybrids that use sources and sinks of chemical, mechanical, pneumatic, hydraulic, and electrical energy. They are machines that have been designed to perform tasks by converting energy from one form (storage) into another (actuation). The fact that they have elements that cross multiple domains, and that they are often made using materials that are capable of very large deformations means that it is difficult for system designers to predict and control their motion and to measure their total efficiency. The control systems for this class of robot are typically open-loop ones, and due to the complexity of analyzing energy transduction from storage to actuation, figures of merit, such as total cost of transport, are very difficult to calculate.[1–3]

Stokes Research Group, Institute for Integrated Micro and Nano Systems, School of Engineering, The University of Edinburgh, Edinburgh, United Kingdom.

In this perspective piece, we suggest that a port-based framework, based on bond-graphs[4] and the port-Hamiltonian theory,[5] will be a useful tool for analyzing the thermodynamics underlying hybrid, multi-domain, soft robotic systems. Using this approach will enable designers to identify where energy is lost between source and actuation, across the chemical, mechanical, pneumatic, hydraulic, and electrical domains, and will pave the way for application of energy-based control methods in soft robotics.

Design paradigms for hard versus soft robotic systems

Hard-bodied and soft-bodied robots are designed by using completely different methodologies, as summarized by Figure 1. One key figure of merit for these machines is efficiency, which is defined as the ratio of task-oriented work out to total energy in. The design methodology and the corresponding ability to predict efficiency are very closely linked.

The design flow for hard robots (Fig. 1a) is one in which simulation is paramount. The system is built by using standardized and well-defined components and rigid links. Testing the physical robot is the last step in the design loop, and it can almost always be replaced with a simulation. The system is controlled by making a predictive model, which is often based on defining the Jacobian of the system and then applying well-established methodologies using inverse kinematics. The efficiency of this class of robotic systems is relatively easy to predict, as it relies on the composition of efficiencies of each of the well-defined components (motors, links, end effectors) in the system. This design flow has parallels with Hardware Description Languages (HDL) and Object-Oriented Programming (OOP)—which hardware and software engineers use to design and to program computer processors. Using these types of paradigms, designers of complex, hard-bodied robotic systems use well-defined and well-characterized blocks.

In stark contrast, the design flow for soft robots (Fig. 1b) is centered on building systems, and it uses an empirical, experimental-science iterative loop. Soft robotic systems are often built by using composite and multi-domain blocks that

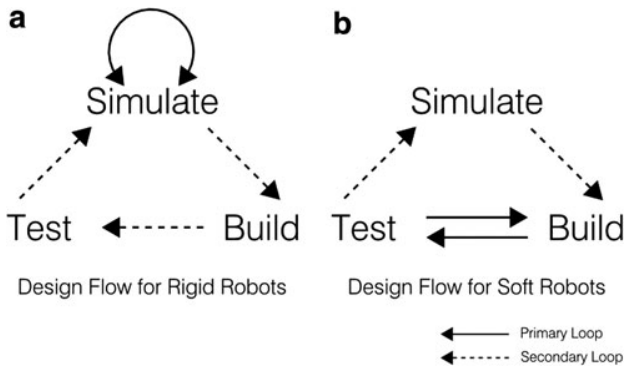

FIG. 1. Overview sketch of the design flows for hard and soft robotic systems, showing: **(a)** The engineering design flow for rigid robotic systems, in which the simulation loop is paramount and the system is built from well-defined blocks. **(b)** The experimental-science design flow for soft robotic systems in which the building loop is paramount as the system is built from poorly characterized blocks.

are not completely characterized. The system control is often an open-loop one, and locomotive actuation sequences are experimentally determined. Significant efforts toward simulating soft material systems has been made by Cotin and Lipson, resulting in programs such as SOFA[6] and VoxCAD[7–9], respectively. Testing the physical device is the key iteration in the design loop and, due to the complexity of simulating large deformations, and their strong dependence on interaction with the environment, this loop cannot (yet) be completely replaced by simulation.

This design flow has parallels with early microprocessor designs that were laid out by hand in an empirical, revisionist, and iterative process. All soft robots convert stored energy (from electrochemical cells,[10–13] pressurized gas,[14–17] energy-dense chemicals[3,18–20]) into task-oriented work (grasping and lifting,[21–23] locomoting,[10,11,16,17,24,25] jumping,[19,20] swimming[13]). In order for system designers to predict how long such a system will run on a given amount of stored energy, they need to understand and model the forms of energy storage and dissipation; only then will they be able to control these systems efficiently.

These types of questions, about efficiency, longevity, and recharging, are common to all sub-fields of mobile robotics, but they are particularly interesting when asked about those robots that: (1) are bioinspired,[3] as they raise questions about how living systems store and recover energy, and insights into how these mechanisms could be improved; (2) use direct, chemical to mechanical, actuation,[19,20] as the multi-domain physics is complex; or (3) interact synergistically with biology, for example, a human body,[26] as the coupling between living and non-living components presents great challenges in both control and safety.

The robotics community is starting to make strides toward developing robots that approach the minimum costs of transport (MCoT) for animals, as defined by Tucker.[1] One characteristic that is common to all robots, soft or otherwise, is the conversion of energy from one or more storage elements to one or more dissipative elements. These dissipative elements include those that perform task-oriented work and those that dissipate heat—resulting in the irreversible loss of energy to the environment.

Robotic systems can, therefore, be analyzed in terms of fundamental quantities: energy, work, and heat. The MIT cheetah robot, for example, is a robot that has been designed with energy in mind. The creators of this robot—Seok *et al.*—identify three main sources of energy loss during locomotion: (1) heat losses from the actuators; (2) friction losses in transmission; and (3) interaction losses caused by the interface between the system and the environment. To reduce these sources of energy dissipation, the MIT cheetah system contains regenerative electronic systems, high torque-density motors, low-loss transmission, and low leg inertia.[27] Soft systems hold particular promise for decreasing the MCoT in locomoting systems, as they contain structural and actuating elements that are capable of storing and returning energy. Despite this possibility, no soft systems have yet been developed that come close to the low MCoT of the MIT cheetah.

To use elastic structural and actuating elements the most effectively, designers of soft systems will need to understand two grand challenges: (1) Characterizing soft robots in terms of energy transformation, calculating energetic ‘‘figures of

merit,'' and identifying sources of energy loss; (2) analyzing, modeling, and simulating the whole-body mechanics and dynamics of large-scale deformations in soft robotic systems.

In this article, we offer our perspective on the first of these two grand challenges in soft robotic systems: how to characterize complex, multi-domain hybrid systems. We suggest that a modeling, analysis, and control framework built on bond-graphs and the port-Hamiltonian theory will be of great utility in the future of soft robotics. The framework also provides a link to the second grand challenge, which we do not tackle here. Bond-graphs and the port-Hamiltonian theory describe the flow of energy through a system. They are tools for understanding the thermodynamics and for predicting the dynamic behavior of complex systems.

The role of thermodynamics in robot design—energy: storage, transduction, and dissipation

Thermodynamics is often overlooked when designing tethered, factory-based, robotic systems, as it is a secondary consideration to the task in hand—rapid, precise manipulation in a structured, well-defined, and people-free environment. In contrast, when designing field robotics—where the task is reconnaissance or transportation—analysis and predictions for storage, transduction, and dissipation of the energy within the system are paramount.

There are well-established modeling approaches that focus on energy. For instance, Hamiltonian mechanics is a reformulation of classical Newtonian mechanics that takes as its starting point the Hamiltonian—a quantity that generally corresponds to the total energy contained in a mechanical system. From this single quantity, it is possible to derive differential equations that govern the motion of the system. Although initially applied only to discrete (lumped-parameter) systems, the Hamiltonian field theory has generalized the concepts of Hamiltonian mechanics to continuum systems. More recently, these ideas have been extended by the port-Hamiltonian theory,[5] which generalizes Hamiltonian mechanics further to the case of multi-domain, dissipative, and mixed discrete-continuum systems with inputs and outputs. We believe that this theoretical framework provides an ideal tool for the analysis of soft robotic systems.

In two of our previous papers—on hybrid hard and soft robots,[11] and on using explosions to power soft robots[19]—we began to introduce the idea of analyzing the efficiency and capabilities of these robots by discussing what was known about the transduction of energy in each system. In this article, we use these systems to illustrate the application of a generalized framework for describing energy flow and dynamics for these types of robots. Once expressions for the total energy, power transfer, and dissipation in a robotic system have been formulated by using this approach, they can be used for control and to optimize for efficiency. In the Supplementary Data (Supplementary Data are available online at www.liebertpub.com/soro), we work through two examples that relate to the two systems shown in Figure 3: a rigid link robotic arm and a soft, continuously deformable octopus tentacle. In the Supplementary Data (Figs. S1–S5), we use the same energy-based analytical tools to derive the equations of motion for each of these two systems.

Modeling of complex systems—a brief introduction to bond-graphs

Bond-graphs. In the 1950 s at MIT, Henry Paynter developed pictorial representations of interacting energetic elements, bond-graphs, as a way of modeling complex systems.[4] These graphs are a way of representing the flow of power in systems, and they allow designers to test their assumptions and to draw relationships between interacting elements across multiple domains. Bond-graph theory centers on the concept of ports that connect effort and flow variables, which together carry power. Table 1 shows some flow and effort variables for multiple domains.

Table 1. Variables Used in Bond-Graphs and Port-Hamiltonian Theory That Describe the Flow and Effort That Together Carry Power Transfer Between a Range of Domains, Including Thermal, Mechanical, Pneumatic, Chemical, Electrical, and Magnetic

	Effort, e	Flow, f	Generalized Momentum, p $p = \int$ e dt	Generalized Displacement, q q $= \int$ f dt
Electrical	Voltage, V [V]	Current, I [A]	Magnetic Flux Linkage, φ [Wb]	Charge, q [C]
Magnetic	Magnetomotive Force, e_m [A·turns]	Magnetic Flux Rate, φ [Wb/sec]	Not defined	Magnetic Flux, φ [Wb]
Mechanical (Translational)	Force, F [N]	Velocity, v [m/s]	Momentum, $p = \int$ F dt [N·sec]	Displacement, r [m]
Mechanical (Rotational)	Torque, τ [N·m]	Angular Velocity, ω [rad/sec]	Angular momentum, b $= \varphi = \int \tau$ dt [N·m·sec]	Angular displacement, θ [rad]
Hydraulic/ Pneumatic	Pressure, P [N/m^2]	Volumetric Flow, dQ/dt [m^3/sec]	Momentum of a flow tube, $\Gamma = \int$ P dt [N/m^{2}s]	Volume, Q [m^3]
Thermal	Temperature, T [K]	Entropy Flow, dS/dt [W/K]	Not defined	Entropy, S [J/K]
Thermal	Pressure, P [N/m^2]	Volume Change, dV/dt [m^3/sec]	Not defined	Volume, V [m^3]
Chemical	Chemical Potential, μ [J/mol]	Molar Flow, dN/dt [mole/sec]	Not defined	Number of moles, N [mol]
Chemical	Enthalpy, H [J/kg]	Mass Flow, dm/dt [g/sec]	Not defined	Mass, m [g]

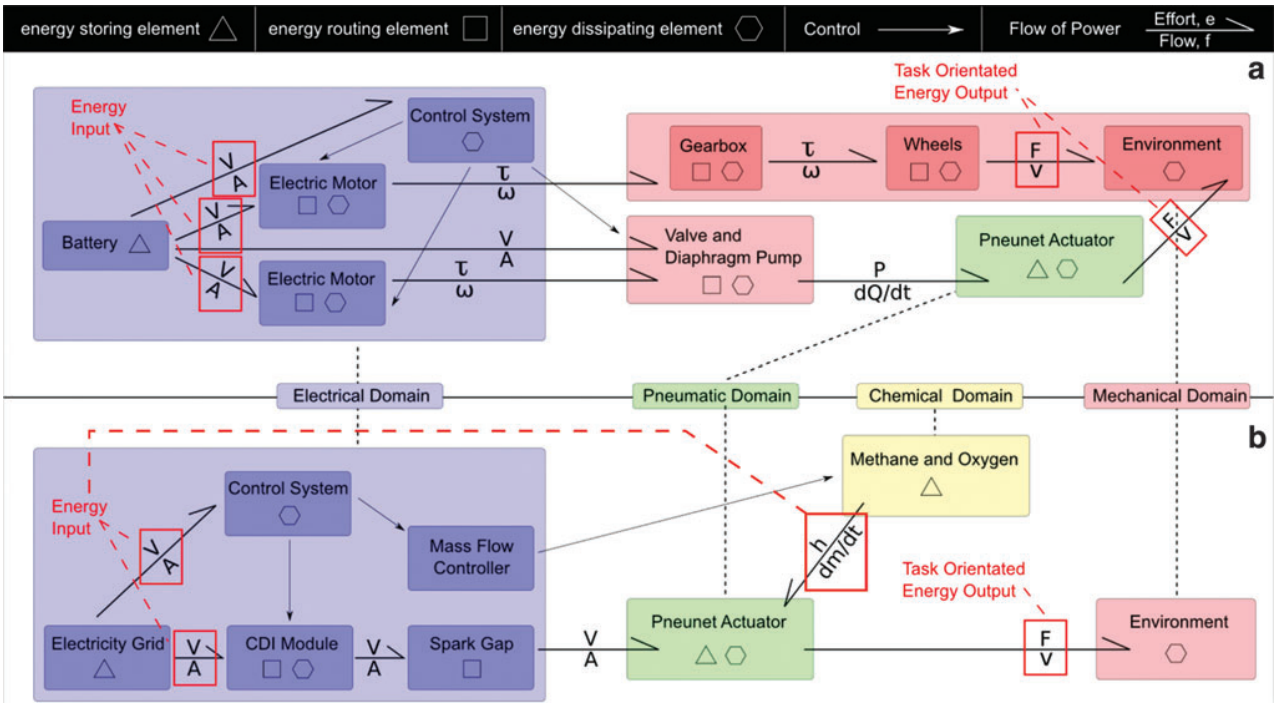

FIG. 2. Word bond-graph diagrams showing: the control; the sources; the sinks; and the flow of energy between mechanical, electrical, pneumatic, and chemical domains in: **(a)** A hybrid combining hard and soft robots,[2] and **(b)** A soft robot powered by explosions.[4] This type of diagram can be used to identify assumptions about the model, and to break down complex systems based on the flow and dissipation of energy, from storage through transmission, and to task-oriented work performed. The effort and flow variables used are described in Table 1. Color images available online at www.liebertpub.com/soro

In the bond-graph diagrams, ''ports'' between system blocks are connected with half-arrow bonds showing the usual direction of power flow. The properties of a port are the most easily understood by considering the basic electrical circuit theory, in which the flow variable is current (I), and the effort variable is voltage (V). Loss would be characterized by dissipative elements representing Ohmic (I^2R) heating. The ideas, however, have direct analogs across multiple physical domains; see Table 1 for examples.

Word bond-graph analysis of two soft robotic systems

Bond-graph analysis of a hybrid soft robotic system. Figure 2a (derived from Supplementary Fig. S6a) shows a word bond-graph multi-domain block diagram for a hybrid soft robotic system. In this system, energy is derived from the electricity grid and task-oriented energy is dissipated by the interaction of the wheels and the pneunets with the environment. The global efficiency of this system can be calculated as the ratio between the sum of the electrical input energy and the mechanical output from the reaction of the wheels and the pneunet with the environment. This bond-graph analysis allows us to identify what we need to know to simulate this system. For example, we do not know how to simulate the link between the power into a pneunet actuator (from pressure and volumetric flow rate) and the power out (force and velocity). This analysis also reveals what type of sensors we would need to deploy in the system to monitor the flow and dissipation of energy. If we consider Table 1, we can see that there are a variety of parameters that designers would not routinely

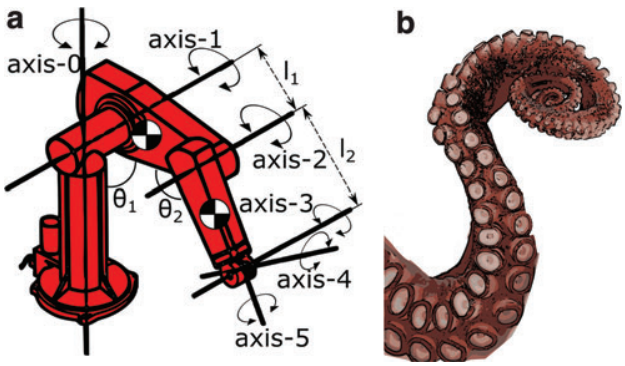

FIG. 3. Clearly, there are significantly different challenges in modeling the kinematics and energetics of: **(a)** A simple rigid bodied system (PUMA robot), and **(b)** A complex soft-bodied system (Octopus). These two systems can perform the same task—gripping—but each uses completely different mechanics, control systems, friction models, and so on. Control paradigms that have been developed for rigid bodied systems such as the PUMA robot (e.g., deriving the Jacobian and computing the inverse kinematics) have little or no relevance to soft-bodied systems that have more characteristics in common with the octopus arm. The task-oriented work performed by each system—such as gripping and lifting an object—is, however, the same. Color images available online at www.liebertpub.com/soro

include in a non-energy-based system controller. This type of insight is critical in the design of energy optimal systems.

Bond-graph analysis of a soft robot powered by explosions. Figure 2b (derived from Supplementary Fig. S6b) shows a word bond-graph multi-domain block diagram for a soft robot that is powered by explosions. The global efficiency of this system can be calculated as the ratio between the sum of the electrical and chemical input energy and the mechanical output from the reaction of the pneunet with the environment. After this process, as described earlier, we find that we do not know how to simulate the link between power into an exploding soft actuator (spark voltage and current, and enthalpy and mass flow rate) and the power out (force and velocity). We can measure the energy in (chemical potential, mass flow) and the useful work out (potential energy developed in jumping); therefore, we have a measure of the energy that is dissipated in the system, but predicting or simulating this block is complex.

From bond-graph to dynamics: the port-Hamiltonian approach

In the previous two sections, we discussed how the construction of a word bond-graph can help in identifying sources of energy loss and in evaluating the efficiency of a system. Bond-graphs can also be powerful tools for taking a high-level description of a system to the point of mathematical analysis and simulation. To begin this process, we must detail the energetic transformations occurring within each block of an abstract word bond-graph. This is a recursive process in which blocks are replaced with more detailed bond-graphs. The aim is to arrive at a system description in which each block represents a fundamental energy storage, transport, transduction, or dissipation element with a well-defined constitutive relationship between its power-conjugate flow and effort variables. Several excellent examples of how to reduce word bond-graphs to a minimal set of fundamental elements covering many physical domains can be found in the literature.[28]

Having produced a detailed bond-graph describing a system, it is possible to apply the tools of the port-Hamiltonian theory to derive the differential-algebraic equations governing the dynamics of the system.[28] This theory extends energy-conservative Hamiltonian mechanics to the case of multi-domain, dissipative systems with inputs and outputs. The central quantity in this theory is the Hamiltonian—which generally represents the total energy stored within a system and can be constructed by consideration of the energy storage elements in a bond-graph. In Hamiltonian mechanics, this quantity is usually a sum of kinetic and mechanical potential (e.g., gravitational, elastic) energy. In port-Hamiltonian theory, it may equally contain terms for chemical energy or energy associated with electric and magnetic fields. These elements are interconnected mathematically via a power-conservative Dirac structure, whose form may be derived from the energy transport and transduction elements appearing in a detailed bond-graph. This structure not only allows the individual stores of energy represented in the Hamiltonian to interact but also connects them to dissipative elements that irreversibly remove energy from the system as heat. The fundamentals of energy storage, transport, transduction, and dissipation are common to both hard and soft robotics. Thus, the tools of the port-Hamiltonian theory can be applied equally well to either. In the case of an entirely lumped-parameter system, for example a traditional robot with discrete electronics and rigid mechanical elements, the port-Hamiltonian dynamics equations take the following form:

$$x'(t) = \left[J\left(x'\right) - R(x)\right]\partial_x H(x) \text{ where } \partial_x = \frac{\partial}{\partial x}$$

In a completely distributed-parameter system, they take the form:

$$x'(X,t) = \left[J\left(x'\right) - R(x)\right]\partial_x H(x) \text{ where}$$
$$\partial_x = \frac{\partial}{\partial x} - \frac{\partial}{\partial t}\left[\frac{\partial}{\partial_t x}\right] - \nabla.\left[\frac{\partial}{\partial_X x}\right]$$

In the lumped-parameter case, x is a vector of state variables that are derived from the bond-graph's flow and effort variables, and H is the Hamiltonian. In the distributed-parameter case, x is now a vector of field variables (e.g., the mechanical displacement and momentum fields for a deformable soft body) that depend on spatial coordinates X, and H is the Hamiltonian density—usually the energy density. In both cases, J is a skew-symmetric map representing the power-conservative Dirac structure of the system, and R is a perturbation to J that allows for dissipation. Combinations of lumped- and distributed-parameter elements, a situation commonly encountered in soft robotics, are equally well treated by the port-Hamiltonian approach.

The procedure for deriving these equations of motion from a given bond-graph is systematized, and it can even be carried out algorithmically.[16] This means that the roboticist is able to focus on an intuitive, pictorial representation (the bond-graph) of the system being designed. Furthermore, once a detailed bond-graph has been constructed for a given subsystem, it can be reused several times. So long as constitutive equations for the elements in the system can be provided, the difficult work of deriving the system's dynamics is taken care of.

The port-Hamiltonian theory can also be put to good use in developing controllers for complex systems. For instance, there has been much success in using passivity or energy-shaping control to alter the static and dynamic behavior of port-Hamiltonian systems.[28,29] Given the generality and strong physical basis of this theoretical approach, many of the control techniques can be readily applied to soft, continuum systems.[30]

Gaining insights by using an energy-based analytical framework

The step-by-step framework we are proposing allows system designers to start with a complex system and to move toward an energy-based system controller; this approach is composed of six steps: (1) Writing the word bond-graph; (2) refining to a detailed bond-graph; (3) minimizing the bond-graph; (4) developing the port-Hamiltonian and Dirac structures; (5) deriving the equations of motion; and finally (6) coding the system controller.

A limitation, which we identified by constructing both of the bond-graph analyses that we presented earlier in this

article, is that the block representing the pneumatic actuator has not yet been represented mathematically. This abstract block represents a complex interplay of elements: 3D viscoelastic polymers are subjected to surface pressures from a compressible gas, whereas dynamic reaction forces appear due to an interaction of the whole network with a surface. On breaking this system into more basic energetic components, we realize that we do not know how to model the storage and loss of energy in the viscoelastic polymer. The construction of bond-graphs for these systems and progression toward simulation has highlighted exactly what empirical work is critical for the analysis of the system; we need to develop explicit constitutive relations for the viscoelastic polymer.

Note, however, that this need not stop us from proceeding to analysis, simulation, and control. If we approximate this constitutive relation—for instance, by assuming infinitesimal strains and a linear material response[31]—we can begin by using the tools of the port-Hamiltonian theory to derive the dynamics for the entire, multi-domain system, and thus begin computational analysis. All models are based on theories; they require us to explicitly state our assumptions, and they allow us to test our understanding. The approach of building bond-graphs and moving toward simulation by making successive approximations can help us find out where we should focus our future efforts on theoretical and empirical work.

Conclusions

Implications for future robotic systems

In this perspective piece, we have discussed how the use of bond-graphs and the port-Hamiltonian theory generalizes domain-specific knowledge and allows engineers to analyze complex and hybrid systems. We hope to popularize a mature framework for addressing energetic concerns in soft robotics, and we expect that it may also be used, systematically, to derive equations governing coupled, multi-domain dynamics. Using the insights gained from this type of holistic system overview—and one based on energy—engineers will be able to use elastic, energy-storing, structural, and actuating elements the most effectively in future soft robotic systems. Bond-graphs are clearly a useful tool for conceptualizing a system at various levels of abstraction. The application of the port-Hamiltonian theory requires us to make quantitative modeling decisions, and to identify those areas in which idealization or empirical analysis is the most needed, the methods we have discussed here offer a significant step toward incorporating mathematical analysis, simulation, and control into the design flow of complex soft robotic systems.

Acknowledgments

The authors thank the members of The Stokes Research Group at The University of Edinburgh, The Robosoft Community, and the MINIMAL consortium for useful conversations and comments on this article. This study was supported by EPSRC via the Robotarium Capital Equipment and CDT Capital Equipment Grants (EP/L016834/1), and by the FP7 Robosoft CA and MINIMAL grants. Markus Nemitz gratefully acknowledges support from the CDT in Integrative Sensing and Measurement (EP/L016753/1).

Author Disclosure Statements

No competing financial interests exist.

References

1. Tucker VA. The Energetic Cost of Moving About. Am Sci 1975;63:413–419.
2. Roberts TJ, Kram R, Weyand PG. Energetics of bipedal running. I. Metabolic cost of generating force. J Exp Biol 1998; 201(Pt 19):2745–2751.
3. Messner P, Paik J, Shepherd R, Kim S. Energy for biomimetic robots: Challenges and solutions. Soft Robot 2014;2: 106–109.
4. Paynter HM. An Epistemic Prehistory of Bond Graphs (Bond Graphs for Engineers) Breedveld PC, Dauphin-Tanguy G (Eds). Amsterdam: Elesvier, 1992.
5. Bedford A. Hamilton's Principle in Continuum Mechanics. Boston-London-Melbourne: Pitman Publishing, 1985.
6. Duriez C, Allard J, Faure F, Bensoussan P-J, Delingette H, Cotin S. EP4A: Software and computer based simulator research: Development and outlook SOFA—An open source framework for medical simulation. Simul Healthc 2007;2:284–285.
7. Hiller J, Lipson H. Dynamic simulation of soft multimaterial 3d-printed objects. Soft Robot 2014;1:88–101.
8. Hiller J, Lipson H. Dynamic simulation of soft heterogeneous objects. arXiv preprint arXiv:1212.2845. 2012.
9. Lipson H. Challenges and opportunities for design, simulation, and fabrication of soft robots. Soft Robot 2014;1: 21–27.
10. Lin H-T, Leisk G, Trimmer B. GoQBot: A Caterpillar-Inspired Soft-Bodied Rolling Robot. Bioinspir Biomim 2011;6:026007.
11. Stokes A, Shepherd R, Morin S, Ilievski F, Whitesides G. A hybrid combining hard and soft robots. Soft Robot 2013; 1:70–74.
12. Marchese AD, Onal CD, Rus D. Soft robot actuators using energy-efficient valves controlled by electropermanent magnets. San Francisco, CA: IEEE/RSJ International Conference on Intelligent Robots and Systems (IROS), 2011.
13. Marchese AD, Onal CD, Rus D. Autonomous Soft Robotic Fish Capable of Escape Maneuvers Using Fluidic Elastomer Actuators. Soft Robot 2014;1:75–87.
14. Gupta U, Shim J, Bertoldi K, Walsh CJ. Pneumatic networks for soft robotics that actuate rapidly. Adv Funct Mater 2014;24:2163–2170.
15. Pigula FA, Mooney DJ, Bertoldi K, Walsh CJ. A bioinspired soft actuated material. Adv Mater 2014;26:1200–1206.
16. Shepherd RF, Ilievski F, Choi W. Multigait Soft Robot. Proc Natl Acad Sci U S A 2011;108:20400–20403.
17. Tolley M, Shepherd R, Mosadegh B, Galloway K, Wehner M, Karpelson M, *et al.* A Resilient, Untethered Soft Robot. Soft Robot 2014;1:213–223.
18. Loepfe M, Schumacher CM, Lustenberger UB. An Untethered, Jumping Roly-Poly Soft Robot Driven by Combustion. Soft Robot 2015;2:33–41.
19. Shepherd RF, Stokes AA, Freake J, Barber J. Using explosions to power a soft robot. Angew Chem Int Ed Engl 2013; 52:2892–2896.
20. Bartlett N, Tolley M, Overvelde J, Weaver J, Mosadegh B, Bertoldi K, *et al.* A 3D-printed, functionally graded soft robot powered by combustion. Science 2015;349:161–165.

21. Ilievski F, Mazzeo AD, Shepherd RF, Chen X, Whitesides GM. Soft robotics for chemists. Angew Chem Int Ed Engl 2011;50:1890–1895.
22. Laschi C, Cianchetti M, Mazzolai B, Margheri L. Soft robot arm inspired by the octopus. Adv Robot 2012;26: 709–727.
23. Calisti M, Giorelli M, Levy G, Mazzolai B, Hochner B, Laschi C. An octopus-bioinspired solution to movement and manipulation for soft robots. Bioinspir Biomim 2011;6: 036002.
24. Wei T, Stokes AA, Webb B. A Soft Pneumatic Maggot Robot. 5th International Conference on Biomimetic and Biohybrid Systems 2016 Jul 19. Edinburgh: Springer International Publishing, 2016.
25. Boxerbaum AS, Chiel HJ, Quinn RD. Continuous wave peristaltic motion in a robot. Int J Robot Res 2012;31:302–318.
26. Wehner M, Tolley MT, Mengüç Y, Park YL. Pneumatic energy sources for autonomous and wearable soft robotics. Soft Robot 2014;1:263–274.
27. Seok S, Wang A, Chuah MY, Hyun DJ, Lee J, Otten DM. design principles for energy-efficient legged locomotion and implementation on the MIT Cheetah Robot. IEEE/ ASME Transact Mech 2015;20:1117–1129.
28. Duindam V, Macchelli A, Stramigioli S, Bruyninckx H. Modeling and Control of Complex Systems (The Port-Hamiltonian Approach). New York: Springer-Verlag 2009.
29. Ortega R, Schaft V, Mareels I, Maschke B. Putting energy back in control. IEEE Control Syst Mag 2001;21:18–33.
30. Siuka A, Schöberl M, Schlacher K. Port-Hamiltonian Modelling and Energy-Based Control of the Timoshenko Beam. Acta Mech 2011;222:69–89.
31. Landau LD, Lifshitz EM, Sykes JB, Bell, JS, Alverson AC. Mechanics. Phys Today 1962;15:48.

Address correspondence to:
Adam A. Stokes
Stokes Research Group
Institute for Integrated Micro and Nano Systems
School of Engineering
The University of Edinburgh
The King's Buildings
Edinburgh EH9 3LJ
United Kingdom

E-mail: a.a.stokes@ed.ac.uk

Simulating Soft Robotic Systems: Insights from a Thermodynamic Perspective

Dylan Ross, Markus Nemitz and Adam A. Stokes[1*]

SUPPLEMENTAL INFORMATION - 1

[1]Soft Systems Group, Institute for Integrated Micro and Nano Systems, School of Engineering, The University of Edinburgh, The King's Buildings, Edinburgh, EH9 3LJ, UK.

(*) Author to whom correspondence should be addressed: a.a.stokes@ed.ac.uk

Supplemental Analysis Details

Please see supplied PDF file for mathematical analysis, and Figures S1-S5.

Supplemental Figure Captions

Figure S6: Analysing: the control; the sources and sinks of energy; and the ports between domains in: A) A hybrid soft robotic system[2], and B) A soft robot powered by explosions[4].

Simulating Soft Robotic Systems: Insights from a Thermodynamic Perspective

SUPPLEMENTAL INFORMATION - II

Dylan Ross[1], Markus P. Nemitz[1] and Adam A. Stokes[1*]

[1]Stokes Research Group, Institute for Integrated Micro and Nano Systems, School of Engineering, The University of Edinburgh, The Kings Buildings, Edinburgh, EH9 3LJ, UK.

(*) Author to whom correspondence should be addressed: a.a.stokes@ed.ac.uk

S1 Introduction

In this document we will show how dynamical equations governing the evolution of a system can be derived from an expression for the *energy* contained in the system. The procedure we follow is based upon Hamilton's principle of least action, which is at the core of the port-Hamiltonian theory discussed in the main text. A detailed, mathematically rigorous treatment of how to apply the principle of least action to discrete or continuous systems, with or without dissipation, is given in [**Bedford1985**]. We aim to give a briefer account, with applications to two systems of interest : a 2-DOF robot arm composed of rigid links and revolute joints, and a deformable elastic material as might be found in a soft robotics application. We will assume some basic familiarity with continuum mechanics and the calculus of variations.

S2 Preliminaries

Lemma S2.1. *If a function f satisfies*

$$\int_{t_0}^{t_1} f(t)g(t)\ dt = 0 \tag{S.1}$$

for any smooth function g which vanishes at the limits of integration, then f is identically zero

$$f(t) = 0 \tag{S.2}$$

Definition S2.2. *Suppose that we have a function $y(t,\cdot)$ defined for $t \in (t_0, t_1)$. Then a comparison function $y^*(t,\cdot)$ for $y(t,\cdot)$ is defined as*

$$y^*(t,\cdot) = y(t,\cdot) + \epsilon\eta(t,\cdot) \tag{S.3}$$

where ϵ is a constant parameter and η is an arbitrary function which satisfies any requirements on y and vanishes at t_0 and t_1.

Definition S2.3. *The variation δy of a function $y(t,\cdot)$ is defined as*

$$\delta y = \left[\frac{\partial}{\partial\epsilon} y^*\right]_{\epsilon=0} = \eta \tag{S.4}$$

where $y^* = y^*(t,\cdot)$ is a comparison function for y

Definition S2.4. *The variation of any quantity $I(y, \cdot)$ which depends on a function y is defined as*

$$\delta(I(y,\cdot)) = \left[\frac{\partial}{\partial\epsilon} I(y^*,\cdot)\right]_{\epsilon=0} = \left[\frac{\partial}{\partial\epsilon} I^*\right]_{\epsilon=0} \tag{S.5}$$

where y^* is a comparison function for y.

Definition S2.5. *Suppose that the configuration of a mechanical system may be completely specified by s time-varying quantities q_i called generalised coordinates. Hamilton's principle states that these quantities must satisfy*

$$\delta S = \int_{t_1}^{t_2} \delta L + \delta W \ dt = 0 \tag{S.6}$$

where the quantity $L = L(q_i, \dot{q}_i)$ is called the Lagrangian of the system. In most circumstances the Lagrangian takes the form $L(q_i, \dot{q}_i) = T(q_i, \dot{q}_i) - U(q_i)$, with T denoting kinetic energy and U denoting potential energy. The time derivatives $\dot{q}_i$ are called generalised velocities.

δW is the virtual work done on the system by external forces, and takes the form $\delta W = Q_i \delta q_i$, where Q_i is the generalised force conjugate to coordinate q_i.

S3 The Euler-Lagrange Equations for a Mechanical System with Finite Degrees of Freedom

Hamilton's principle S5.1 provides a *global* requirement on the functions q_i. By using some elementary calculus, along with definitions for the variation of a quantity S2.3, S2.4 and the fundamental lemma of the calculus of variations S2.1 presented in the previous section, we may derive

local requirements on the q_i. In particular, we aim to prove the following theorem.

Theorem S3.1. *The evolution over time of the s coordinates q_i of a mechanical system is given by the s second-order differential equations (called the Euler-Lagrange equations)*

$$\frac{d}{dt}\left[\frac{\partial L}{\partial \dot{q}_i}\right] - \frac{\partial L}{\partial q_i} - Q_i = 0 \tag{S.7}$$

We will proceed assuming that only a single coordinate q is required to describe our system; it is straightforward to show that our results also hold in the case of several coordinates.

We begin by finding the variation $\delta L(q, \dot{q})$. To this end, we introduce the comparison coordinate $q^* = q + \epsilon\eta$, with comparison velocity $\dot{q}^* = \dot{q} + \epsilon\dot{\eta}$. We may then write the Lagrangian in terms of these functions as $L^* = L(q^*, \dot{q}^*)$. The definition S2.4 tells us that we must differentiate this expression with respect to ϵ, which gives us

$$\begin{aligned}\frac{\partial L^*}{\partial \epsilon} &= \frac{\partial L^*}{\partial q^*}\frac{\partial q^*}{\partial \epsilon} + \frac{\partial L^*}{\partial \dot{q}^*}\frac{\partial \dot{q}^*}{\partial \epsilon} \\ &= \frac{\partial L^*}{\partial q^*}\eta + \frac{\partial L^*}{\partial \dot{q}^*}\dot{\eta}\end{aligned} \tag{S.8}$$

Setting $\epsilon = 0$ in accordance with S2.4 then gives

$$\delta L = \frac{\partial L}{\partial q}\delta q + \frac{\partial L}{\partial \dot{q}}\dot{\delta q} \tag{S.9}$$

Substituting this expression for δL into the definition of Hamilton's principle S5.1 gives

$$\int_{t_1}^{t_2} \frac{\partial L}{\partial q}\delta q + \frac{\partial L}{\partial \dot{q}}\dot{\delta q} + Q\delta q \;\; dt = 0 \tag{S.10}$$

The second term may be integrated by parts to obtain

$$\int_{t_1}^{t_2} \frac{\partial L}{\partial \dot{q}} \dot{\delta q} \ dt = \left[\frac{\partial L}{\partial \dot{q}} \delta q \right]_{t_1}^{t_2} - \int_{t_1}^{t_2} \frac{d}{dt} \left[\frac{\partial L}{\partial \dot{q}} \right] \delta q \ dt \tag{S.11}$$

However, since $\delta q = \eta$ must vanish at t_1 and t_2 by definition S2.2 the first term on the right hand side must be equal to zero. Therefore, we may substitute the integrand of the second term back into S.12 to obtain

$$\int_{t_1}^{t_2} \left(\frac{\partial L}{\partial q} - \frac{d}{dt} \left[\frac{\partial L}{\partial \dot{q}} \right] + Q \right) \delta q \ dt = 0 \tag{S.12}$$

Since $\delta q = \eta$ is an arbitrary function according to S2.2, we may use the fundamental lemma of the calculus of variations S2.1 to write

$$\frac{\partial L}{\partial q} - \frac{d}{dt} \left[\frac{\partial L}{\partial \dot{q}} \right] + Q = 0 \tag{S.13}$$

which proves theorem S5.2 for the case of a mechanical system described by a single coordinate.

S4 Modelling the Mechanics of a 2DOF Manipulator

S4.1 Kinematic quantities

$\mathbf{r}_1$ is the displacement vector from the origin of the fixed inertial frame to the centre of mass of the first rigid body. $r_1 = |\mathbf{r}_1|$ is the length of this vector. x_1 and y_1 are the x- and y-components of this vector, respectively.

$\mathbf{r}_2$ is the displacement vector from the centre of the revolute joint joining the two rigid bodies to the centre of mass of the second rigid body. x_2 and y_2 are the x- and y-components of this vector, respectively. $r_2 = |\mathbf{r}_2|$ is the length of this vector.

l_1 is the distance between the origin of the fixed inertial frame and the revolute joint connecting the two rigid bodies.

θ_1 is the angle between the horizontal x axis and the first rigid body. θ_2 is the angle of the second rigid body relative to the first. We also define the variables $\omega_1 = \theta_1$ and $\omega_2 = \theta_1 + \theta_2$ for convenience.

The kinematic quantities may all be written in terms of the angles θ_1, θ_2 as

$$\begin{aligned} x_1 &= r_1 c_1 \\ y_1 &= r_1 s_1 \\ x_2 &= l_1 c_1 + r_2 c_{12} \\ y_2 &= l_1 s_1 + r_2 s_{12} \\ \omega_1 &= \theta_1 \\ \omega_2 &= \theta_1 + \theta_2 \end{aligned} \tag{S.14}$$

Where the notation $c_i = \cos\theta_i$, $s_i = \sin\theta_i$, $c_{12} = \cos\theta_1 + \theta_2$, $s_{12} = \sin\theta_1 + \theta_2$ has been used.

S4.2 Energetic quantities

The Lagrangian for the 2DOF robotic manipulator is $L = T - U$. The kinetic energy T may be written

$$T = \frac{1}{2}\left[\mu_1\left(\dot{x}_1^2 + \dot{y}_1^2\right) + \mu_2\left(\dot{x}_2^2 + \dot{y}_2^2\right) + I_1\dot{\omega}_1^2 + I_2\dot{\omega}_2^2\right] \tag{S.15}$$

where μ_1 and μ_2 are the total masses of the first and second bodies, respectively, and I_1, I_2 are their moments of inertia about the z-axis. We have used the six quantities x_1, y_1, x_2, y_2, ω_1, and $\omega 2$ in stating the kinetic energy function, but we may express it in terms of θ_1 and θ_2 by using the

kinematic relations S.14, noting that their derivatives with respect to time are

$$\begin{aligned}
\dot{x}_1 &= -r_1 s_1 \dot{\theta}_1 \\
\dot{y}_1 &= r_1 c_1 \dot{\theta}_1 \\
\dot{x}_2 &= -\left[l_1 s_1 + r_2 s_{12}\right] \dot{\theta}_1 - r_2 s_{12} \dot{\theta}_2 \\
\dot{y}_2 &= \left[l_1 c_1 + r_2 c_{12}\right] \dot{\theta}_1 + r_2 c_{12} \dot{\theta}_2 \\
\dot{\omega}_1 &= \dot{\theta}_1 \\
\dot{\omega}_2 &= \dot{\theta}_1 + \dot{\theta}_2
\end{aligned} \tag{S.16}$$

Using these equalities and the trigonometric identity $s_i^2 + c_i^2 = 1$ we may write

$$\frac{1}{2}\left[\mu_1\left(\dot{x}_1^2 + \dot{y}_1^2\right) + I_1 \dot{\omega}_1^2\right] = \frac{1}{2}\left[\mu_1 r_1^2 + I_1\right] \dot{\theta}_1^2 \tag{S.17}$$

Similarly, the expression

$$\frac{1}{2}\left[\mu_2\left(\dot{x}_2^2 + \dot{y}_2^2\right) + I_2 \dot{\omega}_2^2\right] \tag{S.18}$$

may be written

$$\frac{1}{2}\left[\mu_2\left(r_2^2\dot{\theta}_2^2 + (l_1^2 + r_2^2 + 2l_1 r_2 c_2)\dot{\theta}_1^2 + 2(l_1 r_2 c_2 + r_2^2)\dot{\theta}_1\dot{\theta}_2\right) + I_2(\dot{\theta}_1^2 + \dot{\theta}_2^2 + \dot{\theta}_1\dot{\theta}_2)\right] \tag{S.19}$$

where we have used the identity $c_1 c_{12} + s_1 s_{12} = c_2$. Combining S.17 and S.19, and grouping terms in $\dot{\theta}_1^2$, $\dot{\theta}_2^2$, and $\dot{\theta}_1\dot{\theta}_2$, we find the kinetic energy as a quadratic form in the $\dot{\theta}_i$

$$
\begin{aligned}
T = & \frac{1}{2}\left[\mu_1 r_1^2 + \mu_2(l_1^2 + r_2^2 + 2l_1 r_2 c_2) + I_1 + I_2\right]\dot{\theta}_1^2 \\
& + \frac{1}{2}\left[\mu_2 r_2^2 + I_2\right]\dot{\theta}_2^2 \\
& + \frac{1}{2}\left[\mu_2(r_2^2 + 2l_1 r_2 c_2) + 2I_2\right]\dot{\theta}_1\dot{\theta}_2
\end{aligned}
\tag{S.20}
$$

To simplify what follows, we introduce the three constants

$$
\begin{aligned}
a &= \mu_1 r_1^2 + \mu_2(l_1^2 + r_2^2)I_1 + I_2 \\
b &= \mu_2 l_1 r_2 \\
d &= \mu_2 r_2^2 + I_2
\end{aligned}
\tag{S.21}
$$

allowing us to rewrite S.20 as

$$
T = \frac{1}{2}\left[a + 2bc_2\right]\dot{\theta}_1^2 + \frac{1}{2}d\dot{\theta}_2^2 + \left[d + bc_2\right]\dot{\theta}_1\dot{\theta}_2 \tag{S.22}
$$

Since the links of the manipulator are rigid the potential energy U is entirely gravitational and takes the form

$$
U = (\mu_1 r_1 + \mu_2 l_1)g s_1 + \mu_2 r_2 s_{12} \tag{S.23}
$$

The virtual work done by torques τ_1 and τ_2, which act on the first and second joints, respectively, is

$$
\delta W = \tau_1 \delta\theta_1 + \tau_2 \delta\theta_2 \tag{S.24}
$$

S4.3 Equations of motion

For the 2DOF robotic manipulator, the Euler-Lagrange equations S5.2 take the form

$$\frac{d}{dt}\left[\frac{\partial T}{\partial \dot{\theta}_i}\right] - \frac{\partial T}{\partial \theta_i} - \frac{\partial U}{\partial \theta_i} = \tau_i \tag{S.25}$$

Calculating each term for the first joint angle θ_1, we see that

$$-\frac{\partial T}{\partial \theta_1} = 0 \tag{S.26}$$

$$-\frac{\partial U}{\partial \theta_1} = -(\mu_1 r_1 + \mu_2 l_1) g c_1 - \mu_2 r_2 g c_{12} \tag{S.27}$$

$$\frac{\partial T}{\partial \dot{\theta}_1} = [a + 2bc_2]\,\dot{\theta}_1 + [d + bc_2]\,\dot{\theta}_2$$

$$\frac{d}{dt}\left[\frac{\partial T}{\partial \dot{\theta}_1}\right] = [a + 2bc_2]\,\ddot{\theta}_1 + [d + bc_2]\,\ddot{\theta}_2 - 2bs_2\dot{\theta}_1\dot{\theta}_2 - bs_2\dot{\theta}_2^2 \tag{S.28}$$

Calculating each term in S.25 for the second joint angle θ_2 gives us

$$-\frac{\partial T}{\partial \theta_2} = bs_2\dot{\theta}_1^2 + bs_2\dot{\theta}_1\dot{\theta}_2 \tag{S.29}$$

$$-\frac{\partial U}{\partial \theta_2} = -\mu_2 r_2 g c_{12} \tag{S.30}$$

$$\frac{\partial T}{\partial \dot{\theta}_2} = d\dot{\theta}_2 + [d + bc_2]\,\dot{\theta}_1$$

$$\frac{d}{dt}\left[\frac{\partial T}{\partial \dot{\theta}_2}\right] = [d + bc_2]\,\ddot{\theta}_1 + d\ddot{\theta}_2 - bs_2\dot{\theta}_1\dot{\theta}_2 \tag{S.31}$$

Substituting equations S.26, S.27, and S.28 into S.25 gives

$$[a + 2bc_2]\,\ddot{\theta}_1 + [d + bc_2]\,\ddot{\theta}_2 - 2bs_2\dot{\theta}_1\dot{\theta}_2 - bs_2\dot{\theta}_2^2 - (\mu_1 r_1 + \mu_2 l_2)gc_1 - \mu_2 r_2 g c_{12} = \tau_1 \tag{S.32}$$

Likewise, substuting equations S.29, S.30, and S.31 into S.25 gives

$$[d + bc_2]\,\ddot{\theta}_1 + d\ddot{\theta}_2 + bs_2\dot{\theta}_1{}^2 - \mu_2 r_2 g c_{12} = \tau_2 \tag{S.33}$$

Equations S.32 and S.33 are two nonlinear second-order differential equations which completely determine the evolution of the joint angles θ_1 and θ_2 over time, under the action of applied torques τ_1 and τ_2. These equations may also be written in matrix form as

$$\begin{bmatrix} a + 2bc_2 & d + bc_2 \\ d + bc_2 & d \end{bmatrix} \begin{bmatrix} \ddot{\theta}_1 \\ \ddot{\theta}_2 \end{bmatrix} + \begin{bmatrix} -2bs_2\dot{\theta}_2 & -bs_2\dot{\theta}_2 \\ bs_2\dot{\theta}_1 & 0 \end{bmatrix} \begin{bmatrix} \dot{\theta}_1 \\ \dot{\theta}_2 \end{bmatrix} + \begin{bmatrix} -g((\mu_1 r_1 + \mu_2 l_1)c_1 + \mu_2 r_2 c_{12}) \\ -g\mu_2 r_2 c_{12} \end{bmatrix} = \begin{bmatrix} \tau_1 \\ \tau_2 \end{bmatrix} \tag{S.34}$$

which is clearly adheres to the standard manipulator form

$$\mathbf{M}(\theta)\ddot{\theta} + \mathbf{D}(\theta, \dot{\theta})\dot{\theta} + \mathbf{G}(\theta) = \tau \tag{S.35}$$

S5 The Euler-Lagrange Equations for Systems with Infinite Degrees of Freedom

Definition S5.1. *Suppose that the configuration of a continuous system may be completely specified by a field $\phi(t, X)$. Hamilton's principle states that this field must satisfy*

$$\delta S = \int_T \int_\Omega [\delta \mathcal{L} + \delta W] \, dV \, dt = 0 \tag{S.36}$$

where the quantity $\mathcal{L} = \mathcal{L}(\phi, \dot{\phi}, \nabla\phi)$ is the Lagrangian density of the system. For mechanical systems, the Lagrangian density usually takes the form $\mathcal{L}(\phi, \dot{\phi}, \nabla\phi) = \mathcal{T}(\phi, \dot{\phi}) - \mathcal{U}(\phi, \nabla\phi)$, with $\mathcal{T}$ denoting kinetic energy density and $\mathcal{U}$ denoting potential energy density. Integration is performed over a volume in three-dimensional space Ω and an interval of time T.

δW measures the virtual work done on the system by external forces. It is assumed that this term can be decomposed into surface and bulk components

$$\int_T \int_\Omega \delta W \, dV \, dt = \int_T \left[\int_{\partial\Omega_2} Q_s \delta\phi \, dS + \int_\Omega Q_b \delta\phi \, dV \right] dt \tag{S.37}$$

where $\partial\Omega$ is the surface of Ω and $\partial\Omega_2$ is a subsurface on which the field ϕ has not been prespecified (if ϕ were specified on $\partial\Omega_2$, then $\delta\phi$ would vanish on this surface and the associated integral would be zero).

Theorem S5.2. *The evolution of a field $\phi(t, X)$ specified by a Lagrangian density $\mathcal{L}(\phi, \dot{\phi}, \nabla\phi)$ over a period of time T and region of space Ω is given by*

$$\frac{\partial}{\partial t} \frac{\partial \mathcal{L}}{\partial \dot{\phi}} + \nabla \cdot \frac{\partial \mathcal{L}}{\partial \nabla \phi} - \frac{\partial \mathcal{L}}{\partial \phi} - Q_b = 0 \tag{S.38}$$

Boundary conditions on the field $\phi(t, X)$ or its derivatives may be specified on a subsurface $\partial B_1 \subset \partial B$. Boundary conditions on the complementary region $\partial B_2 \subset \partial B$ where the field is not explicitly

specified are given by the equations

$$\frac{\partial \mathcal{L}}{\partial \nabla \phi} + Q_s = 0 \tag{S.39}$$

Together, S.38 and S.39 are called the Euler-Lagrange equations for the field ϕ.

The proof of this theorem will proceed exactly as for the case of a system with finite degrees of freedom. We find the variation $\delta\mathcal{L}$ by introducing a comparison field $\phi^*(t, X) = \phi(t, X) + \epsilon\eta(t, X)$ with comparison derivatives $\dot{\phi}^* = \dot{\phi} + \epsilon\dot{\eta}$ and $\nabla\phi^* = \nabla\phi + \epsilon\nabla\eta$. We substitute these new fields into the Lagrangian density to give $\mathcal{L}^* = \mathcal{L}^*(\phi^*, \dot{\phi}^*, \nabla\phi^*)$.

The definition S2.4 suggests that we should now differentiate this quantity with respect to ϵ, which gives the expression

$$\begin{aligned} \frac{d}{d\epsilon}\mathcal{L}^* &= \frac{\partial \mathcal{L}^*}{\partial \phi^*}\frac{d\phi^*}{d\epsilon} + \frac{\partial \mathcal{L}^*}{\partial \dot{\phi}^*}\frac{d\dot{\phi}^*}{d\epsilon} + \frac{\partial \mathcal{L}^*}{\partial \nabla \phi^*}\frac{d\nabla\phi^*}{d\epsilon} \\ &= \frac{\partial \mathcal{L}^*}{\partial \phi^*}\eta + \frac{\partial \mathcal{L}^*}{\partial \dot{\phi}^*}\dot{\eta} + \frac{\partial \mathcal{L}^*}{\partial \nabla \phi^*}\nabla\eta \end{aligned} \tag{S.40}$$

Setting ϵ equal to zero then gives

$$\delta\mathcal{L} = \frac{\partial \mathcal{L}}{\partial \phi}\delta\phi + \frac{\partial \mathcal{L}}{\partial \dot{\phi}}\delta\dot{\phi} + \frac{\partial \mathcal{L}}{\partial \nabla \phi}\nabla\delta\phi \tag{S.41}$$

Substituting this expression for $\delta\mathcal{L}$ into the definition of Hamilton's principle yields

$$\delta S = \int_T \int_\Omega \left[\frac{\partial \mathcal{L}}{\partial \phi}\delta\phi + \frac{\partial \mathcal{L}}{\partial \dot{\phi}}\delta\dot{\phi} + \frac{\partial \mathcal{L}}{\partial \nabla \phi}\nabla\delta\phi + \delta W\right] dV\, dt = 0 \tag{S.42}$$

Isolating the second term in the integrand, swapping the integration order, and integrating by parts with respect to time gives

$$\int_\Omega \int_T \left[\frac{\partial \mathcal{L}}{\partial \dot{\phi}} \delta\dot{\phi}\right] dt\, dV = \int_\Omega \left(\left[\frac{\partial \mathcal{L}}{\partial \dot{\phi}} \delta\phi\right]_{t_0}^{t_1} - \int_T \left[\frac{\partial}{\partial t}\frac{\partial \mathcal{L}}{\partial \dot{\phi}} \delta\phi\right] dt \right) dV = \int_T \int_\Omega \left[-\frac{\partial}{\partial t}\frac{\partial \mathcal{L}}{\partial \dot{\phi}} \delta\phi\right] dV\, dt \tag{S.43}$$

Isolating the third term in the integrand of S.42 and integrating by parts with respect to space gives

$$\begin{aligned} \int_T \int_\Omega \left[\frac{\partial \mathcal{L}}{\partial \nabla\phi} \nabla\delta\phi\right] dV\, dt &= \int_T \left(\oint_{\partial\Omega} \left[\frac{\partial \mathcal{L}}{\partial \nabla\phi} \delta\phi\right] dS - \int_\Omega \left[\nabla \cdot \frac{\partial \mathcal{L}}{\partial \nabla\phi} \delta\phi\right] dV \right) dt \\ &= \int_T \oint_{\partial\Omega_2} \left[\frac{\partial \mathcal{L}}{\partial \nabla\phi} \delta\phi\right] dS\, dt + \int_T \int_\Omega \left[-\nabla \cdot \frac{\partial \mathcal{L}}{\partial \nabla\phi} \delta\phi\right] dV\, dt \end{aligned} \tag{S.44}$$

where we have supposed that some boundary conditions have been supplied for the field ϕ on a subsurface $\partial\Omega_1$ of $\partial\Omega$. In this case, the variation of the field $\delta\phi$ must vanish on $\partial\Omega_1$. As a result, the surface integral in S.44 must be taken only over the complement of $\partial\Omega_1$, which we call $\partial\Omega_2$.

Expressions S.37, S.43, S.44 allow us to rewrite S.42 as

$$\delta S = \int_T \int_\Omega \left[\frac{\partial \mathcal{L}}{\partial \phi} - \frac{\partial}{\partial t}\frac{\partial \mathcal{L}}{\partial \dot{\phi}} - \nabla \cdot \frac{\partial \mathcal{L}}{\partial \nabla\phi} + Q_b\right] \delta\phi\, dV\, dt + \int_T \oint_{\partial\Omega_2} \left[\frac{\partial \mathcal{L}}{\partial \nabla\phi} + Q_s\right] \delta\phi\, dS\, dt = 0 \tag{S.45}$$

Since the variation $\delta\phi$ is an arbitrary field, we may suppose that it vanishes on Ω or $\delta\Omega$ individually. Setting $\delta\phi$ to be zero on $\partial\Omega_2$ and arbitrary on Ω before using the fundamental lemma of the calculus of variations S2.1, we see that the coefficient of $\delta\phi$ in the first integral must be identically zero. This gives us the first Euler-Lagrange equation

$$\frac{\partial \mathcal{L}}{\partial \phi} - \frac{\partial}{\partial t}\frac{\partial \mathcal{L}}{\partial \dot{\phi}} - \nabla \cdot \frac{\partial \mathcal{L}}{\partial \nabla\phi} + Q_b = 0 \tag{S.46}$$

This equation describes evolution of the field ϕ over time and space. Next, we take $\delta\phi$ to be zero on Ω and arbitrary on $\partial\Omega_2$. Applying the fundamental lemma gives the second Euler-Lagrange

equation

$$\frac{\partial \mathcal{L}}{\partial \nabla \phi} + Q_s = 0 \tag{S.47}$$

which specifies boundary conditions on the subsurface $\partial\Omega_2$.

S5.1 Kinematic quantities

B represents the region in space occupied by the interior of the material body in a reference state.

∂B is the surface of the material body in its reference state.

$\bar{B} = B \cup \partial B$ is the closure of B and ∂B, and is the entirety of the region of space occupied by the material body in its reference state.

dV denotes an element of volume in B.

dS denotes an element of surface in ∂B. N is then the outward-pointing unit normal vector defined at each surface element dS.

X are the coordinates of material points in $\bar{B}$.

B_t represents the region in space occupied by the interior of the material body in its deformed state at time t.

∂B_t is the surface of the material body in its deformed state at time t, and is the entirety of the region of space occupied by the material body in its deformed state at time t.

$\bar{B}_t = B_t \cup \partial B_t$ is the closure of B_t and ∂B_t.

dV_t denotes an element of volume in B_t.

dS_t denotes an element of surface in ∂B_t. N is then the outward-pointing unit normal vector defined at each surface element dS_t.

x are the coordinates of material points in $\bar{B}_t$.

The relationship $x = \chi(X, t)$ maps the coordinates of material points in the reference configuration to the coordinates of the same material points in the deformed configuration at time t. x will therefore be called the motion of the mechanical system.

$F = \frac{\partial x}{\partial X}$ is called the *deformation gradient* of the motion of the system.

$J = \det F$ is called the *jacobian determinant* of the motion of the system.

S5.2 Boundary conditions

$\tau(X, t)$

We will assume that the surface ∂B may be divided into two complementary subsurfaces ∂B_1 and ∂B_2 such that $\partial B = \partial B_1 \cup \partial B_2$ and $\partial B_1 \cap \partial B_2 = \emptyset$. We will assume the motion on ∂B_1 is specified. For instance, we may hold ∂B_1 fixed in some reference frame. We will assume that motion of ∂B_2 is not kinematically constrained, and that external forces may act over this surface. We will provide a mathematical treatment of these forces in the next two sections.

S5.3 Energetic quantities

The kinetic energy density $\mathcal{T}$ of the solid body in the deformed configuration is

$$\mathcal{T} = \frac{1}{2}\rho v \cdot v \tag{S.48}$$

The potential energy density $\mathcal{U}$ of the deformed configuration is assumed to be a function of the deformation gradient $F = \nabla\chi$.

$$\mathcal{U} = \rho E(F) = \rho E(\nabla\chi) \tag{S.49}$$

The Lagrangian density $\mathcal{L}$ is then the difference in kinetic and potential energy densities

$$\mathcal{L} = \frac{1}{2}\rho v \cdot v - \rho E(\nabla\chi) \tag{S.50}$$

We denote externally applied body forces acting throughout the volume of the deformed body as $Q_b = \rho b$, and surface forces as $Q_s = s_0$.

S5.4 Equations of motion

We may now use our expression for the Lagrangian density S.50 of the displacement field χ to find each term appearing in the Euler-Lagrange equations S.46 and S.47

$$\begin{aligned}
\frac{\partial \mathcal{L}}{\partial \chi} &= 0 \\
\frac{\partial}{\partial t}\frac{\partial \mathcal{L}}{\partial \dot{\chi}} &= \rho\ddot{\chi} \\
\frac{\partial \mathcal{L}}{\partial \nabla\chi} &= -\rho\frac{\partial E}{\partial \nabla\chi} = -S \\
\nabla \cdot \frac{\partial \mathcal{L}}{\partial \nabla\chi} &= -\nabla \cdot \rho\frac{\partial E}{\partial \nabla\chi} = -\nabla \cdot S
\end{aligned} \tag{S.51}$$

where $S = \rho\frac{\partial E}{\partial \nabla\chi}$ is the first Piola-Kirchoff stress tensor. Putting these terms into the Euler-Lagrange equations S.46 and S.47 gives

$$\rho\ddot{\chi} = \nabla \cdot S + \rho b \tag{S.52}$$

with boundary conditions on ∂B_2

$$s_0 = S \tag{S.53}$$

Equations S.52 and S.53, together with the expression for the first Piola-Kirchoff stress tensor

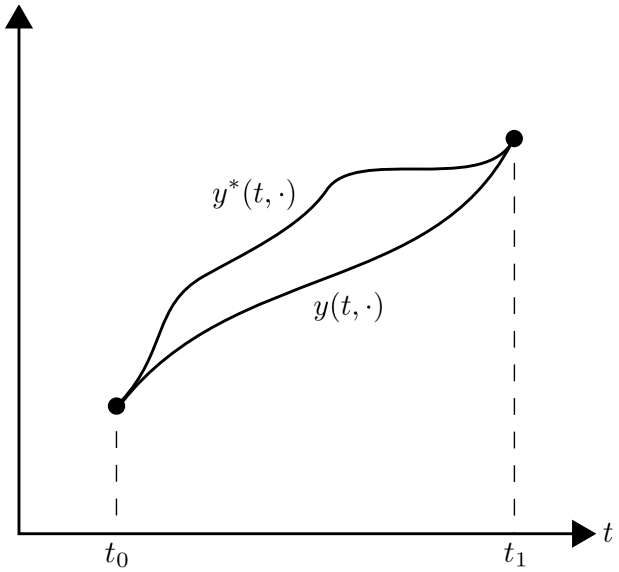

Figure S1: The relationship of a function $y(t)$ to its comparison function $y^*(t) = y(t) + \epsilon\eta(t)$ over the interval $[t_0, t_1]$.

above, allow us to completely determine the displacement χ and stress S fields for our solid body once a constitutive model for the internal energy E is specified in terms of the deformation gradient $F = \nabla\chi$. Linear elasticity theory can be seen as a special case in which we approximate E as a quadratic form in the linear strain tensor.

References

[1] Bedford, A. *Hamilton's principle in Continuum Mechanics* in *Research Notes in Mathematics 139*, Boston-London-Melbourne, Pitman Advanced Publ. Program, 1985.

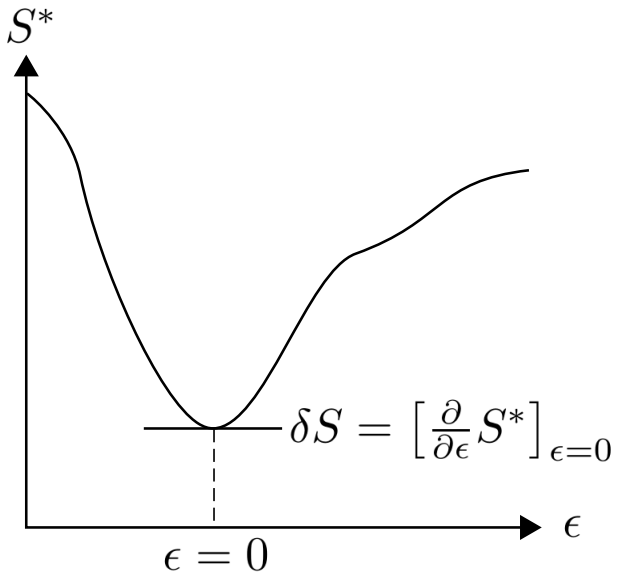

Figure S2: Hamilton's principle tells us that the path $q(t)$ taken by a mechanical system extremizes the scalar action S. Here we plot the action S^* computed for comparison paths $q^*(t) = q(t) + \epsilon\eta(t)$ with a particular choice of the arbitrary function $\eta(t)$ and with different values of the constant ϵ. At $\epsilon = 0$ the comparison function equals the true path, $q^* = q$, and the variation of the action $\delta S = \left[\frac{\partial}{\partial \epsilon} S^*\right]_{\epsilon=0}$ is zero.

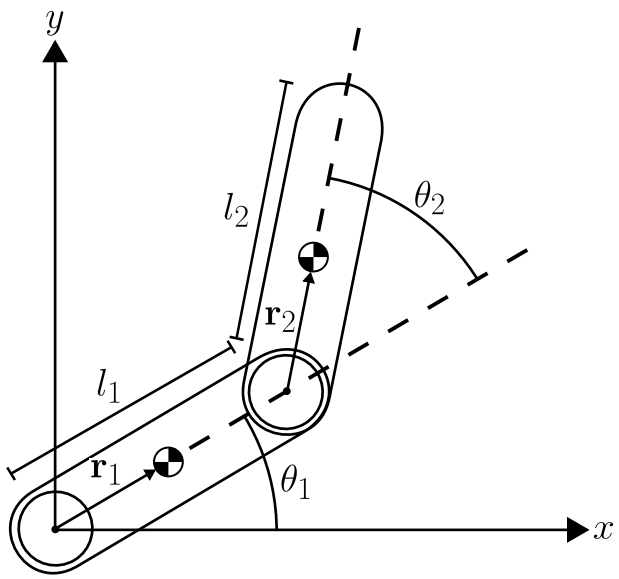

Figure S3: The robotic manipulator to be modelled. The two rigid bodies rotate about the z-axis, which can be imagined as coming out of the page.

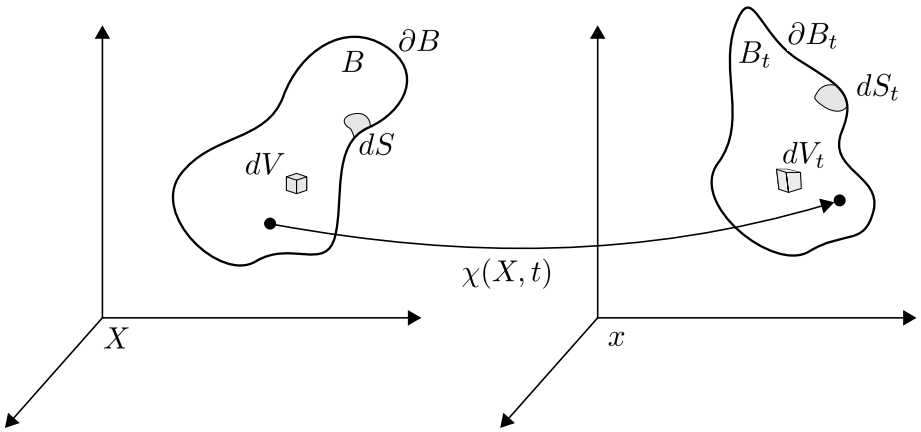

Figure S4: Kinematic quantities used to describe a continuously deformable material.

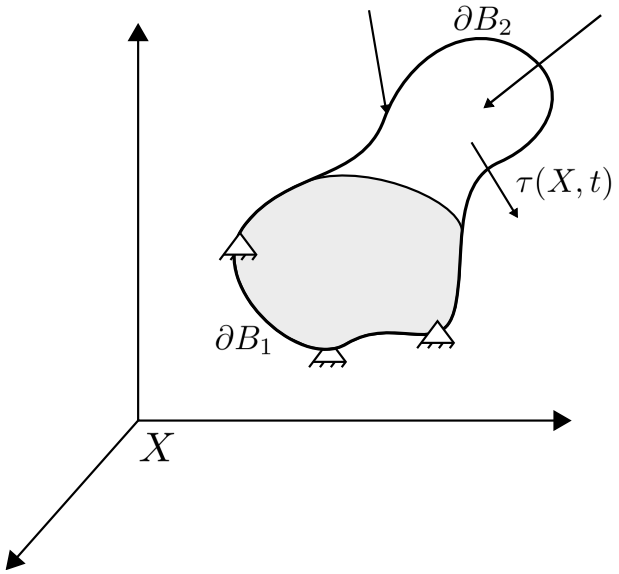

Figure S5: Different boundary conditions may be specified on complementary subsurfaces of a continuously deformable material.

Chapter 6

Model extensions

6.1 Introduction

In this chapter, I present some initial extensions of the models presented in chapters 3 and 4. I begin modelling the mechanics of the larva in three spatial dimensions, and develop a simple model of the larval ventral nerve cord that appears to perform pattern generation. The work in this chapter is unpublished, and should not be viewed as a finished theoretical contribution. Rather, this work should demonstrate that the models presented in this thesis are ripe for further investigation and extension. I hope that the work in this chapter provides a tangible starting point for researchers to further build on the models developed in earlier chapters.

Perhaps the most "obvious" development is the extension of the planar mechanical model of chapters 3 and 4 to three spatial dimensions. A straightforward way to do this would be to include all possible deformations of the larval midline – axial compression/expansion, transverse bending in two directions ("horizontal" and "vertical"), and torsion around the midline. This would still neglect radial compression/expansion as the volume of the larva would not be modelled (only the midline). However, this extension would allow a much greater section of the larval behavioural repertoire to be theoretically examined. Some examples of behaviours that would become theoretically accessible in three dimensions are rearing, lifting, rolling, righting, and burrowing. I have made preliminary investigations into the mechanical basis of both righting and rolling by focusing exclusively on either transverse bending or torsional degrees of freedom, while neglecting all other degrees of freedom, with some promising results. These are presented in the following subsections, titled "Mechanics of self-righting behaviour", and "Mechanics of rolling behaviour".

There is also substantial scope for extending the neural model presented in this thesis. Perhaps most importantly, the neural model as it stands has no intrinsic dynamics and thus cannot explain the existence of endogenous activity patterns in isolated neural preparations. However, as argued in the discussion of chapter 3, our model architecture does resemble that of a ring attractor, a type of network structure capable of sustaining a stable "bump" of neural activity in a particular location. With the inclusion of a slight forward or backward bias, this "bump" should move, producing travelling waves of neural activity resembling those observed in the real larva.

A seemingly unrelated problem is how to produce peristaltic waves in which more than one segment is actively compressed at a given time, an effect observed in the real larva but not present in our models. I give a physical motivation for why the larva might compress several segments at once in S3 Appendix, Chapter 3, noting that the larva should prefer to transfer power into the axial modes with high Q-factor and low spatial frequency, corresponding to broad compressions spread across several segments, as these modes experience less viscous friction and thus are more efficient than the modes with low Q-factor and high spatial frequency. I tackle this problem in the subsection below titled "Modelling the VNC as a sensory filter" by finding linear control laws that will provide positive feedback reinforcement to only the high-Q modes during travelling wave motion. Surprisingly, the feedback matrices governing these control laws are exactly the same as the weight matrices used in many ring attractor models. I subsequently construct a simple ring attractor model of the VNC based on this weighting scheme, showing that it does indeed produce propagating waves of activity when isolated from the body.

Main conclusions:

- Initial models of self-righting and rolling mechanics have been produced. These behaviours could not be captured in the previous planar models presented earlier in this thesis.

- The dynamics of the rolling model can produce a C-shaped bend that rotates around the body axis, as observed during rolling behaviour in the real larva.

- The dynamics of the self-righting model should cause all segments to (torsionally) align with the head when it is fixed to the substrate, as observed during self-righting behaviour in the real larva.

- An initial model of the larval ventral nerve cord has been presented. This model

builds upon the ring-attractor architecture presented in chapter 3.

- The dynamics of the VNC model produces a stable, spatially localised bump of neural activity that propagates along the nerve cord in the absence of sensory input, as observed in the isolated nerve cord of the real animal.

Limitations:

- While the mechanics of self-righting and rolling have been modelled, these models neglect neural control of these behaviours entirely.
- Self-righting and rolling mechanics are not yet incorporated into the models of chapter 3 and 4 – a more complete model of 3-dimensional mechanics is yet to be constructed.
- A thorough comparison of the VNC model to available experimental data is yet to be completed.

6.2 Mechanics of self-righting behaviour

When the larva is turned on its back, it displays self-righting behaviour in which it initially swings its head around seemingly at random, attaches its mouth hooks to the substrate once contact is made, then propagates a torsional wave along the body which aligns the rest of the body with the head.

Investigating righting behaviour thus requires us to model the torsion around the body axis of the larva. We can do this by modelling the animal's segments as discrete massive disks interacting via a quadratic elastic potential energy. The kinetic energy of the i'th segment is

$$T = \frac{1}{2} I \dot{\phi}_i^2 \tag{6.1}$$

where I is the moment inertia of the segment about the body axis, ϕ_i is the rotation of the i'th segment around the body axis, relative to the surface normal of the (assumed planar) environment, and $\dot{\phi}$ is thus the torsional angular velocity of the i'th segment.

Elastic energy is stored whenever the body is in torsion, i.e. when the difference in rotation of two neighbouring segments differs. We model this potential energy as

$$U = \frac{1}{2} k \left[\phi_i - \phi_{i-1}\right]^2 \tag{6.2}$$

Writing the kinetic and potential energies in vector notation gives

$$T = \frac{1}{2} I \dot{\phi}^T \dot{\phi} \tag{6.3}$$

$$U = \frac{1}{2} k \phi^T \mathbf{D}_{2,f} \phi \tag{6.4}$$

where $\mathbf{D}_{2,f}$ is the $N \times N$ second difference matrix with free boundary conditions

$$\mathbf{D}_{2,f} = \begin{bmatrix} 1 & -1 & & & \\ -1 & 2 & -1 & & \\ & \ddots & \ddots & \ddots & \\ & & -1 & 2 & -1 \\ & & & -1 & 1 \end{bmatrix} \tag{6.5}$$

Which can be combined to form the Lagrangian

$$L = \frac{1}{2} I \dot{\phi}^T \dot{\phi} - \frac{1}{2} k \phi^T \mathbf{D}_{2,f} \phi \tag{6.6}$$

We next introduce the following Rayleigh dissipation function to model the effects of viscous damping

$$R = -\eta \dot{\phi}^T \mathbf{D}_{2,f} \dot{\phi} \tag{6.7}$$

where η is the torsional coefficient of viscosity. The dissipative Lagrange equations are then

$$\frac{\mathrm{d}}{\mathrm{d}t} \left[\frac{\partial L}{\partial \dot{\phi}} \right] = \frac{\partial L}{\partial \phi} + \frac{\partial R}{\partial \dot{\phi}} \tag{6.8}$$

substituting our expressions for the Lagrangian and Rayleigh dissipation function gives

$$I \ddot{\phi} = -k \mathbf{D}_{2,f} \phi - \eta \mathbf{D}_{2,f} \dot{\phi} \tag{6.9}$$

We next find the equilibria of this system by looking for extrema of the elastic potential, for which

$$\frac{\partial U}{\partial \phi} = \mathbf{0} \tag{6.10}$$

Imposing this condition gives

$$\mathbf{D}_{2,f}\phi = 0 \tag{6.11}$$

i.e. the equilibria belong in the nullspace of $\mathbf{D}_{2,f}$. Since this matrix is of rank $N-1$, there must exist a one-dimensional family of equilibria. Inspection of the second difference matrix shows that these must correspond to $\phi = [c, c, \cdots, c]^T$, i.e. at equilibrium, all segments are aligned with a constant rotation relative to the substrate. If we assume that one segment is fixed relative to the substrate (e.g. if the mouth hooks are attached to the substrate at the head, as occurs during righting behaviour) then we must have an equilibrium in which all body segments are aligned with the substrate.

Since the Rayleigh dissipation function is negative definite, any motion must cause the body to lose energy and tend towards it's mechanical equilibrium at the minimum of the potential energy. Thus, regardless of starting configuration, if one segment is fixed relative to the substrate, then the rest of the body will eventually align with this segment and come to rest. For the larva, this means that attachment of the mouth hooks to the substrate is sufficient for self-righting.

What of the transitory behaviour? How does the body get from it's starting configuration to the righted, aligned configuration?

We can gain some insight by noting that the continuum limit of the model transforms the second difference matrix into a second derivative with respect to the distance along the body axis, x, so that the equations of motion become

$$I\frac{\partial^2\phi}{\partial t^2} = -k\frac{\partial^2\phi}{\partial x^2} - \eta\frac{\partial^2}{\partial x^2}\frac{\partial\phi}{\partial t} \tag{6.12}$$

This is simply the standard (conservative) wave equation with an additional damping term. So, we expect the motion of the body to consist of travelling waves of torsion which slowly decay, ultimately acting to align all of the body segments.

6.3 Mechanics of rolling behaviour

Under suitable nociceptive input, the larva produces an escape response in which it curls into a C-shaped bend and then rapidly rolls "sideways", maintaining a C-shaped configuration relative to the substrate as it rolls.

To investigate rolling behaviour, we must therefore model the bending of the larva both "horizontally" and "vertically". We accomplish this by modelling the midline of the larva as an anistropic elastic rod capable of bending in two dimensions, but

incapable of torsional or axial deformations. The model midline is discretised into a set of N point masses located at the boundaries between body segments. We focus on the small-amplitude behaviour of the model, describing the configuration of the larva by the deflection of each segment boundary in y (lateral) and z (ventrodorsal) dimensions relative to its equilibrium configuration. We denote the flexural natural frequencies associated with each axis of deflection as $\omega_y = \sqrt{k_y/m}$ and $\omega_z = \sqrt{k_z/m}$, respectively, where k_y and k_z are the flexural stiffnesses in each direction.

The Hamiltonian (total energy) of the larva is then given by

$$H(\mathbf{y},\mathbf{z},\mathbf{p}_y,\mathbf{p}_z) = \frac{1}{2}\left[\mathbf{p}_y^T\mathbf{p}_y + \omega_y^2\mathbf{y}^T\mathbf{D}_4\mathbf{y} + \mathbf{p}_z^T\mathbf{p}_z + \omega_z^2\mathbf{z}^T\mathbf{D}_4\mathbf{z}\right] \tag{6.13}$$

where $\mathbf{D}_4$ is the $N \times N$ fourth difference matrix with free boundary conditions

$$\mathbf{D}_4 = \begin{bmatrix} 1 & -2 & 1 & & & & \\ -2 & 5 & -4 & 1 & & & \\ 1 & -4 & 6 & -4 & 1 & & \\ & \ddots & \ddots & \ddots & \ddots & \ddots & \\ & & 1 & -4 & 6 & -4 & 1 \\ & & & 1 & -4 & 5 & -2 \\ & & & & 1 & -2 & 1 \end{bmatrix} \tag{6.14}$$

Since $\mathbf{D}_4$ is a real symmetric matrix, we can decompose it according to the eigendecomposition $\mathbf{D}_4 = \Phi\Lambda\Phi^T$ where Φ is the orthogonal matrix of eigenvectors of $\mathbf{D}_4$ and Λ is the diagonal matrix of eigenvalues of $\mathbf{D}_4$. Therefore, making a linear transformation to *modal* coordinates given by $Y = \Phi^T y$, $P_Y = \Phi^T p_y$ and $Z = \Phi^T z$, $P_Z = \Phi^T p_z$ simplifies the Hamiltonian to

$$H(\mathbf{Y},\mathbf{Z},\mathbf{P}_Y,\mathbf{P}_Z) = \frac{1}{2}\left[\mathbf{P}_Y^T\mathbf{P}_Y + \omega_y^2\mathbf{Y}^T\Lambda\mathbf{Y} + \mathbf{P}_Z^T\mathbf{P}_Z + \omega_z^2\mathbf{Z}^T\Lambda\mathbf{Z}\right] \tag{6.15}$$

Due to the fact Λ is diagonal, this expression is simply a sum of independent harmonic oscillator energies

$$H(\mathbf{Y},\mathbf{P}_Y,\mathbf{Z},\mathbf{P}_Z) = \sum_{i=1}^{N}\frac{1}{2}\left[P_{Y,i}^2 + \omega_y^2\lambda_i Y_i^2\right] + \sum_{i=1}^{N}\frac{1}{2}\left[P_{Z,i}^2 + \omega_z^2\lambda_i Z_i^2\right] \tag{6.16}$$

where the oscillator frequencies are given by $\omega_y\sqrt{\lambda_i}$ and $\omega_z\sqrt{\lambda_i}$.

We will focus on the pair of bending modes with the lowest non-zero frequency, which correspond to C-shaped bending of the larva, though in principle all of what

follows should apply to any other pair of modes with identical spatial components. We will set the modal coordinates and momenta of all other bending modes to 0 and denote the natural frequencies of the two C-shaped modes as ω_1 and ω_2. In this case the Hamiltonian simplifies to

$$H(Y,Z,P_Y,P_Z) = \frac{1}{2}\left[P_Y^2 + P_Z^2 + \omega_1^2 Y^2 + \omega_2^2 Z^2\right] \tag{6.17}$$

where we have dropped the subscript on the modal coordinates and momenta for notational clarity.

In what follows we will first consider the isotropic case in which $\omega_1 = \omega_2 = \omega$ and then consider the anisotropic case in which the natural frequencies differ.

Starting with the isotropic case, we find the Hamiltonian simplifies further to

$$H(Y,Z,P_Y,P_Z) = \frac{1}{2}\left[P_Y^2 + P_Z^2 + \omega^2(Y^2 + Z^2)\right] \tag{6.18}$$

The dynamics for the modal coordinates and momenta can be obtained from Hamilton's equations

$$\dot{Y} = \frac{\partial H}{\partial P_Y} = P_Y \tag{6.19}$$

$$\dot{Z} = \frac{\partial H}{\partial P_Z} = P_Z \tag{6.20}$$

$$\dot{P}_Y = \frac{\partial H}{\partial Y} = -\omega^2 Y \tag{6.21}$$

$$\dot{P}_Z = \frac{\partial H}{\partial Z} = -\omega^2 Z \tag{6.22}$$

differentiating the first and second equations and substituting into the third and fourth equations, respectively, gives the second-order harmonic oscillator dynamics

$$\ddot{Y} + \omega^2 Y = 0 \tag{6.23}$$

$$\ddot{Z} + \omega^2 Z = 0 \tag{6.24}$$

which have the well-known solutions

$$Y = A\cos(\omega t + \alpha), \quad Z = B\cos(\omega t + \beta) \tag{6.25}$$

setting $\alpha = 0$ and $\beta = \pm\pi/2$ gives

$$Y = A\cos(\omega t), \quad Z = \pm B\sin(\omega t) \tag{6.26}$$

These are the parametric equations of an ellipse, which is described either clockwise or anti-clockwise about the origin over time depending upon the choice of a plus or minus sign in the Z equation. These solutions correspond to the C-shaped bend of the larva rotating around the body at a rate ω.

Alternatively, we may shift to a coordinate system in which the C-shaped bend stays in a fixed orientation relative to the world. In this case the body-fixed coordinate system must rotate at a rate $-\omega$. This corresponds to rolling behaviour, in which the C-shaped bend is held against the plane of the substrate by ground reaction forces which do not allow the bend to penetrate into the substrate itself, and the larval body rotates/rolls against the substrate.

6.4 Modelling the VNC as a sensory filter

In chapter 3, I observed that during locomotion the *Drosophila* larva ought to transfer power preferentially into the high Q-factor, low spatial frequency, modes of its body, as these experience less viscous friction and are therefore more efficient. This corresponds to the observation that, during peristalsis, the larva actively compresses several segments at any given moment (corresponding to a low spatial frequency pattern of muscular activation along the body wall).

Let us now examine how the VNC can accomplish this preferential transfer of power into the high-Q modes. We will proceed from the axial mechanical model presented in chapters 2 and 3, focusing only on the pair of modal coordinates associated with the lowest spatial and temporal frequency and the lowest damping ratio. From now on we will denote these coordinates $X^{(1)}$ and $X^{(2)}$. We will proceed by constructing a VNC model that uses proprioceptive inputs to estimate the modal velocities, $\dot{X}^{(1)}$ and $\dot{X}^{(2)}$, and then uses these estimates directly to orchestrate power flow.

To begin, we will neglect the dynamics of the VNC and assume that sensory information can be directly, instantaneously passed to the motor outputs. To achieve positive power flow, the VNC must apply a modal control that is proportional to the corresponding modal velocity. This is most straightforwardly achieved by setting these quantities to be equal $U^{(1)} = \dot{X}^{(1)}$ and $U^{(2)} = \dot{X}^{(2)}$.

Alternatively, we can use the fact that for wave motion the two high-Q modes oscillate sinusoidally with a 90 degree phase shift, and that the velocity and position of each modal coordinate are also separated by a 90 degree phase shift. In other words, if we assume the modal coordinates are producing a travelling wave, so that Equation 9 (within the published paper) holds, then we have

$$\dot{X}^{(1)} = A\omega\sqrt{\lambda_i}\sin\left(\omega\sqrt{\lambda_i}t\right) = \omega\sqrt{\lambda_i}X^{(2)} \tag{6.27}$$

and

$$\dot{X}^{(2)} = \pm A\omega\sqrt{\lambda_i}\cos\left(\omega\sqrt{\lambda_i}t\right) = -\omega\sqrt{\lambda_i}X^{(1)} \tag{6.28}$$

For a travelling wave in the opposite direction we must interchange the coordinates $X^{(1)}$ and $X^{(2)}$ in our calculations so that

$$\dot{X}^{(2)} = \omega\sqrt{\lambda_i}X^{(1)}, \quad \dot{X}^{(1)} = -\omega\sqrt{\lambda_i}X^{(2)} \tag{6.29}$$

Clearly this allows the *velocity* of one of the modes to be estimated from the *position* of the other. This implies the control laws $U^1 = X^2$ and $U^2 = -X^1$ or $U^1 = -X^2$ and $U^2 = X^1$, with the choice of control law indicating whether we are orchestrating power flow into a forward or backward wave.

We now convert these putative control laws from modal coordinates into our original coordinate system in order to find the corresponding mappings of sensory inputs into muscle tensions. Under the first scheme, we have

$$\mathbf{u} = \Phi_1 U^1 + \Phi^2 U^2 = \Phi_1 \dot{X}^1 + \Phi^2 \dot{X}^2 = \Phi^1 \Phi^{1,T} \dot{\mathbf{x}} + \Phi^2 \Phi^{2,T} \dot{\mathbf{x}} = \left[\Phi^1 \Phi^{1,T} + \Phi^2 \Phi^{2,T}\right] \dot{\mathbf{x}} \tag{6.30}$$

where the sensorimotor transformation matrix in square brackets can be calculated explicitly from our earlier expressions for the eigenvectors, and has the element

$$\cos\left(\frac{2\pi(j-k)}{N-1}\right) \tag{6.31}$$

in the j'th row and k'th column. Under the second control scheme we have

$$\mathbf{u} = \Phi_1 U^1 + \Phi^2 U^2 = \pm\left(\Phi_1 X^2 - \Phi^2 X^1\right) = \pm\left(\Phi^1 \Phi^{2,T} \mathbf{x} - \Phi^2 \Phi^{1,T} \mathbf{x}\right) = \pm\left[\Phi^1 \Phi^{2,T} + \Phi^2 \Phi^{1,T}\right] \mathbf{x} \tag{6.32}$$

where once again the sensorimotor transformation matrix in square brackets can be calculated explicitly from our earlier expressions for the eigenvectors, and has the element

$$\pm \sin\left(\frac{2\pi(j-k)}{N-1}\right) \tag{6.33}$$

in the j'th row and k'th column.

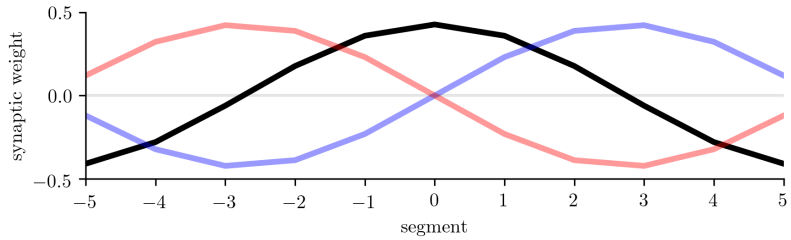

Figure 6.1: Three possible sensorimotor connection schemes for power flow into high-Q modes: stretch rate (direction independent, black), stretch for forward propagation (red), stretch for backward propagation (blue)

These mappings tell us that the muscle fibres within a segment should display cosine-tuning to the pattern of stretch rates, or sine-tuning to the pattern of stretches, along the body wall. The first mapping can be seen to roughly correspond to the connectivity of our previous model, but it has a broader tuning of excitation and inhibition allowing preferential power flow into only the high-Q modes. The second pair of mappings can be understood as utilising the properties of wave motion to predict the stretch rate at a point in the body by looking to the stretch either to the left or right of that point – during wave motion, the current pattern of segmental compression in one part of the body forms a good estimate of future segmental compression further along the body, since this pattern will propagate over time.

I note that the particular connectivity patterns derived here are determined by the mechanical models presented in the previous chapters, so that modifying the assumptions in those models could lead to alternative connectivity schemes. In particular, relaxing the fixed-length (internal incompressibility) constraint should act to introduce an impedance discontinuity into the axial mechanics (see discussion of Chapter 3) and thus should alter the eigenvectors/mode shapes presented here.

6.4.1 Fusing the sensorimotor mappings

How might we combine these different schemes? We believe this could be accomplished by including a ring attractor architecture in the model. This is motivated by the observation that the sensorimotor connection weights we have derived from the requirement for power flow into the high-Q modes of the body, are exactly the weights used in ring attractor models. Secondly, ring attractors are generally considered useful tools in the integration of distinct sensory inputs to form an estimate of an angular variable – in the larva, the current position of the compression-rate wave in the body is an angular variable, since head and tail are mechanically coupled via the visceral piston.

Therefore, we construct a ring attractor using the standard dynamics

$$\dot{v}_i = r\left[\tanh(\mathbf{w}_i^T\mathbf{v} + \mathbf{z}_i^T\mathbf{x}) - v_i\right] \tag{6.34}$$

where v_i is the firing rate within the i'th segment of the VNC, $\mathbf{w}_i$ is the weight vector decribing connections from segments of the VNC into the i'th segment, $\mathbf{z}_i$ is the weight vector decribing connections from the mechanical state variables into the VNC (i.e. sensory feedback connections), and r is a rate parameter governing the overall timescale of neural dynamics.

In line with standard approaches in the study of ring attractors and with the weighting scheme we derived from the mechanics, we set the weight vector $\mathbf{w}_i$ to be a cosine centred on the i'th segment, so that the j'th element of $\mathbf{w}_i$ is given by

$$w_{i,j} = a\cos\left(\frac{2\pi(j-i)}{N}\right) \tag{6.35}$$

where a is a gain parameter. The weights $\mathbf{z}_i$ are exactly those derived from the mechanics, so stretch sensitivity is given by a sine function while stretch rate sensitivity is given by a cosine centred on the i'th segment

$$z_{i,j} = A\cos\left(\frac{2\pi(j-i)}{N}\right),\ j \in [0,N] \tag{6.36}$$

$$z_{i,j} = B\sin\left(\frac{2\pi(j-i)}{N}\right),\ j \in [N,2N] \tag{6.37}$$

where A and B are gain parameters.

6.4.2 Coupling the VNC to the body

We now study the closed-loop dynamics of the system by allowing the VNC model to produce muscle forces. We take muscle tension in the i'th body segment to be given by the rectified neural activity within the corresponding segment of the VNC, since muscles should be able to cause only active compressions and not extensions. We introduce frictive losses due to tissue viscosity into the mechanical model, and check whether the VNC model is capable of maintaining locomotion.

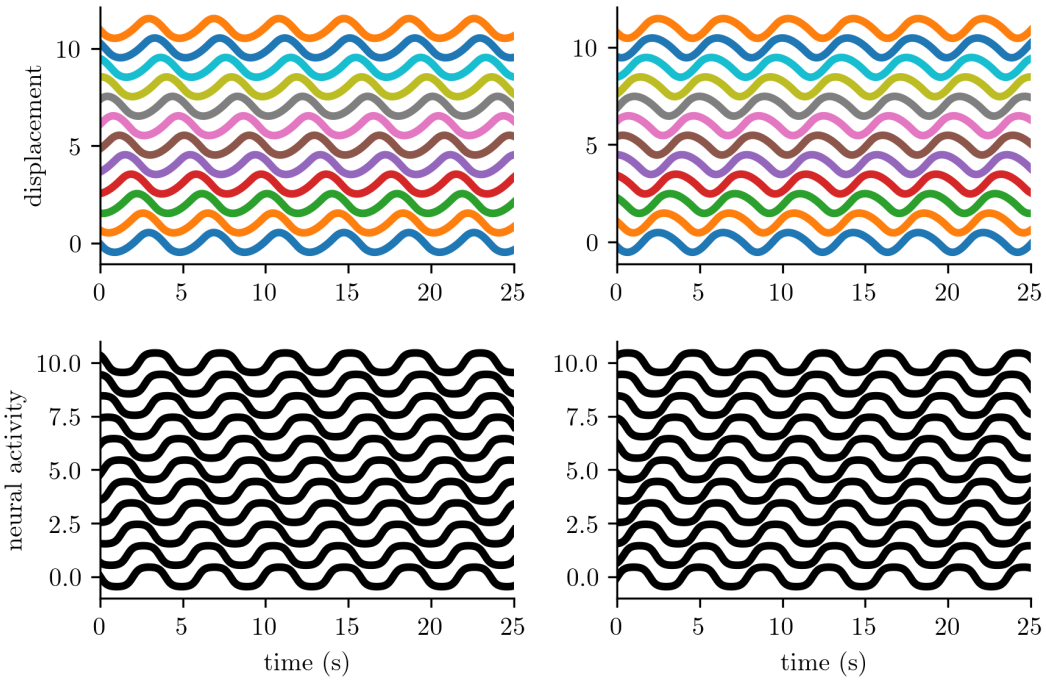

Figure 6.2: Forward and backward waves in the closed-loop system.

Figure 6.3: Power flow in closed-loop system.

We then introduce a forward/backward bias via nearest-neighbour connections within the VNC, in which there is slight excitation from one segment to the next and slight inhibition from one segment to the preceding segment, or vice versa. The VNC weight vectors are now

$$w_{i,j} = a\cos\left(\frac{2\pi(j-i)}{N}\right) + b \begin{cases} 1 & j = i-1 \\ -1 & j = i+1 \\ 0 & \text{otherwise} \end{cases} \tag{6.38}$$

where the parameter b has been introduced in order to set the strength of nearest-neighbour interactions.

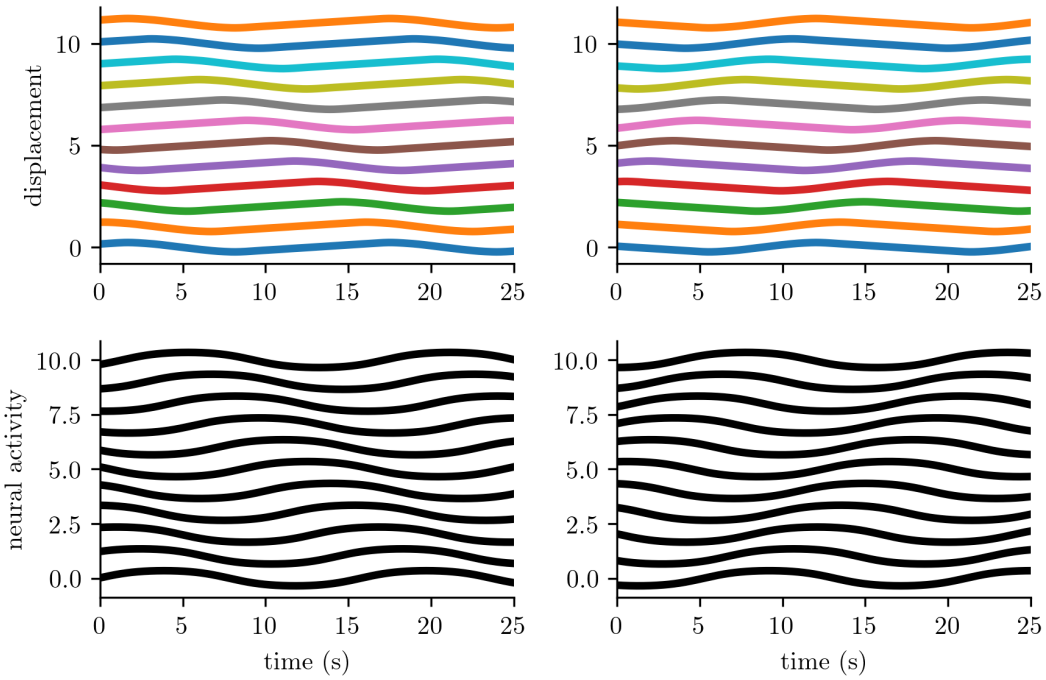

Figure 6.4: Persistence of neural waves in absence of sensory input.

We next remove sensory input from the VNC model. In this case, waves of activity can be seen to propagate through the nerve cord. The speed of propagation is reduced compared to peristalsis in the intact model, matching experimental observations. This is due to the fact that the nearest-neighbour interaction is fairly weak.

Indeed, in the intact model it is possible for mechanical waves to propagate opposite to that predicted by the imposed bias in the VNC – i.e. waves may propagate forward along the body despite the fact that the nearest-neighbour connections would cause them to propagate backwards in the isolated VNC. In this case the peristaltic wave travels slightly more slowly in the intact model that it otherwise would have.

This suggests that the observed activity patterns in the larval VNC may not in fact correspond to “fictive locomotion” as is often claimed, but could be a product of a fairly weak biasing influence in the VNC network, which is revealed only when the larva is dissected, and which functions as a simple propagation speed control rather than as a central pattern generator.

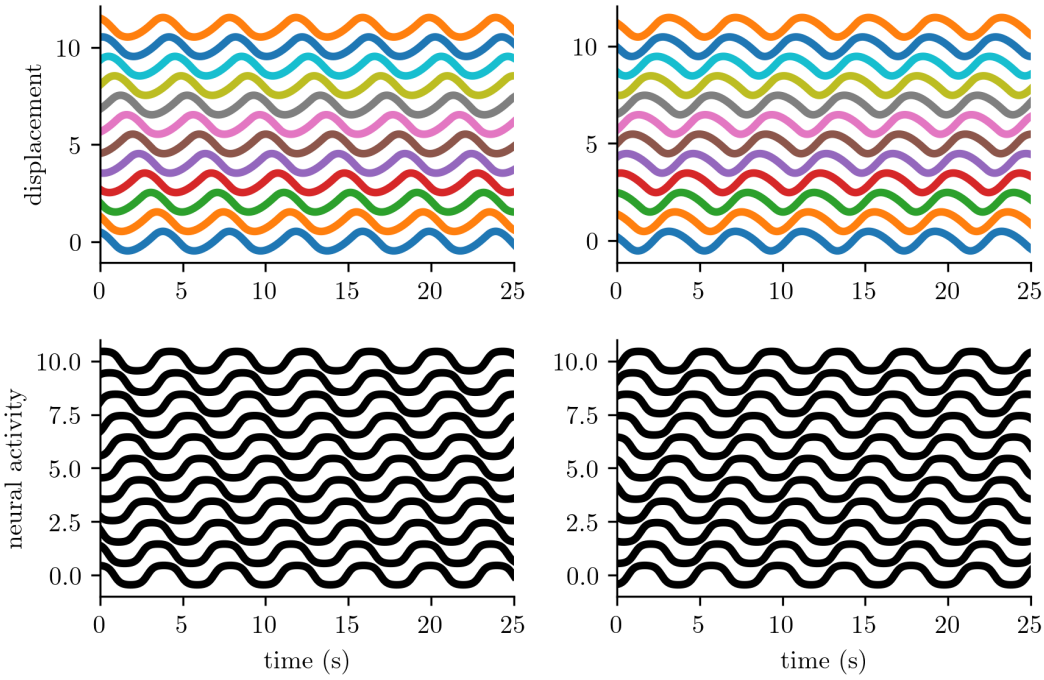

Figure 6.5: Waves can propagate against the internal directional bias. Waves may propagate backward despite the nearest-neighbour coupling within the VNC preferring forward waves (left) or vice versa (right).

Chapter 7

Discussion and future directions

In this thesis I have primarily investigated the generation of locomotion, exploration, and taxis behaviours in the *Drosophila* larva.

In chapter 2, I presented a model of the axial mechanics of the larva, and demonstrated how the animal's body physics could be exploited to produce peristalsis by using linear, segmentally localised, positive feedback of strain rate. This chapter is primarily based upon, and includes a complete reproduction of, the paper *A Model of Larval Biomechanics Reveals Exploitable Passive Properties for Efficient Locomotion* (2015).

In chapter 3, I extended the mechanical model to study motion in the plane, including both axial and transverse deformations of the body. I developed the previous feedback law into a simple model of the larval nervous system. The model included both a segmentally localised reflex arc as well as long-range, mutual inhibition between segments. The complete model was capable of generating both peristalsis and spontaneous reorientation, leading to emergent exploration behaviour in the form of a deterministic superdiffusion process grounded in the chaotic mechanics of the larva's body. This chapter is primarily based upon, and includes a complete reproduction of, the paper *Modelling the mechanics of exploration in larval* Drosophila (2019, *in production*).

In chapter 4, I further extended the model to include taxis behaviour. This was accomplished by introducing new transverse reflexes which, similar to the axial reflexes developed in chapters 2 and 3, perform feedback of the local bending velocity. These reflexes were coupled to a descending sensory input which determined the strength and sign of the reflex. This chapter is primarily based upon, and includes a complete reproduction of, the paper *A Neuromechanical Model of Larval Chemotaxis* (2018).

While in chapter 2 I used a Newtonian approach to modelling the mechanics of the larva, in chapters 3 and 4 I developed the mechanical models within a Hamiltonian, energy-focused, framework. Inspired by the ease with which the models could be developed and analysed within this framework, in chapter 5 I focused on the application of energy-based modelling techniques within the field of soft robotics, arguing for the adoption of a port-Hamiltonian modelling approach in this field. Soft robots tend to "cross" several physical domains, including mechanical, chemical, and electromagnetic components. For this reason a Hamiltonian (energy) based approach is particularly appealing, since energy and power flow are essentially domain-independent. This chapter is primarily based upon, and includes a complete reproduction of, the paper *Controlling and Simulating Soft Robotic Systems: Insights from a Thermodynamic Perspective* (2016).

As each chapter is based upon a published paper, each includes a detailed discussion of the conclusions, implications, and significance of the work contained within. Here I will focus on the major contributions of this body of work as a whole, before moving on to discuss key areas for future research.

7.1 Major contributions

- This thesis presents the first model of the axial mechanics of the *Drosophila* larva, along with the first integrated neuromechanical model of peristalsis in the *Drosophila* larva. It presents the first and only existing model of the planar mechanics of the *Drosophila* larva, and the first and only existing integrated neuromechanical model of peristalsis, turning, and exploration.

- This thesis presents a strong proof of principle, that chaotic body mechanics can drive spontaneous exploration behaviour even in the absence of neural decision-making or central pattern generation, and without neural chaos or stochasticity. Even if/when the models presented here are falsified or extended, this proof of principle may be useful in studying other animals, and strikingly demonstrates the potential importance of understanding mechanics when studying animal behaviour.

- The neural models developed in this thesis provide novel, falsifiable predictions that differ from those made by other models of the larval motor system. The models I have presented are motivated by clear physical principles, they are both

conceptually and architecturally simpler than existing alternative models, and they better fit the existing experimental data on the structure of the larval motor system. This will hopefully contribute to the development of experimental programs investigating larval neurobiology.

- The thesis suggests a useful energy-based modelling approach to be deployed in the emerging field of soft robotics.

7.2 Further developments

Possible future developments of the work presented in this thesis fall roughly into two broad groups: experimental and theoretical. I will consider each in turn.

7.2.1 Experimental directions

The mechanical models presented in this thesis require validation. All of the models presented assume that the viscoelastic response of larval tissues is well-approximated by a linear, Kelvin-Voigt constitutive model, i.e. elastic potential energy is approximated as a positive-definite quadratic form in the generalised internal coordinates (segmental stretches and segmental bending angles), while viscous power loss is treated as a negative-definite quadratic form in the generalised internal velocities/momenta (segmental stretch rates and segmental bending rates). A range of substrate interaction models are used, but all are of Coulomb type (a constant friction force which is independent of the magnitude of velocity).

These models are often employed as starting points in biomechanical modelling, and as argued in the discussion of chapter 3, I believe the general character of the results obtained from the mechanical models of this thesis should be independent of the particular choice of viscoelastic constitutive model. However, real tissue responses are often very complex and may lead to interesting behaviour that lay beyond the accessibility of the modelling approach used here. As one potential example, incorporating a quartic dependence of the elastic potential energy on the axial stretches (i.e. a cubic elastic response) would transform the axial mechanics into the form of a Fermi-Pasta-Ulam (FPU) lattice. The FPU system is known to exhibit soliton solutions, which may be of considerable interest in studying peristaltic wave propagation. However, whether such modifications of the model are warranted should depend upon experimental determination of real tissue responses.

I have (informally) observed that the results of the planar mechanical model are sensitive to the particular choice of friction parameters (as mentioned in the discussion of chapter 3). Experimental investigation of how exactly the larva mechanically interacts with its environment would be very useful in informing future development of (neuro)mechanical models of larval behaviour.

Moving on from potential mechanical experiments, the neural model I have constructed in this thesis (reaching its most developed form in chapter 4) opens up several avenues for experimental inquiry. These are extensively detailed in the discussion sections of chapters 3 and 4.

7.2.2 Theoretical directions

The models presented in this thesis may be extended in several different ways. In particular, chapter 6 leaves open some fertile directions for theoretical development.

First, the initial models of torsional and transverse mechanics, used to investigate self-righting and rolling behaviours in chapter 6, ought to be incorporated into the model of axial and transverse mechanics of chapters 3 and 4. This would allow a substantial portion of the larval behavioural repertoire to be modelling simultaneously – including rearing, lifting, rolling, righting, burrowing, peristalsis, turning, exploration, and taxis. This extension will require development of models of substrate interaction in three dimensions, where contact with the substrate can be made and broken by any part of the larva's cuticle, and the larva can even move through the substrate itself.

Second, the neural control of self-righting, rolling, rearing, etc. will need to be modelled. There has been subtantial experimental investigation of the neural circuits involved in producing rolling behaviour in reponse to noxious stimuli Ohyama et al. (2013, 2015). This work should be leveraged during the modelling process.

Finally, the preliminary model of the larval ventral nerve cord as a ring attractor (chapter 6) should be extensively compared to existing experimental data. The model promises to easily explain some experimental results that are not explained by existing models of the VNC Pehlevan et al. (2016). For instance, it appears that the current position of a peristaltic wave can be stored within the VNC, allowing halted waves to "restart" where they ended Inada et al. (2011). Existing models have struggled to reproduce this finding Pehlevan et al. (2016), but our model should be able to account for this phenomenon, as it is based on a ring attractor architecture rather than a rhythm generator architecture, and should therefore be capable of sustaining a stable bump of

activity, at a particular spatial location, indefinitely. However, the model presented in chapter 6 may struggle to explain some other experimental results. In particular, it has been observed that surgical ablation of VNC segments does no effect the ability of the VNC to propagate waves of activity Pulver et al. (2015). When only a few VNC segments remain, the neural activity within those segments appears to oscillate. It seems that this should be easier to explain with a model built upon a rhythm generator architecture than a ring attractor structure.

Bibliography

Adams, C. M., Anderson, M. G., Motto, D. G., Price, M. P., Johnson, W. A., and Welsh, M. J. (1998). Ripped pocket and pickpocket, novel drosophila deg/enac subunits expressed in early development and in mechanosensory neurons. *The Journal of Cell Biology*, 140(1):143–152.

Adler, J. (1966). Chemotaxis in Bacteria. *Science*, 153(3737):708–716.

Adler, M., Mayo, A., and Alon, U. (2014). Logarithmic and Power Law Input-Output Relations in Sensory Systems with Fold-Change Detection. *PLoS Computational Biology*, 10(8):e1003781.

Ainsley, J. A., Pettus, J. M., Bosenko, D., Gerstein, C. E., Zinkevich, N., Anderson, M. G., Adams, C. M., Welsh, M. J., and Johnson, W. A. (2003). Enhanced locomotion caused by loss of the ¡em¿drosophila¡/em¿ deg/enac protein pickpocket1. *Current Biology*, 13(17):1557–1563.

Alexander, R. M. (2003). *Principles of Animal Locomotion*. Princeton University Press, 1 edition.

Alves-Silva, J., Hahn, I., Huber, O., Mende, M., Reissaus, A., and Prokop, A. (2008). Prominent actin fiber arrays in drosophila tendon cells represent architectural elements different from stress fibers. *Molecular Biology of the Cell*, 19(10):4287–4297.

Apostolopoulou, A., Hersperger, F., Mazija, L., Widmann, A., Wüst, A., and Thum, A. (2014). Composition of agarose substrate affects behavioral output of drosophila larvae. *Frontiers in Behavioral Neuroscience*, 8:11.

Arrese, E. L. and Soulages, J. L. (2010). Insect fat body: Energy, metabolism, and regulation. *Annual Review of Entomology*, 55(1):207–225.

Bate, M. (1990). The embryonic development of larval muscles in drosophila. *Development*, 110(3):791–804.

Beckervordersandforth, R. M., Rickert, C., Altenhein, B., and Technau, G. M. (2008). Subtypes of glial cells in the drosophila embryonic ventral nerve cord as related to lineage and gene expression. *Mechanisms of Development*, 125(5):542 – 557.

Berg, H. C. and Brown, D. A. (1972). Chemotaxis in *Escherichia coli* analysed by Three-dimensional Tracking. *Nature*, 239:500–504.

Berni, J. (2015). Genetic Dissection of a Regionally Differentiated Network for Exploratory Behaviour in *Drosophila* Larvae. *Current Biology*, 25:1319–1326.

Berni, J., Pulver, S. R., Griffith, L. C., and Bate, M. (2012). Autonomous circuitry for substrate exploration in freely moving *Drosophila* larvae. *Current Biology*, 22(20):1861–70.

Berri, S., Boyle, J. H., Tassieri, M., Hope, I. A., and Cohen, N. (2009). C. elegans locomotion: a unified multidisciplinary perspective. *BMC Neuroscience*, 10(1):P16.

Berrigan, D. and Pepin, D. J. (1995). How maggots move: Allometry and kinematics of crawling in larval diptera. *Journal of Insect Physiology*, 41(4):329 – 337.

Bhounsule, P., Cortell, J., and Ruina, A. (2012). Design and control of ranger: an energy-efficient, dynamic walking robot. pages 441–448.

Boyle, J., Berri, S., and Cohen, N. (2012). Gait modulation in c. elegans: An integrated neuromechanical model. *Frontiers in Computational Neuroscience*, 6:10.

Braitenberg, V. (1986). *Vehicles: Experiments in Synthetic Psychology*. MIT Press.

Brooks, R. A. (1991). Intelligence without representation. *Artificial Intelligence*, 47(1):139 – 159.

Bush, B. M. (1965). Proprioception by the coxo-basal chordotonal organ, cb, in the legs of the crab, *Carcinus Maenas*. *Journal of Experimental Biology*, 42:285–297.

Caldwell, J. C., Miller, M. M., Wing, S., Soll, D. R., and Eberl, D. F. (2003). Dynamic analysis of larval locomotion in drosophila chordotonal organ mutants. *Proceedings of the National Academy of Sciences*, 100(26):16053–16058.

Cattaert, D. and Birman, S. (2001). Blockade of the central generator of locomotor rhythm by noncompetitive nmda receptor antagonists in drosophila larvae. *Journal of Neurobiology*, 48(1):58–73.

Chapman, G. (1950). Of the movement of worms. *Journal of Experimental Biology*, 27:29–39.

Choi, J. C., Park, D., and Griffith, L. C. (2004). Electrophysiological and morphological characterization of identified motor neurons in the drosophila third instar larva central nervous system. *Journal of Neurophysiology*, 91(5):2353–2365.

Collins, S., Ruina, A., Tedrake, R., and Wisse, M. (2005). Efficient bipedal robots based on passive-dynamic walkers. *Science*, 307(5712):1082–1085.

Couton, L., Mauss, A. S., Yunusov, Y., Diegelmann, S., F., E. J., and Landgraf, M. (2015). Development of connectivity in a motorneuronal network in *Drosophila* larvae. *Current Biology*, 25(5):568–576.

Davies, A., Louis, M., and Webb, B. (2015). A Model of *Drosophila* Larva Chemotaxis. *PLOS Computational Biology*, 11(11):1–24.

Ekeberg, O. (1993). A combined neuronal and mechanical model of fish swimming. *Biological Cybernetics*, 69:363–374.

Ekeberg, O. and Grillner, S. (1999). Simulations of neuromuscular control in lamprey swimming. *Philosophical Transactions of the Royal Society B*, 354(1385):895–902.

Enriquez, J., de Taffin, M., Crozatier, M., Vincent, A., and Dubois, L. (2012). Combinatorial coding of drosophila muscle shape by collier and nautilus. *Developmental Biology*, 363(1):27 – 39.

Fechner, G. T. (1860). *Elemente der Psychophysik*. Holt, Rinehart and Winston.

Fox, L. E., Soll, D. R., and Wu, C.-F. (2006). Coordination and modulation of locomotion pattern generators in *Drosophila* larvae: effects of altered biogenic amine levels by the tyramine beta hydroxlyase mutation. *The Journal of Neuroscience*, 26(5):1486–98.

Gepner, R., Mihovilovic Skanata, M., Bernat, N. M., Kaplow, M., and Gershow, M. (2015). Computations underlying *Drosophila* photo-taxis, odor-taxis, and multi-sensory integration. *eLife*, 4:e06229.

Gerber, B. and Stocker, R. F. (2006). The Drosophila Larva as a Model for Studying Chemosensation and Chemosensory Learning: A Review. *Chemical Senses*, 32(1):65–89.

Gjorgjieva, J., Berni, J., Evers, J. F., and Eglen, S. J. (2013). Neural circuits for peristaltic wave propagation in crawling *Drosophila* larvae: analysis and modeling. *Frontiers in computational neuroscience*, 7:1–24.

Godoy-Herrera, R. (1986). The development and genetics of digging behaviour in *Drosophila* larvae. *Heredity*, 56:33–41.

Gomez-Marin, A., Stephens, G. J., and Louis, M. (2011). Active sampling and decision making in *Drosophila* chemotaxis. *Nature Communications*, 2(441):1–10.

Greer-Phillips, S. E., Alexandre, G., Taylor, B. L., and Zhulin, I. B. (2003). Aer and Tsr guide *Escherichia coli* in spatial gradients of oxidizable substrates. *Microbiology*, 149:2661–2667.

Grillner, S. (2006). Biological Pattern Generation: The Cellular and Computational Logic of Networks in Motion. *Neuron*, 52(5):751–766.

Grillner, S. and Wallen, P. (1984). How does the Lamprey Central Nervous System make the Lamprey Swim? *Journal of Experimental Biology*, 112:337–357.

Grueber, W. B., Jan, L. Y., and Jan, Y. N. (2002). Tiling of the drosophila epidermis by multidendritic sensory neurons. *Development*, 129(12):2867–2878.

Grueber, W. B., Ye, B., Yang, C.-H., Younger, S., Borden, K., Jan, L. Y., and Jan, Y.-N. (2007). Projections of *Drosophila* multidendritic neurons in the central nervous system: links with peripheral dendrite morphology. *Development*, 134:55–64.

Hamlet, C. L., Hoffman, K. A., Tytell, E. D., and Fauci, L. J. (2018). The role of curvature feedback in the energetics and dynamics of lamprey swimming: A closed-loop model. *PLoS Computational Biology*, 14(8).

Heckscher, E. S., Lockery, S. R., and Doe, C. Q. (2012). Characterization of Drosophila larval crawling at the level of organism, segment, and somatic body wall musculature. *The Journal of Neuroscience*, 32(36):12460–71.

Hernandez-Nunez, L., Belina, J., Klein, M., Si, G., Claus, L., Carlson, J. R., and Samuel, A. D. (2015). Reverse-correlation analysis of navigation dynamics in *Drosophila* larva using optogenetics. *eLife*, 4:e06225.

Hoang, B. and Chiba, A. (2001). Single-cell analysis of drosophila larval neuromuscular synapses. *Developmental Biology*, 229(1):55 – 70.

Holland, O. (2003). The first biologically inspired robots. *Robotica*, 21:351–363.

Hoyle, G. (1977). *Identified Neurons and Behaviour of Arthropods*. Springer US.

Hu, B. and Tu, Y. (2014). Behaviours and Strategies of Bacterial Navigation in Chemical and Nonchemical Gradients. *PLoS Computational Biology*, 10(6).

Hughes, C. L. and Thomas, J. B. (2007). A sensory feedback circuit coordinates muscle activity in *Drosophila*. *Molecular and Cellular Neuroscience*, 35(2):383 – 396.

Hwang, R. Y., Zhong, L., Xu, Y., Johnson, T., Zhang, F., Deisseroth, K., and Tracey, W. D. (2007). Nociceptive neurons protect ¡em¿drosophila¡/em¿ larvae from parasitoid wasps. *Current Biology*, 17(24):2105–2116.

Inada, K., Kohsaka, H., Takasu, E., Matsunaga, T., and Nose, A. (2011). Optical Dissection of Neural Circuits Responsible for *Drosophila* Larval Locomotion with Halorhodopsin. *PLOS ONE*, 6(12):1–10.

Inestrosa, N. C., Sunkel, C. E., Arriagada, J., Garrido, J., and Godoy-Herrera, R. (1996). Abnormal development of the locomotor activity in yellow larvae of drosophila: a cuticular defect? *Genetica*, 97(2):205–210.

Ito, K., Urban, J., and Technau, G. M. (1995). Distribution, classification, and development ofdrosophila glial cells in the late embryonic and early larval ventral nerve cord. *Roux's archives of developmental biology*, 204(5):284–307.

Jan, L. Y. and Jan, Y. N. (1976). Properties of the larval neuromuscular junction in drosophila melanogaster. *The Journal of Physiology*, 262(1):189–214.

Jenett, A., Rubin, G., Ngo, T.-T., Shepherd, D., Murphy, C., Dionne, H., Pfeiffer, B., Cavallaro, A., Hall, D., Jeter, J., Iyer, N., Fetter, D., Hausenfluck, J., Peng, H., Trautman, E., Svirskas, R., Myers, E., Iwinski, Z., Aso, Y., DePasquale, G., Enos, A., Hulamm, P., Lam, S., Li, H.-H., Laverty, T., Long, F., Qu, L., Murphy, S., Rokicki, K., Safford, T., Shaw, K., Simpson, J., Sowell, A., Tae, S., Yu, Y., and Zugates, C. (2012). "a gal4-driver line resource for *Drosophila* neurobiology". *Cell Reports*, 2(4):991–1001.

Jürgens, G. (1987). Segmental organisation of the tail region in the embryo of drosophila melanogaster. *Roux's archives of developmental biology*, 196(3):141–157.

Kadakia, N. and Emonet, T. (2019). Front-end Weber-Fechner gain control enhances the fidelity of combinatorial odor coding. *eLife*, 8:e45293.

Kane, E. A., Gershow, M., Afonso, B., Larderet, I., Klein, M., Carter, A. R., de Bivort, B. L., Sprecher, S. G., and Samuel, A. D. T. (2013). Sensorimotor structure of *Drosophila* larva phototaxis. *Proceedings of the National Academy of Sciences*, 110(40):E3868–E3877.

Kier, W. M. (2012). The diversity of hydrostatic skeletons. *Journal of Experimental Biology*, 215:1247–1257.

Kier, W. M., Trivedi, D., Rahn, C. D., and Walker, I. D. (2008). Soft robotics: Biological inspiration, state of the art, and future research. *Applied Bionics and Biomechanics*, 5(3):99–117.

Kim, M. D., Wen, Y., and Jan, Y.-N. (2009). Patterning and organization of motor neuron dendrites in the drosophila larva. *Developmental Biology*, 336(2):213 – 221.

Kohsaka, H., Okusawa, S., Itakura, Y., Fushiki, A., and Nose, A. (2012). Development of larval motor circuits in *Drosophila*. *Development, Growth, and Differentiation*, 54(3):408–419.

Kohsaka, H., Takasu, E., Morimoto, T., and Nose, A. (2014). A Group of Segmental Premotor Interneurons Regulates the Speed of Axial Locomotion in *Drosophila* Larvae. *Current Biology*, 24:2632–2642.

Kurdyak, P., Atwood, H. L., Stewart, B. A., and Wu, C.-F. (1994). Differential physiology and morphology of motor axons to ventral longitudinal muscles in larval drosophila. *Journal of Comparative Neurology*, 350(3):463–472.

Lahiri, S., Shen, K., Klein, M., Tang, A., Kane, E., Gershow, M., Garrity, P., and Samuel, A. D. T. (2011). Two alternating motor programs drive navigation in *Drosophila* larva. *PLOS ONE*, 6(8):e23180.

Landau, L. D. and Lifshitz, E. M. (1976). *Mechanics*, volume 1 of *Course of Theoretical Physics*. Butterworth-Heinemann, 3 edition.

Landgraf, M., Bossing, T., Technau, G. M., and Bate, M. (1997). The origin, location, and projections of the embryonic abdominal motorneurons of drosophila. *Journal of Neuroscience*, 17(24):9642–9655.

Landgraf, M., Sánchez-Soriano, N., Technau, G. M., Urban, J., and Prokop, A. (2003). Charting the drosophila neuropile: a strategy for the standardised characterisation of genetically amenable neurites. *Developmental Biology*, 260(1):207 – 225.

Landgraf, M. and Thor, S. (2006). Development of drosophila motoneurons: Specification and morphology. *Seminars in Cell & Developmental Biology*, 17(1):3 – 11. Drosophila as a Model for the Central Nervous System Frog Embryo Development.

Luo, L., Gershow, M., Rosenzweig, M., Kang, K., Fang-Yen, C., and Garrity, P. A. (2010). Navigational Decision Making in *Drosophila* Thermotaxis. *The Journal of Neuroscience*, 30(12):4261–4272.

Macnab, R. M. and Koshland, J. R. (1972). The Gradient-Sensing Mechanism in Bacterial Chemotaxis. *PNAS*, 69(9):2509–2512.

Mauss, A., Tripodi, M., Evers, J. F., and Landgraf, M. (2009). Midline signalling systems direct the formation of a neural map by dendritic targeting in the drosophila motor system. *PLOS Biology*, 7(9):1–18.

McGeer, T. (1990). Passive dynamic walking. *The International Journal of Robotics Research*, 9(2):62–82.

McLachlan, N. W. (1947). *Theory and Application of Mathieu Functions*. Clarendon Press.

Merritt, D. and Whitington, P. (1995). Central projections of sensory neurons in the *Drosophila* embryo correlate with sensory modality, soma position, and proneural gene function. *The Journal of Neuroscience*, 15(3):1755–1767.

Ohyama, T., Jovanic, T., Denisov, G., Dang, T. C., Hoffmann, D., Kerr, R. A., and Zlatic, M. (2013). High-throughput analysis of stimulus-evoked behaviors in *Drosophila* larva reveals multiple modality-specific escape strategies. *PLOS ONE*, 8(8):1–21.

Ohyama, T., Schneider-Mizell, C. M., Fetter, R. D., Aleman, J. V., Franconville, R., Rivera-Alba, M., Mensh, B. D., Branson, K. M., Simpson, J. H., Truman, J. W., Cardona, A., and Zlatic, M. (2015). A multilevel multimodal circuit enhances action selection in *Drosophila*. *Nature*, 520:644–639.

Okusawa, S., Kohsaka, H., and Nose, A. (2014). Serotonin and downstream leucokinin neurons modulate larval turning behavior in *Drosophila*. *The Journal of Neuroscience*, 34(7):2544–2558.

Pehlevan, C., Paoletti, P., and Mahadevan, L. (2016). Integrative neuromechanics of crawling in *D. melanogaster* larvae. *eLife*, 5:e11031.

Pierce-Shimomura, J. T., Chen, B. L., Mun, J. J., Ho, R., Sarkis, R., and McIntire, S. L. (2008). Genetic analysis of crawling and swimming locomotory patterns in c. elegans. *Proceedings of the National Academy of Sciences*, 105(52):20982–20987.

Pierce-Shimomura1999 (1999). The Fundamental Role of Pirouettes in *Caenorhabditis elegans* Chemotaxis. *Journal of Neuroscience*, 19(21):9557–9569.

Proske, U. and Gandevia, S. C. (2012). The proprioceptive senses: Their roles in signalling body shape, body position and movement, and muscle force. *Physiological Reviews*, 92:1651–1697.

Pulver, S. R., Bayley, T. G., Taylor, A. L., Berni, J., Bate, M., and Hedwig, B. (2015). Imaging fictive locomotor patterns in larval *Drosophila*. *Journal of Neurophysiology*, 114(5):2564–2577.

Pulver, S. R. and Griffith, L. C. (2010). Spike integration and cellular memory in a rhythmic network from Na^+/K^+ pump current dynamics. *Nature Neuroscience*, 13(1):53–59.

Qi, Y. L. and Adler, J. (1989). Salt taxis in Escherichia coli bacteria and its lack in mutants. *PNAS*, 86(21):8358–8362.

Rickert, C., Kunz, T., Harris, K.-L., Whitington, P. M., and Technau, G. M. (2011). Morphological Characterization of the Entire Interneuron Population Reveals Principles of Neuromere Organization in the Ventral Nerve Cord of *Drosophila*. *The Journal of Neuroscience*, 31(44):15870–15883.

Robertson, J. L., Tsubouchi, A., and Tracey, W. D. (2013). Larval defense against attack from parasitoid wasps requires nociceptive neurons. *PLOS ONE*, 8(10).

Rohrbough, J. and Broadie, K. (2002). Electrophysiological analysis of synaptic transmission in central neurons of drosophila larvae. *Journal of Neurophysiology*, 88(2):847–860.

Rutherford, T. A. and Croll, N. A. (1979). Wave Forms of *Caenorhabditis elegans* in a Chemical Attractant and Repellent and in Thermal Gradients. *The Journal of Nematology*, 11(3):232–240.

Santos, M. G., Jorge, S. A. C., Brillet, K., and Pereira, C. A. (2007). Improving heterologous protein expression in transfected drosophila s2 cells as assessed by egfp expression. *Cytotechnology*, 54(1):15–24.

Schaefer, J. E., Worrell, J. W., and Levine, R. B. (2010). Role of Intrinsic Properties in *Drosophila* Motoneuron Recruitment During Fictive Crawling. *Journal of Neurophysiology*, 104:1257–1266.

Schoofs, A., Hückesfeld, S., Schlegel, P., Miroschnikow, A., Peters, M., Zeymer, M., Spieß, R., Chiang, A.-S., and Pankratz, M. J. (2014). Selection of motor programs for suppressing food intake and inducing locomotion in the drosophila brain. *PLOS Biology*, 12(6):1–17.

Schulze, A., Gomez-Marin, A., Rajendran, V. G., Lott, G., Musy, M., Ahammad, P., Deogade, A., Sharpe, J., Riedl, J., Jarriault, D., Trautman, E. T., Werner, C., Venkadesan, M., Druckmann, S., Jayaraman, V., and Louis, M. (2015). Dynamical feature extraction at the sensory periphery guides chemotaxis. *eLife*, 4:e06694.

Sherman, M. Y., Timkina, E. O., and Glagolev, A. N. (1982). Viscosity taxis in *Escherichia coli*. *FEMS Microbiology Letters*, 13:137–140.

Simon, M. A., Fusillo, S. J., Colman, K., and Trimmer, B. A. (2010). Motor patterns associated with crawling in a soft-bodied arthropod. *Journal of Experimental Biology*, 213(13):2303–2309.

Sokolowski, M. B. and Hansell, K. P. (1992). The foraging locus: behavioral tests for normal muscle movement in rover and sitter drosophila melanogaster larvae. *Genetica*, 85(3):205–209.

Song, W., Onishi, M., Jan, L. Y., and Jan, Y. N. (2007). Peripheral multidendritic sensory neurons are necessary for rhythmic locomotion behavior in *Drosophila* larvae. *Proceedings of the National Academy of Sciences*, 104(12):5199–5204.

Srinivasan, S., Lance, K., and Levine, R. B. (2012). Segmental differences in firing properties and potassium currents in drosophila larval motoneurons. *Journal of Neurophysiology*, 107(5):1356–1365.

Steels, L. (2007). *Fifty Years of AI: From Symbols to Embodiment - and Back*, pages 18–28. Springer Berlin Heidelberg, Berlin, Heidelberg.

Strecher, A. C. and Sprecher, S. G. (2012). "seeing the light: photobehavior in fruit fly larvae". *Trends in Neurosciences*, 35(2):104–110.

Suslak, T. J., Armstrong, J. D., and Jarman, A. P. (2011). A general mathematical model of transduction events in mechano-sensory stretch receptors. *Network: Computation in Neural Systems*, 22(1-4):133–142.

Suster, M. L. and Bate, M. (2002). Embryonic assembly of a central pattern generator without sensory input. *Nature*, 416(6877):174–178.

Szigeti, B., Deogade, A., and Webb, B. (2015). Searching for motifs in the behaviour of larval *Drosophila melanogaster* and *Caenorhabditis elegans* reveals continuity between behavioural states. *Journal of The Royal Society Interface*, 12(113).

Tastekin, I., Riedl, J., Schilling-Kurz, V., Gomez-Marin, A., Truman, J., and Louis, M. (2015). Role of the subesophageal zone in sensorimotor control of orientation in *Drosophila* larva. *Current Biology*, 25(11):1448–1460.

Tian, L., Hires, S. A., Mao, T., Huber, D., Chiappe, M. E., Chalasani, S. H., Petreanu, L., Akerboom, J., McKinney, S. A., Schreiter, E. R., Bargmann, C. I., Jayaraman, V., Svoboda, K., and Looger, L. L. (2009). Imaging neural activity in worms, flies and mice with improved gcamp calcium indicators. *Nature Methods*, 6:871–.

Tsunoda, S. and Salkoff, L. (1995). The major delayed rectifier in both drosophila neurons and muscle is encoded by shab. *Journal of Neuroscience*, 15(7):5209–5221.

Tytell, E. D., Holmes, P., and A.H. Cohen (2011). Spikes alone do not behaviour make: Why neuroscience needs biomechanics. *Current Opinion in Neurobiology*, 21(5):816–822.

Volk, T. (1999). Singling out *Drosophila* tendon cells: a dialogue between two distinct cell types. *Trends in Genetics*, 15(11):448 – 453.

Walter, W. G. (1953). *The Living Brain*. Norton.

Ward, S. (1973). Chemotaxis by the Nematode *Caenorhabditis elegans*: Identification of Attractants and Analysis of the Response by Use of Mutants. *PNAS*, 70(3):817–821.

Wiersma, C. A. G. and Boettiger, E. G. (1959). Unidirectional movement fibres from a proprioceptive organ of the crab, *Carcinus Maenas*. *Journal of Experimental Biology*, 36:102–112.

Williams, T. L. and McMillen, T. (2015). Strategies for swimming: exploration of the behaviour of a neuro-musculo-mechanical model of the lamprey. *Biology Open*, 4:253–258.

Wystrach, A., Lagogiannis, K., and Webb, B. (2016). Continuous lateral oscillations as a core mechanism for taxis in *Drosophila* larvae. *eLife*, 5:e15504.

Xiang, Y., Yuan, Q., Vogt, N., Looger, L. L., Jan, L. Y., and Jan, Y. N. (2010). Light-avoidance-mediating photoreceptors tile the drosophila larval body wall. *Nature*, 468:921–.

Yarali, A., Ehser, S., Hapil, F. Z., Huang, J., and Gerber, B. (2009). Odour intensity learning in fruit flies. *Proceedings of the Royal Society B: Biological Sciences*, 276(1672):3413–3420.

Zhang, J., Schulze, K. L., Hiesinger, P. R., Suyama, K., Wang, S., Fish, M., Acar, M., Hoskins, R. A., Bellen, H. J., and Scott, M. P. (2007). Thirty-one flavors of drosophila rab proteins. *Genetics*, 176(2):1307–1322.

Zill, S. N. (1985). Plasticity and proprioception in insects i. responses and cellular properties of individual receptors of the locust metathoracic femoral chordotonal organ. *Journal of Experimental Biology*, 116:435–461.

Špela Schrader and Merritt, D. J. (2007). Dorsal longitudinal stretch receptor of drosophila melanogaster larva – fine structure and maturation. *Arthropod Structure & Development*, 36(2):157 – 169.

Špela Schrader and Merritt, D. J. (2010). The role of the trp channel nompc in *Drosophila* larval and adult locomotion. *Neuron*, 67(3):373 – 380.